UCL

Adsorption and desorption of model interstellar ices on a dust grain analogue surface

John Leonard Edridge

Thesis for the degree of Doctor of Philosophy

University College London

Chemistry

2010

I, John Leonard Edridge, confirm that the work presented in this thesis is my own. Where information has been derived from other sources, I confirm that this has been indicated in this thesis.

Signed:……

Abstract

Molecular ices freeze out on the surface of dust grains within the interstellar medium (ISM). Dust grains form 1% of the mass of the ISM, and are comprised of siliceous or carbonaceous material. Molecular ices are H_2O-rich, with major components including CO and CO_2, along with trace amounts of sulphur containing molecules, including SO_2. CS_2 ice has also been detected in cometary comae.

Previous studies of the adsorption and desorption of H_2O-rich ices show that the H_2O structure dictates the desorption, diffusion and trapping of molecules within the ice. This is important in star forming regions, where the evaporation of molecular ices is not spontaneous. Hence, the chemical composition of the resultant star or planetary system is affected by these processes in molecular ices.

There is little previous experimental work concerning the adsorption and desorption of sulphur bearing ices. Therefore a study of CO_2, SO_2 and CS_2-bearing, H_2O-rich, ices adsorbed on a carbonaceous surface at ≤ 33 K, has been conducted using reflection absorption infrared spectroscopy (RAIRS) and temperature programmed desorption (TPD). Qualitative inspection of the ices shows that the molecular size impacts the ability of a species to diffuse or trap within the ice. Quantitative analysis of the TPD spectra has also been conducted, to determine desorption energies and orders. These have been used in an astrochemical model, simulating the warming of ices in a star forming region.

A model has also been created to simulate RAIR spectra of adsorbate layers on a surface. Experiments show that amorphous CO and CO_2 ices exhibit unusual splitting of the C-O stretch, typically characteristic of crystalline ice. A model was developed to investigate this splitting within the amorphous ice. Results show that this splitting occurs as a function of the dielectric properties of the ice.

Acknowledgements

For Rachel

Firstly, I would like to thank my PhD supervisor, Dr Wendy Brown, for being a great mentor, having faith in me, trusting me and giving me the support and motivation I needed when I needed it. I would also like to thank Wendy for being a great friend and for always being there for me and patient with me, especially when things in my personal life were going badly.

Next I would like to thank my family for all of their support in completing this PhD. I would like to thank mum and Paul for financial support, without which I would not have been able to complete this PhD. I am literally in your debt! I would also like to thank Dawn and Leah for all of the emotional support they've given me over the years, helping me relax and vent stress! I would also like to thank mum again for reading this thesis, trying to understand what it says and checking my grammar for me!

I also want to thank all of the people I've worked with in the laboratory over the years. In particular I want to thank Dr Daren Burke, with whom I worked with in the first two years of my PhD, and who showed me most of what I know about experimental surface science. I would also like to thank the two undergraduate research project students I worked closely with on the CO_2 and SO_2 experiments, Kati Freimann and Kathryn Summers. I would also like to thank all of the support and technical staff, in particular Roy Northeast, Dave Knapp, Len Parrish, Michael Williams and Dr Michael Parkes.

I would like to thank all of my friends for their support whilst completing this PhD. In particular I would like to thank Dr Elspeth Latimer, who has been there with me and for me throughout this entire project, during both the good and bad times. Not only has Elz been there with me, sharing gossip over lunch, drinking copious amounts of tea and indulging in procrastination. I would like to thank her for being my moral compass, putting up with my perpetual moaning and literally slapping me back to reality when I've needed it. I would also like to thank, in no particular order, Tom, Hugh, Hinnah, Dad, Al, Pru, Jack, Heather, Tom, Nick, Dave, Ross and Jarvis for providing a welcome distraction.

Finally, but certainly not least importantly, I would like to thank Kathryn for putting up with me whilst writing this thesis, as well as for all of the things that words cannot describe and that don't need to be said.

Contents

List of Figures

List of Tables

List of Abbreviations

ASW	Amorphous Solid Water
AU	Arbitrary Units (as used on TPD spectra)
AU	Astronomical Units
CI	Crystalline Ice
FWHM	Full Width Half Maximum
HOPG	Highly Oriented Pyrolytic Graphite
ISM	Interstellar Medium
ISO	Infrared Space Observatory
LEED	Low Energy Electron Diffraction
LO	Longitudinal Optical or Orthogonal Optical
OFHC	Oxygen-Free High Conductivity Copper
PAH	Polycyclic Aromatic Hydrocarbon
QMS	Quadrupole Mass Spectrometer
RAIRS	Reflection Absorption Infrared Spectroscopy
RGA	Residual Gas Analysis
TMP	Turbo-Molecular Pump
TO	Transverse Optical
TPD	Temperature Programmed Desorption
TSP	Titanium Sublimation Pump
UHV	Ultra High Vacuum
UV	Ultraviolet

Chapter 1: Introduction

This thesis describes laboratory experiments performed to investigate the adsorption and desorption of a range of astrophysically relevant ices on an interstellar dust grain analogue surface. In particular, reflection absorption infrared (RAIR) experiments were conducted on pure ices of CO, CO_2 and H_2O, adsorbed on a highly oriented pyrolytic graphite (HOPG) surface below 33 K, and used as a diagnostic tool for the creation of an infrared simulation. RAIR and temperature programmed desorption (TPD) experiments have also been performed, investigating pure and H_2O dominated ices containing CO_2, CS_2 and SO_2. These results have been used to study the observed trapping and diffusion properties of adsorbates in a H_2O matrix as a function of the size of the volatile molecule. This data has also been used to derive kinetic information about the desorption process, which can be used in astrochemical models to simulate the evaporation of ices in star forming regions within the interstellar medium (ISM).

1.1. Interstellar Medium

The Milky Way, a barred spiral galaxy 10^6 light years in diameter, is part of the Local Group of approximately 30 galaxies. It is home to the Solar System as one of many known planetary systems, and the Sun as one of up to 4×10^{11} stars. As viewed from Earth (figure 1.1), the Milky Way appears as a diffuse band of light. However, upon closer inspection, dark clumps are observed in the Milky Way, initially described as 'holes in the sky'[1,2]. These regions are not empty and void however, and are in fact composed of clouds of gas and dust. It is within these clouds, in the vast region between the stars known as the ISM, where new stars are born.

The ISM comprises ≈10% of the mass of the Galaxy. This in turn is predominantly composed of gas, 99%, with 1% of the mass of the ISM being found in dust grains. The gas within the ISM is composed of 93% H and H_2 and 6% He. The remaining 1% of the gas within the ISM is made up of heavier elements, such as C, N, O and trace amounts of other elements. The matter within the ISM is not uniformly distributed and a variety of regions, characterised by temperature and H atom density, can be identified.

The majority of the volume of the ISM, up to ≈70%, is known as the hot ionised medium or coronal interstellar gas[3]. With a mean temperature of up to 10^6 K and density down to 10^{-4} atoms cm^{-3}, the hot ionised medium contains no molecules, with the dominant species being H^+. The conditions of the hot ionised medium are so harsh that highly ionised species such as O^{6+} are found. Also occupying much of the volume of the ISM is the intercloud

Figure 1.1. The Milky Way as viewed from the Earth's surface in Chile. Taken from http://apod.nasa.gov/apod/ap051004.html.

medium. The intercloud medium is a region of gas which fills up to ≈20% of the volume of the ISM. This region is also relatively hot, 10^4 K, and diffuse, 0.1 atoms cm^{-3}, with the dominant species being H.

The majority of the mass of the ISM is found in clouds of cold gas and dust, surrounded by the intercloud medium, and occupies less than 1% of the volume of the ISM. The temperature and density of these clouds are an indication of the evolution of the cloud, which forms part of the evolutionary cycle of star formation and death[2,4]. Diffuse clouds have a temperature and density of around 100 K and 100 atoms cm^{-3}. They are composed predominantly of atomic H, with partial formation of H_2, and trace concentrations of CO and H_2CO. Over time, diffuse clouds cool and collapse to become dense molecular clouds or dark clouds, figure 1.2. These clouds have a rich composition of molecules, and characteristically have a temperature between 10 - 20 K and density up to 10^6 atoms cm^{-3}. A relatively high dust grain density, typically around 10^4 grains cm^{-3}, is also observed in these clouds, which has a significant impact on the chemistry within these regions.

The dust grains within dense molecular clouds play several pivotal roles in the chemistry within these regions. Firstly, as evidenced by the fact that molecular clouds appear as dark patches in the sky, dust grains shield the cloud from visible and ultraviolet (UV) radiation. This hinders photo-dissociation processes of the molecular species within the cloud, allowing a rich composition of molecules to exist with appreciable lifetimes. Dust grains also act as a third

Figure 1.2. The Snake Nebula, also known as Barnard 72, is one of many dark clouds of gas and dust which obscure the light from background star clusters. Taken from http://apod.nasa.gov/apod/ap050521.html.

body for surface chemistry, accounting for the formation of several molecular species, as well as acting as a reservoir for interstellar ices. Therefore, as a direct result of dust grains, the composition of dense molecular clouds is varied. To date over 140 molecules have been detected within the ISM, in both the gas phase and on the surface of dust grains, as summarised in table 1.1. Also indicated in table 1.1 are the components of interstellar ice mantles, most of which are formed via surface chemistry on the dust grain surface.

Due to the low temperature within these clouds, gravitational forces play a pivotal role over astrophysical timescales. Pockets of hydrogen gas within dense molecular clouds may begin to condense and collapse, in many cases initiated by the shockwave of an astrophysically recent and nearby supernova. Eventually this collapse results in the formation of a protostar, and as a direct result will lead to the gradual warming of the surrounding region, described as a hot core. The warming in hot core regions will promote chemistry on the surface of interstellar dust grains, as well as allowing for the thermal desorption of icy mantles from the dust grain surface. Once evaporated, the warm gas may undergo further chemistry to produce a rich mixture of saturated organic molecules. The protostar and consequent rotating accretion disk, formed from the remnants of the collapsing dense cloud, and composed of the gas and dust warmed and processed by the hot core and protostar, may then evolve to give a planetary

system such as the Solar System. Therefore the chemical composition of the gas, dust and icy mantles is of critical importance to the makeup of a new star system, whether a planetary system evolves, and may even be an important factor in determining whether the planetary system supports life.

Table 1.1. Table showing some of the molecules detected in the ISM to date. Adapted from http://astrochemistry.net/. Molecules found in icy mantles are shaded in grey[5-7].

Number of atoms					
2	3	4	5	6	7+
H_2	H_3^+	CH_3	CH_4	C_2H_4	CH_3CH_3
CH	CH_2	NH_3	NH_4^+	CH_3OH	CH_3NH_2
CH^+	NH_2	H_3O^+	CH_2NH	CH_3CN	CH_3CCH
NH	H_2O	C_2H_2	H_3CO^+	CH_3NC	c-C_2H_4O
OH	H_2O^+	H_2CN	SiH_4	NH_2CHO	CH_3CHO
OH^+	C_2H	$HCNH^+$	c-C_3H_2	CH_3SH	C_2H_5OH
HF	HCN	H_2CO	H_2CCC	H_2CCCC	CH_3OCH_3
C_2	HNC	c-C_3H	CH_2CN	HCCCCH	CH_2CHCN
CN	HCO	l-C_3H	H_2CCO	$H_2C_3N^+$	CH_3CH_2CN
CN^+	HCO^+	HCCN	NH_2CN	c-H_2C_3O	C_3H_4O
CO	HN_2^+	HNCO	HCOOH	HC_2CHO	CH_3CH_2CHO
CO^+	HOC^+	$HNCO^-$	C_4H	C_5H	CH_3COCH_3
N_2^+	HNO	$HOCO^+$	C_4H^-	HC_4N	CH_3CONH_2
SiH	H_2S	H_2CS	HC_3N	C_5N	CH_2OHCHO
NO	H_2S^+	C_3N	HCCNC		CH_3COOH
CF^+	C_3	C_3O	HNCCC		$HCOOCH_3$
HS	C_2O	HNCS	C_5		$HOCH_2CH_2OH$
HS^+	OCN^-	SiC_3	SiC_4		CH_3C_4H
HCl	CO_2	C_3S			CH_2CCHCN
SiC	CO_2^+				CH_3C_3N
SiN	N_2O				C_6H
CP	HCS^+				C_6H^-
CS	NaCN				C_6H_2
SiO	MgCN				HCCCCCCH
PN	MgNC				HC_5N
AlF	c-SiC_2				NH_2CH_2COOH
NS	AlNC				C_6H_6
SO	SiCN				C_7H
SO^+	SiNC				CH_3C_6H
NaCl	C_2S				C_8H
SiS	OCS				C_8H^-
AlCl	SO_2				HC_7N
S_2					HC_9N
FeO					$HC_{11}N$
KCl					

During the formation of a planetary system, dust particles aggregate into lumps of rock, most of which become incorporated into planetary bodies. However, due to a variety of processes and collisions, some of these rocks are knocked into an elliptical orbit. These are known as comets. Depending on the process in which a comet was formed, the cometary ice may have the same chemical composition as the solar nebula in which it was formed.

Therefore, to further understand the conditions in which our Solar System was created specifically, investigations into cometary ices are also of great importance[2].

1.2. Dust Grains

Although only 1% of the mass of the ISM is composed of dust grain particles, they play a crucial role in the chemistry that occurs in star forming regions. It has been shown from chemical models that gas phase chemistry alone cannot account for the abundance of H_2, along with a number of other molecular species. Dust grains are also required to account for the composition of interstellar ices, where the abundance of species found in ices, such as H_2O, NH_3, CH_4 and CH_3OH for example, are not accountable from accretion onto the grain surface from the gas phase. Therefore, dust grains are believed to act as a third body in formation reactions, acting as both a reservoir and catalyst for reactions.

The composition of interstellar dust grains is not entirely known, however, clues about the nature of dust grains are obtained from interstellar extinction and polarisation[2], as shown in figure 1.3, and from the infrared spectrum of interstellar ices and dust grains[8,9], shown in figure 1.4. The shape of the extinction curve in the low wavenumber region, up to 4 μm^{-1}, suggests that the majority of dust grains have a mean radius of 0.1 µm. A bump in the

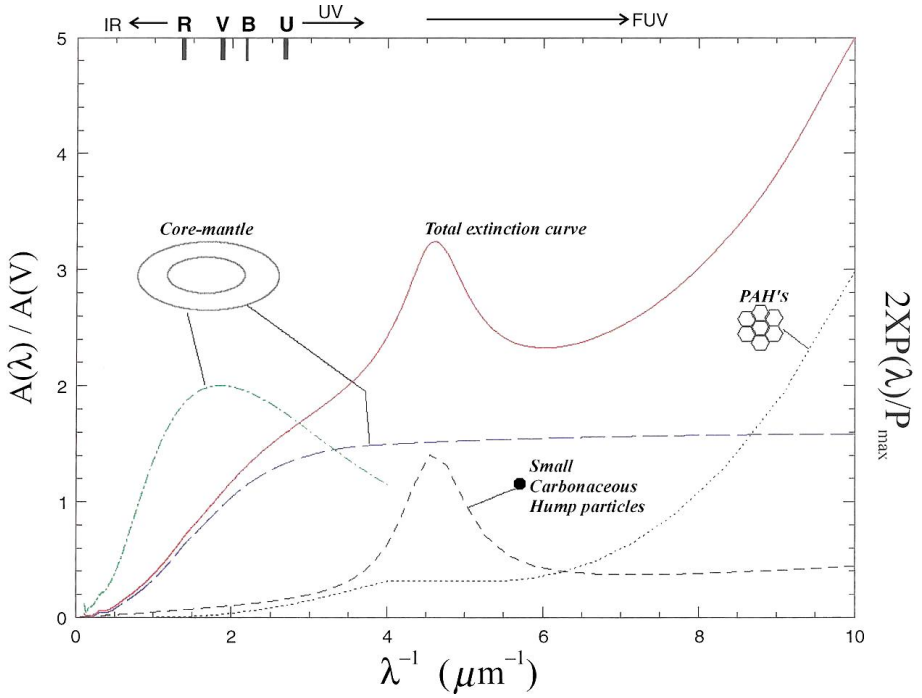

Figure 1.3. The average extinction curve (solid line) and mean polarisation curve (dash-dot line) of the diffuse interstellar medium, taken from reference [2]. Also shown are three fits to the average extinction curve showing extinction from 0.1 µm radius grains (long dashed line), a fit responsible for the 216 nm hump in the extinction curve (short dashed line) and a fit responsible for the ultraviolet extinction (dotted line).

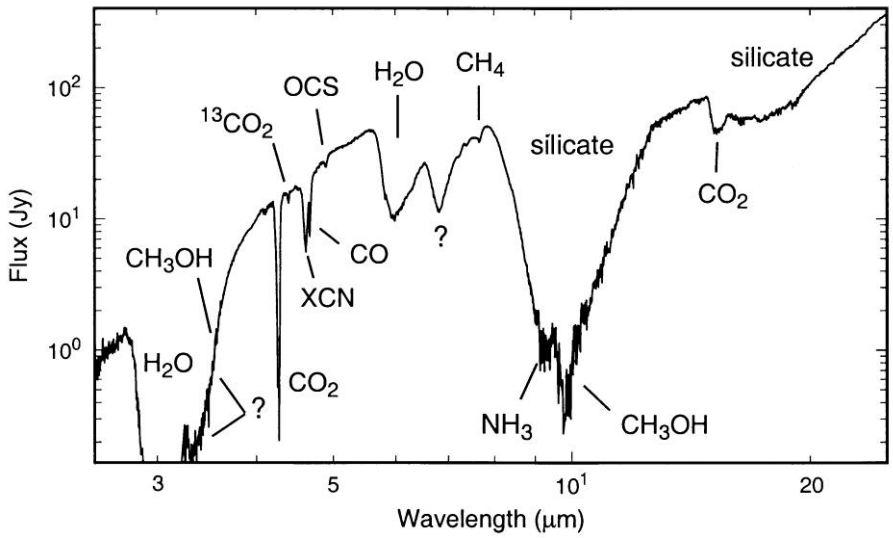

Figure 1.4. Infrared spectrum of W33A taken from the short wavelength spectrometer on the infrared space observatory. Taken from reference [9].

extinction curve is observed at 4.6 μm^{-1} which is thought to be characteristic of very small carbonaceous particles, with a radius of approximately 0.003 μm[2,3]. The steady rise in the extinction curve at short wavelengths, known as the ultraviolet extinction, is the result of larger, polycyclic aromatic hydrocarbon (PAH) particles as well as small siliceous particles[2,3]. Further evidence for siliceous particles within the dust grains is observed in the infrared spectrum of molecular clouds. Figure 1.4 shows the infrared spectrum, taken from the short wavelength spectrometer on the infrared space observatory, of the star forming region W33A[9]. The silicate absorption is clearly observed. The depletion of several condensable elements from the average solar abundance, such as O, Mg and Fe, also suggests that dust grains may be composed of pyroxenes, $Mg_xFe_{1-x}SiO_3$, and olivines, $Mg_{2x}Fe_{2-2x}SiO_4$.[10] Evidence for the shape of interstellar dust grains is also given. The interstellar polarisation must be caused by non-spherical particles which are aligned to a magnetic field[2,3]. This indicates that dust grains are elongated in shape, and are generally oriented within a dense cloud.

In summary, dust grains are known to be elongated particles which range in size between 1 nm - 1 μm[10,11]. They are known to be composed of siliceous and carbonaceous material. Although the exact structure of the dust grains is unknown, a popular model considers the grain as a refractory silicate core covered with an organic refractory mantle[2,11,12]. The carbonaceous material has been ascribed to graphite[13], amorphous carbon[14], hydrogenated amorphous carbon[15] and PAHs[16] to name but a few. There is no universal model for a dust grain analogue due to the complex and uncertain composition of interstellar grains. Several dust grain analogues have been used in previous studies ranging from inert surfaces such as Au[17-24] and CsI[25-35] to more astophysically relevant surfaces including siliceous surfaces, olivine[36-38] and Si[39-49], as well as carbonaceous surfaces such as amorphous carbon[36,50-52] and

HOPG[20,53-74]. Therefore, the use of HOPG as a dust grain analogue in laboratory based studies, as used in the experiments described in this thesis, is suitable. HOPG is composed of sheets of graphene, one atom thick layers of carbon densely packed into a honeycomb crystal lattice[75,76]. HOPG has previously been used to study the formation of H_2 and HD[53,54,63-73] and to investigate the adsorption and desorption of molecular ices including H_2O, NH_3, CH_3OH and C_2H_5OH[20,55-62,73,74].

Understanding the chemical and physical behaviour of an adsorbate on a surface is essential to surface science. This includes understanding how the adsorbates are bonded to the surface, and how the surface affects the adsorption of molecular ices. For example, CO has been shown to be physisorbed on an HOPG surface[77], where only weak van der Waals forces hold the adsorbate on the surface. The binding strength of physisorbed species is characteristically found to be < 60 kJ mol^{-1}. Conversely, CO is adsorbed onto a more reactive surface, such as Cu(111), via chemisorption[78,79]. In these systems, the adsorbate is held on the surface via strong chemical bonds and the binding strength is characteristically in excess of 60 kJ mol^{-1}. As interstellar dust grains are thought to be generally inert, it is expected that the majority of interstellar ice mantles are physisorbed on the dust grain surface.

1.3. Ice Mantles

As evidenced by infrared spectra of molecular clouds within the ISM, shown in figure 1.4, dust grains act as a reservoir for interstellar ices. At the low temperatures of molecular clouds, down to 10 K, gas phase species readily condense onto the surface of dust grains, forming icy mantles, where the mantle composition does not reflect the gas phase composition or abundances[80]. This is due to a range of processes, including the formation of more complex molecules on the grain surface, as well as energetic processing of the ices by UV radiation and cosmic rays[80-88], as depicted in figure 1.5[2,62,80,89]. Table 1.2 shows the typical composition and abundances of icy mantles, with respect to H_2O, in a range of star forming regions[9,90-112]. The abundances are also compared with typical abundances in cometary ices[4,113].

In a molecular cloud, where the H:H_2 ratio is typically high, common for immature clouds, reactive gaseous species such as H, D, C, N, O and CO condense onto the dust grain surface and form new species via thermal hopping and quantum tunnelling[80,84]. As the H:H_2 ratio is high, hydrogenation processes dominate, and polar (H_2O, NH_3, CH_4 and CH_3OH rich) ices form on the surface[80,82,84,85,114-116]. If the H:H_2 ratio is low however, typical for more mature clouds, species such as C, N, O and CO are free to react forming apolar (CO, CO_2, O_2 and N_2 rich) ices[27,80,115,117]. Ices may also undergo energetic processing, via thermal processes, UV or cosmic radiation from nearby stars, or a protostar and hot core[80-88]. This processing has been shown, via

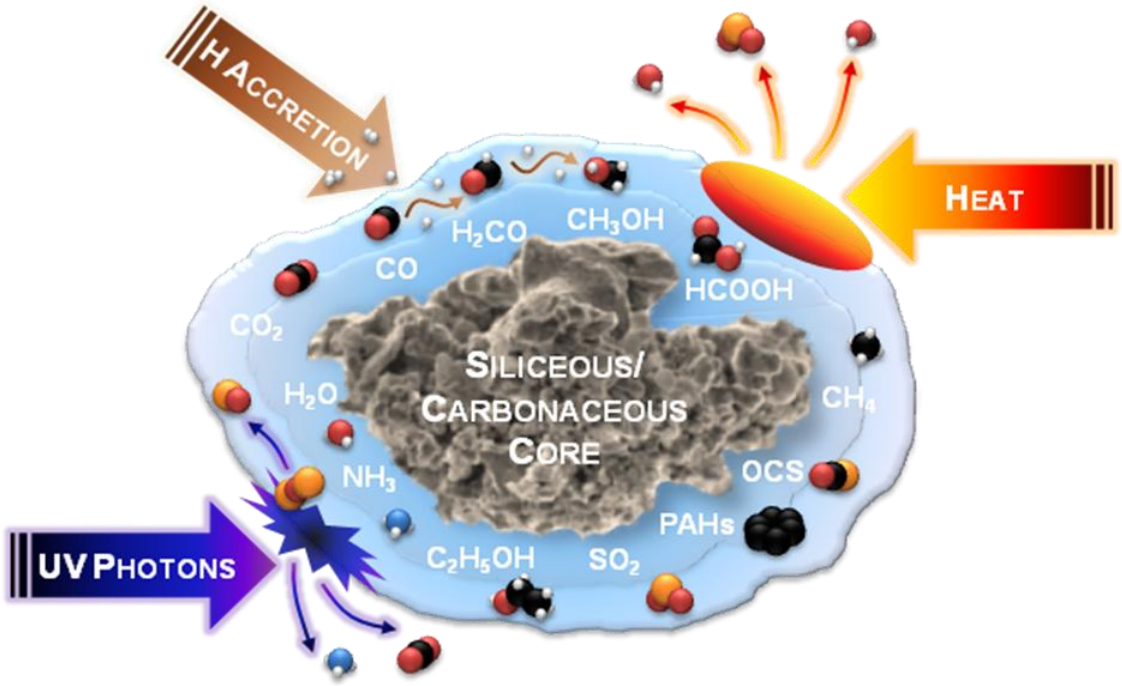

Figure 1.5: Schematic diagram of the energetic processes occurring on a typical ice mantle covered dust grain surface. Adapted from references [2,62,80,89].

laboratory based experiments, to allow for the formation of more complex organic species, such as C_2H_5OH[24,81,87]. Desorption processes also occur upon warming of the icy mantles, where the processed molecules are released into the gas phase to drive the formation of larger organic molecules.

Table 1.2. Ice abundance toward infrared sources and comets with respect to H_2O.

Ice	Elias 16[a]	NGC 7538 IRS9[b]	GL 7009S[c]	W33A[d]	GL 2136[e]	Sgr A*[f]	Comets[g]
H_2O	100	100	100	100	100	100	100
CO	25	16	15	8	2	< 12	5-30
CO_2	18	22	21	13	16	14	3-20
CH_4		2	4	1.5		2	1
CH_3OH	< 3	5	30	18	6	< 4	0.3-5
H_2CO		4	3	6	3	< 3	0.2-1
HCOOH		3		7		3	0.05
H_2S				< 0.2			
OCS	< 0.2		0.2	0.2			0.5
NH_3	≤9	13		15		20-30	0.1-1.8
XCN	< 0.5	1	1.5	3.5	0.3		0.01-0.4
SO_2		< 0.5		0.31			

From references; a = [94,95,100,102,107-109], b = [90,92,95,96,100,103,104,112], c = [98,99], d = [9,91,92,95,96,99,101,110-112], e = [93,95,100,103,105,106,115], f = [97,100] and g = [4,113].

The evaporation of icy mantles in hot core regions is not instantaneous and the ice constituents do not necessarily evaporate together[118]. This has consequences for the understanding of the gas phase chemistry in star forming regions, as reactive volatile species

are not injected into the gas phase at the same time. An example of this can be shown by the study of the desorption of a range of astrochemically relevant molecules from H_2O-rich ices[19], where the desorption of many species is dictated by the desorption of the H_2O itself.

Studies of the adsorption of H_2O on a surface below 120 K show that amorphous solid water (ASW) is formed[119-121]. ASW is thought to be the most abundant phase of H_2O ice in the ISM. It is a porous, low density phase of solid H_2O ice and is a metastable form of liquid H_2O. The exact morphology, porosity and density of ASW is not precisely known, and is a function of the temperature, pressure and angle of deposition[119-121]. Conversely, adsorption of H_2O onto a surface above 140 K produces crystalline ice (CI), a dense, ordered and non-porous form of solid H_2O. ASW can undergo an irreversible phase transition to CI upon warming to temperatures above 140 K. Between 120 - 140 K, ASW is thought to undergo a 'liquid like' transformation, where pores in the ice close[119-121]. These features of ASW have direct consequences for the desorption of volatile molecules inserted into the ASW ice. For example, small volatile molecules may diffuse through the porous ASW matrix to desorb at their natural sublimation temperature. The diffusion of larger molecules may be hindered, depending on the size of the pores in the ASW film. ASW also has the ability to trap volatile molecules within its pores as a result of the 'liquid like' transformation of ASW. This results in the desorption of the volatile molecules at temperatures well above their natural sublimation temperature. Two desorption features are commonly observed for the desorption of astrochemically relevant molecules from H_2O-rich ices[19], coincident with the desorption features of H_2O. These include a 'molecular volcano' of the volatile molecules with the ASW - CI transition, and co-desorption with the desorption of CI. The molecular volcano occurs as the volatile molecules, trapped within the closed pores of ASW, are violently released as the H_2O molecules rearrange, re-opening the pores, and forming CI. In some cases, some volatiles may remain in the CI, embedded in the H_2O matrix, to desorb coincident with the desorption of CI.

1.3.1. Cometary Ices

In addition to interstellar ices, cometary ices are also of interest. Comets are the relics of a collapsing cloud, formed as a star and planetary system is created[2]. As such, they are composed of the same material from the protostellar nebula from which the planetary system was formed. As the comets in our Solar System formed, with the formation of our Sun and planets, they were thrown out to distances of 50,000 astronomical units (AU) (where 1 AU is the distance between the Sun and the Earth, 1.5×10^{11} m). At these distances from the Sun, hundreds of billions of comets reside in the Oort cloud, where they remain 'nascent', and are too small to be observed from Earth. However, due to gravitational perturbations, some

comets such as Hale-Bopp, shown in figure 1.6, which approached the centre of the Solar System in 1997, are observable to Earth and satellite based observations[4,113,122-124]. The nucleus of Hale-Bopp is relatively small, only kilometres in diameter[2]. As a comet approaches the Sun, it warms up and the ice and dust from the nucleus boils off, creating the long tail and coma usually associated with comets. This tail can be several hundreds of thousands of kilometres in length[2].

Figure 1.6. Picture of Hale-Bopp Comet taken in 1997 as it passed close to Earth. Taken from http://apod.nasa.gov/apod/ap050522.html.

Understanding whether any energetic processing of the cometary ice has occurred once the solar and planetary system has formed, as well as the extent of the cometary processing, is therefore of great importance to understanding how the cometary ice deviates from its original, protostellar ice. Previous investigations report that abundances and compositions of cometary ices are found to be similar to those typically found in star forming regions of the ISM[2,4,107], as shown in table 1.2. This is a critical discovery, as the investigation of cometary ices is therefore of direct relevance to understanding the conditions of the protostellar nebular in which the Sun and Earth were formed. Analogous to interstellar ices, H_2O is the most abundant species within the ice, followed by CO, with other major constituents including CO_2 and CH_3OH, with trace abundances of other species including OCS, SO_2 and CS_2.[4,113,122-124] Mass spectrometric evidence from the Giotto and Vega space probes have also provided proof that the dust particles of comet Halley are composed of siliceous refractory material (Si, Mg and Fe) with organic, carbonaceous material (C, O and N)[125,126]. This correlation between cometary dust and ice, and that found in star forming regions of the ISM suggests that cometary volatiles undergo little processing in the 'nascent' state in the solar nebula[2,122]. Therefore, comets are often considered to be the best probe to investigate the origins of our Solar System.

1.4. Sulphur Chemistry in the ISM

As this thesis discusses the adsorption and desorption of molecular ices containing sulphur bearing molecules, and since these species are found in both interstellar and cometary ices, an understanding of the sulphur chemistry in the ISM is of importance. Sulphur has a relatively high cosmic abundance, approximately 4% of the abundance of carbon, and is predominantly found ionised in diffuse regions and in a neutral state within dark molecular clouds[127]. Fifteen sulphur containing molecules have been detected in the gas phase within the ISM[7,127-130], including CS[131,132], SO[133], H_2S[134], OCS[135] and SO_2[136]. However, the observed abundance of gas phase sulphur containing molecules is found to be depleted by up to 90% within dark molecular clouds[127,137]. Steady state models of cold molecular clouds have shown that gas phase S, CS and SO accounts for the majority of the observed sulphur-bearing species[137,138]. The remaining sulphur is thought to be composed of sulphur-bearing ices adsorbed on the surface of dust grains[127,129,139] or undetectable molecules or ions such as S_2 or S^+.[127,129]

Sulphur bearing molecules contained within ices on the surface of dust grains are found predominantly in the form of H_2S within dense regions[128,140,141]. Upon warming, H_2S evaporates into the gas phase where it undergoes a number of chemical reactions to create a range of sulphur containing species. A number of gas phase models and reaction schemes have been created to investigate sulphur chemistry within regions of star formation[127,128,138,140,142-145]. These models show that warm H_2S is readily dissociated to release SH and S[140].

$$H_2S \xrightarrow{H} SH \xrightarrow{H} S \qquad 1.1$$

The study of sulphur chemistry in the gas phase, and on the surface of interstellar dust grains, has been shown to be particularly useful as a tracer for the chemical evolution of star forming regions[127,138,140,142,143,145-147]. The chemistry of sulphur in the ISM is not analogous to the chemistry of oxygen in the ISM, despite their chemical similarities. For example, the gas phase reactions which play a critical role in the formation of OH and H_2O within diffuse clouds, in particular:

$$O^+ + H_2 \rightarrow OH^+ + H \qquad 1.2$$

$$OH^+ + H_2 \rightarrow H_2O^+ + H \qquad 1.3$$

$$H_2O^+ + H_2 \rightarrow H_3O^+ + H \quad 1.4$$

are exothermic. However, the sulphur substituted analogues to reactions 1.2 - 1.4:

$$S^+ + H_2 \rightarrow SH^+ + H \quad 1.5$$

$$SH^+ + H_2 \rightarrow H_2S^+ + H \quad 1.6$$

$$H_2S^+ + H_2 \rightarrow H_3S^+ + H \quad 1.7$$

are endothermic, and therefore cannot account for the abundance of H_2S, for example[144]. Instead, H_2S is formed on the surface of a dust grain in the diffuse regions via hydrogenation of SH[127].

From the products of reaction 1.1, a range of other sulphur containing species can be easily formed, including SO and SO_2[138,140,144]:

$$SH + O \rightarrow SO + H \quad 1.8$$

$$S + OH \rightarrow SO + H \quad 1.9$$

$$S + O_2 \rightarrow SO + O \quad 1.10$$

$$SO + O \rightarrow SO_2 + h\nu \quad 1.11$$

$$SO + OH \rightarrow SO_2 + H \quad 1.12$$

as well as CS and OCS[138,140,144]:

$$SO + C \rightarrow CS + O \quad 1.13$$

$$CO + S \rightarrow OCS + h\nu \quad 1.14$$

The time dependence of the abundance of SO and SO_2 in the *'early time'* of a hot core, up to 5×10^5 years[138], shows that these molecules are good candidates for use as *'chemical clocks'*, to measure the time elapsed since the core began to warm. For example, the SO:SO_2

ratio can be used to determine the age of a hot core. At times of less than 10^5 years, the abundance of SO has been shown to be characteristically higher than that of SO_2. The opposite is observed for hot cores over 10^5 years of age, where the SO:SO_2 ratio is < 1. The production of SO_2 from H_2S has also been shown to be temperature dependent[140], as well as being dependent on the availability of OH and therefore in competition with the formation of H_2O. For example, at low gas temperatures, ≈100 K, corresponding to a low mass star, most of the sulphur from H_2S converts to SO_2 as a direct result of the abundance of OH at these temperatures, leading to low H_2S:SO_2 and SO:SO_2 ratios. Conversely, at higher gas temperatures, corresponding to a higher mass star, ≈300 K, O and OH are efficiently converted to H_2O, and as such are not abundant enough to form SO and SO_2. Therefore the SO:SO_2 ratio is also temperature dependent.

Time and temperature dependence have also been observed in the production of OCS[140]. For example, above 200 K, efficient formation of OCS, via equation 1.14, is observed up to around 2×10^4 years[140]. However at lower temperatures, the predicted abundance of OCS falls, as the only viable formation routes occur via $HOCS^+$ and HCS, which are known to be minor sulphur bearing species.

Although gas phase models of the sulphur chemistry in the ISM have been able to predict the abundances of SO, SO_2 and CS[128,140], they have not been able to accurately reproduce the abundance of OCS for example. These models have been solely based upon the evaporation of pure H_2S ices upon warming in a hot core region, however OCS and SO_2 ices have also been observed in these regions[101,102,112]. The observed abundances of OCS in dense molecular clouds and young hot core regions also shows more OCS on the surface of dust grains than in the gas phase[101,102]. Therefore it is implied that OCS and SO_2 are also formed on the surface of dust grains in these dense regions, and once evaporated, will contribute to the gas phase abundances, unaccounted for by the gas phase formation models.

Steps to understand the formation of sulphur containing molecules on the surface of a dust grain analogue have been taken[130,148], via irradiation of CO, CO_2 and H_2O-rich SO_2 and H_2S-bearing ices. Efficient formation of OCS in H_2O-dominated H_2O:CO:H_2S ices has been observed, as well as the formation of CS_2 and SO_2 in CO and CO_2-rich H_2S-bearing ices respectively[130,148]. However, as discussed previously, a complete understanding of the desorption of these ices is of importance to better understand the gas phase chemistry in star forming regions, and has yet to be performed. Therefore a complete study of the adsorption and desorption of SO_2 and CS_2-bearing, H_2O-rich ices has been conducted, and will be discussed with, and compared to, work describing CO_2 and OCS[62]-bearing H_2O-rich ices on an astrophysically relevant dust grain analogue.

1.5. Previous Work

As previously discussed, H_2O is a major constituent of interstellar ices in dense molecular clouds and young hot core regions. Therefore a wide range of experimental studies have been conducted to study the formation, processing and desorption of pure H_2O ices as well as H_2O-rich ices[17-19,28,31-33,41-43,48,55,61,62,74,149-154]. Here, a brief discussion of a selection of previous studies, highlighting the motivation for this study is given.

Kay et al[119,121,155-161] have performed extensive investigations of the porosity, trapping and diffusion properties of ASW. The nature of ASW has been investigated by studying the adsorption of H_2O on a range of surfaces, including Au(111), Ru(001) and Pt(111), at a range of temperatures, from 20 K to 150 K, and even by growing ASW as a function of deposition angle and deposition rate. For example, by studying the thermal desorption of N_2 from a range of ASW surfaces, grown at different angles of deposition at 26 K[121], ASW is shown to be highly porous at deposition angles approaching 70° and non-porous, or dense, at deposition angles ≤ 20°. Background deposition of H_2O from ambient vapour has been shown to produce a highly porous ASW structure. The effect of the porosity of ASW on the diffusion, trapping and release of adsorbed volatile molecules has also been investigated. TPD spectra of binary and reverse layers of Ar deposited on and below films of porous and dense ASW were investigated. Diffusion of Ar through a dense ASW film was not observed, indicated by the lack of trapping of Ar in binary layers of Ar on dense ASW, and the lack of Ar desorption at its natural sublimation temperature from reverse layers of dense ASW on Ar. Conversely, diffusion of Ar through a porous ASW film was observed[119]. As already discussed, the release of volatile molecules trapped within an ASW film occurs coincident with the desorption features of ASW. A molecular volcano of the trapped volatile molecules is observed coincident with the ASW - CI transition[156], as well as co-desorption with the evaporation of CI[155].

The thermal desorption of pure H_2O ice from a Au surface at 10, 100 and 130 K has also been investigated by Fraser et al[149]. Growth of a monolayer, followed by multilayers of ASW, was observed upon adsorption of H_2O on the surface at 10 K. Depositing thick films of H_2O on the surface at different temperatures was also performed to show that different forms of H_2O ice were produced. High and low density ASW were formed by depositing H_2O onto the surface at 10 and 100 K respectively, and CI was formed by depositing H_2O on the surface at 130 K. Quantitative analysis of the TPD spectra of multilayer ASW and CI was also performed, assuming an order of desorption of 0 and pre-exponential factor for the desorption process of 1×10^{30} molec cm^{-2} s^{-1}, to derive energies for the desorption process of each ice. These were found to be 46.6 kJ mol^{-1} for ASW and 48.0 kJ mol^{-1} for CI. These kinetic data were then subsequently used to model the desorption and trapping of CO in an ASW ice in a chemical

simulation[17], providing evidence that the evaporation of icy mantles does not occur spontaneously.

Collings et al[17-19] have also conducted a brief survey of the desorption of a wide range of astrophysically relevant H_2O-rich ices, including CO, CO_2, CS_2 and SO_2-bearing ices, on a Au substrate at 8 K. Three ice configurations were investigated; pure ices, sequentially adsorbed ice layers on a pre-adsorbed H_2O ice, and mixed ices co-adsorbed with H_2O. The desorbates were grouped into three categories, based upon their desorption behaviour with H_2O; CO-like, H_2O-like and intermediate species. CO-like species, including the most volatile species CO, N_2, O_2 and CH_4, show two desorption features above the natural sublimation temperature of the ice in layered and mixed H_2O-rich ices. These were observed as a molecular volcano coincident with the ASW - CI transition[156] and co-desorbing with CI. The observation of these desorption features in layered and mixed ices, as well as the desorption of the ice constituents at their natural sublimation temperatures in mixed ices, indicated that CO-like species are able to diffuse and trap within a H_2O ice matrix. H_2O-like species, including NH_3, CH_3OH and HCOOH show characteristics similar to H_2O. Unlike CO-like species, H_2O-like species do not show any behaviour characteristic of diffusion or trapping within the H_2O ice matrix, and indicate strong hydrogen-bonding interactions between the ice constituents and H_2O. Finally, intermediate species, including H_2S, OCS, CO_2, SO_2 and CS_2, showed hindered diffusion through the H_2O film, with no desorption of the ice constituents at their natural sublimation temperature in mixed ices. However, the molecular volcano with the ASW - CI transition is observed in layered and mixed ices indicating trapping of the intermediate species.

The work of Collings et al has been built upon over the years by the group led by Brown[55-62,74], to provide a detailed study of pure and H_2O-rich ices on an astrophysically relevant dust grain analogue surface. Included in this work is an infrared and thermal desorption study of pure H_2O ice, grown on a HOPG surface below 100 K, conducted by Bolina et al[55,162]. RAIR spectra of a range of exposures of H_2O show the formation of bulk, or multilayer, ASW, physisorbed on the surface. Two infrared features are observed in the RAIR spectrum of ASW, a very broad feature near 3400 cm^{-1} and a small feature at 1677 cm^{-1}, assigned to the O-H stretching mode, ν_{OH}, and H-O-H scissors mode of ASW respectively. Warming the ASW ice to 150 K, or adsorbing H_2O onto a warm surface prior to collecting a RAIR spectrum, shows that the ν_{OH} mode is characteristically altered. Three distinct features are observed in the ν_{OH} mode of H_2O following warming to 150 K at 3180, 3322 and 3394 cm^{-1}, characteristic of CI. Complete desorption of the H_2O ice is observed following warming to 175 K. TPD experiments were also conducted to investigate the thermal desorption of a range of thicknesses of H_2O ice. Desorption of multilayer H_2O produces a TPD spectrum with a peak temperature of ≈164 K and a bump on the low temperature leading edge of the desorption peak at 153 K[20]. This bump is

characteristic of the ASW - CI phase transition, where the peak at 164 K corresponds to the desorption of CI.

Ulbricht et al have performed a survey of the desorption of a range of adsorbates, including CO, CO_2 and H_2O, adsorbed on a bare HOPG surface, as well as on a single walled carbon nanotube surface, at 20 K[163]. Whilst the TPD survey of Ulbricht et al was not directly motivated by understanding the desorption of interstellar ices, it provides a comparison to this work for a range of astrochemically relevant ices desorbing from a bare HOPG surface. Derivation of kinetic parameters was also performed for the desorption of these ices, including determining the energies for the desorption of each molecular ice.

Other work of specific interest is that of Sandford and Allamandola[31-35,80,152,164,165], who have studied the infrared spectra of a range of astrophysically relevant ices, adsorbed on a CsI window at 10 K. Their studies included pure ices and layered and mixed polar and apolar ices, including H_2O, CO, CO_2, H_2S and SO_2. In particular, it was shown that infrared spectra of CO and CO_2 ices have temperature dependent features which are characteristically different when mixed in a polar or apolar ice. This led to the use of the observed infrared features of CO and CO_2 as a tool to determine the thermal and chemical nature of interstellar ices in a range of regions. In addition to characterising the behaviour of ice constituents as a function of the chemical nature and temperature of the ice, Sandford and Allamandola et al constructed a library of surface binding energies (ΔH_S) of each ice, and calculated residence times for each ice constituent on an astrophysical timescale. Surface binding energies were determined by assuming that the desorption of ices follows[33]:

$$R_S = \nu_0 \exp\frac{-\Delta H_S}{kT} \qquad 1.15$$

where R_S is the rate of re-evaporation from the surface, ν_0 is the lattice vibrational frequency of the molecule on the surface and T is the surface temperature. This is accomplished isothermally, by warming the ice to a predetermined temperature and holding the ice at this temperature whilst measuring the loss of ice, via sublimation, as a function of time. The measured loss of material was then used to derive the binding energy of the ice on the surface via equation 1.16[33]:

$$\frac{\Delta H_S}{k} = -T\ln\frac{a_m\{(\tau\Delta\nu)_i - (\tau\Delta\nu)_f\}}{\nu_0 t_f A} \qquad 1.16$$

where a_m is the area of the molecular site on the surface, t_f is the total time over which the loss of material is observed, A is the integrated absorbance of the vibrational band[32,152] and $(\tau\Delta\nu)_i$ and $(\tau\Delta\nu)_f$ are the integrated band strength at time, t = 0 and t = f respectively.

This technique has been successful in determining binding energies for a range of molecular ices, although there are two obvious problems with this approach. As discussed in chapter 2, the rate of desorption (r_{des}) of a molecular ice follows a standard rate equation known as the Polanyi-Wigner equation[166]:

$$r_{des} = \frac{d\theta}{dt} = \nu_n \theta^n \exp\frac{-E_{des}}{RT_s} \qquad 1.17$$

where ν_n is the pre-exponential factor for desorption, θ is the coverage of the molecules on the surface, E_{des} is the desorption activation energy and T_S is the surface temperature. Comparison of equations 1.15 and 1.17 shows obvious similarities. However, the rate of re-evaporation used by Sandford and Allamandola is not dependent on the coverage of the ice on the surface, and hence the order of the desorption process is 0. A desorption order of 0 is characteristic of weakly bound, bulk, or multilayer, desorbing species, and is a valid assumption which is often used by the group of McCoustra et al[17-20]. This assumption affects the pre-exponential factor for desorption however, where the units for the pre-exponential factor are given by (molec m^{-2})$^{1-n}$ s^{-1}. A 0th order desorption process has a pre-exponential factor with units of molec m^{-2} s^{-1} as opposed to a frequency, s^{-1}, and is a function of several factors including the size of the molecule, entropy of the ice system as well as the vibrational frequency of the adsorbed molecules[163]. Therefore, assuming that ν_0 can be represented by the lattice vibrational frequency of the surface bound molecule alone, a value often found to be $1 \times 10^{12 - 13}$ s^{-1}, is not a valid assumption, as the pre-exponential for multilayer species have been shown to be to the order of $1 \times 10^{28 - 32}$ molec m^{-2} s^{-1}[1,55-57,59,60,163].

A second problem with the approach of Sandford and Allamandola is the fact that they rely on the assumption that the integrated area of the infrared bands used to determine the surface binding energy, via equation 1.16, only changes as a function of the number of molecules on the surface. However, it has been shown that the size of an infrared absorption band is a function of several factors, including chemical and physical interactions within the ice[55]. For example, previous studies of the H_2O ν_{OH} mode show that this vibrational band changes as a function of increasing surface temperature due to the ASW - CI transition[55,162]. Therefore careful selection of appropriate infrared bands for use in this analysis has to be made.

A detailed infrared and thermal desorption study of CO_2-bearing H_2O-rich ices on a Si wafer above 80 K has also been conducted by Maté and Gálvez[41-43]. These studies also provided evidence for the trapping of CO_2 within an ASW layer. However, the desorption of CO_2 at its natural sublimation temperature was not observed, and pure CO_2 ices were not investigated, as the natural sublimation of CO_2 is around 80 K. Infrared and TPD investigations of the trapping and diffusion properties of CO_2-bearing CH_3OH-rich ices were also conducted on a Si wafer at 85 K[44]. Analogous to studies investigating the diffusion and trapping of CO_2 through an ASW ice, trapping of CO_2 in a CH_3OH-rich ice is observed, and desorption features of CO_2 coincide with the phase transition of amorphous CH_3OH to crystalline CH_3OH as well as the desorption of crystalline CH_3OH. Therefore, the composition of the polar ice in which trapping of volatile molecules occurs affects the desorption of the ice constituents, where the desorption features of CH_3OH do not occur at the same temperatures as those of ASW. Surface binding energies for CO_2 adsorbed on ASW, CI, amorphous CH_3OH and crystalline CH_3OH were also determined, using the same approach as Sandford and Allamandola. It was found that the surface binding energy for CO_2 adsorbed on all four ice systems studied was the same, within experimental error, and was found to be between 19.7 and 20.7 ± 2 kJ mol^{-1}.

These experimental investigations, determining the diffusion and trapping properties of astrochemically relevant ices from a H_2O-rich matrix, as well as desorption energies for the observed desorption processes, are of vital importance to astrophysical simulations. As discussed previously, several models assume the evaporation of molecular ices to occur spontaneously as soon as the hot core begins to warm. However, evidence from experimental studies indicates that this is not the case, and therefore inclusion of the observed desorption processes into these models is required to improve the accuracy and validity of the astrophysical simulation. As briefly touched upon, desorption energies, as well as other kinetic parameters, can be derived from TPD spectra via application of equation 1.17. These kinetic parameters can be implemented in to astrophysical models[58], such as the models employed by Viti and Williams[118,167-169], to describe the injection of volatile reactive species from the icy mantles into the gas phase. The time in which a protostar begins to burn hydrogen, and the time in which the protostar reaches the 'main-sequence' of stars may span up to 1×10^6 years[167]. As a consequence of this, the warming in hot core regions, from the temperature of the dense molecular cloud of 10 K, to the temperature in which all ices have desorbed from the dust grain surface, is not instantaneous. As the evaporation of ices is not instantaneous, understanding the evaporation of a range of ices, including the temperatures at which they desorb, and therefore when they are injected into the gas phase, is of extreme importance to further understand the gas phase chemistry of star forming regions.

1.6. Motivation for this work

As discussed in this introduction, understanding the chemical and thermal nature of interstellar ices is of direct relevance to understanding the formation of stars, planets and even life. In particular, understanding the adsorption, desorption, diffusion and trapping properties of sulphur-bearing molecules in H_2O-rich ices is vital to further understand the composition and morphology of interstellar ices in dense clouds, and their evaporation upon warming in star forming regions. Therefore a complete investigation, using RAIR and TPD experiments, of pure and H_2O dominated ices containing CO_2, CS_2 and SO_2 has been conducted for the first time.

Interstellar ices are observed via infrared and radio spectroscopy, which can be compared with laboratory based experiments to identify the chemical composition and nature of the ice. Therefore the infrared spectra of typical interstellar ices, adsorbed on a dust grain analogue, are useful for the characterisation and identification of interstellar ices in a range of regions. Hence, a detailed understanding of the optical properties of ices on a dust grain analogue surface is necessary, to help provide accurate assignments of the features observed in the infrared spectra of these ices.

Understanding the role of sulphur-bearing molecules in an interstellar ice analogue has a number of motivations. Firstly, the adsorption and desorption of sulphur-bearing ices has astrophysical implications for the gas phase composition and chemistry in both diffuse and dense molecular clouds, and in particular is of importance in star forming regions. This includes understanding the degree of trapping and diffusion of these molecules in a H_2O-rich ice. Therefore RAIRS and TPD experiments of pure ices and layered and mixed H_2O-containing ices have been performed. Kinetic data for the desorption of sulphur-bearing ices from pure and H_2O rich ices, can also be derived. These data can then be used in astrochemical models to simulate the evaporation of ices, and hence the injection of molecules into the gas phase to drive chemical formation, on astrophysical timescales using astrophysical heating rates.

A second motivation for the investigation of sulphur-bearing molecular ices is to better understand the effect of changing the size of the molecule on the adsorption and desorption of the ice. This is achieved by comparing the experimental results from CO_2 ices with the sulphur substituted analogues of CO_2, namely SO_2 and CS_2. Experimental results for OCS-bearing ices[62] will also be discussed to provide a complete comparison between the sulphur substituted analogues of CO_2. Studying the differences between CO_2, OCS, SO_2 and CS_2 has implications in astrochemistry as well as being of general physical chemical interest.

CO_2, SO_2 and CS_2 are all classified as 'intermediate desorbing species' as determined by Collings et al[19]. Therefore CO_2, SO_2 and CS_2 should behave in a similar manner to each other upon adsorption and desorption from pure and H_2O-rich ices, where the major difference is an increased size of the molecule. CO_2, SO_2 and CS_2 have bond lengths of 116.3, 143.1 and 155.26 pm respectively and O, C and S atoms have covalent radii of 66, 73 and 105 pm and van der Waals radii of 152, 170 and 180 pm respectively. Therefore CO_2 is the smallest molecule, with SO_2, OCS then CS_2 being the largest molecule, as depicted in figure 1.7.

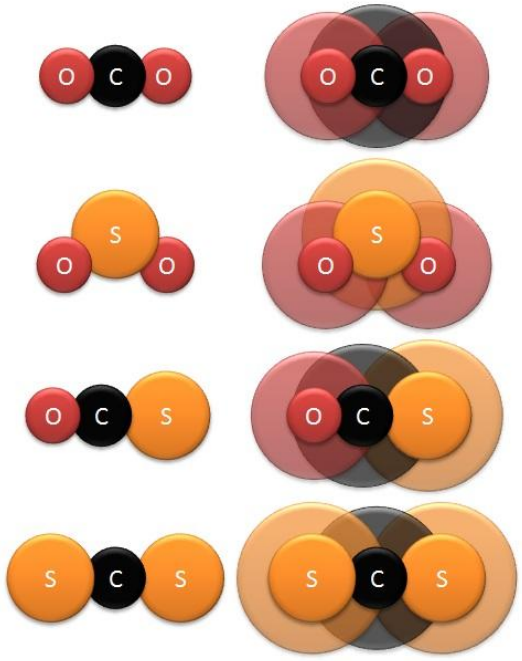

Figure 1.7. Scaled diagram showing the covalent (left) and van der Waals (right) radii of the sulphur substituted analogues of CO_2.

Understanding how these molecules behave in a H_2O-rich ice is of direct importance to astrochemistry, as well as providing an insight into the trapping and diffusion of the species within a H_2O matrix. This has obvious implications into the evaporation of molecular ices, as molecules that trap within a H_2O film will only be injected into the gas phase when H_2O evaporates. Studying the series of molecular ices from CO_2 to CS_2 may provide an 'upper limit' for the constraint of diffusion through an ASW film and hence provide astronomers a more reliable tool to simulate which molecules may diffuse or trap in a H_2O rich ice, as well as the degree of trapping observed.

1.7. References

1. Williams D.A. and Herbst E., *Surf. Sci.*, **500**, (2002), 823-837
2. Greenberg J.M., *Surf. Sci.*, **500**, (2002), 793-822
3. Zeilik M. and Gregory S.A., *Introductory Astronomy and Astrophysics, 4th ed.*, Thomson Learning: USA, 1998
4. Cottin H., Gazeau M.C. and Raulin F., *Planet Space Sci.*, **47**, (1999), 1141-1162
5. Boudin N., Schutte W.A. and Greenberg J.M., *Astron. Astrophys.*, **331**, (1998), 749-759
6. Ehrenfreund P. and Charnley S.B., *Annu. Rev. Astron. Astrophys.*, **38**, (2000), 427-483
7. Gibb E.L., Whittet D.C.B., Boogert A.C.A. and Tielens A.G.G.M., *Astrophys. J. Supp. Ser.*, **151**, (2004), 35-73
8. Whittet D.C.B. et al, *Astron. Astrophys.*, **315**, (1996), L357-L360
9. Gibb E.L. et al, *Astrophys. J.*, **536**, (2000), 347-356
10. Draine B.T., *Annu. Rev. Astron. Astrophys.*, **41**, (2003), 241-289
11. Mathis J.S., *Annu. Rev. Astron. Astrophys.*, **28**, (1990), 37-70
12. Greenberg J.M., *Astrophys. Space Sci.*, **128**, (1986), 17-31

13. Mathis J.S., *Astrophys. J.*, **442**, (1994), 176-186
14. Bussoletti E., Colangeli L. and Orofino V., *Astrophys. J.*, **321**, (1987), L87-L90
15. Duley W.W. and Williams D.A., *Mon. Not. R. Astron. Soc.*, **205**, (1983), 67-70
16. Li A. and Draine B.T., *Astrophys. J.*, **554**, (2001), 778-802
17. Collings M.P., Dever J.W., Fraser H.J., McCoustra M.R.S. and Williams D.A., *Astrophys. J.*, **583**, (2003), 1058-1062
18. Collings M.P., Dever J.W., Fraser H.J. and McCoustra M.R.S., *Astrophys. Space Sci.*, **285**, (2003), 633-659
19. Collings M.P. et al, *Mon. Not. R. Astron. Soc.*, **354**, (2004), 1133-1140
20. Green S.D. et al, *Mon. Not. R. Astron. Soc.*, **398**, (2009), 357-367
21. Ioppolo S., Cuppen H.M., Romanzin C., van Dishoeck E.F. and Linnartz H., *Astrophys. J.*, **686**, (2008), 1474-1479
22. Öberg K.I. et al, *Astrophys. J.*, **662**, (2007), L23-L26
23. Öberg K.I., van Dishoeck E.F. and Linnartz H., *Astron. Astrophys.*, **496**, (2009), 281-293
24. Schriver A., Schriver-Mazzuoli L., Ehrenfreund P. and d'Hendecourt L., *Chem. Phys.*, **334(1-3)**, (2007), 128-137
25. Bouwman J. et al, *Astron. Astrophys.*, **476**, (2007), 995-1003
26. Dartois E., Demyk K., d'Hendecourt L. and Ehrenfreund P., *Astron. Astrophys.*, **351**, (1999), 1066-1074
27. Ehrenfreund P. et al, *Astron. Astrophys.*, **315**, (1996), L341-L344
28. Ehrenfreund P. et al, *Astron. Astrophys.*, **350**, (1999), 240-253
29. Hodyss R., Johnson P.V., Orzechowska G.E., Goguen J.D. and Kanik I., *Icarus*, **194**, (2008), 836-842
30. van Broekhuizen F.A., Groot I.M.N., Fraser H.J., van Dishoeck E.F. and Schlemmer S., *Astron. Astrophys.*, **451**, (2006), 723-731
31. Sandford S.A., Allamandola L.J., Tielens A.G.G.M. and Valero G.J., *Astrophys. J.*, **329**, (1988), 498-510
32. Sandford S.A. and Allamandola L.J., *Icarus*, **76**, (1988), 201-224
33. Sandford S.A. and Allamandola L.J., *Astrophys. J.*, **355**, (1990), 357-372
34. Sandford S.A. and Allamandola L.J., *Astrophys. J.*, **417**, (1993), 815-825
35. Sandford S.A. and Allamandola L.J., *Icarus*, **106**, (1993), 478-488
36. Katz N., Furman I., Biham O., Pirronello V. and Vidali G., *Astrophys. J.*, **522(1)**, (1999), 305-312
37. Pirronello V., Biham O., Liu C., Shen L.O. and Vidali G., *Astrophys. J.*, **483(2)**, (1997), L131-L134
38. Pirronello V., Liu C., Shen L.Y. and Vidali G., *Astrophys. J.*, **475(1)**, (1997), L69-L72
39. Baratta G.A. and Palumbo M.E., *J. Opt. Soc. Am. A*, **15(12)**, (1998), 3076-3085
40. Baratta G.A., Palumbo M.E. and Strazzulla G., *Astron. Astrophys.*, **357**, (2000), 1045-1050
41. Gálvez O. et al, *Astron. Astrophys.*, **472**, (2007), 691-698
42. Gálvez O., Maté B., Herrero V.J. and Escribano R., *Icarus*, **197**, (2008), 599-605
43. Maté B. et al, *J. Phys. Chem. A*, **112**, (2008), 457-465
44. Maté B., Gálvez O., Herrero V.J. and Escribano R., *Astrophys. J.*, **690**, (2009), 486-495
45. Palumbo M.E., *J. Phys. Chem. A*, **101**, (1997), 4298-4301
46. Palumbo M.E. et al, *Astron. Astrophys.*, **334**, (1998), 247-252
47. Palumbo M.E., Castorina A.C. and Strazzulla G., *Astron. Astrophys.*, **342**, (1999), 551-562
48. Palumbo M.E. and Baratta G.A., *Astron. Astrophys.*, **361**, (2000), 298-302
49. Palumbo M.E., Baratta G.A., Collings M.P. and McCoustra M.R.S., *Phys. Chem. Chem. Phys.*, **8**, (2006), 279-284
50. Andersson P.U., Någård M.B., Witt G. and Pettersson J.B.C., *J. Phys. Chem. A*, **108**, (2004), 4627-4631
51. Mennella V., Baratta G.A., Palumbo M.E. and Bergin E.A., *Astrophys. J.*, **643**, (2006), 923-931
52. Pirronello V., Liu C., Roser J.E. and Vidali G., *Astron. Astrophys.*, **344(2)**, (1999), 681-686
53. Baouche S. et al, *J. Chem. Phys.*, **125(8)**, (2006), 084712

54. Baouche S. et al, *J. Chem. Phys.*, **131(24)**, (2009), 244707
55. Bolina A.S., Wolff A.J. and Brown W.A., *J. Phys. Chem. B*, **109**, (2005), 16836-16845
56. Bolina A.S., Wolff A.J. and Brown W.A., *J. Chem. Phys.*, **122**, (2005), 044713
57. Bolina A.S. and Brown W.A., *Surf. Sci.*, **598**, (2005), 45-56
58. Brown W.A., Viti S., Wolff A.J. and Bolina A.S., *Faraday Discussions*, **133**, (2006), 113-124
59. Brown W.A. and Bolina A.S., *Mon. Not. R. Astron. Soc.*, **374**, (2007), 1006-1014
60. Burke D.J., Wolff A.J., Edridge J.L. and Brown W.A., *J. Chem. Phys.*, **128**, (2008), 104702
61. Burke D.J., Wolff A.J., Edridge J.L. and Brown W.A., *Phys. Chem. Chem. Phys.*, **10(32)**, (2008), 4956-4967
62. Burke D.J. and Brown W.A., *Phys. Chem. Chem. Phys.*, **12**, (2010), 5947-5969
63. Creighan S.C., Perry J.S.A. and Price S.D., *J. Chem. Phys.*, **124(11)**, (2006), 114701
64. Hornekaer L. et al, *Phys. Rev. Lett.*, **97(18)**, (2006), 186102
65. Hornekaer L. et al, *Phys. Rev. Lett.*, **96(15)**, (2006), 156104
66. Hornekaer L., Xu W., Otero R., Laegsgaard E. and Besenbacher F., *Chem. Phys. Lett.*, **446(4-6)**, (2007), 237-242
67. Islam F., Latimer E.R. and Price S.D., *J. Chem. Phys.*, **127(6)**, (2007), 064701
68. Latimer E.R., Islam F. and Price S.D., *Chem. Phys. Lett.*, **455(4-6)**, (2008), 174-177
69. Perry J.S.A. et al, *Meas. Sci. Technol.*, **13**, (2002), 1414-1424
70. Perry J.S.A. and Price S.D., *Astrophys. Space Sci.*, **285(3-4)**, (2003), 769-776
71. Sljivancanin Z. et al, *J. Chem. Phys.*, **131(8)**, (2009), 084706
72. Wiesendanger R. et al, *Surf. Sci.*, **189**, (1987), 24-28
73. Williams D.A., Brown W.A., Price S.D., Rawlings J.M.C. and Viti S., *Astron. Geophys.*, **48(1)**, (2007), 25-34
74. Wolff A.J., Carlstedt C. and Brown W.A., *J. Phys. Chem. C*, **111**, (2007), 5990-5999
75. Borghesi A. and Guizzetti G., Graphite (C). *in Handbook of Optical Constants of Solids II*, Palik E.D. (Ed.), Academic Press, (1991), 449-460
76. Leitner T., Kattner J. and Hoffmann H., *Applied Spectr.*, **57(12)**, (2003), 1502-1509
77. Boyd D.A., Hess F.M. and Hess G.B., *Surf. Sci.*, **519**, (2002), 125-138
78. Eve J.K. and McCash E.M., *Chem. Phys. Lett.*, **313**, (1999), 575-581
79. Eve J.K. and McCash E.M., *Chem. Phys. Lett.*, **360(3-4)**, (2002), 202-208
80. Allamandola L.J., Bernstein M.P., Sandford S.A. and Walker R.L., *Space Sci. Rev.*, **90**, (1999), 219-232
81. d'Hendecourt L., Allamandola L.J., Grim R.J.A. and Greenberg J.M., *Astron. Astrophys.*, **158**, (1986), 119-134
82. d'Hendecourt L.B., Allamandola L.J. and Greenberg J.M., *Astron. Astrophys.*, **152**, (1985), 130-150
83. Greenberg J.M., *Astrophys. Space Sci.*, **39**, (1976), 9-18
84. Tielens A.G.G.M. and Hagen W., *Astron. Astrophys.*, **114**, (1982), 245-260
85. Brown P.D. and Charnley S.B., *Mon. Not. R. Astron. Soc.*, **244**, (1990), 432-443
86. Moore M.H., Donn B., Khanna R. and A'Hearn M.F., *Icarus*, **54**, (1983), 388-405
87. Bernstein M.P., Sandford S.A., Allamandola L.J., Chang S. and Scharberg M.A., *Astrophys. J.*, **454**, (1995), 327
88. Prasad S.S. and Tarafdar S.P., *Astrophys. J.*, **267**, (1983), 603-609
89. Fraser H.J., Collings M.P. and McCoustra M.R.S., *Rev. Sci. Instrum.*, **73(5)**, (2002), 2161-2170
90. Allamandola L.J., Sandford S.A., Tielens A.G.G.M. and Herbst E., *Astrophys. J.*, **399**, (1992), 134-146
91. Boogert A.C.A. et al, *Astron. Astrophys.*, **315**, (1996), L377-L380
92. Boogert A.C.A. et al, *Astron. Astrophys.*, **336**, (1998), 352-358
93. Brooke T.Y., Sellgren K. and Geballe T.R., *Astrophys. J.*, **517**, (1999), 883-900
94. Chiar J.E., Adamson A.J., Kerr T.H. and Whittet D.C.B., *Astrophys. J.*, **455**, (1995), 234-243
95. Chiar J.E., Adamson A.J. and Whittet D.C.B., *Astrophys. J.*, **472**, (1996), 665-672
96. Chiar J.E. et al, *Astrophys. J.*, **498**, (1998), 716-727
97. Chiar J.E. et al, *Astrophys. J.*, **537(2)**, (2000), 749-762

98. d'Hendecourt L. et al, *Astron. Astrophys.*, **315**, (1996), L365-L368
99. Dartois E. et al, *Astron. Astrophys.*, **342**, (1999), L32-L35
100. Gerakines P.A. et al, *Astrophys. J.*, **522**, (1999), 357-377
101. Palumbo M.E., Tielens A.G.G.M. and Tokunaga A.T., *Astrophys. J.*, **449**, (1995), 674-680
102. Palumbo M.E., Geballe T.R. and Tielens A.G.G.M., *Astrophys. J.*, **479**, (1997), 839-844
103. Pendleton Y.J., Tielens A.G.G.M., Tokunaga A.T. and Bernstein M.P., *Astrophys. J.*, **513**, (1999), 294-304
104. Schutte W.A. et al, *Astron. Astrophys.*, **315**, (1996), L333-L336
105. Schutte W.A., Gerakines P.A., Geballe T.R., van Dishoeck E.F. and Greenberg J.M., *Astron. Astrophys.*, **309**, (1996), 633-647
106. Skinner C.J., Tielens A.G.G.M., Barlow M.J. and Justtanont K., *Astrophys. J.*, **399**, (1992), L79-L82
107. Tegler S.C. et al, *Astrophys. J.*, **439**, (1995), 279-287
108. van de Bult C.E.P.M., Greenberg J.M. and Whittet D.C.B., *Mon. Not. R. Astron. Soc.*, **214**, (1985), 289-305
109. Whittet D.C.B. et al, *Astrophys. J.*, **498**, (1998), L159-L163
110. Geballe T.R., *Mon. Not. R. Astron. Soc.*, **251**, (1991), 24-25
111. Smith R.G., *Mon. Not. R. Astron. Soc.*, **249**, (1991), 172-176
112. Boogert A.C.A., Schutte W.A., Helmich F.P., Tielens A.G.G.M. and Wooden D.H., *Astron. Astrophys.*, **317**, (1997), 929-941
113. Hudson R.L. and Moore M.H., *Icarus*, **140**, (1999), 451-461
114. Charnley S.B., Kress M.E., Tielens A.G.G.M. and Millar T.J., *Astrophys. J.*, **448**, (1995), 232-239
115. Tielens A.G.G.M., Tokunaga A.T., Geballe T.R. and Baas F., *Astrophys. J.*, **381**, (1991), 181-199
116. Hasegawa T.I., Herbst E. and Leung C.M., *Astrophys. J. Supp. Ser.*, **82(1)**, (1992), 167-195
117. Ehrenfreund P., Boogert A.C.A., Gerakines P.A., Tielens A.G.G.M. and van Dishoeck E.F., *Astron. Astrophys.*, **328**, (1997), 649-669
118. Viti S., Collings M.P., Dever J.W., McCoustra M.R.S. and Williams D.A., *Mon. Not. R. Astron. Soc.*, **354(4)**, (2004), 1141-1145
119. Ayotte P. et al, *J. Geophys. Res. Planets*, **106(E12)**, (2001), 33387-33392
120. Cholette F. et al, *J. Phys. Chem. B*, **113(13)**, (2009), 4131-4140
121. Stevenson K.P., Kimmel G.A., Dohnalek Z., Smith R.S. and Kay B.D., *Science*, **283**, (1999), 1505-1507
122. Bockelée-Morvan D. et al, *Astron. Astrophys.*, **353**, (2000), 1101-1114
123. Despois D., Crovisier J., Bockelée-Morvan D. and Colom P., Formation of comets: Constraints from the abundance of Hydrogen Sulfide and other sulfur species. *at Astrochemistry of Cosmic Phenomena* (IAU), Singh P.D. (Ed.), (1992), 459-460
124. Jackson W.M., Scodinu A. and Xu D., *Astrophys. J.*, **607**, (2004), L139-L141
125. Kissel J. et al, *Nature*, **321**, (1986), 336-337
126. Kissel J. et al, *Nature*, **321**, (1986), 280-282
127. Duley W.W., Millar T.J. and Williams D.A., *Mon. Not. R. Astron. Soc.*, **192**, (1980), 945-957
128. Hatchell J., Thompson M.A., Millar T.J. and Macdonald G.H., *Astron. Astrophys.*, **338(713)**, (1998), 722
129. Ruffle D.P., Hartquist T.W., Caselli P. and Williams D.A., *Mon. Not. R. Astron. Soc.*, **306**, (1999), 691-695
130. Ferrante R.F., Moore M.H., Spiliotis M.M. and Hudson R.L., *Astrophys. J.*, **684**, (2008), 1210-1220
131. Penzias A.A., Solomon P.M., Wilson R.W. and Jefferts K.B., *Astrophys. J.*, **168**, (1971), L53
132. Zuckerman B., Morris M, Palmer P. and Turner B.E., *Astrophys. J.***(173)**, (1972), L125
133. Gottlieb C.A. and Ball J.A., *Astrophys. J.*, **184**, (1973), L59
134. Thaddeus P., Kutner M.L., Penzias A.A., Wilson R.W. and Jefferts K.B., *Astrophys. J.*, **176**, (1972), L73

135. Jefferts K.B., Penzias A.A., Wilson R.W. and Solomon P.M., *Astrophys. J.*, **168**, (1971), L111-L113
136. Snyder L.E. et al, *Astrophys. J.*, **198**, (1975), L81-L84
137. Tieftrunk A., Pineau des Forêts G., Schilke P. and Walmsley C.M., *Astron. Astrophys.*, **289**, (1994), 579-596
138. Millar T.J. and Herbst E., *Astron. Astrophys.*, **231**, (1990), 466-472
139. Trasferetti B.C., Davanzo C.U., Zoppi R.A., da Cruz N.C. and de Moraes M.A.B., *Phys. Rev. B.*, **64**, (2001), 125404
140. Charnley S.B., *Astrophys. J.*, **481**, (1997), 396-405
141. Minh Y.C., Ziurys L.M., Irvine W.M. and McGonagle D., *Astrophys. J.*, **360**, (1990), 136-141
142. Buckle J.V. and Fuller G.A., *Astron. Astrophys.*, **399**, (2003), 567-581
143. Doty S.D., van Dishoeck E.F., van der Tak F.F.S. and Boonman A.M.S., *Astron. Astrophys.*, **389**, (2002), 446-463
144. Oppenheimer M. and Dalgarno A., *Astrophys. J.*, **187**, (1974), 231-235
145. Yamada M., Osamura Y. and Kaiser R.I., *Astron. Astrophys.*, **395**, (2002), 1031-1044
146. Benz A.O. et al, *Astron. Astrophys.*, **475**, (2007), 549-558
147. van der Tak F.F.S., Boonman A.M.S., Braakman R. and van Dishoeck E.F., *Astron. Astrophys.*, **412**, (2003), 133-145
148. Moore M.H., Hudson R.L. and Carlson R.W., *Icarus*, **189**, (2007), 409-423
149. Fraser H.J., Collings M.P., McCoustra M.R.S. and Williams D.A., *Mon. Not. R. Astron. Soc.*, **327**, (2001), 1165-1172
150. Fraser H.J., Collings M.P., Dever J.W. and McCoustra M.R.S., *Mon. Not. R. Astron. Soc.*, **353**, (2004), 59-68
151. Gerakines P.A., Schutte W.A., Greenberg J.M. and van Dishoeck E.F., *Astron. Astrophys.*, **296**, (1995), 810-818
152. Sandford S.A. and Allamandola L.J., *Icarus*, **87**, (1990), 188-192
153. Schriver-Mazzuoli L., Chaabouni H. and Schriver A., *J. Molec. Struc.*, **644**, (2003), 151-164
154. Wood B.E. and Roux J.A., *J. Opt. Soc. Am.*, **72(6)**, (1982), 720-728
155. Smith R.S., Huang C., Wong E.K.L. and Kay B.D., *Surf. Sci.*, **367(1)**, (1996), L13-L18
156. Smith R.S., Huang C., Wong E.K.L. and Kay B.D., *Phys. Rev. Lett.*, **79(5)**, (1997), 909-912
157. Smith R.S., Huang C. and Kay B.D., *J. Phys. Chem. B*, **101**, (1997), 6123-6126
158. Smith R.S. and Kay B.D., *Nature*, **398**, (1999), 788-791
159. Smith R.S., Dohnálek Z., Kimmel G.A., Stevenson K.P. and Kay B.D., *Chem. Phys.*, **258**, (2000), 291-305
160. Zubkov T., Smith R.S., Engstrom T.R. and Kay B.D., *J. Chem. Phys.*, **127(18)**, (2007), 184707
161. Zubkov T., Smith R.S., Engstrom T.R. and Kay B.D., *J. Chem. Phys.*, **127(18)**, (2007), 184708
162. Bolina A.S., PhD Thesis. University College London, (2005)
163. Ulbricht H., Zacharia R., Cindir N. and Hertel T., *Carbon*, **44**, (2006), 2931-2942
164. Allamandola L.J., Sandford S.A. and Valero G.J., *Icarus*, **76(2)**, (1988), 225-252
165. Hudgins D.M., Sandford S.A., Allamandola L.J. and Tielens A.G.G.M., *Astrophys. J. Supp. Ser.*, **86**, (1993), 713-870
166. de Jong A.M. and Niemantsverdriet J.W., *Surf. Sci.*, **233**, (1990), 355-365
167. Viti S. and Williams D.A., *Mon. Not. R. Astron. Soc.*, **305**, (1999), 755-762
168. Viti S., Natarajan S. and Williams D.A., *Mon. Not. R. Astron. Soc.*, **336**, (2002), 797-802
169. Roberts J.F., Rawlings J.M.C., Viti S. and Williams D.A., *Mon. Not. R. Astron. Soc.*, **382(2)**, (2007), 733-742

Chapter 2: Experimental Apparatus and Techniques

As described in chapter 1, the regions of interest in the interstellar medium (ISM) have extremely low pressures and temperatures. In order to understand the chemical processes in the ISM, these harsh conditions need to be recreated in the laboratory. The lowest pressures achievable in the laboratory are several orders of magnitude higher than the regions of interest in the ISM, however they are low enough for surface science techniques under the timescales available for laboratory based experiments. The low temperatures of the ISM are easily reproduced in the laboratory. These conditions are achieved using an ultra high vacuum (UHV) chamber and a coldfinger, cooled by a closed cycle Helium refrigerator.

2.1. UHV Chamber

The experimental apparatus (figure 2.1) has previously been described in detail[1], and consists of a UHV chamber, pumped by a combined ion and titanium sublimation pump (TSP) (Captorr ion pump & Boostivac TSP, Physical Electronics). Coupled with the ion pump is a

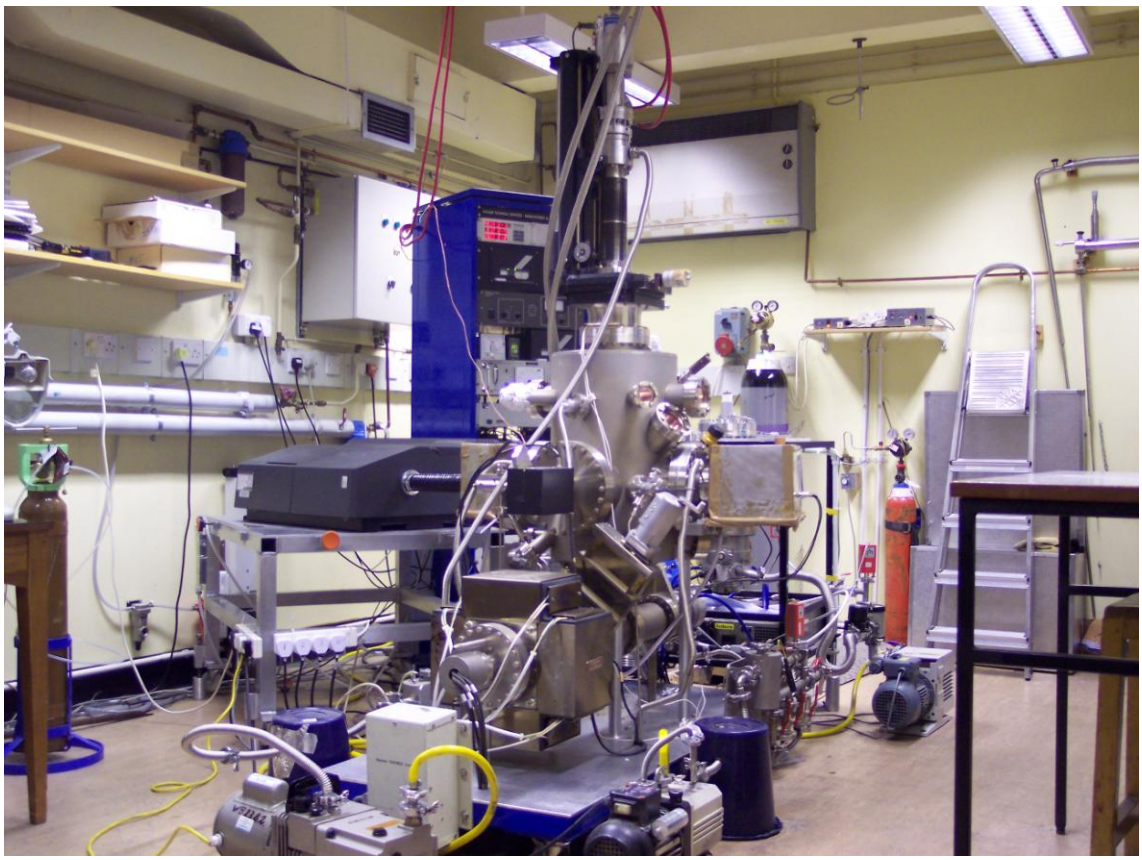

Figure 2.1. UHV chamber and experimental apparatus used to recreate and study the interstellar ice analogues discussed in this thesis.

turbo-molecular pump (TMP) (Turbovac 151, Leybold Ltd.) backed by a rotary pump (Trivac D5E, Leybold). The combined ion pump and TSP, and the TMP, are independently connected to the UHV chamber via a pair of gate valves. This allows the UHV chamber to be vented to atmosphere whilst keeping the ion pump under vacuum, as well as allowing the UHV chamber to be pumped from atmosphere to high vacuum (≈1 × 10^{-8} mbar) in stages. The UHV chamber reaches a base pressure of ≤ 2 × 10^{-10} mbar and the pressure inside the chamber is monitored via an ion gauge (ITL Ltd.). A schematic diagram showing the pump and pressure gauge setup is shown in figure 2.2.

The HOPG sample is mounted on a closed cycle Helium refrigerator (HC-2D-1, SHI-APD Cryogenics Inc.) cooled cold finger, see section 2.2, reaching base temperatures of ≤ 20 K. The sample temperature is monitored via an N-type thermocouple connected to a temperature control module (ε2408, Eurotherm Ltd.). The cold finger is mounted on a high precision manipulator (Omniax Translator, MX Series, VG, UK), allowing micrometer precision movement of the sample in three dimensions. Sample rotation through 360° is also achieved via the use of a differentially pumped rotary feedthrough. Therefore the sample can be cooled to low temperature and its position manipulated to a high level of accuracy, all under UHV, essential for the surface science techniques employed in this study.

The UHV chamber consists of two experimental levels. The upper level is equipped with the ion gauge, an ion gun (Physical Electronics Ltd.) for metal surface sputtering as well as low energy electron diffraction (LEED) optics (ErLEED-1000A, Specs GmbH) for surface electron diffraction experiments. Neither the ion gun, or LEED optics were used in this study. The lower level is equipped with a quadrupole mass spectrometer (QMS) (HAL 201, Hiden Analytical Ltd.) for temperature programmed desorption (TPD) experiments and residual gas analysis (RGA). The QMS is fitted with a stainless steel shroud with a 10 mm diameter aperture facing the centre of the UHV chamber and cold finger. This is to reduce detection of residual gas from within the UHV chamber during TPD experiments, so

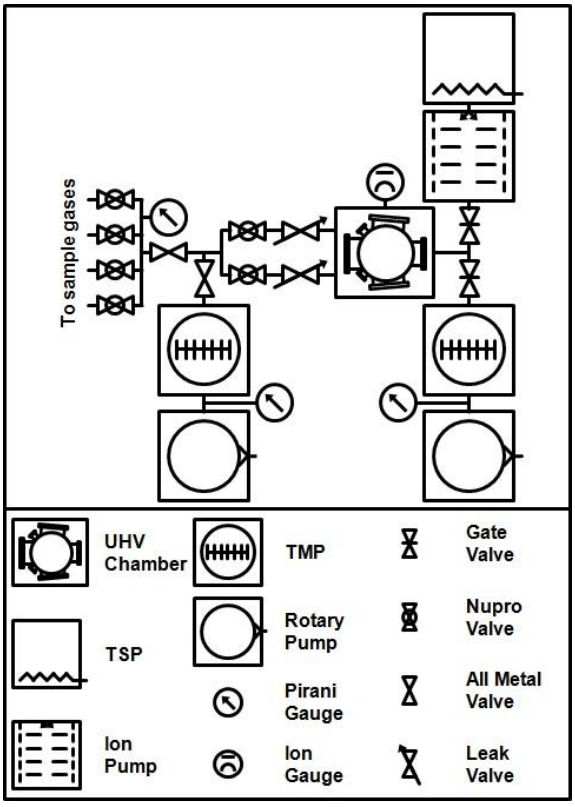

Figure 2.2. Diagram showing the experimental chamber and dosing manifold with all associated pumps and pressure gauges. Adapted from reference [1].

that the QMS signal is from the line of sight of the sample. Differentially pumped KBr windows are fitted at the lower experimental level for performing reflection absorption infrared spectroscopy (RAIRS) experiments. A set of parabolic and flat mirrors (Aero Research Ltd.) are mounted on the UHV chamber, in such an arrangement so as to focus infrared light from a Fourier transform infrared spectrometer (RS1 Research Series, Mattson Instruments) on to the sample surface. The reflected light is then focused into a liquid nitrogen cooled mercury cadmium telluride detector (EG&G Optoelectronics). The infrared beam path outside the UHV chamber is kept under a constant purge of dry, CO_2 free, air to reduce infrared absorbance from gas phase H_2O and CO_2 in the atmosphere. Several viewing ports are also installed on the chamber to allow for sample observation during installation and movement.

Two fine control leak valves (LVM Series Leak Valve, VG) are also connected to the lower experimental level for controlled dosing of sample gas into the chamber (figure 2.2). The sample gases are handled in a stainless steel manifold which allows up to two gases to be dosed into the chamber simultaneously, and several gases to be dosed into the chamber in succession. The dosing manifold is pumped by an air cooled TMP (Turbovac 50, Leybold Ltd.), backed by a rotary pump (Trivac D5E, Leybold).

2.2. Cold Finger and Sample Mount

To perform TPD experiments and to investigate the effect of warming on the infrared spectra of surface ices, the ability to warm and cool the sample in a controlled manner is required. It is also necessary to warm the sample to high enough temperatures to ensure surface cleanliness, as well as to allow the sample to cool as rapidly as possible following cleaning, thus preventing residual gases in the chamber from contaminating the surface prior to each experiment. The most important aspect of the control over the sample temperature, especially from an astrophysical point of view, is the ability to cool the sample to low enough temperatures analogous to those found in the ISM.

2.2.1. Cold Finger

The sample is attached, via the sample mount, to the end of a closed cycle Helium refrigerator cooled cold finger. The flange on which the cold finger and Helium expander are mounted has four additional ports. Two of these ports are mounted with power feedthroughs, each of which are connected to two lengths of 0.6 mm diameter Ag plated Cu wire insulated with Kapton, forming part of the resistive heating circuit as discussed later. The other two ports are mounted with N-type thermocouple feedthroughs, each of which is connected to a

length of Nicrosil-Nisil (Ni-Cr-Si/Ni-Si alloy) wire, also known as N-type thermocouple wire. One of the N-type thermocouple wires is attached to the end of the cold finger, to monitor the cooling of the cold finger, the other is used to monitor the sample temperature. All wires are tightly wound around the cold finger, with the heating wires also being passed through two heat sink stages. This is to reduce the effect of conduction from the wires, which are at room temperature at one end of the cold finger, to the sample which is at base temperature. The cold finger is shrouded by a Au coated radiation shield prior to installation into the UHV chamber, to reduce heating of the sample from blackbody radiation from the UHV chamber walls. The radiation shield has a 180° slit cut out, corresponding to the position of the sample, to allow for RAIRS and TPD experiments.

2.2.2. Sample Mount

Several considerations need to be taken into account when designing the sample mount. Firstly, the sample must be in good thermal contact with the mount to allow for efficient cooling of the sample to achieve a very low base temperature. Secondly, the sample must also be in contact with the resistive heating circuit to allow for controlled warming of the sample, without warming the sample mount and cold finger. Finally, the sample mount must be electrically isolated from the cold finger and sample so that the resistive heating circuit does not short through the cold finger or sample mount.

As discussed by Bolina[1], an ideal material on which the HOPG sample can be mounted is sapphire. At low temperature, the thermal conductivity of sapphire is high, to allow for efficient cooling of the sample. Conversely, at high temperature, as the sample is being warmed for instance, the thermal conductivity of sapphire is low, reducing the conduction of heat from the sample to the cold finger. Finally, sapphire is electrically insulating, and will therefore allow the resistive heating circuit to be completed without a short through the cold finger or sample mount.

The sample mount described here, figure 2.3, is a modified version of the sample mount described by Bolina[1], to allow the HOPG sample to be cooled via the closed cycle Helium refrigerator, as opposed to the liquid Nitrogen cooled cold finger used previously. The sample mount was designed by Burke[2] and is composed of an oxygen-free high conductivity copper (OFHC) plate attached directly to the end of the cold finger. Several layers of Ag foil are used to increase thermal conductivity between the cold finger and OFHC plate. The resistive heating circuit is passed through an electrically isolated stage, attached directly to the back of the OFHC plate. This is composed of two OFHC blocks, isolated from the OFHC plate via a sapphire spacer, and isolated from each other via a ceramic spacer. To ensure electrical insulation Mo

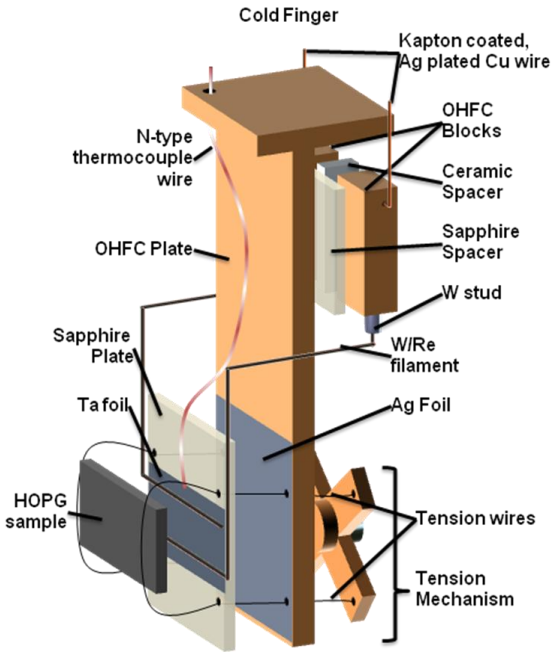

Figure 2.3. Diagram showing the sample mount and tension mechanism used to attach the HOPG sample to the cold finger, allowing rapid and controlled cooling and warming of the sample. Ceramic insulation and Mo screw attachments have been omitted. Adapted from reference [1].

screws, insulated with a ceramic sleeve and hat, are used to attach the resistive heating stage to the OFHC plate. The Kapton insulated Ag plated Cu heating wires are screwed into each half of the OFHC cylinder in such an arrangement that the resistive heating circuit does not short through the sample mount. A short rod of W is attached, recessed into a hole bored into the bottom of each OFHC block, and held in place with Mo screws. Into this rod a small hole is bored, into which a length of 0.5 mm diameter W/Re (75% W, 25% Re) alloy filament is attached via silver solder. These W/Re filaments can then be attached to the sample to complete the resistive heating circuit.

The HOPG sample, 20 × 10 × 2 mm (Goodfellow Ltd., UK), is cleaned via the *'Scotch tape'* method prior to mounting[3] and is attached to the sapphire block via a tension wire system. The sapphire is blackened by the amorphous carbon from a candle to reduce any infrared features from the sapphire surface in the RAIRS experiments. Sandwiched between the HOPG sample and the sapphire block are the W/Re filaments, thermocouple wire and a piece of Ta foil the same size as the HOPG sample. The thermocouple wire is spot welded to the Ta foil so that the temperature of the Ta foil and the HOPG sample can be monitored. The Ta foil is positioned in direct contact with the sapphire block, directly beneath the HOPG sample, with the thermocouple wire in direct contact with the HOPG sample. The W/Re filaments are placed between the Ta foil and HOPG sample (separated by ≈5 mm). The HOPG sample has grooves cut into the back of it, corresponding to the position of the W/Re filaments and thermocouple wire, to create a snug fit. The sample then sits on top of the Ta foil in direct contact with the foil, the thermocouple wire and the W/Re filaments. Tension wires are then passed over the HOPG sample (≈2 mm from the edges of the HOPG sample) and fastened into the tension mechanism, electrically insulated from the OHFC plate via ceramic sleeves, in such a way that the wires apply an even force over the sample.

The tension mechanism is composed of an OFHC cross into which four holes are drilled corresponding to the holes in the sapphire block through which the tension wires are passed.

It is held in place via small stainless steel screws, with a large stainless steel screw through the centre of the cross. As the central screw is tightened, the OFHC cross is moved away from the sapphire block and the tension wires tighten. An OHFC cap is placed on the end of the screw to allow an even distribution of force on the sapphire block as the tension mechanism is tightened. This method of tension mounting allows the HOPG sample to be cooled to ≤ 20 K, via thermal contact with the sapphire block. It also provides effective and reproducible resistive heating of the sample up to 500 K from room temperature, or up to 300 K from base temperature, without significant warming of the sapphire block and cold finger.

2.3. Sample Cleaning

The HOPG sample was cleaned prior to each experiment to ensure that no residual gas from the chamber was adsorbed onto the surface during the experiment. This was achieved by warming the sample from base temperature to 300 K for 3 minutes. Previous sample cleaning was achieved by warming to 500 K for 3 minutes[1]. However, due to the lower sample temperature, which is regularly at 20 K in the experiments described in this thesis, warming to 500 K requires a larger current to be passed through the resistive heating wires. This puts strain on the W/Re filaments, greatly reducing their lifetime. Warming to 500 K from base temperature also warms the sapphire plate by a considerable amount, and increases the amount of time it takes for the sample to return to base temperature. Achieving a base temperature of 20 K, following warming to 300 K for 3 minutes, reproducibly took approximately 10 minutes. A quick flash of the sample to 150 K was also performed, immediately prior to experimentation, to further clean the sample. Sample cleanliness was confirmed by the absence of any desorbing species, or any increase in chamber pressure, during TPD experiments with no dosage.

2.4. Experimental Techniques

RAIRS experiments for pure CO, CO_2 and H_2O ices adsorbed on HOPG were performed in this thesis, see chapter 3. In addition, RAIRS and TPD experiments of CO_2, CS_2 and SO_2-bearing H_2O ices adsorbed on HOPG were also performed, see chapters 4 - 6 respectively. Both the RAIRS and TPD experimental techniques are well established, and hence will only be briefly discussed here.

2.4.1. Reflection Absorption Infrared Spectroscopy

RAIRS is a standard surface infrared technique, used to study the vibrational spectrum of an adsorbate on a surface[4,5]. This technique has been predominantly used to study adsorbate - metal surface systems, and has been the subject of several reviews[4-9]. RAIRS can also be used to study adsorbates on a HOPG surface, which has been shown to obey the metal surface selection rule[9,10].

Figure 2.4 shows the electric field vector of infrared light incident (I) upon and reflecting (R) from a surface. The electric field vector incident on an interface plane such as a metal surface can be resolved into two components based upon polarisation with respect to the plane of incidence. Light polarised parallel and perpendicular to the plane of incidence is described as p- and s-polarised respectively. Upon reflection, at all angles of incidence, s-polarised light undergoes a 180° phase change, resulting in a zero net vector for s-polarised light. At grazing incidence, common for RAIRS experiments, the net vector for p-polarised light becomes enhanced. As the interaction between the transition dipole moment of a vibration and electric field vector is fundamental to the absorption of infrared light, only adsorbate vibrations perpendicular to the surface, interacting with the p-polarised component of the electric field vector, will appear in RAIR spectra. This is known as the metal surface selection rule. This effect is also observed for HOPG, with a maximum absorption intensity at an angle of incidence of ≈73°,[10] as the HOPG surface displays metal like optical and dielectric properties, including free electrons[9].

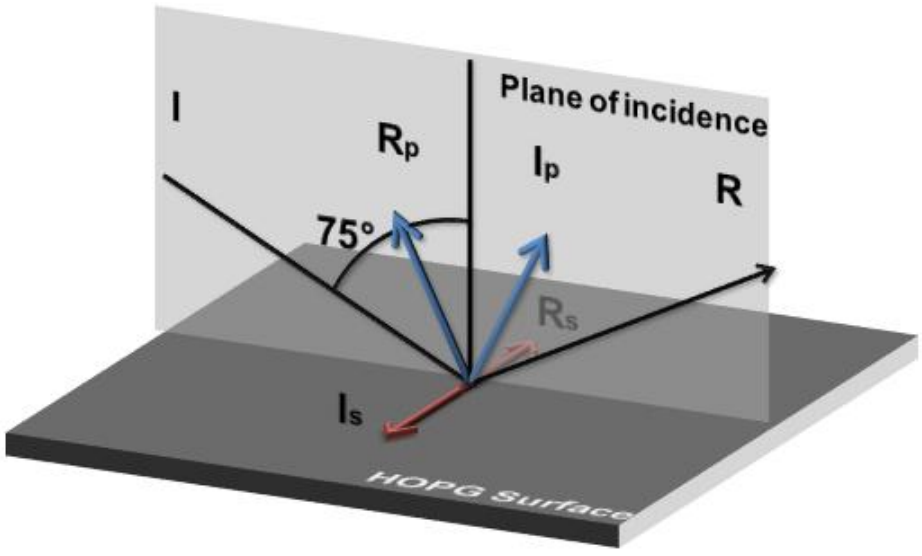

Figure 2.4. Diagram showing the components of the electric field vector upon reflection of light from a HOPG surface. I and R are the incident and reflected components of the electric field vector, subdivided into s and p-polarised components upon reflection. Also shown is the angle of incidence commonly used for a HOPG surface.

2.4.2. Temperature Programmed Desorption

TPD is a conceptually simple surface technique which provides kinetic information concerning the desorption of an adsorbate from a surface, shown schematically in figure 2.5. After deposition of the adsorbate ice, the sample is positioned directly in front of the QMS. The sample temperature is then increased using a controlled linear heating rate, typically 0.5 K s^{-1} in this thesis. The heating rate was monitored via a thermocouple feedback loop, controlled by iTools software (Eurotherm Ltd.) which monitored the sample temperature and regulated the power supply (Xantrex 30-70, Thurlby Thandar Ltd.) to the resistive heating circuit. As the sample is warmed, the adsorbate ice gains energy, and eventually begins to desorb from the surface. The desorbed gas phase molecules, or flux, are then recorded by the QMS, which is set to continuously scan the major mass fragments of the molecules of interest. This results in a TPD spectrum of QMS pressure as a function of time, which is directly proportional to the rate of desorption as a function of temperature due to the linear heating rate.

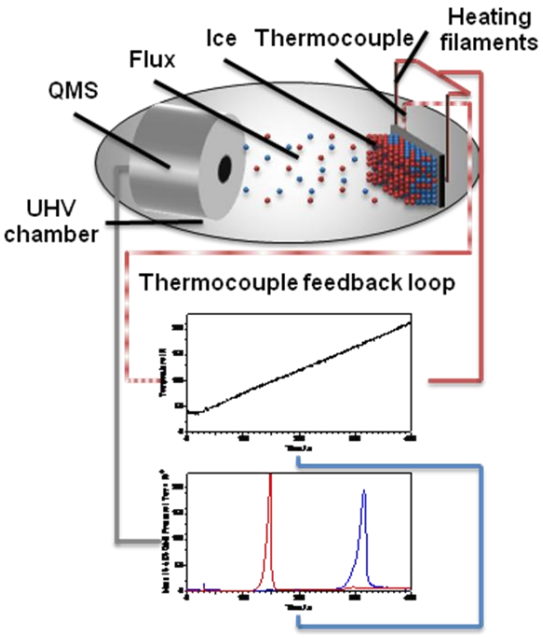

Figure 2.5. Schematic of the TPD experimental setup. Also shown is a schematic of the thermocouple feedback loop, used in conjunction with iTools software, to control the linear heating rate.

2.4.2.1. Quantitative Analysis of TPD Spectra

Kinetic data which describe the desorption process, such as the desorption order, desorption energy and pre-exponential factor, can be derived from TPD spectra via application and rearrangement of the Polanyi-Wigner equation[11] (equation 2.1):

$$r_{des} = \frac{d\theta}{dt} = \nu_n \theta^n \exp\frac{-E_{des}}{RT_s} \qquad (2.1)$$

where r_{des} is the rate of desorption, ν_n is the pre-exponential factor of the desorption process of order n, θ is the coverage, E_{des} is the desorption energy, R is the gas constant and T_s is the

surface temperature. The desorption order, desorption energy and pre-exponential factors can all be determined via rearrangement and manipulation of equation 2.1. To determine the desorption order, the Polanyi-Wigner equation can be expressed as shown in equation 2.2:

$$\ln[I(T)] = n\ln[\theta_{rel}] \tag{2.2}$$

where I(T) is the QMS intensity and θ_{rel} is the relative coverage, taken as the area under the TPD curve. From equation 2.2, the desorption order can be determined from the gradient of a plot of ln[I(T)] against ln[θ_{rel}] at a fixed temperature, using a set of TPD spectra with varying initial adsorbate coverage. A range of fixed temperatures may be used where the leading edges on the low temperature side of the TPD peaks are of interest. The error in the desorption order may be taken as twice the standard deviation in the gradients obtained from a sensible range of fixed temperatures, as discussed in chapters 4 - 6.

The desorption energy can give an indication of the binding strength within an adsorbate layer and between the adsorbate and the surface, and can be determined from further manipulation of the Polanyi-Wigner equation (equation 2.3):

$$\ln[I(T)] - n\ln[\theta_{rel}] = \frac{-E_{des}}{RT_s} \tag{2.3}$$

By plotting ln[I(T)] - n.ln[θ_{rel}] against 1/T for each TPD spectrum, taking the gradient as -E_{des}/R, the desorption energy of an adsorbate can be obtained. The gradient must be taken from the leading edge of the TPD spectra. Since $\Delta I(T)$ and $\Delta\theta_{rel}$ are negligible, the error in ln[I(T)] - n.ln[θ_{rel}] may be taken as $\Delta n.\ln[\theta_{rel}]$, hence propagating the error in the desorption order into the desorption energy.

To determine the pre-exponential factor for desorption, the absolute coverage of the adsorbate on the surface must be determined. This can be achieved by considering the rate of impingement of molecules on the surface as a function of adsorbate exposure. Assuming a sticking probability of 1, the number of molecules (N_M) on the surface as a function of adsorbate exposure, can be given as (equation 2.4):

$$N_M = \frac{10^{-4} LA}{\sqrt{2\pi m k T_g}} \tag{2.4}$$

where L is the dose in Langmuir, where 1 L = 10^{-6} mbar s, A is the surface area, m is the mass of the adsorbate, k is Boltzmann's constant and T_g is the gas temperature, taken as 300 K. As the

QMS has a shroud with a 10 mm diameter, only 39% of the molecules on the surface will be detected in a TPD experiment.

By comparing the number of molecules as a function of exposure with the area under each TPD spectrum, a scaling factor to convert the rate of desorption and area, to an absolute intensity and coverage can be determined. The pre-exponential factor can then be calculated via further rearrangement of the Polanyi-Wigner equation (equation 2.5):

$$\nu_n = \frac{I(T)}{\theta^n \exp\frac{-E_{des}}{RT_s}} \qquad (2.5)$$

The error in ν_n is taken as $\nu_n\sqrt{(\Delta n^2 + \Delta E_{des}^2)}$ since $\Delta I(T)$, $\Delta\theta$ and ΔT are negligible.

This analysis method has been used previously to derive the kinetic data for H_2O, NH_3, CH_3OH and C_2H_5OH ices[12-15] and can be incorporated into astrophysical models simulating the desorption of molecular ices on astronomical timescales[16-18].

2.5. References

1. Bolina A.S., PhD Thesis. University College London, (2005)
2. Burke D.J., *Private Communication*, 2008
3. Wiesendanger R. et al, *Surf. Sci.*, **189**, (1987), 24-28
4. Claybourn M., External Reflection Spectrscopy. *in Handbook of Vibrational Spectroscopy Volume 2*, Chalmers J.M. and Griffiths P.R. (Eds.), John Wiley & Sons Ltd., (2002), 969-981
5. Kattner J. and Hoffman H., External Reflection Spectrscopy of Thin Films on Dielectric Substrates. *in Handbook of Vibrational Spectrscopy Volume 2*, Chalmers J.M. and Griffiths P.R. (Eds.), John Wiley & Sons Ltd, (2002), 1009-1027
6. Bradshaw A.M. and Schweizer E., Infrared Reflection Absorption Spectroscopy of Adsorbed Molecules. *in Spectroscopy of Surfaces*, Clark R.J.H. and Hester R.E. (Eds.), John Wiley & Sons Ltd, (1988), 413-483
7. Hayden B.E., Reflection Absorption Infrared Spectroscopy. Yates J.T. and Madey T.E. (Eds.), (1985), 267-344
8. Hoffman F.M., Infrared Reflection Absorption Spectroscopy of Adsorbed Molecules. *in Surface Science Reports*, Balk P. et al (Eds.), North-Holland Publishing Company, Amsterdam, (1983), 107-192
9. Leitner T., Kattner J. and Hoffmann H., *Applied Spectr.*, **57(12)**, (2003), 1502-1509
10. Heidberg J., Warskulat M. and Folman M., *J. Elec. Spec. Rel. Phenom.*, **54/55**, (1990), 961-970
11. de Jong A.M. and Niemantsverdriet J.W., *Surf. Sci.*, **233**, (1990), 355-365
12. Bolina A.S., Wolff A.J. and Brown W.A., *J. Phys. Chem. B*, **109**, (2005), 16836-16845
13. Bolina A.S., Wolff A.J. and Brown W.A., *J. Chem. Phys.*, **122**, (2005), 044713
14. Bolina A.S. and Brown W.A., *Surf. Sci.*, **598**, (2005), 45-56
15. Burke D.J., Wolff A.J., Edridge J.L. and Brown W.A., *J. Chem. Phys.*, **128**, (2008), 104702
16. Brown W.A., Viti S., Wolff A.J. and Bolina A.S., *Faraday Discussions*, **133**, (2006), 113-124
17. Brown W.A. and Bolina A.S., *Mon. Not. R. Astron. Soc.*, **374**, (2007), 1006-1014
18. Viti S., Collings M.P., Dever J.W., McCoustra M.R.S. and Williams D.A., *Mon. Not. R. Astron. Soc.*, **354(4)**, (2004), 1141-1145

Chapter 3: Reflection Absorption Infrared Spectroscopy of Carbon Monoxide, Carbon Dioxide and Water bearing ices on Highly Oriented Pyrolytic Graphite

3.1. Introduction

Laboratory based infrared studies have been used to produce a library of interstellar ice analogues to compare to infrared observations of the interstellar medium (ISM)[1,2]. Studies like these not only provide comparative infrared spectra to help assign the spectra of molecular clouds, but also provide cross sections of infrared bands to indicate the relative abundances of interstellar molecules[1-6]. A range of laboratory based infrared experiments have also been undertaken to probe the processing of interstellar ices[3,4]. Thorough understanding of the infrared spectra of interstellar ice analogues is of great importance to assign the composition of interstellar ices, understand the processing of ice mantles and to understand the structure and nature of the ice. For example, CO and CO_2 have been shown to be important astrophysical molecules in identifying the thermal history and nature of an interstellar ice.

Observations of CO in particular have suggested that both polar (H_2O, CH_4, CH_3OH rich) and apolar (CO, CO_2, N_2 and O_2 rich) ices exist on the surfaces of interstellar grains in an 'onion like' structure[7,8]. Previous infrared studies of CO[9-41] and CO_2[5,6,10,11,19,20,33,39,42-66] ices have shown that not only are they infrared active, with strong transitions, but they also have infrared modes which are highly susceptible to the local environment.

CO has been detected in the ISM in molecular clouds, in both the gas phase[67,68] and condensed on the surface of interstellar dust grains[7,69-72], as well as in molecular ices observed in the comae of comets[73,74]. Detection of CO in these environments has been accomplished via infrared observation of the CO stretch, ν_{CO}, around 2140 cm^{-1}. In many observations of the CO stretch in a range of interstellar ices, two independent peaks are observed; a broad flat peak around 2136 cm^{-1} and a sharp peak around 2140 cm^{-1}, attributed to CO in polar and apolar ices respectively[1,7,69-71]. The abundance of CO in the gas phase, as well as in icy mantles in molecular clouds, has been reported[1,68,75] and is found to be approximately 10 times greater in the gas phase than within the icy mantle.

CO_2 ices have also been detected in the ISM[76-84], condensed on the surface of dust grains[1,39,85,86], as discussed in more detail in chapter 4. Gas phase CO_2 infrared spectra show three fundamental bands at 2349, 2280 and 660 cm^{-1} assigned to the $^{12}CO_2$ and $^{13}CO_2$ ν_3 stretches and the ν_2 bend respectively[87]. A large number of surface infrared studies, of pure

CO_2 as well as CO_2-bearing polar and apolar ices, have been conducted on a range of surfaces[5,6,10,11,19,20,33,39,42-66]. The infrared spectra of solid CO_2 have been shown to differ depending on the nature of the ice matrix, whether polar or apolar[19,88]. For example, the $^{12}CO_2$ ν_3 stretch is shifted from the gas phase value, 2349 cm^{-1},[87] by approximately 7 - 15 cm^{-1} in apolar ices and 2 - 8 cm^{-1} in polar ices, depending on the exact ice composition[20,43].

Splitting of certain vibrational modes is also observed in many infrared studies of CO and CO_2 bearing ices at grazing incidence[10,16,17,20,34,36,52]. This has previously been assigned to the orthogonal optical (LO) and transverse optical (TO) vibrational coupling within crystalline ices[46,89], known as the Berreman effect[90]. A detailed description of the cause of LO - TO splitting is given in section 3.4, but it is often given the simplified explanation of the coupling of neighbouring vibrations, vibrating in the same or opposite directions to each other. This effect is typically observed for crystalline films due to the periodicity, ordering and alignment of the molecular vibrations. However, this effect has now also been observed in amorphous films of CO and CO_2[10,16,17,20,34,36,52], as well as in thin amorphous films of other adsorbate-surface systems[91-93]. Therefore understanding the optical and physical properties of CO and CO_2, as well as those of other optically similar ices, is important to understand the observation of LO - TO splitting within amorphous ice. As discussed in section 3.3, this can be achieved via the application of a model to simulate the infrared spectra of CO and CO_2 ices, and is the topic of this chapter. An infrared model has previously been created by Palumbo et al[10,20,36] to simulate the transmission infrared spectra of CO and CO_2 on a Si film and the work described in this chapter is an extension of their investigation to study infrared spectra, in the reflection mode, of CO and CO_2 on a carbonaceous surface.

A model has been created based upon the work of Greenler[94-96] and Gardner et al[97-100] to recreate the reflection absorption infrared (RAIR) spectra of CO and CO_2 adsorbed on a highly oriented pyrolytic graphite (HOPG) surface. The RAIR spectrum of H_2O ice adsorbed on a HOPG surface is also investigated for comparison and discussion. This work is compared with the work of Palumbo et al[10,20,36] to validate the model and to provide further evidence for the origin of LO - TO splitting in amorphous ice.

3.2. Experimental

The experimental apparatus and techniques used for all experiments have been described in detail in chapter 2. Research grade CO (BOC Gases, 99.9%), CO_2 (BOC Gases, 99.9%) and H_2O (distilled, deionised) were used in these experiments. The H_2O was purified via repeated freeze-pump-thaw cycles. Ices were grown *in situ* by backfilling the chamber through a high precision leak valve. All exposures are measured in Langmuir, where 1 L = 10^{-6} mbar s, and

were not corrected for ion gauge sensitivity. RAIR spectra were taken at a resolution of 2 cm^{-1} and are the result of the co-addition of 128 scans.

3.3. Infrared Model

Previous infrared models have been created, simulating a range of adsorbate-surface systems[10,20,36,61,94,97-101]. The model described here is based upon the theoretical work proposed by Greenler[94-96], modified and implemented by Gardner et al[97-100]. Gardner's model was created to simulate the far-infrared RAIR spectra of tin-(IV) oxide films on a glass surface, in particular RAIR spectra of $SnCl_4$ and $SnBr_4$ adsorbed on thin films of SnO_2 were investigated[97-100]. Contrary to RAIR investigations of adsorbate films on a metal surface, inverse reflection bands are observed in the RAIR spectra of films adsorbed on a non-metal surface[102]. Inverse reflection bands are those where an increase, rather than decrease, in the intensity of reflected light is observed upon absorption. The model implemented by Gardner et al[97-100] was used to investigate these inverse bands observed in the far infrared.

A model has also been created by Palumbo et al[10,20,36] to investigate the transmission infrared spectra of CO and CO_2 films adsorbed on a crystalline Si surface. This model, modified from the work of Wood and Roux[61], simulated the transmission spectra, taken at non-normal incidence, of amorphous CO and CO_2 ices adsorbed on a surface. As discussed later, this enabled the observation of LO and TO phonon modes within the amorphous ices, not observable at angles of incidence normal to the surface. LO and TO phonon modes are not commonly observed in amorphous ices, and hence the origin of these observations in CO and CO_2 ices was investigated. Although it was found that the optical properties of the CO and CO_2 ice, which are similar to each other, are the cause of these observations, detailed analysis and comparison to an optically dissimilar ice was not conducted.

Therefore a model has been created to simulate the RAIR spectra of CO, CO_2 and H_2O ices on a HOPG surface. The results of these simulations are compared with the simulations of Palumbo et al[10,20,36] to validate the model used here, and to further investigate the physical and optical reasons for the observation of LO and TO phonon modes within an amorphous ice.

As described in chapter 2, RAIRS is a surface vibrational spectroscopy technique which enables the identification and classification of the vibrational bands of an adsorbate on a surface[102,103]. To understand and simulate RAIR spectra, we must first understand how infrared light interacts with reflective and transparent interfaces, as well as with molecular vibrations.

3.3.1. Reflection and Refraction

The wavelength of light absorbed by an adsorbate vibration can be determined by comparing the incident and reflected infrared light upon reflection from a surface. The incident light can be described by electromagnetic wave theory, where light is composed of two component vectors; the electric field vector (**E**) and the magnetic field vector (**B**), oscillating perpendicular to each other and to the direction of the propagating light (**K**), as shown in figure 3.1. Infrared radiation interacts with the change in the molecular dipole moment, induced by a vibration, resulting in a transition dipole moment vector (**T**). The angle between **E** and **T** is fundamental to the intensity loss of an infrared absorption band, where maximum absorption occurs when **E** and **T** are aligned. For linearly polarised light, the angle between **E** and **T** depends only on the orientation of **T**, which leads to the metal surface selection rule, discussed below, and can be used to extract structural information about an adsorbate on a metal surface from RAIR spectra.

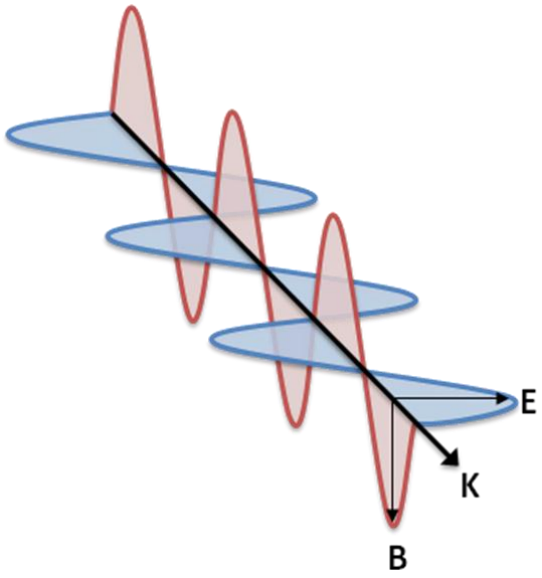

Figure 3.1. Diagram depicting an electromagnetic wave where E = electric field vector, B = magnetic field vector and K = direction of propagating light.

Upon incidence of light on to an interface plane between two optically different media, the incident light ($\mathbf{E_i}$) will split into reflected ($\mathbf{E_r}$) and refracted or transmitted ($\mathbf{E_t}$) light along the plane of incidence (figure 3.2). The angle of refraction (ϕ) can be determined from the angle of incidence (θ) and the refractive indices ($\tilde{n}_a$ and $\tilde{n}_b$) of the two optically different media, a and b, using Snells law of refraction[103]:

$$\tilde{n}_a \sin\theta = \tilde{n}_b \sin\phi \qquad (3.1)$$

where $\tilde{n}_a$, the refractive index of phase a, is defined as follows:

$$\tilde{n}_a = n_a - ik_a \qquad (3.2)$$

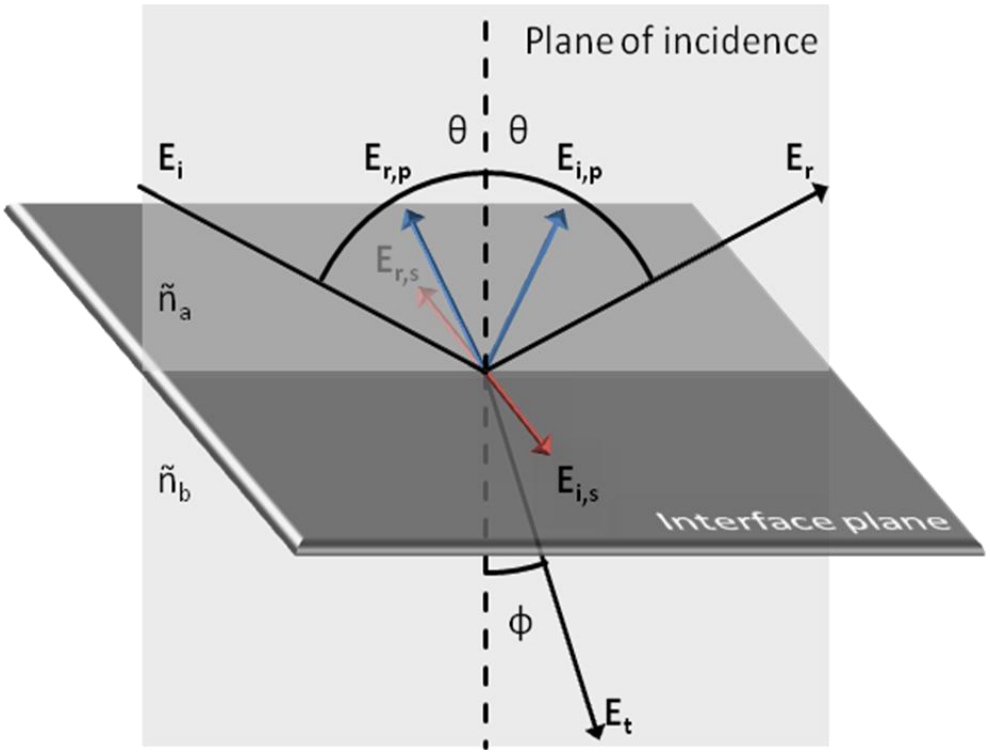

Figure 3.2. Beam geometry and polarisation of infrared light at the interface between two optically different media, a and b. $\tilde{n}_a$ and $\tilde{n}_b$ are the refractive indices of phases a and b respectively, θ and ϕ are the angles of incidence and refraction respectively, E_i, E_r and E_t are the incident, reflected and transmitted components of the electric field vector of the infrared light, $E_{i,p}$ and $E_{r,p}$ are the p-polarised components of the incident and reflected components of the electric field vector and $E_{i,s}$ and $E_{r,s}$ are the s-polarised components of the incident and reflected components of the electric field vector respectively.

Here, n_a is the real part of the refractive index and k_a is the extinction coefficient of phase a. $\tilde{n}_a$ can be real or complex depending on the extinction coefficient of the material. For example, a vacuum has n = 1 and k = 0, and hence $\tilde{n}_a$ is real.

Upon reflection from an interface plane, incident and reflected light can be resolved into two components of the vectors based upon light polarisation. If the polarisation plane is parallel to the plane of incidence, the light is described as p-polarised ($\mathbf{E_p}$ from parallel). Conversely, if the polarisation plane is perpendicular to the plane of incidence, the light is described as s-polarised ($\mathbf{E_s}$ from the German word *senkrecht* for perpendicular). Upon reflection from a metal surface, s-polarised light undergoes a 180° phase change, resulting in a zero net electric field vector for s-polarised light. Conversely, the net vector is enhanced for p-polarised light upon reflection from a metal surface. Therefore, only adsorbate vibrations with a component of the vibration normal to the surface, which interact with p-polarised light, are visible in RAIR spectra. As discussed in chapter 2, this is known as the metal surface selection rule and also holds for HOPG[26,104].

3.3.2. Fresnel Reflection Coefficients

Using the definitions above, a model can be constructed based upon the application of the Greenler equations[94-96], to simulate the RAIR spectra of physisorbed adsorbates on a surface[97-101]. The Greenler equations, which are extensions of the Fresnel equations[103], define the reflectivity (R_{ab}) of light at the interface between two optically different materials, a and b. R_{ab} can be described by the Fresnel reflection coefficient (r_{ab}) between the two phases where:

$$R_{ab} = \left|r_{ab}\right|^2 \tag{3.3}$$

The Fresnel reflection coefficient describes the ratio of the reflected and transmitted electric field amplitude of an electromagnetic wave incident on an interface between two different media. The Fresnel reflection coefficients for s and p-polarised light are derived from the application of the boundary conditions from the electromagnetic wave theory to the Maxwell equations[103]. However, due to the metal surface selection rule, only p-polarised light is observed in RAIR spectra, and hence s-polarised light is omitted. The Fresnel reflection coefficient for p-polarised light may take several forms, depending on the formalism, but can be described as the ratio of the complex amplitudes of the electric field vectors of the reflected and incident waves, and is a function of the angle of incidence[101]. The angular dependent component of the reflection coefficient (ξ_a) is defined as follows:

$$\xi_a = \tilde{n}_a \cos\theta_a \tag{3.4}$$

where θ_a describes the angle of incidence onto the interface between phases a and b. The Fresnel reflection coefficient for p-polarised light is given by:

$$r_{p,ab} = \frac{\tilde{\varepsilon}_b \xi_a - \tilde{\varepsilon}_a \xi_b}{\tilde{\varepsilon}_b \xi_a + \tilde{\varepsilon}_a \xi_b} \tag{3.5}$$

where $\tilde{\varepsilon}_a$ and $\tilde{\varepsilon}_b$ are the complex dielectric constants of phases a and b respectively. The complex dielectric constant of a phase is related to the complex refractive index of the phase by the Maxwell relation[101,103]:

$$\tilde{n}_a = \sqrt{\tilde{\varepsilon}_a} \tag{3.6}$$

Equation 3.5 can then be written as a function of the refractive indices of the two phases and the angles of incidence and refraction at the interface:

$$r_{p,ab} = \frac{\tilde{n}_b^2 \tilde{n}_a \cos\theta_a - \tilde{n}_a^2 \tilde{n}_b \cos\theta_b}{\tilde{n}_b^2 \tilde{n}_a \cos\theta_a + \tilde{n}_a^2 \tilde{n}_b \cos\theta_b} \tag{3.7}$$

Note that θ_b describes the angle of incidence, incident onto the interface between phases b and c, and is also described by ϕ_a, the angle of refraction from the interface between phases a and b.

The most relevant form of the Fresnel coefficient is given in terms of the angle of incidence only[103], which can be determined using Snells law (equation 3.1) and the trigonometric identity:

$$\cos^2\theta + \sin^2\theta = 1 \tag{3.8}$$

leading to the relationship:

$$\tilde{n}_b \cos\theta_b = \sqrt{\tilde{n}_b^2 - \tilde{n}_a^2 \sin^2\theta_a} \tag{3.9}$$

The Fresnel reflection coefficient for reflection at an interface between two phases, a and b, can then be expressed as:

$$r_{p,ab} = \frac{\tilde{n}_b^2 \cos\theta_a - \tilde{n}_a \sqrt{\tilde{n}_b^2 - \tilde{n}_a^2 \sin^2\theta_a}}{\tilde{n}_b^2 \cos\theta_a + \tilde{n}_a \sqrt{\tilde{n}_b^2 - \tilde{n}_a^2 \sin^2\theta_a}} \tag{3.10}$$

Therefore the reflection of p-polarised light impinging on the interface plane between two optically different media, vacuum, adsorbate or surface, can be described by the complex refractive indices of each media, and the angle of incidence of the impinging light. However, to simulate RAIR spectra, the reflection of light through a three layer system, comprising of the vacuum, adsorbate and surface, needs to be considered.

3.3.3. RAIRS Model

As the adsorbate-surface systems described in this chapter consist of pure CO, CO_2 and H_2O ices adsorbed on a HOPG surface, a three layer model (vacuum, ice and HOPG surface) is

required to simulate the RAIR spectra of these ices. The Greenler model[94] considers the reflection of light between three layers, a vacuum, an adsorbate layer and a surface, and hence may be adapted to study the RAIR spectra discussed here. To extend the Fresnel reflection coefficients for a multilayered system, we must take into consideration partial multiple internal reflections between the interfaces, as shown in figure 3.3. For a three phase system, the Fresnel reflection coefficient is given by[97-100]:

$$r_{abc} = \frac{r_{ab} + r_{bc}e^{-2i\beta_{ab}}}{1 + r_{ab}r_{bc}e^{-2i\beta_{ab}}} \tag{3.11}$$

where β_{ab} describes the phase change of light through the interface between phases a and b, and is defined by:

$$\beta_{ab} = \frac{2\pi d_b \xi_b}{\lambda} \tag{3.12}$$

where d_b is the thickness of phase b and λ is the wavelength of the incident light.

Experimental RAIR spectra are obtained by comparing the background infrared spectrum with that of an adsorbate covered surface. Therefore, the RAIR spectra for a three layered

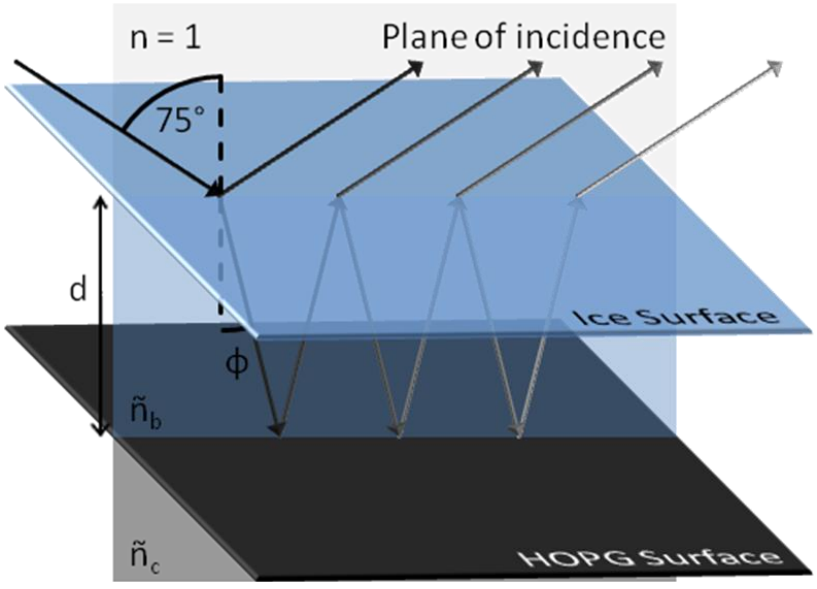

Figure 3.3. Schematic of the RAIRS model of a three phase system (a, b and c), showing multiple internal reflection. As indicated on the figure, $\tilde{n}_a = 1$ ($n_a = 1$, $k_a = 0$), common for a vacuum, $\theta = 75°$, common for the RAIRS technique for a HOPG surface. Also shown are the variables $\tilde{n}_b$ and $\tilde{n}_c$, the complex refractive indices for the ice and HOPG surface respectively (phases b and c respectively), ϕ, the angle of the refracted infrared light between the vacuum and ice (phases a and b) and d, the thickness of the ice (phase b).

model can be simulated from the Fresnel reflection coefficients, with equation 3.3, using the following relationship:

$$\frac{\Delta R}{R} = \frac{R_{abc} - R_{ac}}{R_{ac}} \tag{3.13}$$

where R_{ac} describes the reflectivity between the vacuum and surface with no adsorbate film and R_{abc} describes the reflectivity of the adsorbate covered surface.

Therefore a model can be created, which can be used to simulate the vibrational bands of experimental RAIR spectra, using only;

- The wavelength dependent refractive indices of the adsorbate(s) and surface
- The thickness of the adsorbate film(s)
- The angle of incidence and the wavelength of the incident light.

The wavelength dependent refractive indices of the adsorbates and surface can be found in the literature[10,36,105,106], and the angle of incidence can be taken as 75°, common for the RAIR technique using a HOPG surface[26]. The thickness of the adsorbate film can then be varied between a range of sensible adsorbate film thicknesses. The thicknesses used can be estimated by considering the rate of impingement of molecules on the HOPG surface. By assuming a sticking probability of 1, the number of molecules as a function of exposure adsorbed on the surface can be approximated. For example, a 1 L exposure of CO on the HOPG surface relates to 2.88×10^{14} molec cm^{-2}. By considering the volume of one adsorbate molecule, the volume of the adsorbate film can be approximated. The volume of CO was found by considering the C and O atoms as intersecting spheres with radii equal to the van der Waals radii of C and O atoms, separated by the bond length of CO. Therefore the volume of a 1 L exposure of CO was found to be $\approx 1.47 \times 10^{-14}$ m^3. Finally, considering the surface area of the HOPG surface, the film thickness of a 1 L exposure of CO was found to be ≈0.07 nm. Therefore, simulated RAIR spectra will be collected using a range of film thicknesses between 0.01 - 5 nm, corresponding to sub-monolayer and multilayer coverage of the adsorbate film.

In simulating the RAIR spectra of pure CO, CO_2 and H_2O ices on HOPG, the optical and physical properties of the ice, such as its refractive index, extinction coefficient and dielectric constant, can be probed as a function of the wavelength of light. This will provide insight into the causes of the observed infrared features as a consequence of the properties of the ice. The simulated RAIR spectra will also be compared with experimental RAIR spectra to validate the

results of this model, as well as to discuss the strengths and short comings of this theoretical technique.

3.4. Results and Discussion

Experimental and simulated RAIR spectra were obtained for pure CO, CO_2 and H_2O ices on HOPG. Experimental RAIR spectra for pure CO, CO_2 and H_2O ices adsorbed on a HOPG surface at 26, 28 and 20 K respectively, were collected using the experimental setup described in chapter 2. Simulated RAIR spectra were created using the RAIRS model as described in section 3.3.

HOPG is a semimetal with a uniaxial layered crystalline structure[104,105]. Due to the anisotropic nature of the HOPG surface, two sets of refractive indices, and consequently dielectric constants, are exhibited. These are parallel, or in plane ($\tilde{n}_{ip}$, $\tilde{\varepsilon}_{ip}$) and perpendicular, or out of plane ($\tilde{n}_{op}$, $\tilde{\varepsilon}_{op}$) with respect to the HOPG surface. Figure 3.4 shows the in-plane complex refractive index for HOPG at room temperature in the wavelength region between 1000 and 4000 cm^{-1}, taken from reference [105]. As the RAIRS model is temperature independent, the temperature at which the refractive index for HOPG was collected does not affect the results.

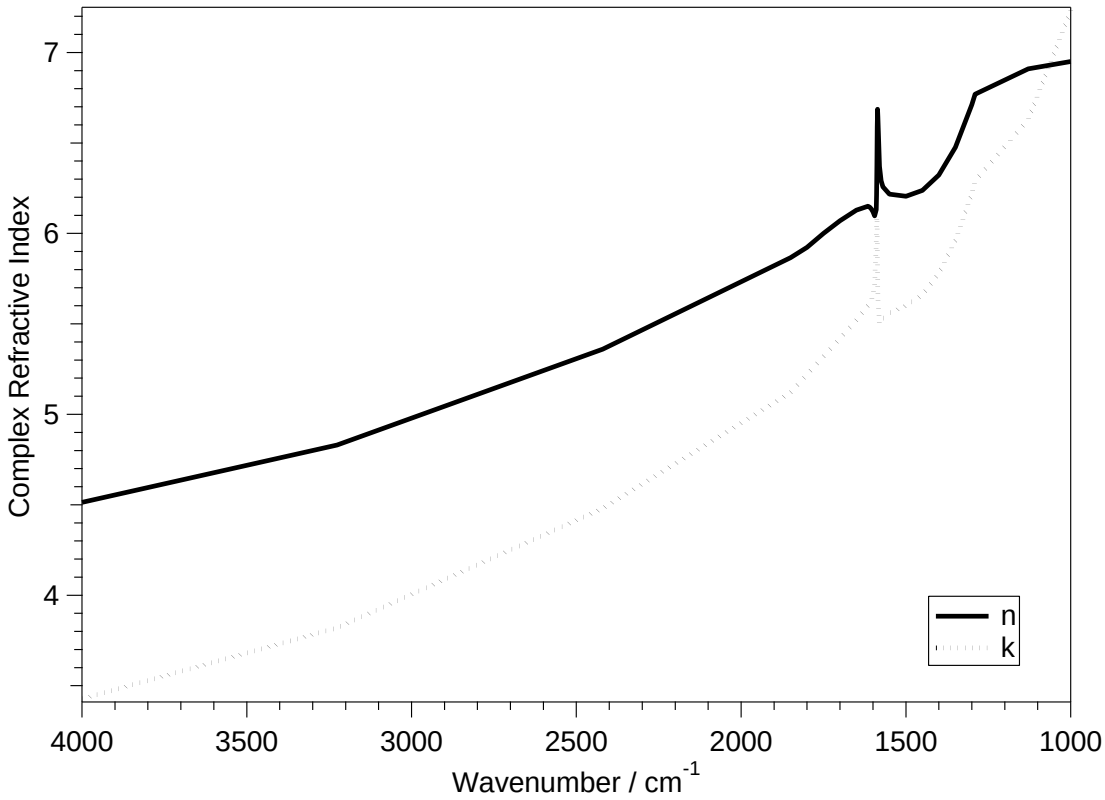

Figure 3.4. In-plane complex refractive index of HOPG, parallel to the HOPG surface. Taken from reference [105].

As there are no significant changes to the optical or structural properties of HOPG in the temperature range at which the RAIR experiments are performed, 20 - 300 K, the complex refractive index for HOPG found at room temperature will not be significantly different to that for HOPG at 20 K.

The in-plane complex refractive index of HOPG in the mid infrared region shows behaviour approaching that of a metal[104], characterised by an extinction coefficient, $k \geq 10$[103]. A feature is observed in the in-plane complex refractive index of HOPG, figure 3.4, around 1587 cm^{-1}, corresponding to the infrared active E_{1u} mode of the graphite lattice, with a transition dipole moment parallel to the HOPG surface[104].

The out-of-plane complex refractive index of HOPG, averaged as n = 1.3, k = 0 over the mid infrared region[104], shows behaviour characteristic of an insulator. As the out-of-plane properties of HOPG describe the optical properties of HOPG perpendicular to the surface, through the bulk of the HOPG sample, they are not involved in the reflection of light incident on the plane between the adsorbate and surface. Therefore the insulator properties of HOPG are not included when simulating the RAIR spectra of adsorbed ices on HOPG.

Using the 'metal like' part of the complex refractive index of HOPG, an angle of incidence of 75° and a refractive index for the vacuum of n = 1, k = 0 (as shown in figure 3.3), a model has been created using Mathcad7 Standard (©1986 - 1997 MathSoft Inc.) to simulate the RAIR spectra of a range of infrared active films adsorbed on a HOPG surface.

3.4.1. CO Ice

Experimental spectra. RAIR spectra were collected for a variety of exposures of CO adsorbed on HOPG at 26 K, shown in figure 3.5. Following a CO exposure of 10 L, an infrared band is observed in the RAIR spectrum at 2142 cm^{-1}. Increasing CO exposure to 30 L shows a shift of the band at 2142 cm^{-1} to 2143 cm^{-1} as well as a low intensity feature appearing at 2137 cm^{-1}. Further increase of CO exposure, up to 100 L, shows an increase in the size of both bands at 2143 and 2137 cm^{-1}, with no further shift in wavenumber of either infrared band.

Gas phase studies of the infrared spectrum of CO show a single fundamental band at 2143.3 cm^{-1}.[23] Therefore, due to the lack of a significant shift in the wavenumber of the observed infrared bands upon adsorption on the surface, physisorbed CO ice is formed on the surface. Also, as the infrared bands do not saturate with increasing CO exposure, it is suggested that multilayers of CO are forming on the surface at 26 K.

Previous studies of amorphous CO adsorbed on a Au surface at 8 K[16,17,36] show two infrared bands at 2142 and 2139 cm^{-1}, also in agreement with studies of CO ices[10,15,20,34,61]. These bands were assigned to the LO and TO modes of the ν_{CO} stretch of multilayer CO respectively[15].

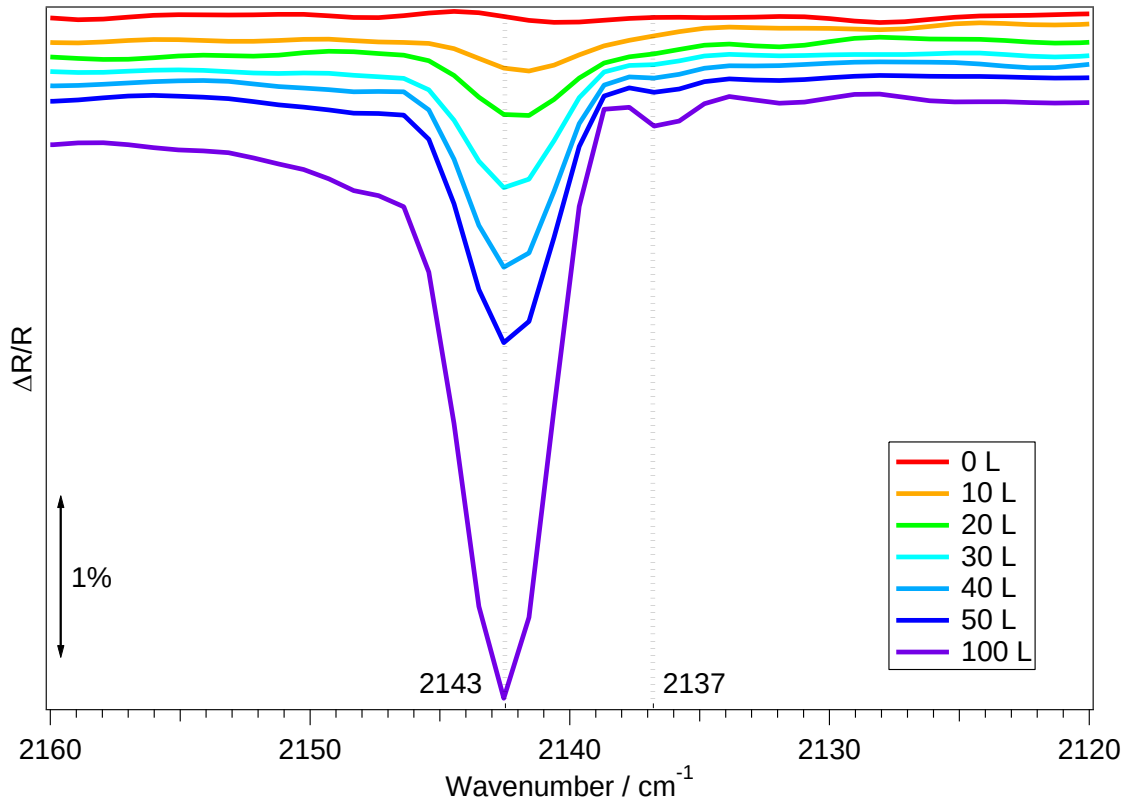

Figure 3.5. RAIR spectra of a range of exposures of CO adsorbed on a bare HOPG surface at 26 K.

However, as discussed previously, observation of LO - TO splitting is usually associated with crystalline ices[36]. Therefore, to investigate the origin of the observation of LO and TO modes of the ν_{CO} stretch in amorphous CO ice, a model was created to simulate the experimental RAIR spectra.

RAIRS Model. RAIR spectra of a film of solid CO adsorbed on a HOPG surface were simulated using the RAIRS model discussed in section 3.3, and are shown in figure 3.6. At all thicknesses of the CO layer, two infrared bands are observed in the ν_{CO} vibrational region, at 2142.6 and 2137.8 cm^{-1}. With the exception of the intensities of the bands, no differences in the RAIR spectra are observed upon increasing the thickness of the CO ice layer in the simulation.

Comparing the experimental and simulated RAIR spectra of CO on HOPG, shown in figure 3.7, shows good agreement between the positions of the LO and TO modes of the ν_{CO} stretch as well as relative intensities of the LO and TO modes. This shows that the model used here is a valid approach for reproducing the infrared spectra of an adsorbate-surface system. However, the simulated RAIR spectrum does not accurately reproduce the band widths of the observed infrared features. For example, the LO mode of the ν_{CO} stretch from the experimental spectrum of a 100 L exposure of CO has a full width half maximum (FWHM) of 3.9 cm^{-1}, as opposed to that in the simulated spectrum which has a FWHM of 1.2 cm^{-1}. The experimental

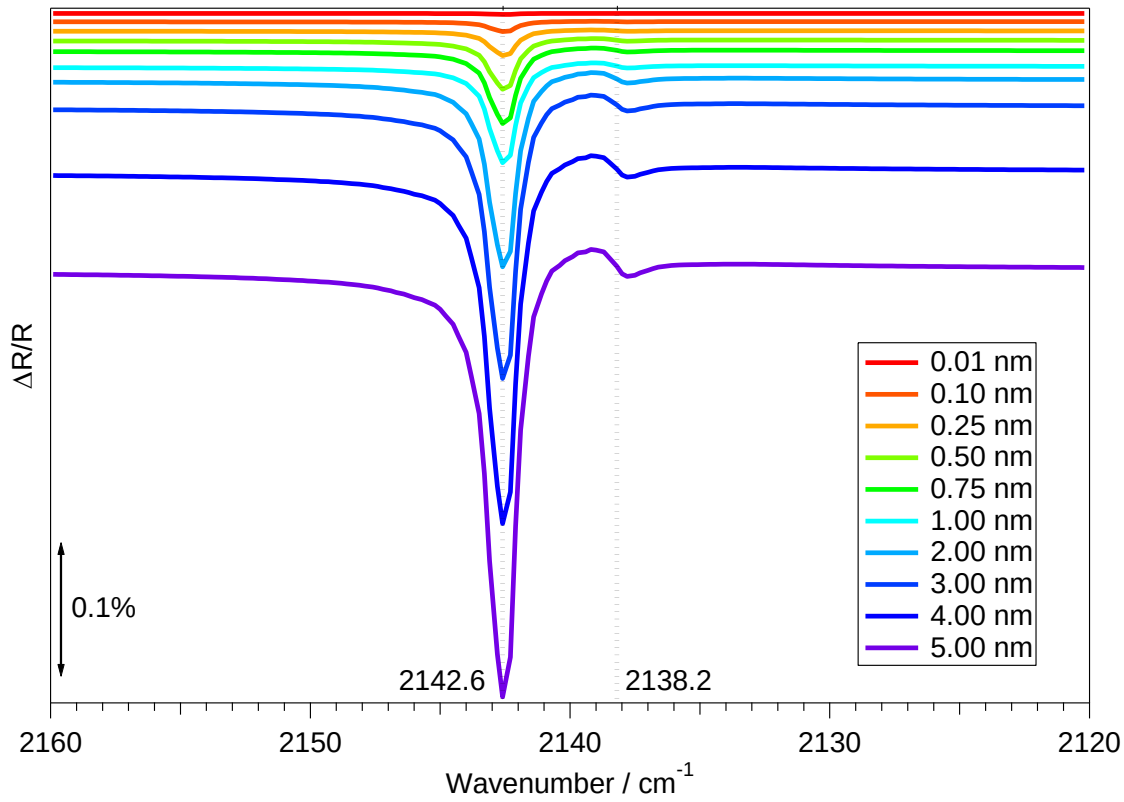

Figure 3.6. Simulated RAIR spectra of solid CO adsorbed on a HOPG surface. A 1 nm thick film equates to a ≈14 L exposure of CO.

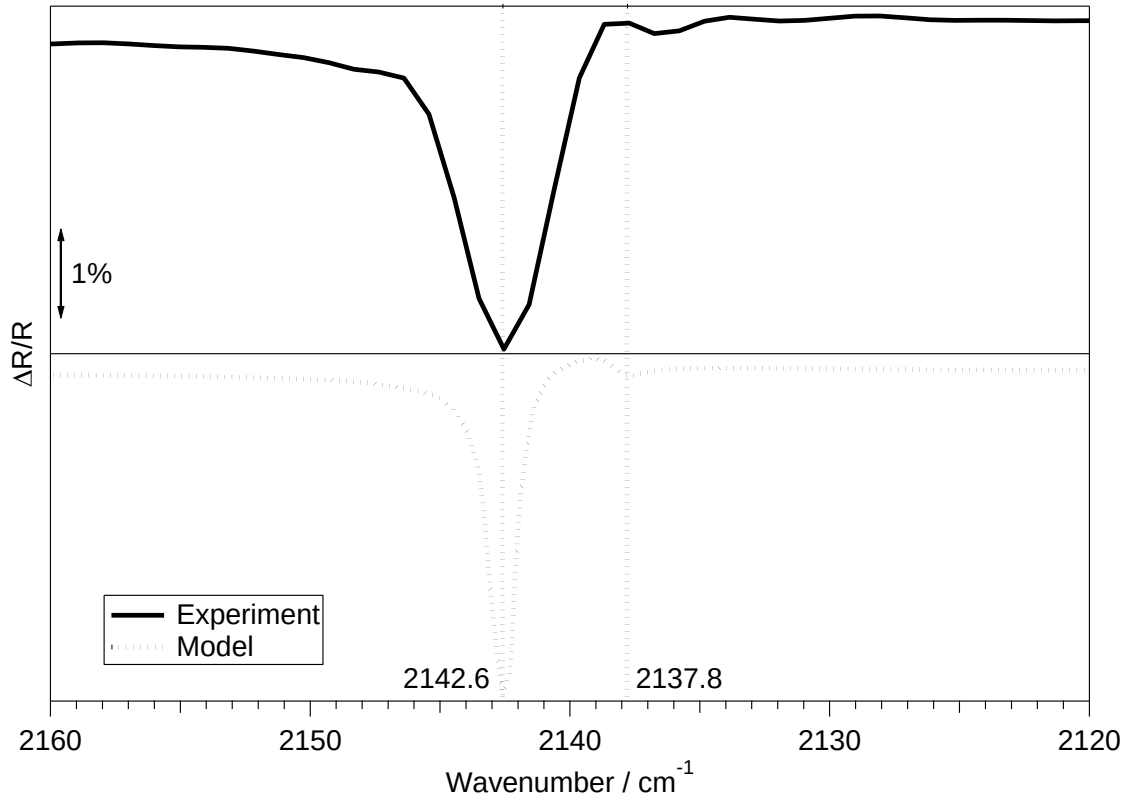

Figure 3.7. Comparison of experimental and simulated RAIR spectra for a 100 L exposure (≈7 nm thickness) of CO adsorbed on bare HOPG at 26 K.

spectra are produced by the co-addition of 128 infrared scans at a resolution of 2 cm^{-1}, leading to broader infrared bands which are not reproduced in the model. The RAIRS model is also not temperature dependent, and therefore cannot be used to investigate the effect of the surface temperature on the positions of the infrared bands. However, a strength of the model is its ability to investigate in detail the optical and physical properties of the ice which are responsible for the observed infrared vibrational bands. By comparing the properties of the ice, such as the refractive index and dielectric constant, with the simulated RAIR spectra, an indication into the origins for the LO - TO splitting can be gained.

Figure 3.8 shows the reflection and extinction coefficients for solid CO at 15 K (top left), taken from reference [36], as well as several physical and optical properties calculated for the CO ice in the wavenumber region of the ν_{CO} stretch, 2120 to 2160 cm^{-1}.

Refractive index and extinction coefficient, n and k. From figure 3.8 (top left), the refractive index shows a minimum and maximum at 2141.6 and 2137.8 cm^{-1} respectively. The extinction coefficient shows a maximum at 2138.7 cm^{-1}. Comparing with the positions of the LO and TO modes observed in the simulated RAIR spectra, at 2142.6 and 2137.8 cm^{-1} respectively, shows close agreement between the optical properties of CO and the observed

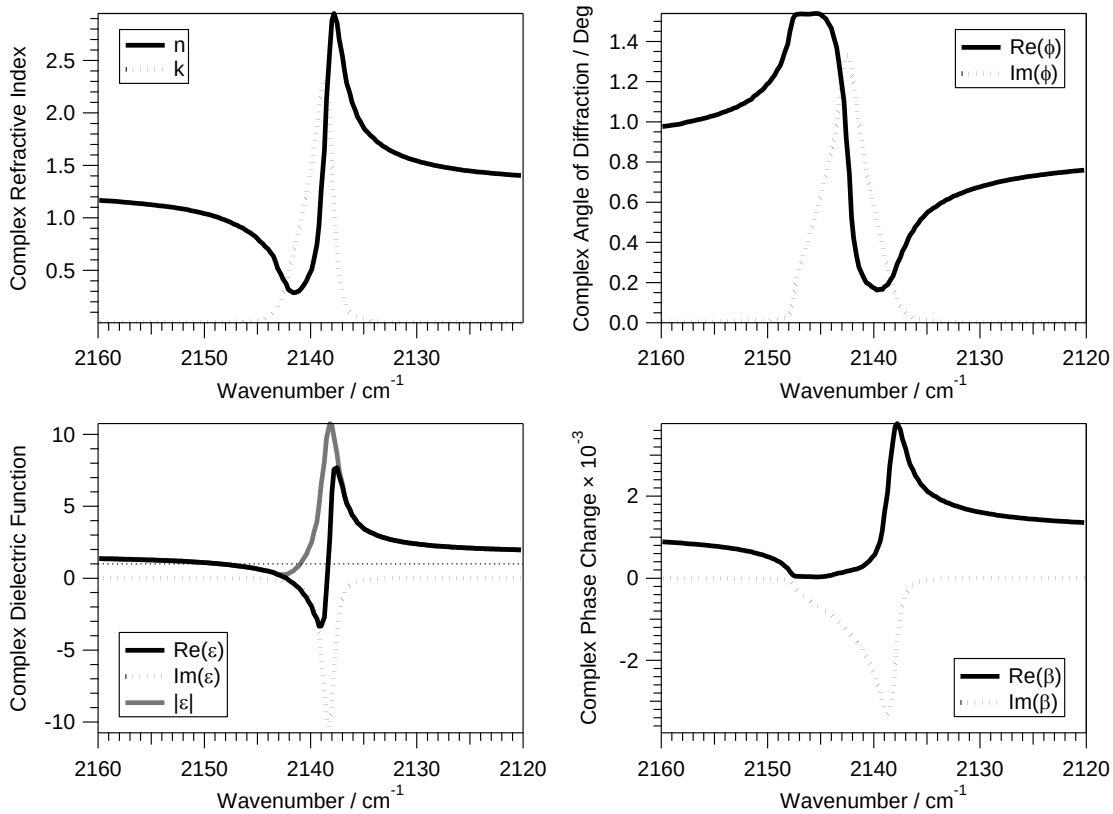

Figure 3.8. Figure showing the functions used in the RAIR model for CO adsorption on a HOPG surface, as a function of wavenumber. Top left. Refractive index of solid CO at 15 K, taken from reference [36]. Top right. Calculated complex angle of refraction, ϕ, between the vacuum and CO film. Bottom left. Calculated complex dielectric function, ε, of solid CO at 15 K. Bottom right. Calculated complex phase change, β, of the light passing through the CO film.

infrared bands. This is as expected, plus exact agreement is observed between the maximum in the value of n and the appearance of the TO mode of the ν_{CO} stretch.

Angle of refraction, ϕ. The angle of refraction of light between the vacuum and CO ice was calculated from Snell's law (equation 3.1), and is shown in figure 3.8 (top right). This was calculated to determine whether the angle of refraction plays a role in the absorption of light by an adsorbate vibration. As evident from equation 3.1, the angle of refraction is complex for an absorbing material at non-normal incidence. At first glance, this is conceptually difficult to understand, as it is expected that the angle of refraction should remain in the plane of incidence and be real, i.e. not have an imaginary component. However, this can be understood by considering the infrared light at each wavelength separately (as a plane wave traversing the ice film), i.e. by considering monochromatic radiation. In a vacuum, the plane wave has wave fronts, planes of constant amplitude and phase. These planes of constant amplitude and phase are parallel to each other and perpendicular to the beam direction. Passing through an absorbing material, the planes of constant phase and amplitude are no longer parallel to each other. The planes of constant phase are perpendicular to the refracted beam direction, as is the case in a non-absorbing material, and hence correspond to the real part of the complex angle of refraction[103]. However, as the amplitude of light will vary across the beam as it passes through the ice, due to absorption of light, the planes of constant amplitude will be parallel to the interface plane. This corresponds to the imaginary part of the complex angle of refraction[103].

From figure 3.8 (top right), the planes of constant phase, or real part of the angle of refraction, show a broad maximum between 2145.5 - 2146.9 cm^{-1}, and a minimum at 2139.7 cm^{-1}. The planes of constant amplitude, or imaginary part of the angle of refraction, show a maximum at 2142.6 cm^{-1}. Comparing to the positions of the LO and TO modes observed in the simulated RAIR spectra, at 2142.6 and 2137.8 cm^{-1}, there is agreement between the imaginary part of the angle of refraction and the LO mode of the ν_{CO} stretch. As the imaginary part of the angle of refraction corresponds to the direction of the planes of constant amplitude, whereby the amplitude of the light decreases as it traverses the adsorbate film, due to absorption, it is clearly expected that this angle corresponds to an absorption band.

Dielectric constant, ε. The complex dielectric constant is calculated from equation 3.6, and is shown in figure 3.8 (bottom left). The importance of the dielectric constant of a crystalline ice with respect to the LO - TO splitting of an adsorbate vibration has been previously catalogued[10,36,90]. In a crystalline film, LO phonons are polarised lattice vibrations propagating parallel to the surface normal, whereas TO phonons are polarised lattice vibrations propagating perpendicular to the surface normal[36,90], as shown in figure 3.9. LO phonon

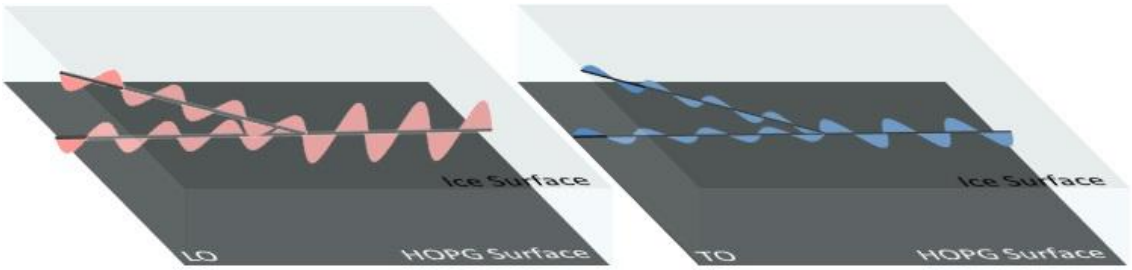

Figure 3.9. Schematic of the interaction of the LO and TO polarised phonon modes with the electric field of incident infrared light. Left. LO phonon vibrations propagating parallel to the surface normal, constructively interacting with the contribution of the electric field vector parallel to the surface normal. Right. TO phonon vibrations propagating perpendicular to the surface normal, constructively interacting with the contribution to the electric field vector perpendicular to the surface normal.

vibrations create an electric field, caused by charge bunching, equal and opposite to the lattice polarisation. Therefore there is no net electric displacement caused by the phonon vibration. In an undamped system, where the amplitude of the phonon vibration does not degrade with time, the LO phonon vibration will occur at the frequency corresponding to $\varepsilon = 0$.[90] Conversely, TO phonon vibrations do not create an electric field, as the shearing motion of the adsorbate molecules do not create charge bunching, and occur at the frequency corresponding to $|\varepsilon| = \infty$.[90]

In a damped system, if the incident infrared radiation has an electric field vector parallel to the surface normal, lattice vibrations that are also parallel to the surface normal, i.e. LO phonon vibrations, will become resonantly enhanced and will occur at frequencies where $|\varepsilon|$ is small[90,107] (figure 3.9). If the incident infrared radiation has an electric field vector perpendicular to the surface normal, lattice vibrations that are also perpendicular to the surface normal, i.e. TO phonon vibrations, will have resonantly enhanced amplitude and will occur at frequencies where $|\varepsilon|$ is large[90,107] (figure 3.9). This effect does not break the metal surface selection rule as p-polarised light has components of the electric field vector both parallel and perpendicular to the surface normal (figure 3.2). This effect has also been observed in amorphous materials[36,91-93] and so it has been argued that periodicity is not required to observed the LO and TO phonon modes of a thin film[36].

The LO and TO phonon modes of CO can be approximated by the minimum and maximum of $|\varepsilon|$ of the CO ice respectively[107]. From figure 3.8 (bottom left), the real part of the dielectric constant shows a minimum and maximum at 2139.2 and 2137.5 cm^{-1} respectively. The imaginary part of the dielectric constant has a minimum at 2138.2 cm^{-1}. Also shown in figure 3.8 (bottom left) is the $|\varepsilon|$ of the CO ice as a function of wavenumber, showing a minimum and maximum at 2142.6 cm^{-1} at $|\varepsilon| = 0.2$ and 2138.2 cm^{-1} at $|\varepsilon| = 10.8$ respectively. Comparing to the positions of the LO and TO modes observed in the simulated RAIR spectra, at

2142.6 and 2137.8 cm^{-1} respectively, there is exact agreement between the minimum in $|\varepsilon|$ and the LO mode of the ν_{CO} stretch and close agreement between the maximum of $|\varepsilon|$ and the TO mode of the ν_{CO} stretch. By considering that in an undamped system, the LO mode should correspond to the frequency where $\varepsilon = 0$, the LO mode is in fact observed as $|\varepsilon| \rightarrow 0$.

Comparing with results for the transmission infrared model of Palumbo et al[10,20,36], the LO and TO phonon modes of CO on a Si surface were observed at 2142.5 and 2138.3 cm^{-1}. This model used the same complex refractive indices[36] as used here, and slight differences in the positions of the LO and TO phonon modes were observed. This is likely due to the different simulation method and surface used in the two cases. However, the positions of the LO and TO modes are in close agreement, validating the model created here. Although the positions of the LO and TO phonon modes was defined for an undamped system in the original work of Berreman[90], the origin of LO - TO splitting in an amorphous CO ice was simply stated, by Palumbo et al[10], as occurring in the frequency range corresponding to an increased reflectivity corresponding to the region where $n < 1$. Therefore the exact properties of the CO ice which cause this effect in amorphous ice is still unknown.

Phase change, β. The phase change of the infrared light as it traverses the ice film was also calculated from equation 3.12, and is shown in figure 3.8 (bottom right). The real part of the phase change shows a broad minimum between 2145.5 - 2146.9 cm^{-1}, and a maximum at 2137.8 cm^{-1}. This broad minimum corresponds to the broad maximum observed in the real part of the angle of refraction, (figure 3.8 (top right)). This is expected, as the real part of the angle of refraction corresponds to the direction of the planes of constant phase as the light traverses the ice. The imaginary part of the phase change shows a minimum at 2138.7 cm^{-1}. Comparing to the positions of the LO and TO modes observed in the simulated RAIR spectra, at 2142.6 and 2137.8 cm^{-1} respectively, shows exact agreement with the minimum of the real part of the phase change of light and the TO mode of the ν_{CO} stretch.

Table 3.1. Summary of the positions of the LO and TO phonon modes from experimental and simulated RAIR spectra of CO on HOPG, along with the positions as predicted from inspection of |ε| and comments describing the optical and physical properties of the ice corresponding to the positions observed in the model.

	Experimental	Model	|ε|		Comments
LO	2143	2142.6	2142.6	0.2	Max Im(ϕ) Min |ε|
TO	2137	2137.8	2138.2	10.8	Max n Max Re(β)

In summary, the optical and physical properties of the CO ice as a function of wavenumber have been calculated in the wavenumber range of the ν_{CO} stretch, and have been compared to the positions of the LO and TO phonon modes from the simulated RAIR spectra, summarised in table 3.1. It was found that although interpretation of the minimum and maximum of $|\varepsilon|$

provided close agreement with the positions observed in the simulated RAIR spectra, exact agreement was only observed for the LO mode of the ν_{CO} stretch, corresponding to $|\varepsilon| \rightarrow 0$. Exact agreement between the maximum in n and Re(β) with the TO mode of the ν_{CO} stretch was also observed, however these optical properties are not expected to directly cause absorption of light by a vibration.

3.4.2. CO_2 Ice

The optical properties and behaviour of CO_2 ice on a surface have been previously shown to be comparable to those of CO ices[10,16,17,19,20,34,36]. Therefore to understand the trends observed in CO ices, and to gain further evidence for the origins for the observed LO - TO splitting, the RAIRS model was extended to investigate CO_2 ices adsorbed on a HOPG surface.

RAIR spectra were collected for a variety of exposures of CO_2 adsorbed on HOPG at 28 K, shown in figure 3.10. The exact details of the spectra will be described in greater detail in chapter 4, and are therefore only briefly discussed here. Following a CO_2 exposure of 10 L, an infrared band is observed in the RAIR spectra at 2376 cm^{-1}, which shifts to 2382 cm^{-1} with increasing CO_2 exposure up to 100 L. Increasing CO_2 exposure shows a low intensity feature

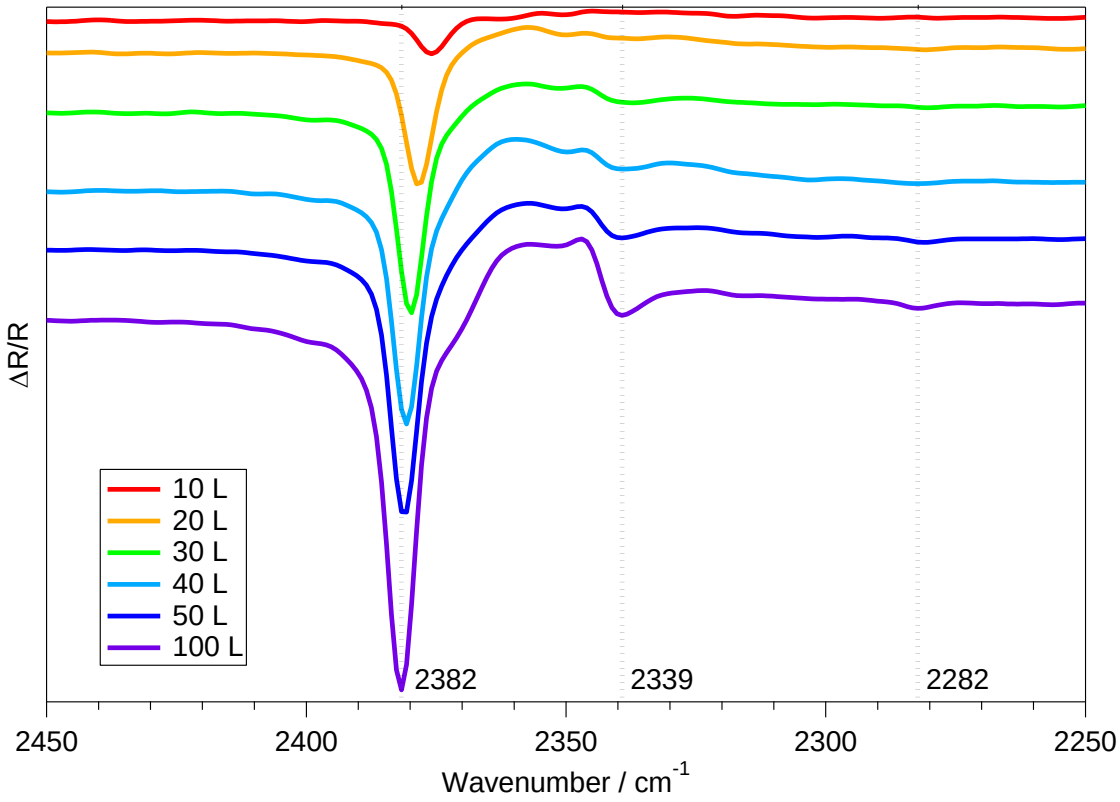

Figure 3.10. RAIR spectra of a range of exposures of CO_2 adsorbed on a bare HOPG surface at 28 K.

appearing at 2339 cm^{-1} following a 20 L exposure, and at 2282 cm^{-1} following a 50 L exposure of CO_2. Further increase of CO_2 exposure, up to 100 L, shows an increase in the size of all observed infrared bands, with no further shift in wavenumber.

Gas phase CO_2 infrared spectra show 3 fundamental infrared active bands at 2349, 2280 and 660 cm^{-1} assigned to the $^{12}CO_2$ and $^{13}CO_2$ ν_3 stretches and the ν_2 bend respectively[87]. As the bands at 2339 and 2282 cm^{-1} are close to those observed for the ν_3 stretches of $^{12}CO_2$ and $^{13}CO_2$ respectively, they can both be assigned to the same vibrational modes, and show that CO_2 is physisorbed on the HOPG surface at 28 K. Comparing to previous studies of amorphous CO_2 adsorbed on a Si surface at 12.5 K[10,20], two infrared bands were observed in the RAIR spectra, in the wavenumber region for the $^{12}CO_2$ ν_3 stretch, at 2377 and 2345 cm^{-1}. In agreement with the assignments of the CO infrared features, these bands were assigned to the LO and TO modes of the $^{12}CO_2$ ν_3 stretch of multilayer CO_2 respectively[10,20]. As discussed previously, observation of LO - TO splitting is usually associated with crystalline ices[36]. Therefore, in conjunction with the CO RAIRS investigation, the origin for the observation of the LO and TO modes of the $^{12}CO_2$ ν_3 stretch in an amorphous ice has been investigated by use of the RAIRS model. No LO - TO splitting is observed for the $^{13}CO_2$ ν_3 stretch and as such, modelling this vibrational band will provide a comparison to a normal infrared absorption peak.

RAIRS Model. RAIR spectra of a film of solid CO_2 adsorbed on a HOPG surface were simulated using the RAIRS model and the results are shown in figure 3.11. At all thicknesses of the CO_2 layer, two infrared bands are observed in the $^{12}CO_2$ ν_3 stretch region, at 2342.6 and 2337.8 cm^{-1} and one infrared band is observed in the $^{13}CO_2$ ν_3 stretch region at 2283 cm^{-1}. In agreement with the simulated RAIR spectra of CO, no changes in the RAIR spectra are observed upon increasing the thickness of the CO ice layer in the simulation, with the exception of the intensities of the infrared bands increasing.

Comparing the experimental and simulated RAIR spectra of CO_2 on HOPG, shown in figure 3.12, shows good agreement between the positions of the LO and TO modes of the $^{12}CO_2$ ν_3 stretch as well as the $^{13}CO_2$ ν_3 stretch, and the relative intensities of the observed infrared bands. However, the experimental RAIR spectra show an increase in the wavenumber of the LO mode of the $^{12}CO_2$ ν_3 stretch with increasing CO_2 exposure. This coverage dependence is not recreated in the RAIRS model of CO_2 on HOPG, and is therefore not a consequence of the optical properties of CO_2. As discussed in chapter 4, the observed coverage dependence of the position of this band is likely caused by a physical interaction between CO_2 molecules within the ice as the thickness of the ice increases. The RAIRS model is limited as it cannot readily simulate physical or chemical interactions within the ice film, or between the ice and surface.

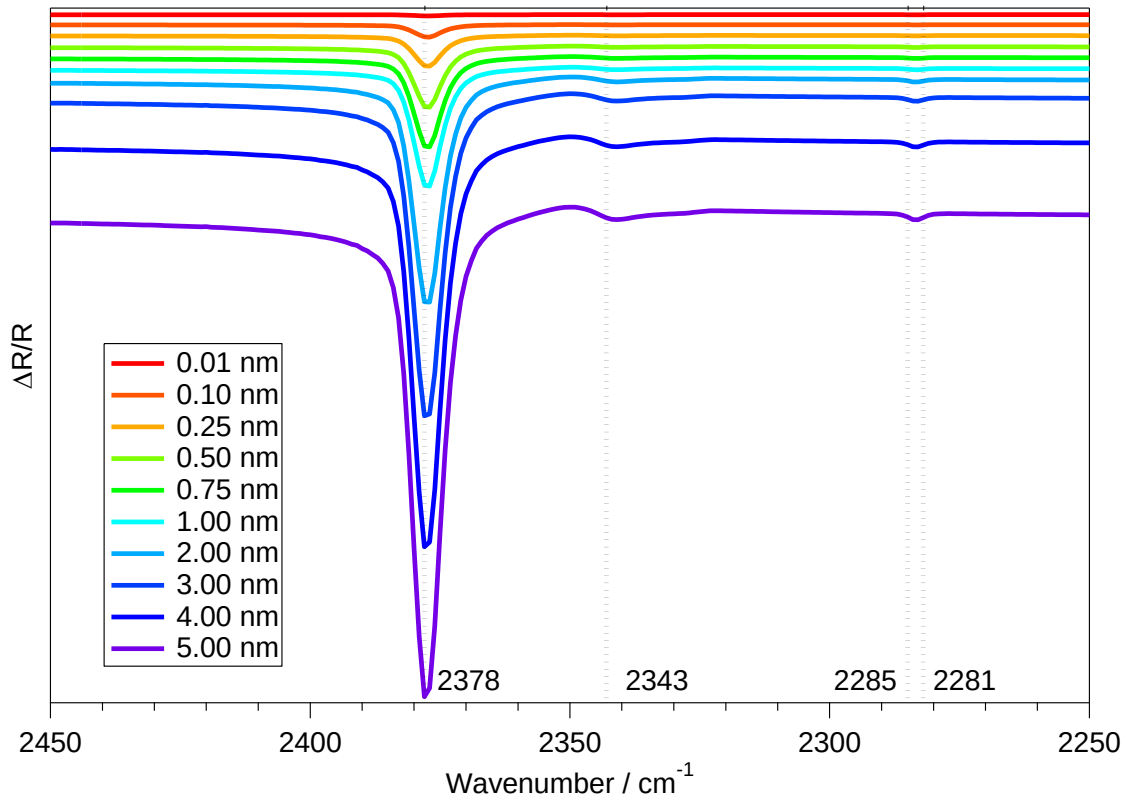

Figure 3.11. Simulated RAIR spectra of solid CO_2 adsorbed on a HOPG surface. A 1 nm thick film equates to a ≈14 L exposure of CO_2.

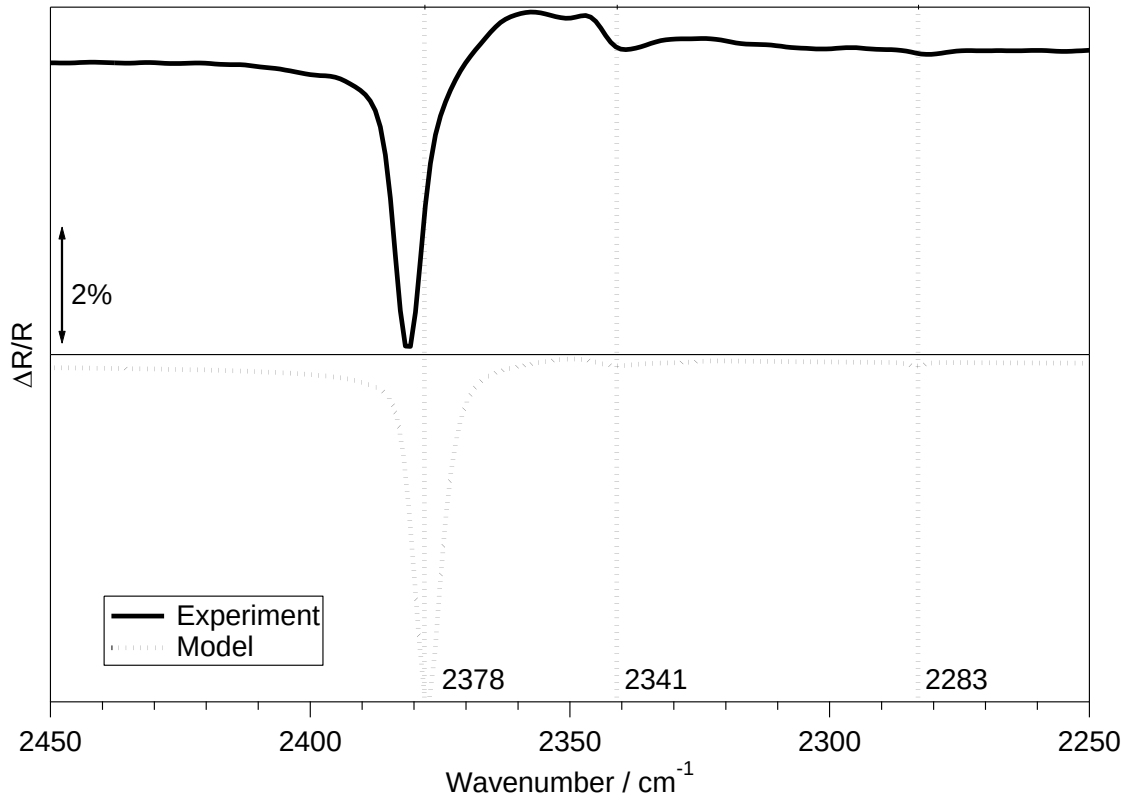

Figure 3.12. Comparison of experimental and simulated RAIR spectra for a 100 L exposure (≈ 7 nm thickness) of CO_2 adsorbed on bare HOPG at 28 K.

To investigate the physical and optical properties of CO_2 responsible for the observed infrared features in the RAIR spectra, the simulated RAIR spectrum of CO_2 will be compared to the optical and physical properties of CO_2, as for CO.

Figure 3.13 shows the reflection and extinction coefficients for solid CO_2 at 12.5 K, taken from reference [10] (top left), as well as several physical and optical properties calculated for the CO_2 ice in the wavenumber region of the $^{12}CO_2$ and $^{13}CO_2$ ν_3 stretches, 2250 - 2450 cm^{-1}.

LO and TO modes of the $^{12}CO_2$ ν_3 stretch. The complex dielectric constant of CO_2, calculated from equation 3.6, is shown in figure 3.13 (bottom left). As for CO RAIR spectra, the LO and TO phonon modes of CO_2 can be approximated by the minimum and maximum of $|\varepsilon|$ of the CO_2 ice respectively[107]. From inspection of $|\varepsilon|$, the LO and TO modes of the $^{12}CO_2$ ν_3 stretch are expected to occur at 2378 cm^{-1} at $|\varepsilon|$ = 0.2 and at 2343 cm^{-1} at $|\varepsilon|$ = 8.9 respectively. Comparing with the positions of the LO and TO modes of the $^{12}CO_2$ ν_3 stretch, observed in the simulated RAIR spectra, at 2378 and 2341 cm^{-1}, there is good agreement between the minimum of $|\varepsilon|$, as $|\varepsilon| \rightarrow 0$, and the LO mode of the $^{12}CO_2$ ν_3 stretch. The TO mode, at 2343 cm^{-1}, is slightly higher than the position observed in the simulated RAIR spectra.

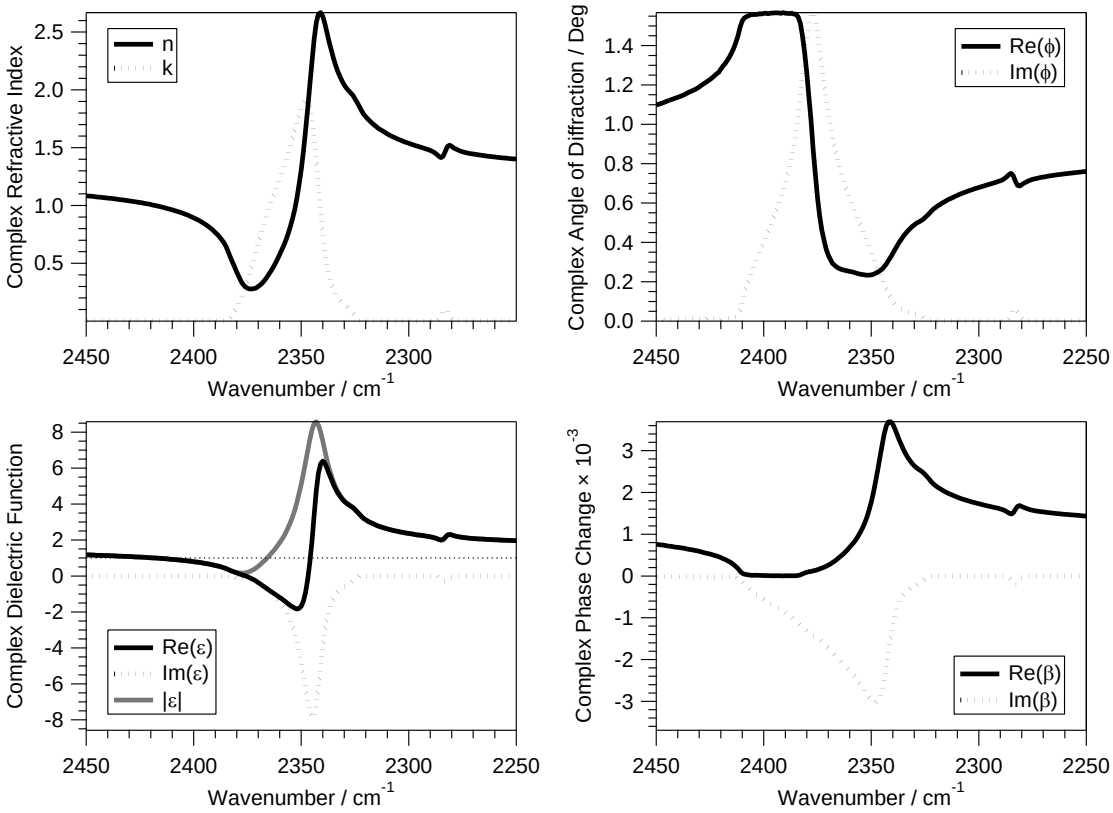

Figure 3.13. Figure showing the functions used in the RAIR model for CO_2 adsorption on a HOPG surface, as a function of wavenumber. Top left. Refractive index of solid CO_2 at 12.5 K, taken from reference [10]. Top right. Calculated complex angle of refraction, ϕ, between the vacuum and CO_2 film. Bottom left. Calculated complex dielectric function, ε, of solid CO_2 at 12.5 K. Bottom right. Calculated complex phase change, β, of the light passing through the CO_2 film.

These trends are in agreement with those observed in the CO RAIR model.

By comparing the position of the TO mode of the $^{12}CO_2$ ν_3 stretch with the refractive index, angle of refraction and phase change of light through the ice, there is agreement with the maximum in n as well as with Re(β) (from equation 3.1), shown in figure 3.13 (bottom right). This trend was also observed in the CO RAIR model. A broad maximum in Re(ϕ), calculated from equation 3.12 (figure 3.13 (top right)), is also observed corresponding to the position of a broad minimum observed in Re(β). Again, both Re(ϕ) and Re(β) describe the phase change of the light as it passes through the ice film, and hence this trend is not surprising.

$^{13}CO_2$ ν_3 stretch. As LO - TO splitting is not observed for the $^{13}CO_2$ ν_3 stretch, inspection of |ε| is not meaningful. However, it should be noted that |ε| does not drop below 1, or approach 0, in the wavenumber region of the $^{13}CO_2$ ν_3 stretch, converse to the observation of |ε| in vibrational regions where LO - TO splitting is observed. Inspection of the optical and physical properties of the CO_2 ice, corresponding to the $^{13}CO_2$ ν_3 stretch, can provide insight into the fundamental properties of the ice which cause infrared absorption in the absence of LO - TO splitting. The $^{13}CO_2$ ν_3 stretch occurs at 2283 cm^{-1} from the simulated RAIR spectra, corresponding to a maximum in k and Im(ϕ) and a minimum in Im(ε) and Im(β). Trends observed between the imaginary parts of ϕ, ε and β with k are expected as the extinction coefficient is directly proportional to each of these functions via equations 3.1, 3.6 and 3.12 with equation 3.2 respectively. Therefore, the observed infrared band can be simply described as coincident with the maximum in k. This is also expected, as k is related to the absorption coefficient, α, by the relationship:

$$\alpha = 2\pi k\sigma \tag{3.14}$$

where σ is the wavenumber. In other words, the optical and physical properties of a vibration which does not show LO - TO splitting are characteristically different to those which do show LO - TO splitting.

Also of interest is a relationship observed between n and the real parts of ϕ, ε and β. This is in agreement with the trend observed between k and the imaginary parts of ϕ, ε and β, as n is directly proportional to each of these functions via equations 3.1, 3.6 and 3.12 with equation 3.2 respectively.

In summary, the optical and physical properties of the CO_2 ice as a function of wavenumber have been calculated in the wavenumber range of the $^{12}CO_2$ and $^{13}CO_2$ ν_3 stretches, and these have been compared to the positions of the infrared features in the simulated and experimental RAIR spectra. These data are summarised in table 3.2. It is found that the LO mode of the $^{12}CO_2$ ν_3 stretch corresponds to a minimum in |ε|, where $|\varepsilon| \rightarrow 0$. Agreement

between the maximum in n and Re(β) with the TO mode of the $^{12}CO_2$ ν_3 stretch is also observed. These trends were also observed in the LO and TO modes of the ν_{CO} stretch of CO. It has also been shown that the $^{13}CO_2$ ν_3 stretch, which does not show LO - TO splitting, has a maximum absorption corresponding to a maximum in k, which is directly proportional to the absorption coefficient, α. For the CO_2 ice, |ε| does not drop below unity in the wavelength region of the $^{13}CO_2$ ν_3 stretch, and therefore does not approach 0 and does not show LO - TO splitting. This may be an indication that the polarisation of the phonon modes within the ice in this wavelength region is weak, and hence there may be no LO or TO polarised phonon vibrations traversing the ice to interact with the incident infrared radiation. To further investigate this, the infrared spectrum of an ice which does not show LO - TO phonon splitting, namely H_2O, has been simulated and compared to the optical and physical properties of the ice.

Table 3.2. Summary of the positions of the LO and TO phonon modes from experimental and simulated RAIR spectra of CO_2 on HOPG, along with the positions as predicted from inspection of |ε| and comments describing the optical and physical properties of the ice corresponding to the positions observed in the model.

	Experimental	Model	|ε|		Comments
$^{12}CO_2$ ν_3 LO	2382	2378	2378	0.2	Min |ε|
$^{12}CO_2$ ν_3 TO	2339	2341	2343	8.9	Max n Max Re(β)
$^{13}CO_2$ ν_3	2282	2283	-	> 1	Max k

3.4.3. H_2O Ice

In contrast to the comparable optical behaviour of CO and CO_2 ices, simulating the RAIR spectra of H_2O ices will allow comparison between the behaviour of polar and apolar ices as well as an investigation of the absorption of infrared bands which are not affected by LO and TO phonon splitting.

Typical RAIR spectra for H_2O adsorbed on a HOPG surface have been previously collected[108]. A RAIR spectrum following deposition of multilayer H_2O shows two infrared bands, a very broad feature around 3430 cm^{-1} and a less intense peak at 1670 cm^{-1}, assigned previously to the ν_{OH} stretching mode and HOH scissors mode of amorphous solid water (ASW) respectively[108].

RAIR spectra of the ν_{OH} stretch of a film of solid H_2O adsorbed on a HOPG surface were simulated using the model discussed earlier. Figure 3.14 (top left) shows the reflection and extinction coefficients for solid H_2O at 10 K, taken from reference [106]. Also shown in figure 3.14 are the other functions and coefficients used in the RAIR model, including the complex angle of refraction (top right), calculated from Snell's law of refraction (equation 3.1), the

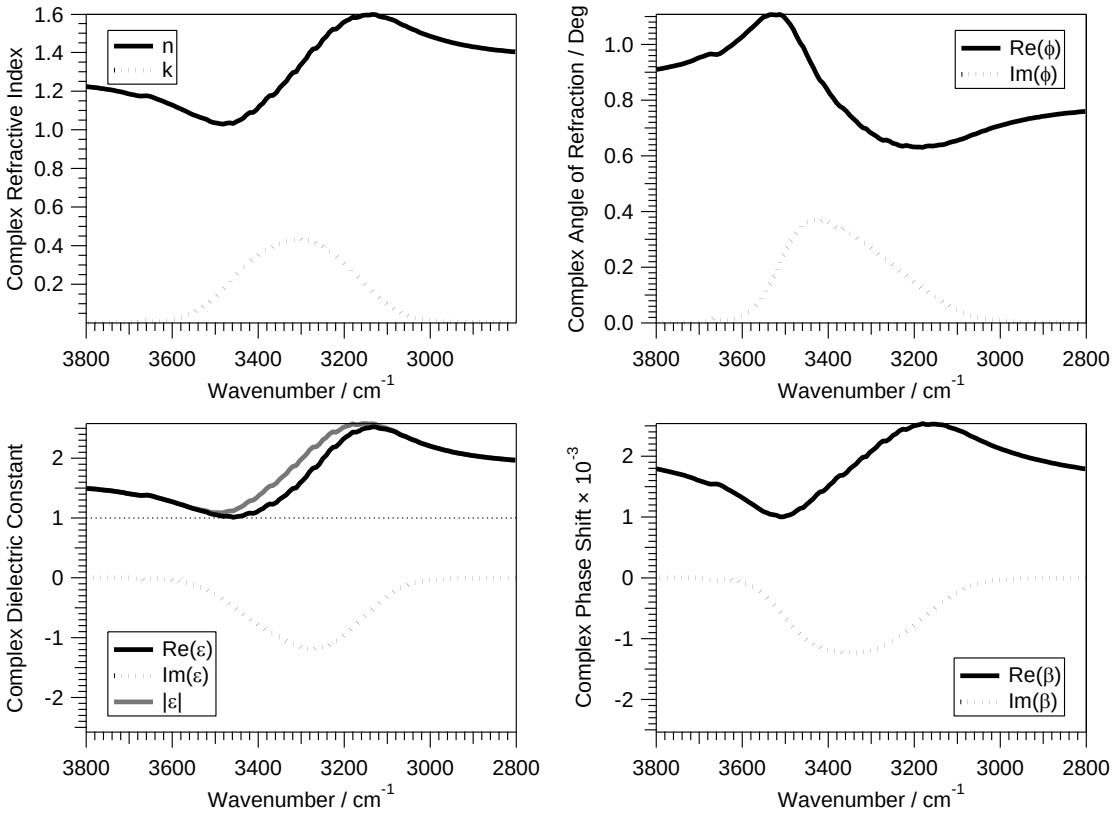

Figure 3.14. Figure showing the functions used in the RAIR model for H_2O adsorption on a HOPG surface, as a function of wavenumber. Top left. Refractive index of solid H_2O at 10 K, taken from reference [106]. Top right. Calculated complex angle of refraction, ϕ, between the vacuum and H_2O film. Bottom left. Calculated complex dielectric function, ε, of solid H_2O at 10 K. Bottom right. Calculated complex phase change, β, of the light passing through the H_2O film.

complex dielectric function (bottom left), calculated from equation 3.7, as well as |ε| and the complex phase change (bottom right), calculated from equation 3.15.

Using the coefficients shown in figure 3.14 in the RAIRS model, a RAIR spectrum of solid H_2O adsorbed on a HOPG surface has been simulated, and is shown in figure 3.15. Figure 3.15 also shows a typical RAIR spectrum of multilayer ASW on HOPG. The simulated RAIR spectrum of ASW shows a broad band centred around 3430 cm^{-1} and a small feature at 3666 cm^{-1}, assigned to the ν_{OH} stretch and OH dangling bond of multilayer ASW respectively[108]. As discussed previously, the RAIRS model used here is temperature independent and does not reflect any physical or chemical processes that occur on the surface. However, as observed in figure 3.15, the ν_{OH} stretch of H_2O is very broad, characteristic of hydrogen bonding within the ice film, and the OH dangling bonds of multilayer ASW are also observed, a characteristic of the surface area of the ice. These infrared features are not being simulated by the RAIR model however. Instead they are caused by the method in which the refractive indices were obtained. The H_2O refractive indices used here were found by satisfying the Kramers-Kronig relation[109] for the experimental transmission spectra of ASW adsorbed on an optically

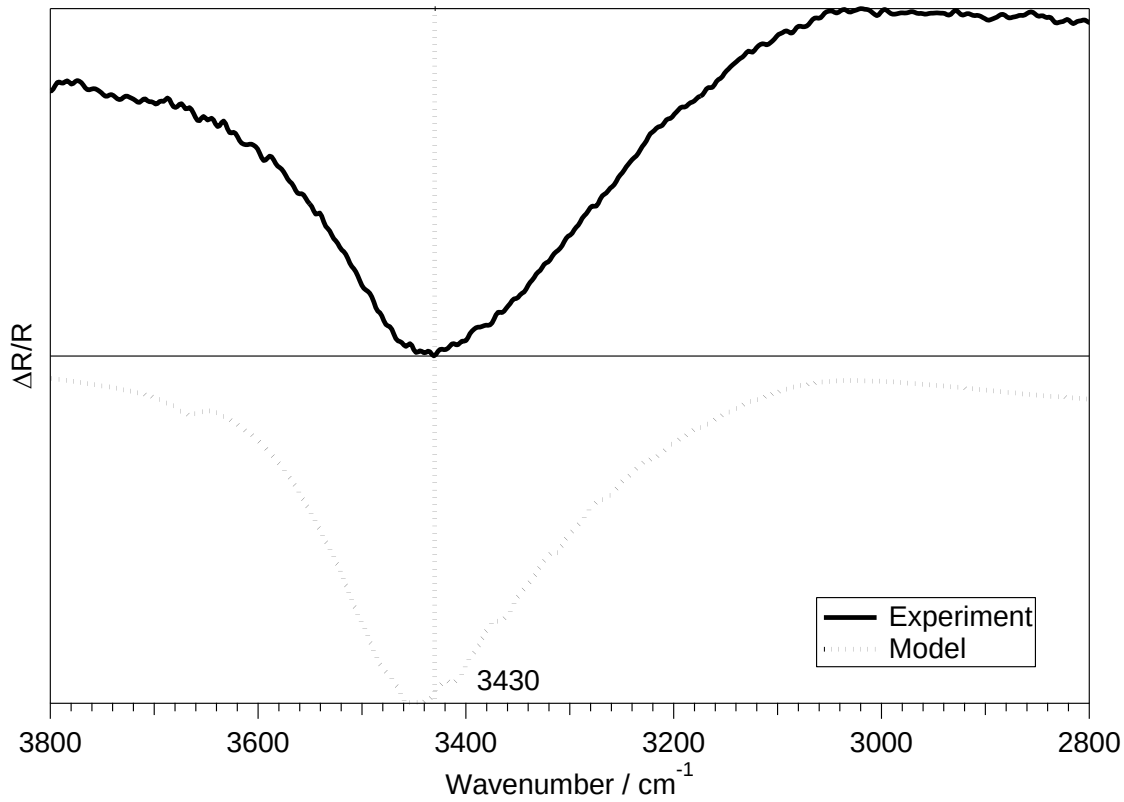

Figure 3.15. Comparison of experimental and simulated RAIR spectra for a 100 L exposure (≈ 9 nm thickness) of H_2O adsorbed on bare HOPG at 20 K.

transparent CsI surface at 10 K[106]. Therefore, the broad nature of ν_{OH} stretch and OH dangling bonds were observed in the experimental infrared spectra and are therefore translated into the optical properties of H_2O upon determination of n and k.

Table 3.3. Summary of the position of the ν_{OH} stretch from experimental and simulated RAIR spectra of H_2O on HOPG, along with the optical and physical properties of the ice corresponding to the positions observed in the model.

	Experimental	Model	|ε|		Comments
ν_{OH}	3430	3440	-	> 1	Max Im(ϕ)

Table 3.3 shows a comparison between the position of the ν_{OH} stretch from experimental and simulated RAIR spectra of H_2O adsorbed on HOPG. As discussed previously, detailed inspection of |ε| is not necessarily meaningful for the position of the vibrational band in an ice which shows no LO - TO splitting. However, it is noted again that the |ε| of the ice, in the wavenumber region of the ν_{OH} stretch, does not drop below unity and therefore does not approach 0 so does not show LO - TO splitting. Although the ν_{OH} stretch does not correspond to the maximum in k at 3304 cm^{-1} (figure 3.14 (bottom left)), as observed for the $^{13}CO_2$ ν_3 stretch, it does correspond to a maximum in Im(ϕ) which, as discussed previously, is related to k via equations 3.1 and 3.2. Hence a general trend in the optical and physical properties of an

ice which does not show LO - TO splitting is observed, which is characteristically different to the trends observed for ices which do show LO - TO splitting.

3.5. Summary and Conclusions

Experimental and simulated RAIR spectra have been obtained for CO, CO_2 and H_2O ices adsorbed on a HOPG surface. Experimental RAIR spectra of CO, CO_2 and H_2O ices are shown to be accurately reproduced by the RAIRS model, validating the model, as well as providing a tool to study the fundamental optical and physical properties responsible for infrared absorption of dielectric ices on a 'metal-like' surface. As has been shown, by comparing the optical and physical properties of each ice in the wavenumber region of an infrared vibration with the simulated RAIR spectra, the LO - TO splitting is observed to occur as $|\varepsilon| \rightarrow 0$ when $|\varepsilon| < 1$. It also appears that the LO and TO phonon modes can be generally approximated by inspection of the positions of the minimum and maximum of $|\varepsilon|$ respectively. For CO and CO_2 ices, the TO phonon mode occurs coincident with the maximum in n. An infrared vibration of CO_2 ice in the wavenumber range where LO - TO splitting is not expected shows a single vibrational band coincident with the maximum in k, as expected, due to the direct relationship with the absorption coefficient.

Table 3.4. Predicted positions of the LO and TO phonon modes of the δ_s and ν_{CO} vibrations of NH_3 and OCS respectively from the model, compared against the observed infrared bands from [110] and [111] respectively.

Ice		Experimental	Model	|ε|		Comments
NH_3	δ_s LO	1080[110]	1076.7	1076.7	0.5	Max Im(ϕ) Min |ε|
	δ_s TO	1057[110]	1052.3	1054.7	11.6	Max n Max Re(β)
OCS	ν_{CO} LO	2073[111]	2085.2	2085.2	0.3	Max Im(ϕ) Min |ε|
	ν_{CO} TO	2019[111]	2015.8	2017.7	5.8	Max n Max Re(β)

Previous studies of the optical properties of CO and CO_2 on a Si surface[10,20,34,36] describe a similar effect for the positions and properties of the TO modes in amorphous ice, where the LO - TO splitting was observed due to the increased reflectivity as a function of $k^2 - n^2$, in the wavenumber region where $n < 1$. As the region where $n < 1$ is related to $|\varepsilon| < 1$, this study is in agreement with that for CO and CO_2 on Si. This study has also built upon the understanding of the properties of an ice exhibiting LO - TO splitting of the vibrational bands, whereby the positions of the LO and TO phonon modes can be predicted for other amorphous ices, for example NH_3 and OCS. Table 3.4 shows the predicted positions of the LO and TO modes of the

NH_3 symmetric deformation, δ_s, and the OCS vibration, ν_{CO}. Using the optical properties of NH_3 and OCS from reference [106], both the NH_3 δ_s and OCS ν_{CO} vibrations are expected to exhibit LO - TO splitting as $|\varepsilon| < 1$. Comparing to the Raman spectra of NH_3 on a brass substrate at 18 K[110] and the infrared spectra of OCS on a HOPG surface at 14 K[111], agreement with the observation and positions of the LO and TO modes of each respective vibration has been shown.

The model is limited however, and cannot be used to simulate RAIR spectra of ice layers involving chemical or physical interactions within or between the layers. For example, the experimental RAIR spectra of CO_2 show a coverage dependence upon adsorption of increasing exposures of CO_2. This is not seen in the simulated RAIR spectra as it is not caused by the optical properties of CO_2. The model can also be modified to simulate RAIR spectra of four or more layers, for example CO or CO_2 covered H_2O ices adsorbed on a HOPG surface could be investigated. However, the optical properties of H_2O in the infrared region of the CO and CO_2 vibrational absorption regions show no absorption features, and are similar to those of a transparent dielectric film. Therefore the model will not simulate any interaction between the CO or CO_2 film and the H_2O layer. The model cannot be simply modified to simulate a rough or heterogeneous surface, as it assumes that the interfaces between the layers is flat and parallel to the surface plane. To simulate more complex interstellar ices, a higher level computational approach would therefore be required. Despite this, a greater understanding of the vibrational properties of a pure amorphous ice is required to better identify and characterise more complex mixed or layered ices, with applications in observing the composition of interstellar ices.

3.6. References

1. Allamandola L.J., Bernstein M.P., Sandford S.A. and Walker R.L., *Space Sci. Rev.*, **90**, (1999), 219-232
2. Greenberg J.M., *Surf. Sci.*, **500**, (2002), 793-822
3. Allamandola L.J., Sandford S.A. and Valero G.J., *Icarus*, **76(2)**, (1988), 225-252
4. d'Hendecourt L., Allamandola L.J., Grim R.J.A. and Greenberg J.M., *Astron. Astrophys.*, **158**, (1986), 119-134
5. Gerakines P.A., Schutte W.A., Greenberg J.M. and van Dishoeck E.F., *Astron. Astrophys.*, **296**, (1995), 810-818
6. Sandford S.A. and Allamandola L.J., *Astrophys. J.*, **355**, (1990), 357-372
7. Tielens A.G.G.M., Tokunaga A.T., Geballe T.R. and Baas F., *Astrophys. J.*, **381**, (1991), 181-199
8. Whittet D.C.B. and Duley W.W., *Astron. Astrophys.*, **2**, (1991), 167-189
9. Allouche A., Verlaque P. and Pourcin J., *J. Phys. Chem. B*, **102**, (1998), 89-98
10. Baratta G.A. and Palumbo M.E., *J. Opt. Soc. Am. A*, **15(12)**, (1998), 3076-3085
11. Baratta G.A., Palumbo M.E. and Strazzulla G., *Astron. Astrophys.*, **357**, (2000), 1045-1050
12. Bouwman J. et al, *Astron. Astrophys.*, **476**, (2007), 995-1003

13. Boyd D.A., Hess F.M. and Hess G.B., *Surf. Sci.*, **519**, (2002), 125-138
14. Camplin J.P., Cook J.C. and McCash E.M., *J. Chem. Soc. Faraday Trans.*, **91(20)**, (1995), 3563-3567
15. Chang H.-C., Richardson H.H. and Ewing G.E., *J. Chem. Phys.*, **89**, (1988), 7561-7568
16. Collings M.P., Dever J.W., Fraser H.J., McCoustra M.R.S. and Williams D.A., *Astrophys. J.*, **583**, (2003), 1058-1062
17. Collings M.P., Dever J.W., Fraser H.J. and McCoustra M.R.S., *Astrophys. Space Sci.*, **285**, (2003), 633-659
18. Devlin J.P., *J. Phys. Chem.*, **96(15)**, (1992), 6185
19. Ehrenfreund P. et al, *Astron. Astrophys.*, **315**, (1996), L341-L344
20. Ehrenfreund P., Boogert A.C.A., Gerakines P.A., Tielens A.G.G.M. and van Dishoeck E.F., *Astron. Astrophys.*, **328**, (1997), 649-669
21. Elsila J., Allamandola L.J. and Sandford S.A., *Astrophys. J.*, **479**, (1997), 818-838
22. Eve J.K. and McCash E.M., *Chem. Phys. Lett.*, **360(3-4)**, (2002), 202-208
23. Ewing G.E. and Pimentel G.C., *J. Chem. Phys.*, **35(3)**, (1961), 925-930
24. Ewing G.E., *J. Chem. Phys.*, **37(10)**, (1962), 2250-2256
25. Fraser H.J., Collings M.P., Dever J.W. and McCoustra M.R.S., *Mon. Not. R. Astron. Soc.*, **353**, (2004), 59-68
26. Heidberg J., Warskulat M. and Folman M., *J. Elec. Spec. Rel. Phenom.*, **54/55**, (1990), 961-970
27. Hoffman F.M. and Weisel M.D., *J. Vac. Sci. Technol. A*, **11(4)**, (1993), 1957-1963
28. Jamieson C.S., Mebel A.M. and Kaiser R.I., *Astrophys. J. Supp. Ser.*, **163**, (2006), 184-206
29. Jiang Y-X., Ding N. and Sun S-G., *J. Electroanal. Chem.*, **563**, (2004), 15-21
30. Lubezky A. and Folman M., *J. Chem. Soc. Faraday Trans.*, **77**, (1981), 791-796
31. Maki A.G., *J. Chem. Phys.*, **35(3)**, (1961), 931-935
32. Matranga C. and Bockrath B., *J. Phys. Chem. B*, **109**, (2005), 4853-4864
33. Mennella V., Baratta G.A., Palumbo M.E. and Bergin E.A., *Astrophys. J.*, **643**, (2006), 923-931
34. Palumbo M.E. and Strazzulla G., *Astron. Astrophys.*, **269**, (1993), 568-580
35. Palumbo M.E., *J. Phys. Chem. A*, **101**, (1997), 4298-4301
36. Palumbo M.E., Baratta G.A., Collings M.P. and McCoustra M.R.S., *Phys. Chem. Chem. Phys.*, **8**, (2006), 279-284
37. Sandford S.A., Allamandola L.J., Tielens A.G.G.M. and Valero G.J., *Astrophys. J.*, **329**, (1988), 498-510
38. Sandford S.A. and Allamandola L.J., *Icarus*, **76**, (1988), 201-224
39. van Broekhuizen F.A., Groot I.M.N., Fraser H.J., van Dishoeck E.F. and Schlemmer S., *Astron. Astrophys.*, **451**, (2006), 723-731
40. Wälchli N., Kampshoff E. and Kern K., *Surf. Sci.*, **368**, (1996), 258-263
41. Zumofen G., *J. Chem. Phys.*, **68(8)**, (1978), 3747-3759
42. Dartois E., Demyk K., d'Hendecourt L. and Ehrenfreund P., *Astron. Astrophys.*, **351**, (1999), 1066-1074
43. Ehrenfreund P. et al, *Astron. Astrophys.*, **350**, (1999), 240-253
44. Hodyss R., Johnson P.V., Orzechowska G.E., Goguen J.D. and Kanik I., *Icarus*, **194**, (2008), 836-842
45. Öberg K.I. et al, *Astron. Astrophys.*, **462**, (2007), 1187-1198
46. Ovchinnikov M.A. and Wight C.A., *J. Chem. Phys.*, **99(5)**, (1993), 3374-3379
47. Bernstein M.P., Cruikshank D.P. and Sandford S.A., *Icarus*, **179**, (2005), 527-534
48. Gálvez O. et al, *Astron. Astrophys.*, **472**, (2007), 691-698
49. Gálvez O., Maté B., Herrero V.J. and Escribano R., *Icarus*, **197**, (2008), 599-605
50. Matè B., Gálvez O., Herrero V.J. and Escribano R., *Astrophys. J.*, **690**, (2009), 486-495
51. Palumbo M.E. et al, *Astron. Astrophys.*, **334**, (1998), 247-252
52. Palumbo M.E. and Baratta G.A., *Astron. Astrophys.*, **361**, (2000), 298-302
53. Kumi G., Malyk S., Hawkins S., Reisler H. and Wittig C., *J. Phys. Chem. A*, **110**, (2006), 2097-2105

54. Malyk S., Kumi G., Reisler H. and Wittig C., *J. Phys. Chem. A*, **111**, (2007), 13365-13370
55. Heidberg J. and Redlich B., *Surf. Sci.*, **368**, (1996), 140-146
56. Falk M., *J. Chem. Phys.*, **86(2)**, (1986), 560-564
57. Falk M. and Seto P.F., *Can. J. Spectrosc.*, **31(5)**, (1986), 134-137
58. Osberg W.E. and Hornig D.F., *J. Chem. Phys.*, **20(9)**, (1952), 1345-1347
59. Heidberg J. et al, *Vacuum*, **38(4/5)**, (1988), 275-277
60. Berg O. and Ewing G.E., *Surf. Sci.*, **220**, (1989), 207-229
61. Wood B.E. and Roux J.A., *J. Opt. Soc. Am.*, **72(6)**, (1982), 720-728
62. Pokrovski K., Jung K.T. and Bell A.T., *Langmuir*, **17**, (2001), 4297-4303
63. Stevens R.W.Jr., Siriwardane R.V. and Logan J., *Energy & Fuels*, **22**, (2008), 3070-3079
64. Andersson P.U., Någård M.B., Witt G. and Pettersson J.B.C., *J. Phys. Chem. A*, **108**, (2004), 4627-4631
65. Matè B. et al, *J. Phys. Chem. A*, **112**, (2008), 457-465
66. Öberg K.I., van Dishoeck E.F. and Linnartz H., *Astron. Astrophys.*, **496**, (2009), 281-293
67. Wilson R.W., Jefferts K.B. and Penzias A.A., *Astrophys. J.*, **161**, (1970), L43-L44
68. Blake G.A., Sutton E.C., Masson C.R. and Phillips T.G., *Astrophys. J.*, **315**, (1987), 621-645
69. Chiar J.E., Adamson A.J., Kerr T.H. and Whittet D.C.B., *Astrophys. J.*, **426**, (1994), 240-248
70. Chiar J.E., Adamson A.J., Kerr T.H. and Whittet D.C.B., *Astrophys. J.*, **455**, (1995), 234-243
71. Chiar J.E. et al, *Astrophys. J.*, **498**, (1998), 716-727
72. Lacy J.H. et al, *Astrophys. J.*, **276**, (1984), 533-543
73. Altwegg K., Balsiger H. and Geiss J., *Space Sci. Rev.*, **90**, (1999), 3-18
74. Crovisier J. and Bockelée-Morvan D., *Space Sci. Rev.*, **90**, (1999), 19-32
75. Allamandola L.J., Sandford S.A., Tielens A.G.G.M. and Herbst E., *Astrophys. J.*, **399**, (1992), 134-146
76. Boogert A.C.A. et al, *Astrophys. J. Supp. Ser.*, **154**, (2004), 359-362
77. Dartois E., Pontoppidan K., Thi W.F. and Muñoz Caro G.M., *Astron. Astrophys.*, **444**, (2005), L57-L60
78. Pontoppidan K.M. et al, *Astrophys. J.*, **622**, (2005), 463-481
79. Watson D.M. et al, *Astrophys. J. Supp. Ser.*, **154**, (2004), 391-395
80. d'Hendecourt L. et al, *Astron. Astrophys.*, **315**, (1996), L365-L368
81. de Graauw Th. et al, *Astron. Astrophys.*, **315**, (1996), L345-L348
82. Gerakines P.A. et al, *Astrophys. J.*, **522**, (1999), 357-377
83. Gibb E.L., Whittet D.C.B., Boogert A.C.A. and Tielens A.G.G.M., *Astrophys. J. Supp. Ser.*, **151**, (2004), 35-73
84. Nummelin A., Whittet D.C.B., Gibb E.L., Gerakines P.A. and Chiar J.E., *Astrophys. J.*, **558**, (2001), 185-193
85. Whittet D.C.B. et al, *Astrophys. J.*, **655**, (2007), 332-341
86. van Dishoeck E.F. et al, *Astron. Astrophys.*, **315**, (1996), L349-L352
87. Herzberg G.Infrared and Raman Spectra of Polyatomic Molecules. D. Van Nostrand Company: N.Y., 1945.
88. Whittet D.C.B. et al, *Astron. Astrophys.*, **315**, (1996), L357-L360
89. Pontoppidan K.M. et al, *Astron. Astrophys.*, **408**, (2003), 981-1007
90. Berreman D.W., *Phys. Rev.*, **130(6)**, (1963), 2193-2198
91. Almeida R.M., *Phys. Rev. B.*, **45(1)**, (1992), 161-170
92. Trasferetti B.C., Davanzo C.U., Zoppi R.A., da Cruz N.C. and de Moraes M.A.B., *Phys. Rev. B.*, **64**, (2001), 125404
93. Wäckelgård E., *J. Phys. Condens. Matter*, **8**, (1996), 4289-4299
94. Greenler R.G., *J. Chem. Phys.*, **44(1)**, (1966), 310-315
95. Greenler R.G., *J. Chem. Phys.*, **50(5)**, (1969), 1963-1968
96. Greenler R.G., *J. Vac. Sci. Technol.*, **12(6)**, (1975), 1410-1417
97. Awaluddin A. et al, *Surf. Sci.*, **502-503**, (2002), 63-69
98. Le Vent S., Pilling M.J. and Gardner P., *Surf. Sci.*, **587**, (2005), 150-158
99. Pilling M.J. et al, *J. Chem. Phys.*, **117(14)**, (2002), 6780-6788
100. Pilling M.J., Gardner P. and Le Vent S., *Surf. Sci.*, **582**, (2005), 1-13

101. McIntyre J.D.E. and Aspnes D.E., *Surf. Sci.*, **24**, (1971), 417-434
102. Kattner J. and Hoffman H., External Reflection Spectrscopy of Thin Films on Dielectric Substrates. *in Handbook of Vibrational Spectrscopy Volume 2*, Chalmers J.M. and Griffiths P.R. (Eds.), John Wiley & Sons Ltd, (2002), 1009-1027
103. Claybourn M., External Reflection Spectrscopy. *in Handbook of Vibrational Spectroscopy Volume 2*, Chalmers J.M. and Griffiths P.R. (Eds.), John Wiley & Sons Ltd., (2002), 969-981
104. Leitner T., Kattner J. and Hoffmann H., *Applied Spectr.*, **57(12)**, (2003), 1502-1509
105. Borghesi A. and Guizzetti G., Graphite (C). *in Handbook of Optical Constants of Solids II*, Palik E.D. (Ed.), Academic Press, (1991), 449-460
106. Hudgins D.M., Sandford S.A., Allamandola L.J. and Tielens A.G.G.M., *Astrophys. J. Supp. Ser.*, **86**, (1993), 713-870
107. Chang I.F., Mitra S.S., Plendl J.N. and Mansur L.C., *Phys. Status Solidi (b)*, **28(2)**, (1968), 663-673
108. Bolina A.S., Wolff A.J. and Brown W.A., *J. Phys. Chem. B*, **109**, (2005), 16836-16845
109. Bergren M.S., Schuh D., Sceats M.G. and Rice S.A., *J. Chem. Phys.*, **69(8)**, (1978), 3477-3482
110. Binbrek O.S. and Anderson A., *Chem. Phys. Lett.*, **15(3)**, (1972), 421-427
111. Burke D.J. and Brown W.A., *Phys. Chem. Chem. Phys.*, **12**, (2010), 5947-5969

Chapter 4: Temperature Programmed Desorption and Reflection Absorption Infrared Spectroscopy of Carbon Dioxide bearing ices on Highly Oriented Pyrolytic Graphite

4.1. Introduction

Since the launch of the Infrared Space Observatory (ISO) in 1995[1] observations of CO_2 in the interstellar medium (ISM) have been made using the Short Wavelength Spectrometer[2]. Prior to this, direct ground and air based observations of CO_2 in the ISM were hindered by atmospheric CO_2. CO_2 is predominantly found in the solid phase in the ISM, with typically less than 5% of interstellar CO_2 being found in the gas phase[3]. CO_2 has been shown to be a major constituent of icy mantles which accumulate on the surface of dust grains in dense interstellar clouds[4]. Infrared observations from the Spitzer Space Telescope[5-8] and ISO[9-13] have shown that CO_2 is found in the solid phase in abundances of 10 - 23% relative to H_2O towards high and low mass stars, field stars and galactic centre sources[14]. The abundance of solid CO_2 has also been found to be up to 37% relative to H_2O towards some low and intermediate mass sources[14,15].

Understanding the nature of CO_2 in the ISM is of great importance for many reasons. Understanding the cosmic evolution of carbon, including characterising the formation of CO_2[16,17] and its role in the formation of larger carbon bearing species (for example glycine[18]), is a key problem in astrophysics[10]. It has also been shown from observation and experimentation that CO_2 is a powerful tracer molecule in investigating the composition, thermal and radiation history of an icy mantle[19,20]. The vibrational modes of CO_2 are characteristically different depending on the composition of the ice matrix, whether apolar (CO, CO_2, O_2 and N_2 rich)[20,21] or polar (H_2O and CH_3OH rich)[20,21], as well as on the evolution of the icy mantle in the cycle of interstellar clouds[20].

Gas phase CO_2 infrared spectra show 5 infrared active bands[22]; three fundamental bands at 2349, 2280 and 660 cm^{-1} assigned to the $^{12}CO_2$ and $^{13}CO_2$ ν_3 stretches and the ν_2 bend respectively, and two combination bands at 3705 and 3600 cm^{-1} assigned to the $\nu_1 + \nu_3$ and $2\nu_2 + \nu_3$ combination modes of CO_2. A large range of surface infrared studies, using both transmission and reflection infrared spectroscopy, of pure CO_2 as well as CO_2-bearing polar and apolar ices have been conducted on a range of surfaces including CsI[14,19,20,23-30], Si[31-37], MgO[38-40], NaCl[41-45], Ge[46], zeolitic[47,48], carbonaceous[49,50], Al[51] and Au[52] surfaces. Comparing infrared studies of CO_2-bearing polar ices[19,23,25,30,33-35,37,51] with CO_2-bearing apolar ices[14,19,20,24,30-32] shows differences in the characteristics of the observed infrared bands. For example, the $^{12}CO_2$

v_3 stretch in polar ices is shifted further from the gas phase value (7 - 15 cm^{-1} depending on ice composition[25]) than in apolar ices (2 - 8 cm^{-1} depending on ice composition[24]). The infrared bands of CO_2 have also been found to be dependent on the temperature of the CO_2-bearing ice[19]. Therefore, the infrared spectrum of CO_2 can be used to determine the nature of interstellar icy mantles.

A small range of temperature programmed desorption (TPD) experiments have also been conducted on pure CO_2 and CO_2-bearing polar ices on a range of surfaces[33,35,39,53,54]. From TPD spectra of pure CO_2 desorbing from a Au surface at 8 K[53] and a highly oriented pyrolytic graphite (HOPG) surface at 20 K[54], multilayers of CO_2 were shown to desorb with a natural sublimation temperature of approximately 80 K.

TPD spectra of CO_2-bearing H_2O ices show characteristics indicating trapping of CO_2 within the H_2O film. Previous studies of the TPD spectra of H_2O on a HOPG surface at 92 K have shown that H_2O multilayers desorb around 164 K, showing a bump on the low temperature side of the main peak at 152 K[55]. These two TPD peaks correspond to desorption of crystalline ice (CI) and the amorphous to crystalline phase transition of amorphous solid water (ASW) respectively. Desorption of CO_2 from CO_2-bearing layered and mixed H_2O ices is observed well above the natural sublimation temperature of CO_2, coincident with the ASW - CI transition and desorption of CI[33,39,53]. Desorption of CO_2 at its natural sublimation temperature from CO_2-bearing layered and mixed H_2O ices was also observed from a Au surface at 8 K[53]. Desorption of CO_2 at its natural sublimation temperature from CO_2-bearing H_2O ices was not observed from a Si surface at 80 K[33] and MgO single crystal at 90 K[39]. However, this is not a consequence of the underlying substrate. Instead it is due to experimental limitations on the substrate temperature, which has a temperature close to the natural sublimation temperature. The observation of CO_2 desorption at its natural sublimation temperature, as well as the trapping of CO_2 in CO_2-bearing mixed and layered H_2O ices, indicates the ability for diffusion of CO_2 within the porous structure of ASW.

The trapping and diffusion of CO_2 within other polar ice matrices has also been investigated. TPD spectra of CO_2-bearing CH_3OH ices desorbing from a Si surface at 85 K[35] show the trapping of CO_2 within the CH_3OH film. Previous studies of the TPD spectra of CH_3OH on a HOPG surface at 97 K have shown that CH_3OH multilayers desorb around 150 K[56]. Also of interest is the observation that the amorphous to crystalline phase transition of CH_3OH ice occurs around 120 K[57], prior to the onset of desorption of CH_3OH. Therefore the amorphous to crystalline phase transition of CH_3OH is not observed in the TPD spectra of pure CH_3OH ices, in contrast to the TPD spectra of ASW ice[55]. Desorption of CO_2 in CO_2-bearing CH_3OH ices is observed well above the natural sublimation temperature of CO_2, coincident with the amorphous to crystalline phase transition of CH_3OH and co-desorption with crystalline CH_3OH.

However, desorption of CO_2 at its natural sublimation temperature from CO_2-bearing CH_3OH ices was not observed from a Si surface at 85 K[35]. Again, this may be due to experimental limitations on the substrate temperature, where the substrate temperature is already above the natural sublimation temperature of CO_2.

As well as providing insight into the qualitative desorption and trapping features of CO_2-bearing ices, TPD can also provide quantitative information on the kinetics of desorption. Although derivation of desorption energies can be achieved via a number of other experimental techniques, including infrared studies[19,33,35], these require a number of assumptions about the kinetic parameters for desorption. Table 4.1 shows the calculated kinetic parameters from a range of previous studies of CO_2 bearing ices. Deriving desorption energies from infrared studies of multilayer CO_2 requires the assumption that the desorption order is 0 and the pre-exponential factor is 3×10^{12} s^{-1}, the average lattice vibration frequency of solid CO_2. Assuming a desorption order of 0, which is common for multilayer populations of an ideal adsorbate[58], with a pre-exponential factor of 3×10^{13} s^{-1}, the units and value of which are common for desorption of monolayer populations of an ideal adsorbate[58], is not a valid assumption. Multilayer populations of ices often desorb with a fractional desorption order and a consequently altered pre-exponential factor[55,56,59,60], and therefore assumptions based upon an ideal adsorbate are not always valid.

Table 4.1. Kinetic data determined from previous studies of CO_2 desorption for a range of CO_2-bearing ices. #determined from TPD, *determined from infrared spectra, †determined from time of flight mass spectra.

CO_2 Ice Composition	Desorption Order, n	Desorption Energy / kJ mol^{-1}	Pre-exponential factor / s^{-1}
#CO_2 monolayers on HOPG[54]	0	24 ± 2	6×10^{14}
#CO_2 multilayers on HOPG[54]	0	23 ± 2	6×10^{14}
*CO_2 on CsI[19]	0	22	3×10^{12}
*CO_2 on H_2O[19]	0	24	3×10^{12}
*CO_2 on ASW[33]	0	21 ± 2	3×10^{12}
*CO_2 on CI[33]	0	20 ± 2	3×10^{12}
*CO_2 on amorphous CH_3OH[35]	0	20 ± 2	3×10^{12}
*CO_2 on crystalline CH_3OH[35]	0	20 ± 2	3×10^{12}
†CO_2 on CI[50]	1	21 ± 2	1×10^{13}
†CO_2 on H_2O[61]	1	25	1×10^{13}

Desorption energies derived from time of flight mass spectrometry[50,61] are also noted in table 4.1. These studies have also made assumptions about the value of the desorption order and pre-exponential factor used. However, assuming a desorption order of 1 with a pre-exponential factor of 1×10^{13} s^{-1}, both common for monolayer populations of an ideal adsorbate[58], is a reasonable assumption although it does not describe the desorption of bulk CO_2 ice. Therefore high quality TPD spectra of a wide range of CO_2-bearing ices are needed, not only to gain a better understanding of the trapping and diffusion behaviour of CO_2 within CO_2-

bearing ices, but also to derive realistic kinetic parameters for the desorption of CO_2, which can be used in astronomical models of star forming regions[62-64].

Given the obvious importance of CO_2 containing ices in the ISM, a complete investigation into the adsorption and desorption properties of a range of CO_2-bearing ices adsorbed on a model carbonaceous grain surface has been undertaken. Whilst there have been several investigations into the adsorption and desorption of CO_2 containing ices on a wide range of surfaces, this is the first complete study of a range of astrophysically relevant ices adsorbed on, and desorbing from HOPG. Previous work[58] shows the importance of investigating adsorption and desorption on a wide range of astrophysically relevant surfaces. Reflection absorption infrared spectroscopy (RAIRS) and TPD have been used to study pure CO_2 ices, binary layered CO_2 and H_2O ices, CO_2:H_2O mixed ices and CO_2 adsorbed on CH_3OH:H_2O mixed ices. Understanding the adsorption and desorption of pure ices is of great importance in understanding and characterising the adsorption and desorption of CO_2 from more complex systems, such as CO_2 on a H_2O surface. Binary layered ices of CO_2 on H_2O and reverse layered ices of H_2O on CO_2 have also been studied, allowing the diffusion and trapping characteristics of CO_2 in a H_2O matrix to be studied. Binary layered ices of CO_2 on pure H_2O and CH_3OH:H_2O mixtures are also compared to investigate the effect of the nature of the polar ice on the behaviour of CO_2. Finally mixtures of CO_2 and H_2O are also studied. Investigations of ice mixtures provide the most realistic analogy to interstellar ices.

4.2. Experimental

The experimental apparatus and techniques used for all experiments have been described in detail in chapter 2. Research grade CO_2 (BOC Gases, 99.9%), CH_3OH (Fisher Scientific, 99.9%) and H_2O (distilled, deionised) were used in these experiments and the CH_3OH and H_2O were purified via repeated freeze-pump-thaw cycles. Ices were grown *in situ* by backfilling the chamber through a high precision leak valve. All exposures are measured in Langmuir, where 1 L = 10^{-6} mbar s, and were not corrected for ion gauge sensitivity. RAIR spectra were taken at a resolution of 2 cm^{-1} and are the result of the co-addition of 128 scans. For the warm RAIRS experiments, the sample temperature was raised and held at a pre-determined temperature for the duration of a spectrum, lasting approximately 5 minutes. TPD spectra of masses 18, 32 and 44, the major mass fragments of H_2O, CH_3OH and CO_2 respectively, were recorded simultaneously. All TPD spectra were recorded at a heating rate of 0.50 ± 0.01 K s^{-1}.

4.3. Results and Discussion

RAIR and TPD spectra were recorded for CO_2-bearing ices adsorbed on a HOPG surface below 33 K. CO_2, H_2O and CH_3OH were dosed onto the HOPG sample in five dosing regimes: pure CO_2 adsorbed on bare HOPG, binary layered ices of CO_2 adsorbed on pre-adsorbed H_2O layers, reverse binary layered ices of H_2O adsorbed on pre-adsorbed CO_2 layers, binary layered ices of CO_2 adsorbed on pre-adsorbed CH_3OH:H_2O mixtures, and well defined mixtures of CO_2 and H_2O co-deposited on bare HOPG (figure 4.1).

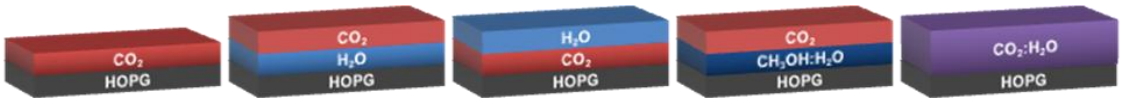

Figure 4.1. The five dosing regimes used to investigate the adsorption and desorption of CO_2-bearing ices adsorbed on HOPG below 33 K. From left to right, pure CO_2, binary layers of CO_2 on H_2O, reverse binary layers of H_2O on CO_2, binary layers of CO_2 on CH_3OH:H_2O mixtures and CO_2:H_2O mixtures.

4.3.1. Pure CO_2 Ice

RAIR and TPD spectra were recorded for a range of exposures of CO_2 adsorbed on a bare HOPG sample at 28 and 33 K respectively. The study of pure CO_2 ices is of importance to determine whether any adsorbate-substrate interactions are involved in the growth and desorption of the ices. Kinetic data about the desorption of pure ices from a bare surface can also be derived from TPD spectra[55,56,59,60]. This data can then be incorporated into astrophysical models simulating the desorption of molecular ices on astronomical timescales[62-64].

4.3.1.1. TPD Data

Figures 4.2 and 4.3 show the TPD spectra recorded for the desorption of a range of exposures of pure CO_2 adsorbed on HOPG at 33 K. At the lowest CO_2 exposure of 1 L, a peak is observed in the TPD spectrum at a temperature of 83 K with a low temperature shoulder at 77 K (figure 4.2). Increasing the CO_2 exposure to 2 L gives a TPD peak with a temperature of 84 K and a low temperature shoulder at 80 K. Further CO_2 exposure, up to 7 L, shows a gradual increase in the size and temperature of the low temperature shoulder, whereas the main peak shows an increase in size but only a very slight increase in temperature. At higher CO_2 exposures, between 5 and 10 L, the low temperature shoulder merges into the main peak prior to dominating the spectrum, showing common leading edges on the TPD spectra in the

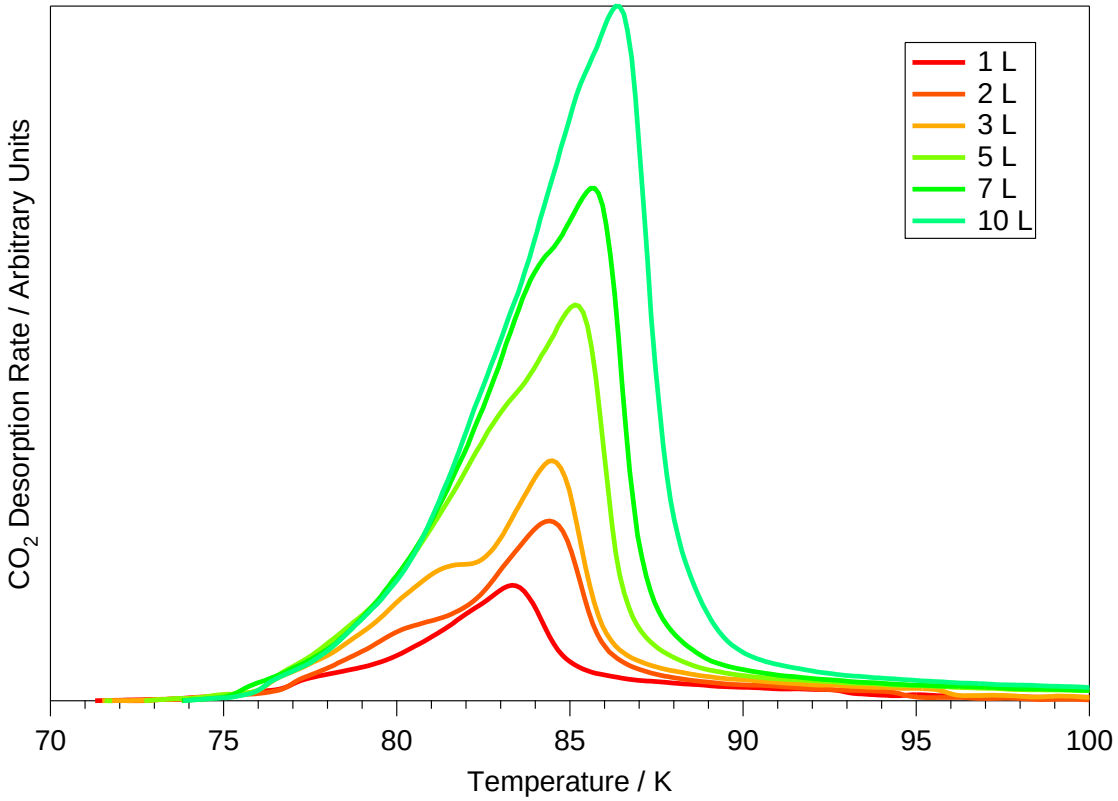

Figure 4.2. TPD spectra of low exposures of CO_2, up to 10 L, adsorbed on a bare HOPG surface at 33 K.

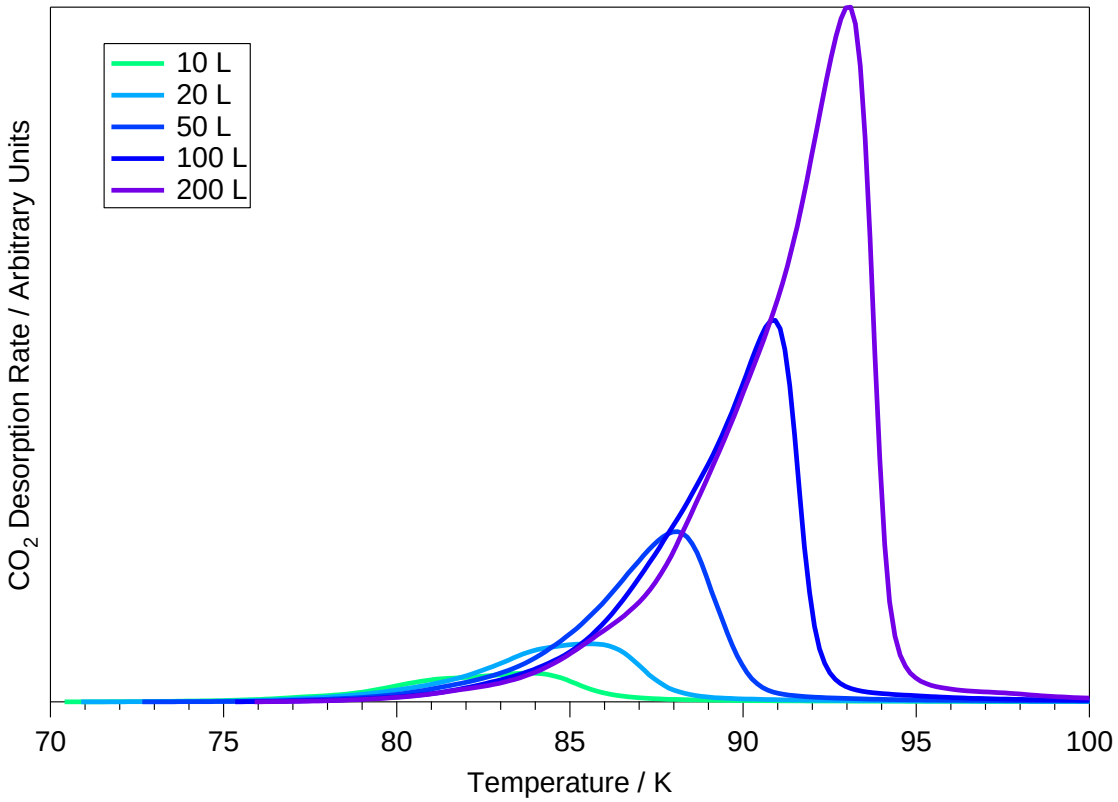

Figure 4.3. TPD spectra of high exposures of CO_2, above 10 L, adsorbed on a bare HOPG surface at 33 K.

temperature range of 75 to 83 K. At CO_2 exposures of 10 L and above (figure 4.3) the leading edges of the TPD spectra no longer overlap. The main TPD peak that grows to dominate the spectrum for CO_2 exposures greater than 5 L increases in temperature with increasing CO_2 dose.

The main TPD peak observed following a 1 L exposure of CO_2 can be assigned to monolayer desorption of CO_2. It is the first peak observed and therefore must be caused by desorption of CO_2 directly associated with the HOPG surface. The monolayer peak appears to remain the dominant peak between CO_2 exposures of 5 and 7 L. It shows characteristics which indicate 1^{st} order desorption, characterised by a slightly non-symmetric peak shape and constant peak temperature, common for surface bound or monolayer desorbing species[58]. The peak which first appears as a low temperature shoulder on the monolayer peak, prior to merging with and dominating this peak upon increasing CO_2 exposure, can be assigned to multilayer desorption of CO_2. The multilayer desorption peak does not saturate with increasing CO_2 exposure and shows characteristics indicating 0^{th} order desorption. 0^{th} order desorption is characterised by a highly non-symmetric peak shape, increasing peak temperature with increasing adsorbate coverage and coincident leading edges, and is common for solid or multilayer desorbing species[58]. Although the leading edges on the multilayer TPD spectra are not perfectly shared, the TPD spectra do show a non-symmetric peak shape and increasing peak temperature with increasing CO_2 coverage. CO_2 multilayers are also observed in the TPD spectra at higher CO_2 exposures than those for CO_2 monolayer formation, as expected for multilayer formation. Comparing to previous TPD studies of multilayers of physisorbed CO_2 on a Au and HOPG surface[53,54], good agreement is observed.

A linear correlation is observed when comparing the integrated area of each TPD spectrum as a function of the exposure of CO_2, as shown in figure 4.4, showing constant uptake of CO_2 on the HOPG surface. This indicates a constant sticking probability for CO_2 adsorption on HOPG and suggests that multilayers of CO_2 are being formed. The linear uptake curve does not saturate at CO_2 exposures of up to 200 L, indicating that CO_2 is physisorbed on the HOPG surface, which is also indicated by the desorption temperature of CO_2 multilayers observed (≈80 - 90 K).

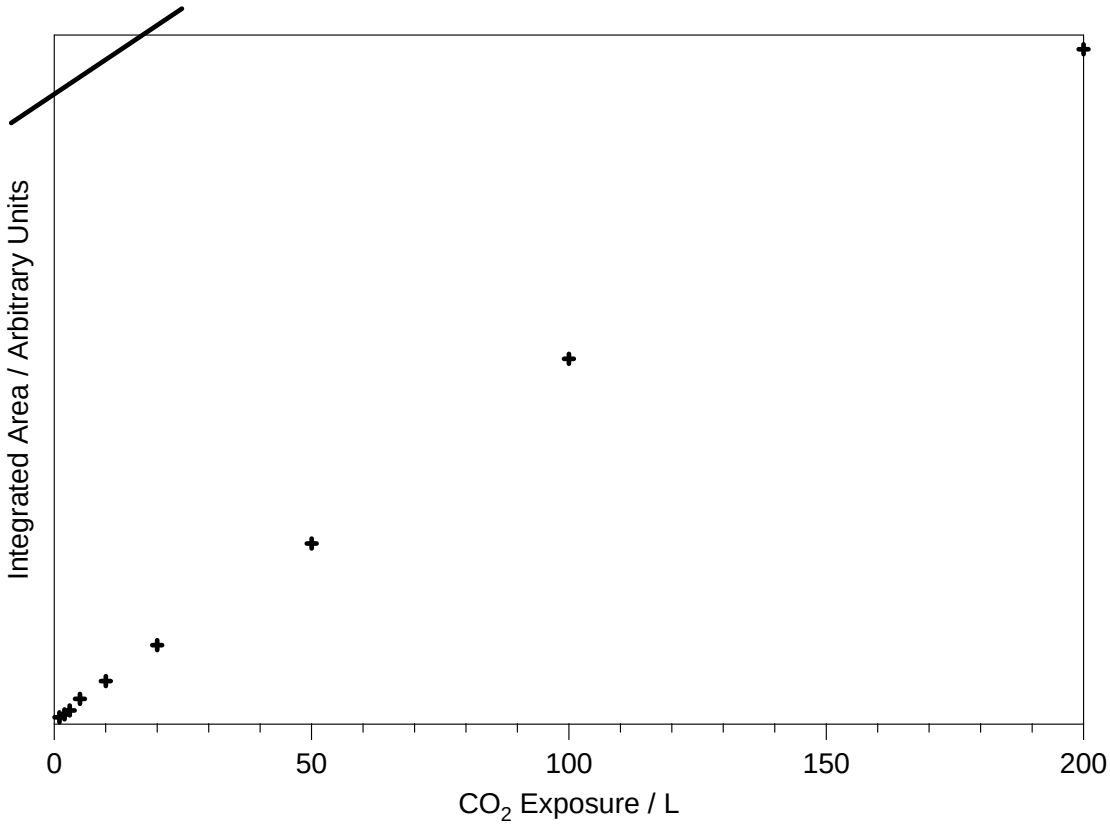

Figure 4.4. Integrated area of the TPD spectra shown in figures 4.2 and 4.3 as a function of exposure of CO_2. The line is supplied as a guide to the eye, and was produced using a linear fit to the data.

4.3.1.2. RAIRS Data

To confirm the assignments of the TPD spectra and compare with previous infrared studies, RAIR spectra were collected for a variety of exposures of CO_2 adsorbed on HOPG at 28 K, shown in figure 4.5. The trends observed for infrared bands in the $^{12}CO_2$ ν_3 vibrational region, 2400 - 2330 cm^{-1}, are discussed as this is the strongest CO_2 vibrational band observed. In addition, this band is not obscured by the $\nu_{(OH)}$ vibrational band of H_2O, discussed later. After a CO_2 exposure of 5 L a single band is visible at 2373 cm^{-1}. This band shifts to 2382 cm^{-1} with increasing CO_2 exposure up to 100 L. Two further bands appear in the RAIR spectra after a total CO_2 exposure of 30 L, a broad band centred at 2373 cm^{-1} and a low intensity band at 2341 cm^{-1}. Increasing the CO_2 exposure further shows an increase in the intensities of all bands with no further frequency shift, and the bands do not saturate.

A linear plot is observed when comparing the integrated area of each infrared band with respect to the exposure of CO_2. The integrated area does not saturate with increasing CO_2 exposure, indicating a constant sticking probability during adsorption of CO_2 and suggesting that CO_2 is physisorbed on the surface, assuming constant molecular orientation with increasing CO_2 exposure. This linear relationship, also observed for the TPD data, suggests that

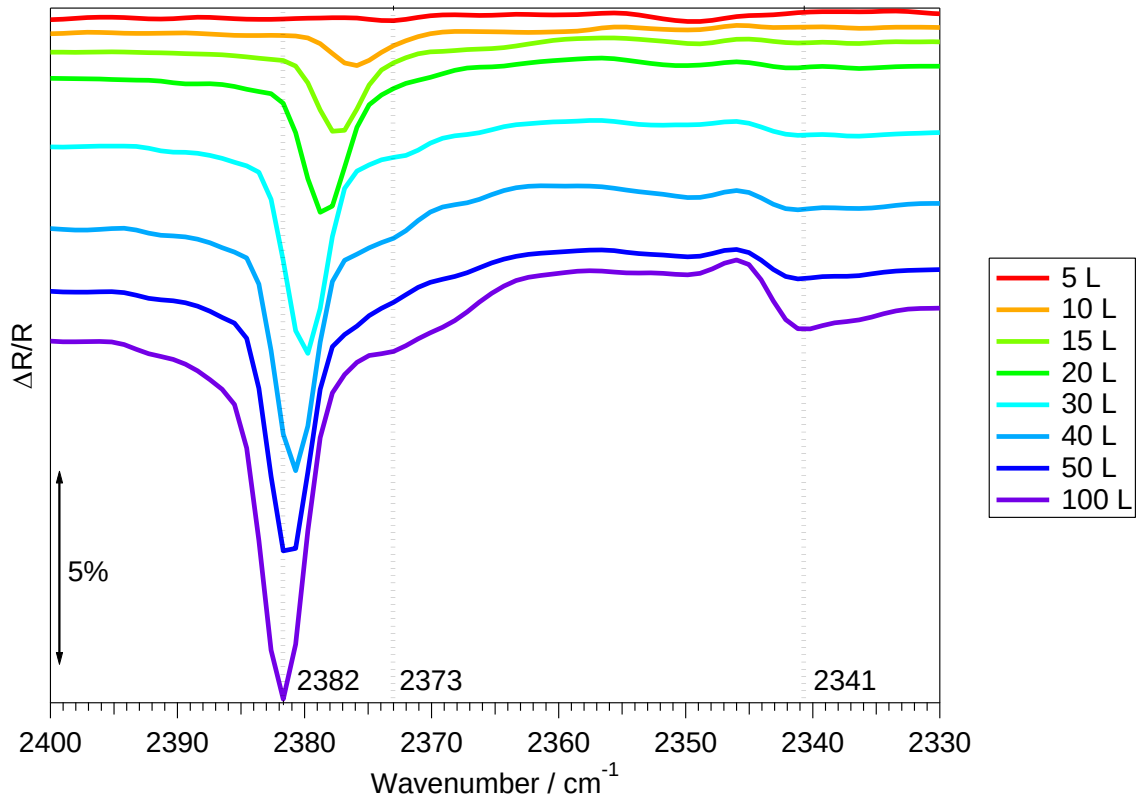

Figure 4.5. RAIR spectra of a range of exposures of CO_2 adsorbed on a bare HOPG surface at 28 K.

multilayers of CO_2 are forming, physisorbed on the HOPG surface at 28 K. This is also implied when comparing the infrared frequencies with those observed for the same vibrations in gas phase spectra. The $^{12}CO_2$ ν_3 vibration is observed at 2349 cm^{-1} in gas phase spectra, close to the observed band at 2341 cm^{-1} in this work. This suggests only a weak interaction upon adsorption, and that CO_2 is physisorbed on the HOPG surface.

Warming the HOPG surface incrementally can provide information about the temperature dependent behaviour of the CO_2 ice adsorbed on HOPG at 28 K. Figure 4.6 shows a 100 L exposure of CO_2 adsorbed on a HOPG surface at 28 K warmed to a range of temperatures. Warming the ice to between 28 and 55 K shows no change in the observed infrared features at 2382 and 2341 cm^{-1}, whereas the feature at 2373 cm^{-1} shifts to 2367 cm^{-1}. Upon warming the HOPG surface to 62 K, the band at 2382 cm^{-1} broadens slightly and shifts down to 2381 cm^{-1}. Further warming to 66 K produces a RAIR spectrum with reduced peak intensities and a further shift of the band at 2382 cm^{-1} to 2378 cm^{-1}. Warming to 73 K leads to desorption of the CO_2 ice.

From comparison with other infrared spectra for amorphous and crystalline CO_2 adsorbed on a range of surfaces[14,19,20,23-52], experimental and theoretical studies of microcrystalline[65-69] CO_2 as well as gas phase[22] CO_2 investigations, assignments of the observed infrared bands can be made. Gas phase studies of the infrared bands between 2000 – 3000 cm^{-1} show two peaks

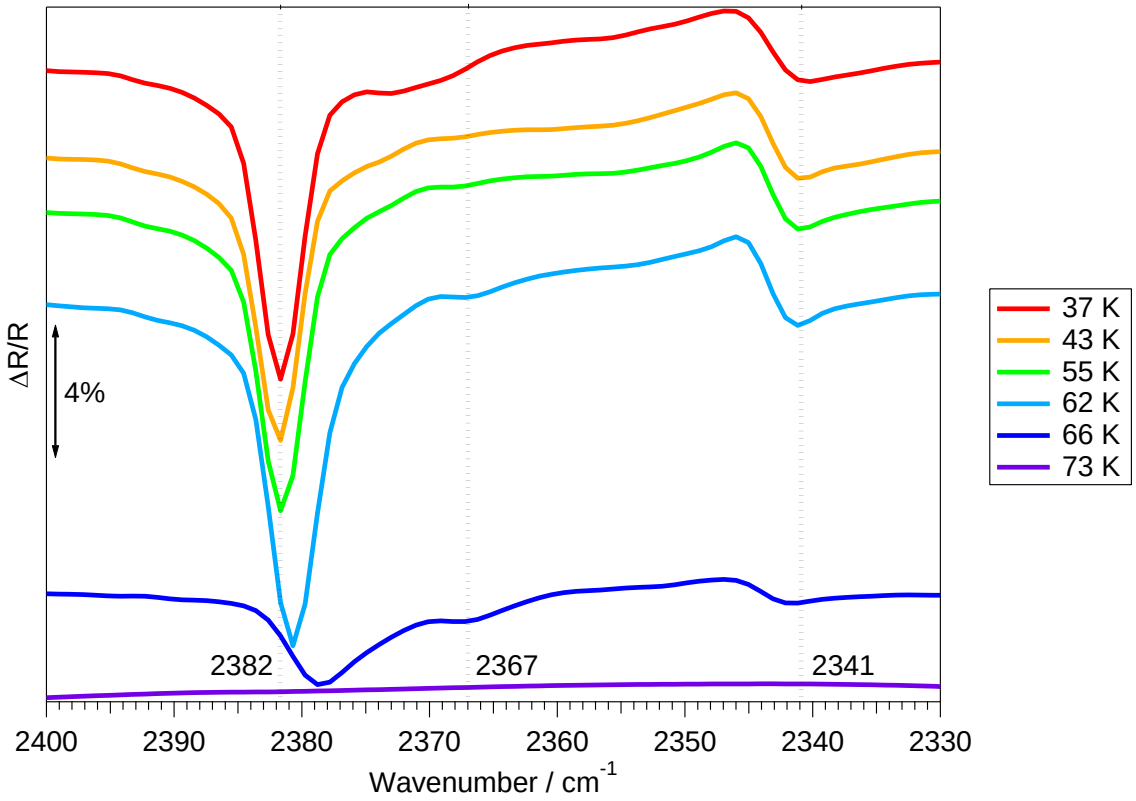

Figure 4.6. RAIR spectra of a 100 L exposure of CO_2 adsorbed on a bare HOPG surface at 28 K warmed to a range of temperatures.

at 2283 and 2349 cm^{-1} relating to the ν_3 stretching mode of $^{13}CO_2$ and $^{12}CO_2$ respectively. Therefore the band at 2341 cm^{-1} can be assigned to the ν_3 stretching mode of $^{12}CO_2$ physisorbed on the HOPG surface at 28 K. This is also in agreement with previous work on the infrared spectra of amorphous and bulk crystalline CO_2[14,19,20,23-52,65-69].

As discussed in chapter 3, the band observed at 2382 cm^{-1} is not observed in infrared studies of amorphous CO_2 ices at normal incidence to the surface, where a single band in the $^{12}CO_2$ ν_3 region around 2341 cm^{-1} is observed. However, a band near 2382 cm^{-1} is observed in infrared investigations of crystalline CO_2 ices[28,65-69] and amorphous CO_2 ices at grazing incidence[24,31,32,37]. Infrared studies of crystalline CO_2 ices generally show a broad, multi-peak, feature between 2340 - 2380 cm^{-1}.[28,67-69] In particular, the study of Ovchinnikov and Wight[28] reported the transverse optical (TO) and orthogonal, or longitudinal optical (LO), modes of the $^{12}CO_2$ ν_3 band, split as a consequence of the crystalline nature of the CO_2 ice, to be at 2344 and 2381 cm^{-1} respectively. This does not explain the observation of the band at 2382 cm^{-1} in amorphous ices. Instead, as discussed by Baratta and Paulmbo[31,32,37] and confirmed in chapter 3, the observed LO - TO splitting is caused by coupling of polarised phonon vibrations within the CO_2 ice with the electric field of the incident radiation at grazing incidence, known as the Berreman effect[70]. Therefore the bands at 2382 and 2341 cm^{-1} are assigned to the LO and TO phonon modes of the $^{12}CO_2$ ν_3 vibration respectively.

The LO phonon mode of the $^{12}CO_2$ ν_3 vibration is observed to increase in frequency upon increasing CO_2 coverage on the HOPG surface, and it decreases in frequency with increasing surface temperature in the temperature range for CO_2 sublimation. Therefore, the position of the CO_2 vibrational mode is directly related to the coverage of CO_2, or thickness of the CO_2 ice on the surface. As discussed in chapter 3, this behaviour is not a direct consequence of the optical nature of CO_2. As the CO_2 ice is physisorbed on the HOPG surface, this effect may be caused by physical interactions between CO_2 molecules on the surface. This effect could be the result of the orientation of CO_2 molecules within the ice, which may alter the polarisation of the phonon vibrations and therefore affect the interaction of the phonon modes with the incident infrared light.

The broad band at 2373 cm^{-1}, which appears to shift to 2367 cm^{-1} upon warming, is not observed in the literature. However, as the coverage of CO_2 on the HOPG surface has been shown to affect the position of the LO phonon mode of the $^{12}CO_2$ ν_3 vibration, the band at 2373 cm^{-1} could also be caused by a modification of the polarisation of the phonon vibrations within the ice. The CO_2 ice is expected to be heterogeneous and amorphous, which could cause disruptions to the phonon vibrations within the ice and therefore may affect the interaction of the incident light with the phonon modes. Also, as the ice is heterogeneous, it would be expected that a band caused by this effect would be broad and would be located between the vibrational positions of the LO and TO phonon vibrations, as observed for the band at 2373 cm^{-1}. Therefore this band could be assigned to a weakly polarised LO phonon mode of the $^{12}CO_2$ ν_3 vibration. However, irrespective of the cause and exact assignment of the observed infrared bands in the $^{12}CO_2$ ν_3 vibrational region, clearly the infrared spectrum of physisorbed CO_2 ice, particularly in the $^{12}CO_2$ ν_3 vibrational region, is complex.

Comparing RAIR and TPD spectra of pure CO_2 ice on HOPG, it is seen that multilayer CO_2 forms on the surface below 33 K. Differences in the warming profiles between the experimental techniques used affect the sublimation of the CO_2 ice. The RAIRS warming experiments, with a slower heating rate, show complete CO_2 desorption between 66 and 73 K. The TPD experiments however, with an overall faster heating rate, show the onset of desorption around 75 K, and complete desorption is observed between 85 and 95 K depending on CO_2 coverage. However, irrespective of the subtle differences between the onset and complete desorption of CO_2 ice in the RAIRS and TPD experiments, good agreement is observed for the sublimation temperature of CO_2 in a temperature range indicative of physisorbed ice. It is also not evident from either RAIR or TPD spectra that any phase changes of the CO_2 film occur upon warming the HOPG surface.

4.3.1.3. Quantitative Analysis of TPD Data

To gain a better understanding of the desorption of CO_2 from a HOPG surface and to provide qualitative information for astrochemical models, analysis of the TPD data has been performed. The methodology used here has been described in detail in chapter 2.

Desorption orders. According to equation 2.2 (chapter 2) the desorption order can be determined from the gradient of a plot of ln[I(T)] versus $\ln[\theta_{rel}]$ at a fixed temperature, using a set of TPD spectra with varying initial CO_2 coverage. This method for obtaining the desorption orders assumes that the desorption energy and pre-exponential factor do not vary with coverage or temperature. This has previously been shown to be a valid assumption for H_2O[55], NH_3[59], CH_3OH[56] and C_2H_5OH[60] ices, and since CO_2 is physisorbed on the HOPG surface should also be a valid assumption in this case. Monolayer desorption rates were taken from the TPD spectra for CO_2 exposures between 1 and 10 L (figure 4.2) and are shown in figure 4.7 (top). Figure 4.7 (bottom left) shows an order plot for monolayer desorption at a fixed temperature

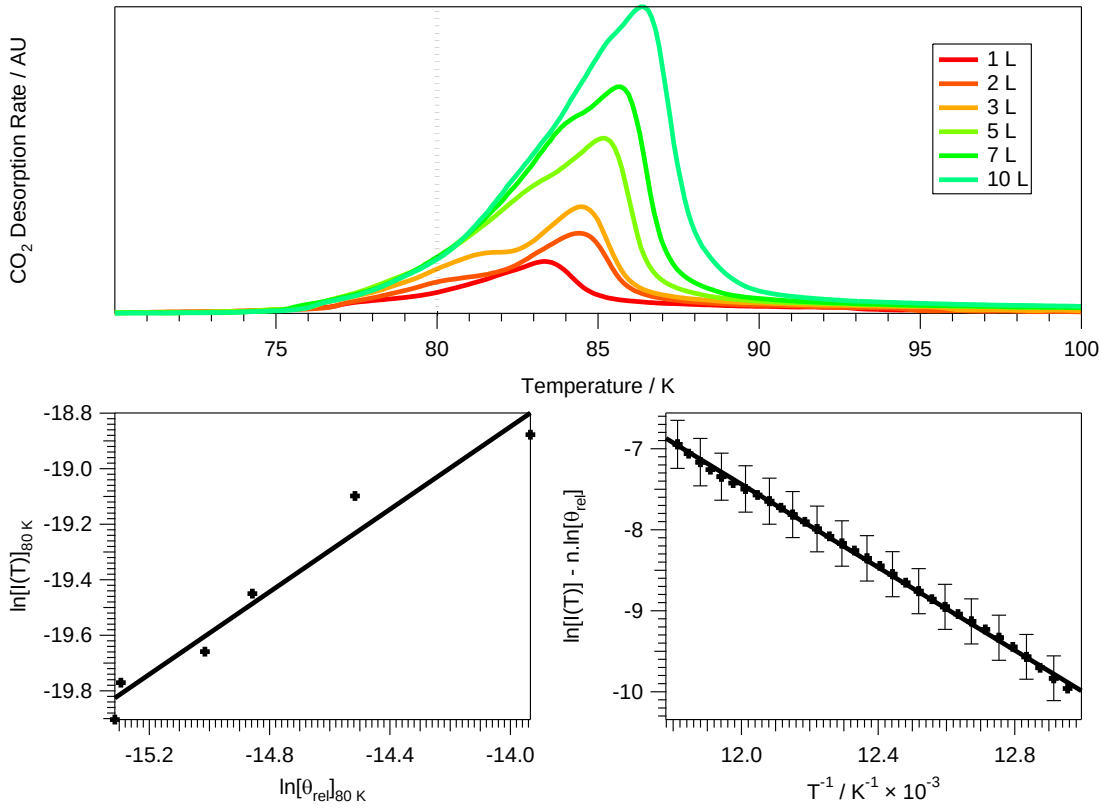

Figure 4.7. (Top) TPD spectra of monolayer CO_2, taken from figure 4.2, showing CO_2 exposures of 1 to 10 L. Also shown as a dotted line is the fixed temperature of 80 K. (Bottom left) Plot of ln[I(T)] against $\ln[\theta_{rel}]$ at a fixed temperature of 80 K producing a gradient for monolayer desorption order. (Bottom right) Plot of ln[I(T)] – n.$\ln[\theta_{rel}]$ against 1/T from the TPD spectrum produced following a 5 L exposure of CO_2, using n as 0.73 ± 0.02. This line has a gradient of $-E_{des}/R$.

of 80 K, with a gradient of 0.74. Using a range of fixed temperatures between 79 and 81 K, shown in table 4.2, the average monolayer desorption order was found to be 0.73 ± 0.02, where the error was taken as twice the standard deviation of the obtained gradients from table 4.2.

Table 4.2. Calculated desorption orders for monolayer CO_2 adsorbed on HOPG at 33 K.

Fixed Temperature / K	Desorption Order, n
79.0	0.73
79.5	0.73
80.0	0.74
80.5	0.73
81.0	0.71

As the leading edges in the TPD spectra for multilayer CO_2 do not overlap at exposures of 10 L and above (figure 4.3), rigorous analysis of these spectra produce small, negative, desorption orders. This is a direct consequence of the behaviour of the leading edges within the set of TPD spectra. For example, at a fixed temperature of 83 K, an inverse correlation between the CO_2 exposure and I(T) is observed for 100, 150 and 200 L exposures. A negative desorption order is unrealistic and would otherwise affect the analysis of the desorption energy and pre-exponential factor. However, as discussed previously, the TPD spectra show other characteristics similar to 0^{th} order desorption, such as asymmetric peak shapes and increasing peak temperature with increasing CO_2 coverage. Also, the calculated desorption orders, although negative, are very close to 0. 0^{th} order desorption is also expected for most multilayer desorbing species[58], therefore the multilayer desorption order will be taken as 0. This is in agreement with the assumptions of previous studies[53,58,71-73].

These values of desorption order are in agreement with the qualitative analysis of the TPD spectra discussed above, and confirm the assignments given. Multilayer desorption is assumed to be 0^{th} order, in agreement with that assumed via qualitative inspection by Ulbricht et al[54]. Monolayer desorption appears to be close to 1^{st} order by observation, but is shown to be fractional order by analysis. This is most likely caused by the overlap of the monolayer and multilayer TPD curves. Due to this overlap, separation of the monolayer and multilayer contributions to CO_2 desorption is difficult. Hence upon analysis, a contribution from the multilayer desorption is observed in the peaks assigned to the monolayer desorbing species. Therefore when analysing CO_2 monolayer desorption, the choice of set temperatures used is important to reduce the multilayer contribution to the monolayer peak.

Desorption Energies. It is also possible to determine the desorption energy of the CO_2 monolayer and multilayers adsorbed on HOPG, to obtain an indication of the binding strength within the monolayer and multilayers, and between the adsorbate and the surface. Using the

desorption orders determined above, the desorption energy of the monolayer and multilayer of CO_2 can be determined via a plot of $\ln[I(T)] - n.\ln[\theta_{rel}]$ against 1/T, taking the gradient as $-E_{des}/R$. The error in $\ln[I(T)] - n\ln[\theta_{rel}]$ was taken to be $\Delta n.\ln[\theta_{rel}]$, thus the error in the desorption order is propagated into the desorption energy gradient. Again it is assumed that the pre-exponential factor and desorption energy do not vary with coverage and temperature. Figure 4.7 (bottom right) shows the gradient for the monolayer desorption energy following a 5 L exposure of CO_2, using a value of n of 0.73 ± 0.02, giving a desorption energy of 21.3 ± 0.8 kJ mol^{-1}. Using the series of TPD traces between 1 and 5 L exposure of CO_2, from figure 4.2, monolayer desorption energies were obtained and are shown in table 4.3. The average monolayer desorption energy was found to be 20.2 ± 2.2 kJ mol^{-1}. The error in the average monolayer desorption energy was calculated via propagation of the errors calculated from the desorption energy gradients from each TPD spectrum as shown in table 4.3.

Table 4.3. Calculated desorption energies for monolayer CO_2 adsorbed on HOPG at 33 K.

CO_2 exposure / L	Desorption Energy, E_{des} / kJ mol^{-1}
1	20.8 ± 1.5
2	19.5 ± 1.1
3	19.3 ± 0.9
5	21.3 ± 0.8

The desorption energy for multilayer CO_2 was obtained using the series of TPD traces between 20 and 200 L exposure of CO_2, from figure 4.3. Desorption energies were obtained for the set of TPD spectra, and are shown in table 4.4. The average multilayer desorption energy was found to be 24.8 ± 1.6 kJ mol^{-1}. As the multilayer desorption order was assumed to be 0, no error from the desorption order could be used to calculate the error in the desorption energy. Therefore the error in the average multilayer desorption energy was taken as twice the standard deviation of the obtained energies from table 4.4.

Table 4.4. Calculated desorption energies for multilayer CO_2 adsorbed on HOPG at 33 K.

CO_2 exposure / L	Desorption Energy, E_{des} / kJ mol^{-1}
20	25.7
50	24.6
100	25.8
150	24.0
200	24.2

Desorption energies have been previously determined for 1 ML (monolayer) and 4 ML coverages of CO_2 on a HOPG surface at 20 K[54], and are quoted as 24 ± 2 and 23 ± 2 kJ mol^{-1} respectively, both of which are within the range of values calculated here. Multilayer desorption energies have also been calculated from infrared spectra of CO_2 ices on CsI at 10 K[19], quoted as 22 kJ mol^{-1}, again close to the energy found here. The monolayer and

multilayer desorption energies calculated here are also comparable with the desorption energies of other physisorbed species[55,56,58-60]. They are also similar to each other, which is reasonable as the monolayer and multilayer contributions to the TPD spectra overlap and merge as the multilayer peak grows and dominates the TPD spectra.

Pre-exponential factors. The pre-exponential factor for desorption can also be determined from the TPD spectra. To determine the pre-exponential factor for desorption, the absolute coverage of CO_2 adsorbed on HOPG must be determined. This can be achieved by calculating the rate of impingement of CO_2 molecules on the HOPG surface. Using the methodology described in chapter 2, the rate of impinging CO_2 molecules on the HOPG surface, as a function of CO_2 exposure, is 4.59×10^{14} molec L^{-1}. However, due to the 10 mm diameter aperture on the quadrupole mass spectrometer (QMS), only 39% of the molecules on the HOPG surface will be detected in a TPD experiment. Therefore the number of molecules which will pass through the QMS aperture as a function of CO_2 exposure will be 1.80×10^{14} molec L^{-1}. This value can then be used to convert the relative coverage, previously taken as the area under each TPD spectrum, into an absolute coverage by scaling using the relationship between the integrated TPD peak area and the actual CO_2 exposure. From figure 4.4, the area under each TPD spectrum, as a function of CO_2 exposure, produced a linear fit with gradient 7.75×10^{-9} L^{-1}, producing a scaling factor for the coverage calculation of 2.32×10^{22} molec.

To determine the pre-exponential factor, the Polanyi-Wigner equation can be rearranged to give an expression for ν_n, as shown in chapter 2. The error in ν_n was taken as $\nu_n\sqrt{(\Delta n^2 + \Delta E_{des}{}^2)}$. Monolayer and multilayer pre-exponential factors were calculated using the TPD spectra for CO_2 exposures of 1 to 10 L and 20 to 200 L respectively and the desorption orders and energies obtained above. The results are shown in table 4.5. The average monolayer and multilayer pre-exponential factors were found to be $9.32 \times 10^{14 \pm 0.9}$ $(\text{molec m}^{-2})^{0.27}$ s^{-1} and $1.07 \times 10^{30 \pm 1.5}$ molec m^{-2} s^{-1} respectively. Units are given as $(\text{molec m}^{-2})^{1-n}$ s^{-1}.

Table 4.5. Calculated pre-exponential factors for monolayer and multilayer CO_2 adsorbed on HOPG at 33 K.

Monolayer		Multilayer	
CO_2 exposure / L	Pre-Exponential Factor, ν_n / $(\text{molec m}^{-2})^{0.27}$ s^{-1}	CO_2 exposure / L	Pre-Exponential Factor, ν_n / molec m^{-2} s^{-1}
1	$1.07 \times 10^{15 \pm 0.5}$	20	$1.72 \times 10^{30 \pm 1.3}$
2	$9.37 \times 10^{14 \pm 0.5}$	50	$9.20 \times 10^{29 \pm 1.5}$
3	$1.04 \times 10^{15 \pm 0.5}$	100	$9.18 \times 10^{29 \pm 1.5}$
5	$9.80 \times 10^{14 \pm 0.5}$	150	$9.19 \times 10^{29 \pm 1.5}$
7	$8.74 \times 10^{14 \pm 0.5}$	200	$8.82 \times 10^{29 \pm 1.4}$
10	$6.90 \times 10^{14 \pm 0.5}$		

Pre-exponential factors for multilayer populations of a range of physisorbed adsorbates[55,56,58-60,63] have been found to range from 8×10^{25} molec m^{-2} s^{-1} for NH_3[59] to 2×10^{37} molec m^{-2} s^{-1} for C_2H_5OH[60], in agreement with the pre-exponential factor determined here. Variations in the pre-exponential factors may be caused by variations in the size of the adsorbed molecule[54]. Pre-exponential factors for a 1st order desorption process are typically taken as $1 \times 10^{12 - 13}$ s^{-1},[19,74,75] relating to the average vibrational frequency of a molecule on a surface and close to the value determined here. The monolayer pre-exponential factor determined here is also comparable to those cited in previous studies of CO_2 desorption[19,33,35,50,54,61] from a range of surfaces.

Comparing the set of kinetic parameters for CO_2 desorption determined here, summarised in table 4.6, with those cited in the literature[19,33,35,50,54,61], table 4.1, some striking differences are evident. Ulbricht et al[54] assumed a desorption order of 0 from qualitative inspection, common for multilayer desorption, but calculated a 1st order pre-exponential factor of $6 \times 10^{14\pm1}$ s^{-1}. Sandford and Allamandola[19] and Gálvez and Maté[33,35] both assumed a desorption order of 0, common for multilayer desorption and pre-exponential factor of 3×10^{12} s^{-1}, common for monolayer desorption. The determination of accurate kinetic parameters has been shown to be of great importance in modelling molecular clouds and star forming regions in the ISM[58,63], whereby the definition between volatiles on a surface and in the bulk of an ice matrix is needed.

Table 4.6. Calculated kinetic parameters for monolayer and multilayer CO_2 desorbing from a bare HOPG surface at 33 K.

	n	E_{des} / kJ mol^{-1}	ν_n / (molec m^{-2})$^{1-n}$ s^{-1}
Monolayer	0.73 ± 0.02	20.2 ± 2.2	$9.32 \times 10^{14 \pm 0.9}$
Multilayer	0	24.8 ± 1.6	$1.07 \times 10^{30 \pm 1.5}$

4.3.2. CO_2/H_2O Ice Layers

The study of binary layered ices of CO_2 adsorbed on H_2O and reverse layered ices of H_2O adsorbed on CO_2 is important in order to understand the effect of H_2O on the adsorption and desorption of CO_2. There is evidence that H_2O rich ices undergo segregation upon warming[76], and so the study of binary and reverse layered ices, not just mixed ices, is of direct relevance to astrochemistry. It is also necessary to understand the effect of H_2O on CO_2 ices in order to better understand more complex systems, such as CO_2:H_2O mixtures.

RAIR and TPD spectra were obtained for CO_2 adsorbed on a 100 L exposure of pre-adsorbed H_2O and a 100 L exposure of H_2O adsorbed on a range of pre-adsorbed exposures of CO_2 on a HOPG surface below 33 K. Previous studies have shown that ASW is formed on a surface by

vapour deposition on cold substrates below 140 K[39,77]. Comparing the RAIR and TPD spectra of a 100 L exposure of pure H_2O with a previous study of the adsorption and desorption of H_2O films[55] indicates that in this study, a 100 L exposure of H_2O leads to the formation of multilayers of ASW.

4.3.2.1. CO_2/H_2O Binary Ice Layers

TPD. Figures 4.8 and 4.9 show TPD spectra for a range of exposures of CO_2 adsorbed on 100 L of pre-adsorbed H_2O on HOPG at 33 K. At the lowest CO_2 exposure of 2 L, three desorption features are observed in the spectrum (figure 4.8), a broad low temperature peak centred at 90 K as well as two high temperature peaks, neither of which were observed in TPD spectra of pure CO_2, at 158 and 167 K. Increasing the CO_2 exposure to 10 L leads to an increase in the size of the low temperature peak with no discernable shift in peak temperature. The two high temperature peaks do not show any significant change in size or peak temperature upon increasing CO_2 coverage between 2 and 10 L. Increasing the CO_2 exposure to 15 L shows an increase in the size of the low temperature peak at 90 K and the high temperature peak at 158 K, with no associated change in peak temperature. However, no change in size or peak

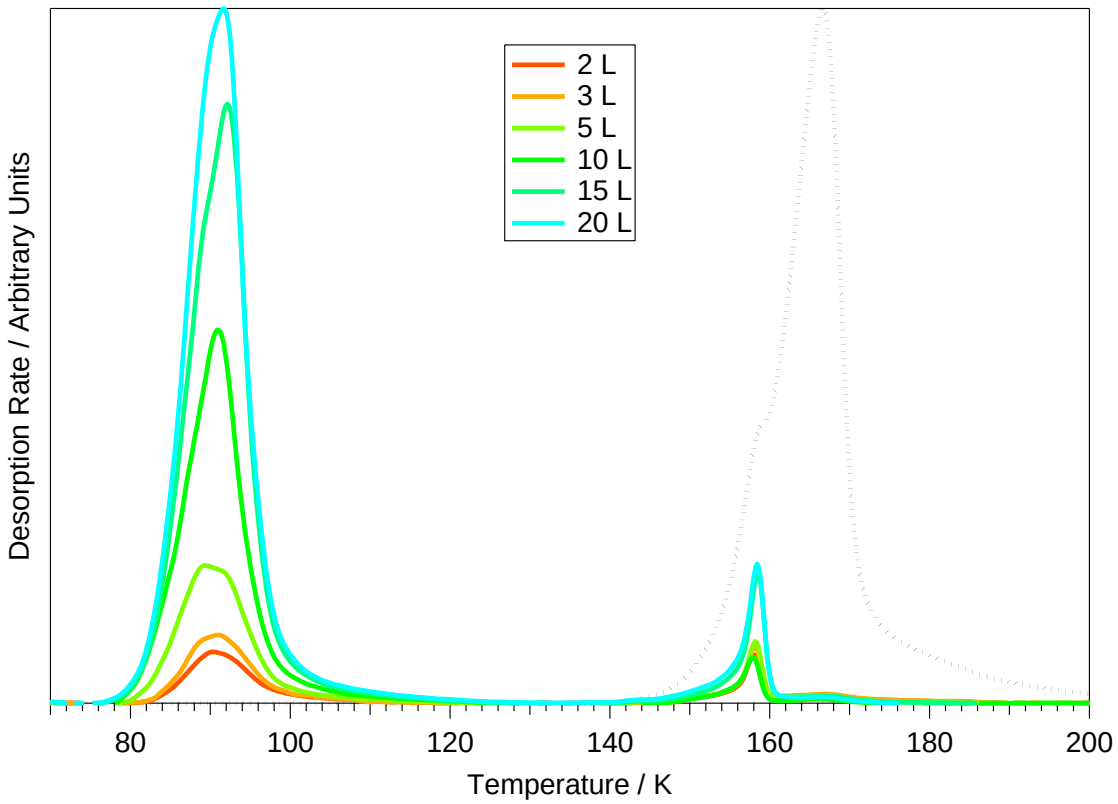

Figure 4.8. TPD spectra of low exposures of CO_2, up to 20 L, adsorbed on 100 L of H_2O on a HOPG surface at 33 K. The H_2O TPD spectrum following a 20 L exposure of CO_2 adsorbed on 100 L of H_2O is shown in black.

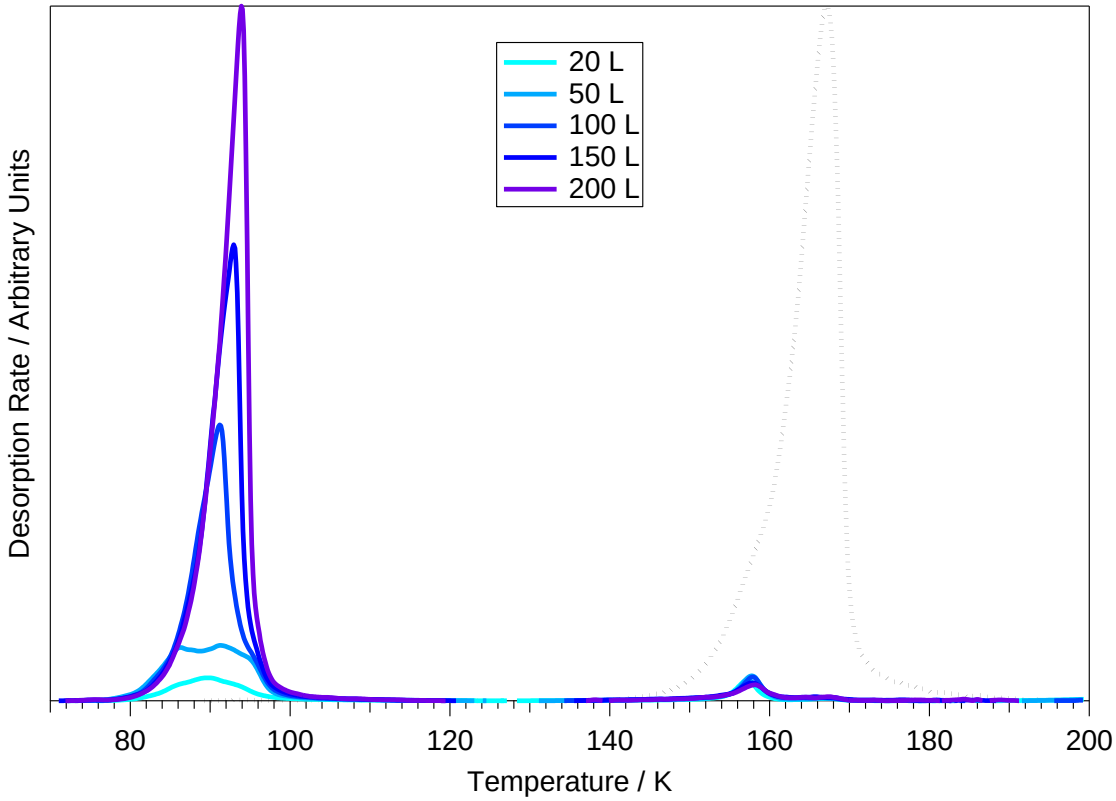

Figure 4.9. TPD spectra of high exposures of CO_2, above 20 L, adsorbed on 100 L of H_2O on a HOPG surface at 33 K. The H_2O TPD spectrum following a 200 L exposure of CO_2 adsorbed on 100 L of H_2O is shown in black.

temperature of the high temperature feature at 167 K is observed between 10 and 15 L exposures of CO_2. No further changes in either of the two high temperature peaks at 158 and 167 K are observed upon increasing CO_2 exposure above 15 L. Further increase of the CO_2 exposure between 20 and 200 L (figure 4.9) shows a gradual increase in temperature of the low temperature peak, from 90 to 94 K. Figures 4.8 and 4.9 also show an example of the H_2O TPD spectrum observed in these experiments. No changes in the H_2O TPD peak are observed with increasing CO_2 exposure. The H_2O TPD feature shows a large peak, with a peak temperature of 167 K and a bump on the leading edge of the spectrum at 158 K. The bump at 158 K is assigned to the irreversible phase change of ASW to CI, caused by a change in the vapour pressure of ASW and CI, and the peak at 167 K is assigned to the desorption of multilayers of physisorbed CI[55].

Integration of the CO_2 TPD peaks from figures 4.8 and 4.9 as a function of CO_2 exposure, shown in figure 4.10, shows a linear relationship between the total CO_2 area and the exposure of CO_2. This constant uptake indicates a constant sticking probability for CO_2 on an ASW surface and suggests that multilayers of CO_2 are being formed. The total integrated area of the CO_2 TPD spectra does not saturate up to a CO_2 exposure of 200 L, indicating that the CO_2 multilayers are physisorbed on the ASW surface at 33 K. Figure 4.10 also shows the

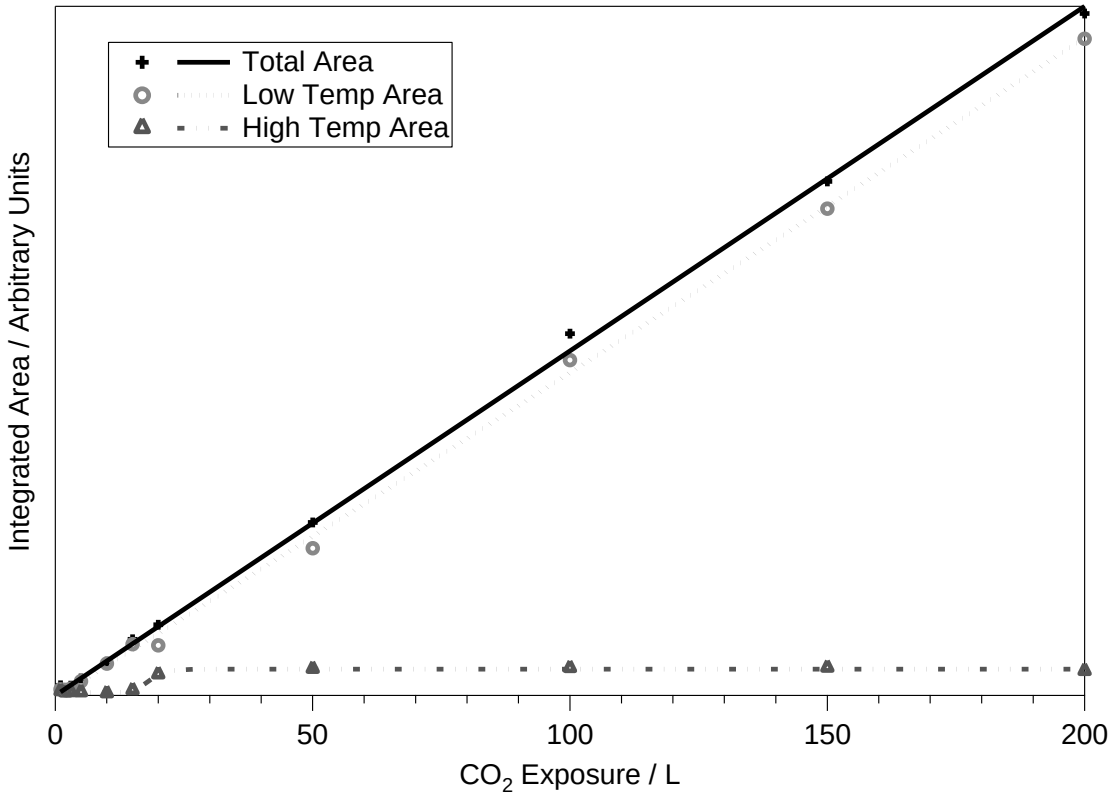

Figure 4.10. Integrated area of the TPD spectra shown in figures 4.8 and 4.9 as a function of exposure of CO_2. The figure shows the areas of the low temperature, 90 to 94 K, peaks, the combined areas of the two high temperature peaks at 158 and 167 K, and the total CO_2 area of all three peaks. Lines are supplied as a guide to the eye.

contributions to the total CO_2 area from the low temperature TPD peak at 90 - 94 K, and the two high temperature peaks at 158 and 167 K. The low temperature peak shows constant growth with increasing CO_2 exposure, whereas the two high temperature peaks saturate following exposures of 20 L and above. The total area of the two high temperature peaks, after saturation, equates to an 8 L exposure of CO_2 when compared to pure CO_2 desorbing from a HOPG surface at 33 K.

Assignment of the CO_2 desorption features from an ASW surface can be made by comparison with the TPD spectra of pure CO_2 on a HOPG surface (figures 4.2 and 4.3), with previous studies of binary ices of CO_2 and H_2O[33,39,53], as well as with studies of binary ices of other volatile molecules with H_2O[39,53,78,79]. As the two high temperature CO_2 TPD peaks occur coincidentally with the features observed in the H_2O TPD spectrum, they can be assigned to CO_2 trapped within the porous ASW surface. This is also confirmed by comparison with the TPD spectra of pure CO_2 desorbing from a bare HOPG surface at 33 K, whereby the lack of the two high temperature peaks in the pure CO_2 TPD spectra indicates that the peaks at 158 and 167 K are caused by the ASW surface. In particular the feature at 158 K can be assigned to volcano desorption of CO_2 with the phase transition of the H_2O film, whereas the feature at 167 K can be assigned to co-desorption of CO_2 with the H_2O film. The ability of ASW to trap

molecules has been shown to depend on its morphology, and evidence for rearrangement of the ASW film at temperatures below the ASW to CI phase transition has been observed[38,39,53,77]. The rearrangement is thought to seal off pores in the ASW surface, trapping volatiles within the ASW. During the ASW to CI phase transition, trapped molecules within the pores of the ASW film are rapidly released, evidenced by a sharp peak in the TPD spectrum referred to as a molecular volcano[38,39,53,77]. Volatiles are also sometimes retained within the H_2O film to desorb with the sublimation of CI[39,53].

Similar assignments can be made for the low temperature TPD peaks for CO_2 desorption from an ASW surface at 33 K as were made for pure CO_2 desorbing from a bare HOPG surface at 33 K. The low temperature TPD feature shows 1st order desorption behaviour below an exposure of 20 L, with a constant peak temperature of 90 K, indicating monolayer growth of CO_2 on the ASW surface. At exposures above 20 L, 0th order behaviour is observed with an increasing peak temperature with increasing CO_2 exposure and common leading edges on the TPD spectra.

Quantitative analysis, as discussed in sections 2 and 4.3, was also conducted on the TPD spectra of CO_2 adsorbed on 100 L of pre-adsorbed H_2O on HOPG at 33 K. CO_2 monolayers were found to desorb from a 100 L film of ASW with an order of 1.09 ± 0.06, desorption energy of 17.5 ± 7.5 kJ mol^{-1} and pre-exponential factor of $2.71 \times 10^{7 \pm 1.8}$ (molec m^{-2})$^{-0.09}$ s^{-1}. Comparing to the kinetic parameters for monolayer desorption of CO_2 from a bare HOPG surface at 33 K, it can be seen that the desorption order, energy and pre-exponential factor are strongly affected by the ASW surface. The desorption order is still found to be close to unity, as expected for monolayer species[58], however it increases from 0.74 to 1.09 when desorbing from an ASW surface as compared to a HOPG surface. The pre-exponential factor is also greatly affected by the ASW surface, decreasing from $9.32 \times 10^{14 \pm 0.9}$ (molec m^{-2})$^{0.26}$ s^{-1} to $2.71 \times 10^{7 \pm 1.8}$ (molec m^{-2})$^{-0.09}$ s^{-1}. This is a direct consequence of the increase in the desorption order for desorption from HOPG as compared to an ASW surface, as the pre-exponential factor is highly influenced by n. Compared to the ordered, homogeneous, nature of a HOPG surface, an ASW surface is heterogeneous with a rough, disordered structure and a wide range of different adsorption sites. This implies that ASW bound CO_2 will desorb from a range of sites, with a range of desorption energies. This is also implied by the broad monolayer desorption peak in the TPD spectrum, as well as the large errors found whilst performing quantitative analysis on the monolayer TPD spectra. This method for determining kinetic parameters can only determine the average kinetic parameters for monolayer desorbing species when adsorbed on a heterogeneous surface.

CO_2 multilayers were found to desorb from a 100 L film of ASW with a desorption order of 0, desorption energy of 25.4 ± 1.4 kJ mol^{-1} and a pre-exponential factor of

$2.06 \times 10^{30 \pm 0.5}$ molec m^{-2} s^{-1}. Comparing to the kinetic parameters found for pure CO_2, clearly multilayer desorption occurs with the same order, energy and pre-exponential factor irrespective of the underlying surface. This is expected as multilayer CO_2 on a HOPG or ASW surface is bound to other CO_2 molecules, and the multilayer kinetic parameters therefore describe CO_2 bound desorption of CO_2.

RAIRS. The characteristics of CO_2 trapping within an ASW film can also be probed by RAIRS which, when compared with TPD spectra, can provide wider evidence for the assignments made. Following a 100 L exposure of H_2O, two infrared bands are observed in the RAIR spectrum, as shown in figure 4.11. A very broad feature is observed around 3400 cm^{-1} and a smaller, but still broad peak is seen at 1670 cm^{-1}. These have been assigned previously to the $\nu_{(OH)}$ stretching mode and HOH scissors mode of ASW respectively[55]. No changes in the H_2O vibrational bands are observed upon exposing the H_2O surface to CO_2.

RAIR spectra of a range of exposures of CO_2 adsorbed on 100 L of pre-adsorbed H_2O on a HOPG surface at 28 K, in the wavenumber range of the $^{12}CO_2$ ν_3 vibration, 2400 to 2330 cm^{-1}, are shown in figure 4.12. At low CO_2 exposures, up to 10 L, a single infrared band is observed in the CO_2 ν_3 region, at 2346 cm^{-1}. A second band is observed in the RAIR spectra upon increasing

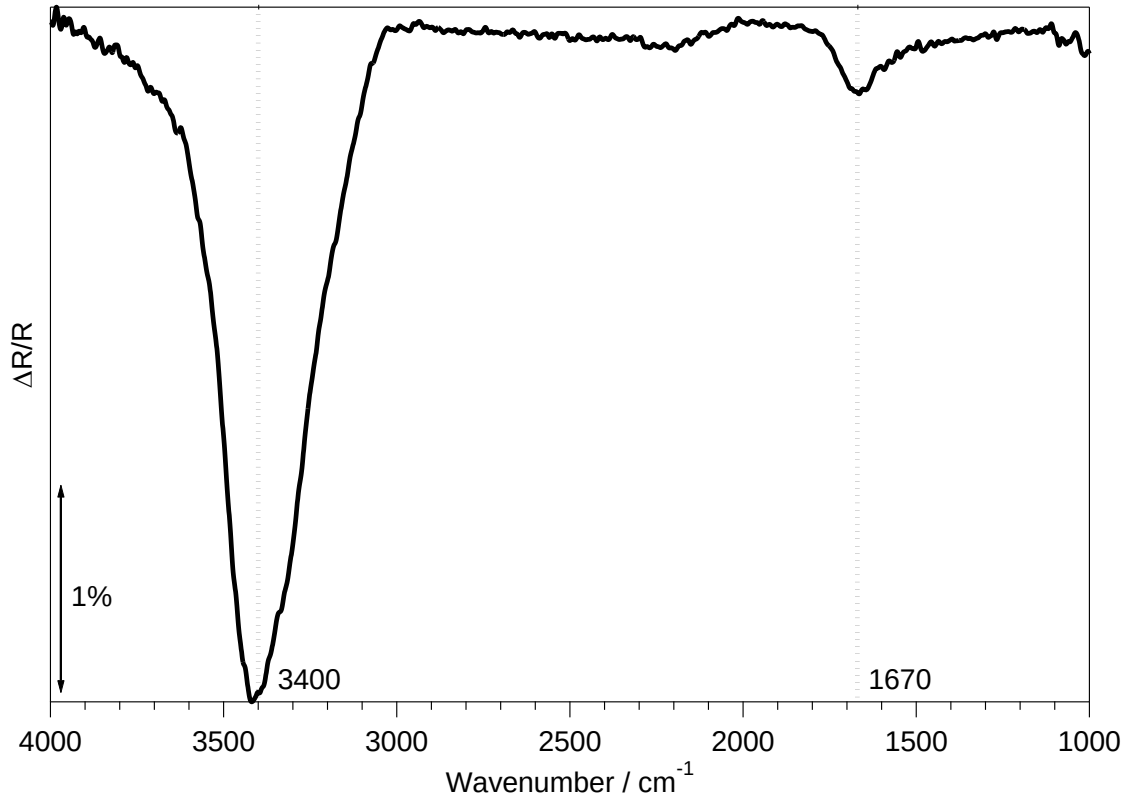

Figure 4.11. RAIR spectra of a 100 L exposure of H_2O adsorbed on a HOPG surface at 28 K.

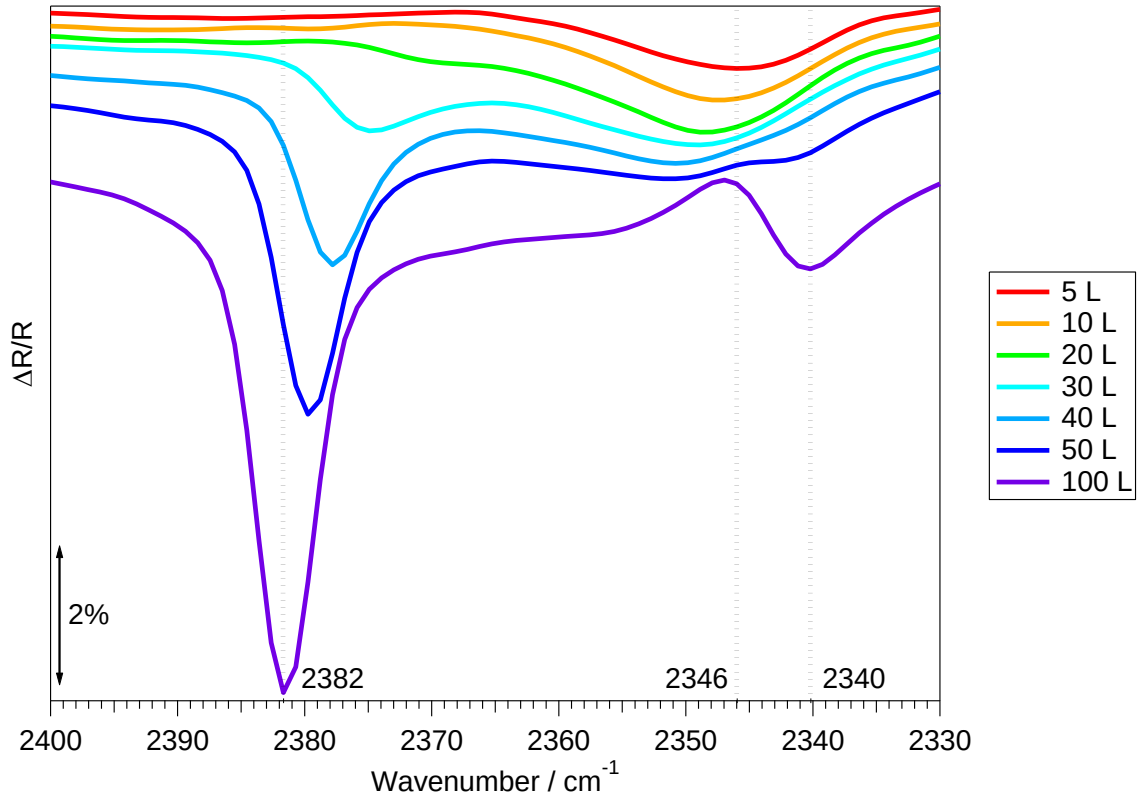

Figure 4.12. RAIR spectra of a range of exposures of CO_2 adsorbed on 100 L of H_2O adsorbed on HOPG at 28 K.

CO_2 exposure to 20 L, where a shift in the band at 2346 cm^{-1} to 2348 cm^{-1} is also observed. Further exposure of CO_2, up to 50 L, shows an increase in size and a shift in wavenumber of the peak at 2370 cm^{-1} to 2380 cm^{-1} as well as a shift in the band at 2348 cm^{-1} to 2351 cm^{-1}. An additional peak at 2340 cm^{-1} is also observed in the RAIR spectra following a 50 L exposure of CO_2. Finally, increasing the CO_2 exposure to 100 L shows a further shift in the bands at 2380 and 2351 cm^{-1} to give a sharp peak at 2382 cm^{-1} and a broad peak at around 2355 cm^{-1} respectively. There is also an increase in the size of the peak at 2340 cm^{-1}, with no associated shift in wavenumber.

Warming the HOPG surface incrementally can provide information about the temperature dependent behaviour of the CO_2 ice adsorbed on ASW as well as about the characteristics of CO_2 trapped in ASW. RAIR spectra, following warming of a 100 L exposure of CO_2 adsorbed on 100 L of H_2O, in the wavelength range of the $^{12}CO_2$ ν_3 and ν_{OH} vibrational regions are shown in figures 4.13 and 4.14 respectively. No spectral shift of any infrared band is observed upon heating the HOPG surface up to 44 K (figure 4.13). At 59 K the band at 2382 cm^{-1} shifts down in wavenumber to 2380 cm^{-1}. Warming further to 65 K shows a significant decrease in the size of the bands at 2380 and 2340 cm^{-1}, as well as an associated shift in wavenumber of the band at 2380 cm^{-1} to 2379 cm^{-1}. Warming to 71 K shows desorption of most of the CO_2, whereby only a

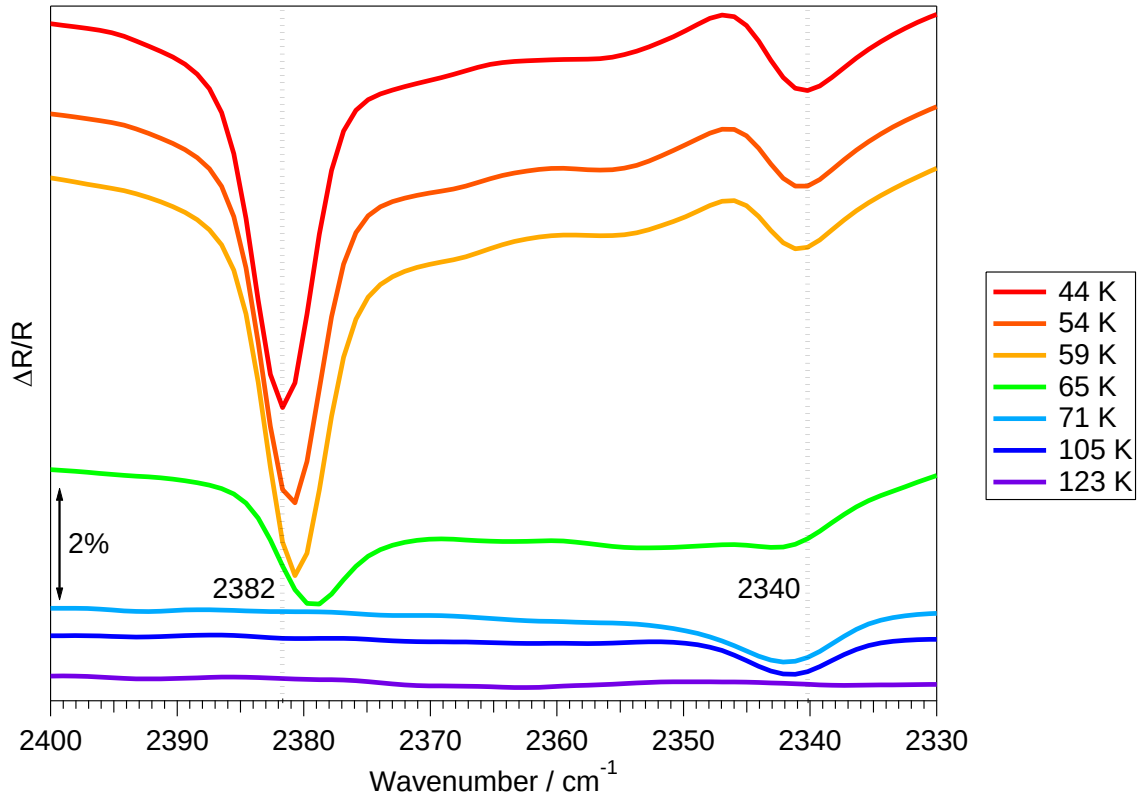

Figure 4.13. RAIR spectra of a 100 L exposure of CO_2 adsorbed on 100 L of H_2O adsorbed on HOPG at 28 K, prior to warming to a range of temperatures.

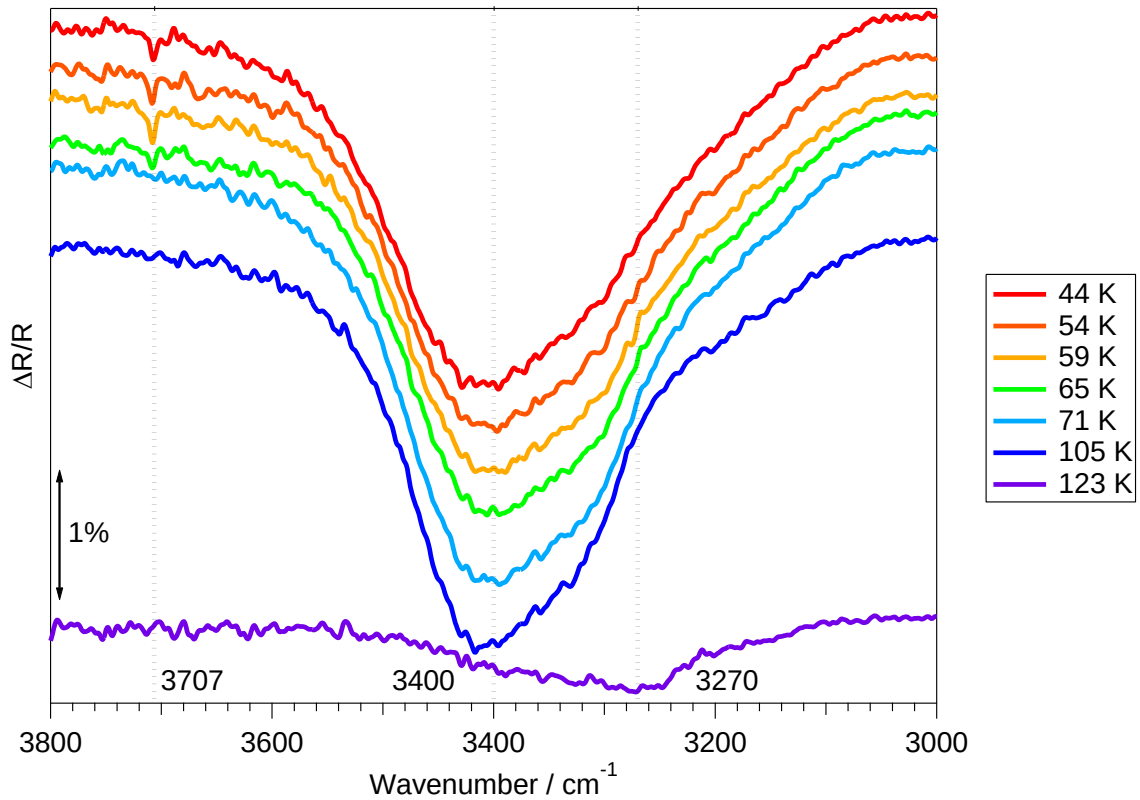

Figure 4.14. RAIR spectra of the ν_{OH} region of a 100 L exposure of CO_2 adsorbed on a 100 L exposure of pre-adsorbed H_2O adsorbed on a HOPG surface at 28 K prior to warming to a range of temperatures.

single CO_2 band is observed at 2342 cm^{-1}. No changes are observed in the band at 2342 cm^{-1} between 71 and 105 K, whereas a slight shift in the $\nu_{(OH)}$ band at 3400 cm^{-1} (figure 4.14) is observed at 105 K. Upon further warming, to 123 K, the $\nu_{(OH)}$ band undergoes a significant shift to 3270 cm^{-1} with an associated decrease in size, and the band at 2342 cm^{-1} (figure 4.13) is no longer visible, indicating desorption of the remaining CO_2.

Assignments of the observed infrared bands can be made by comparison with the RAIR spectra of pure CO_2 adsorbed on a bare HOPG surface at 28 K (figure 4.5). The bands at 2382 and 2340 cm^{-1} are also observed in the pure CO_2 spectra and can be assigned to the LO and TO modes of the $^{12}CO_2$ ν_3 vibration of multilayer CO_2 respectively. The coverage dependence of the LO mode of the $^{12}CO_2$ ν_3 vibration has been previously discussed, whereby similar behaviour in the position of the LO mode of the ν_3 vibration upon increasing CO_2 exposure is observed. The band at 2346 cm^{-1} is the first band to appear in the RAIR spectrum, shifting and broadening upon increasing CO_2 exposure. As it is the first band to appear in the RAIR spectra, it could be assigned to H_2O bound CO_2. As seen in the TPD spectra, H_2O bound CO_2 produces a broad band as a consequence of the heterogeneous nature of the ASW surface, with a large surface area and large range of adsorption sites on the surface. A RAIR peak assigned to a surface bound adsorbate on a flat surface would be expected to saturate once a complete monolayer has formed. However the ASW surface is rough, and hence the saturation of monolayer CO_2 only occurs once the rough surface, including any pores, is saturated. Once the onset of multilayer growth is observed in the infrared spectra at 20 L, characterised by the observation of the LO phonon mode of the $^{12}CO_2$ ν_3 vibration at 2370 cm^{-1}, the 2346 cm^{-1} band shifts with increasing exposure to give a broad peak around 2355 cm^{-1}. This may be caused by an influence on the polarisation of the phonon vibrations within the layered ice analogous to that observed at 2373 cm^{-1} in the pure CO_2 RAIR spectra, accounting for the lack of observation of a band at 2373 cm^{-1}.

Warming the surface above the natural sublimation temperature of CO_2 produces RAIR spectra with a band at 2342 cm^{-1}, not previously observed in the RAIR spectra of CO_2 on a bare HOPG surface at 28 K. Comparing with TPD spectra of binary layers of CO_2 on H_2O (figures 4.8 and 4.9) and with the lack of the 2342 cm^{-1} band in the pure CO_2 RAIR spectra upon warming (figure 4.6), the 2342 cm^{-1} band can be assigned to CO_2 trapped within the ASW surface. The shift in the $\nu_{(OH)}$ band of H_2O from 3400 cm^{-1} to 3270 cm^{-1} between 105 and 123 K has been previously observed[55] and can be assigned to amorphous and crystalline H_2O respectively. RAIR spectra show that the trapped CO_2 desorbs from the ice between 105 and 123 K, as the H_2O film undergoes an ASW - CI transition as observed in the TPD spectra. A second high temperature peak is observed in the TPD spectra of binary layers of CO_2 on H_2O, coincident with desorption of CI and assigned to co-desorption of CO_2 with H_2O. It is therefore expected

that a small amount of CO_2 remains trapped within the CI between the amorphous to crystalline phase transition and desorption of the H_2O film. This is not evident from the RAIR spectra, as no CO_2 band is visible when the surface is warmed to 123 K. This may be due to the differences in the experimental techniques used, whereby the TPD technique is more sensitive to low adsorbate coverage. As the co-desorption peak in the TPD spectra is very small, it is likely to be too weak to be observed in the RAIR spectra.

4.3.2.2. H_2O/CO_2 Reverse Ice Layers

To gain better insight into the trapping and diffusion of CO_2 in and through an ASW film, TPD spectra of reverse binary layered ices of H_2O adsorbed on CO_2 on a bare HOPG surface at 33 K were collected. Figure 4.15 shows a comparison between a 20 L exposure of CO_2 adsorbed on 100 L H_2O, from figures 4.8 and 4.9, and a 100 L exposure of H_2O adsorbed on 20 L CO_2, adsorbed on a HOPG surface at 33 K. Three desorption features are observed in the TPD spectra of reverse binary ice layers of H_2O on CO_2, a peak with a low temperature shoulder at 96 K followed by two high temperature peaks at 158 and 167 K. The low temperature peak

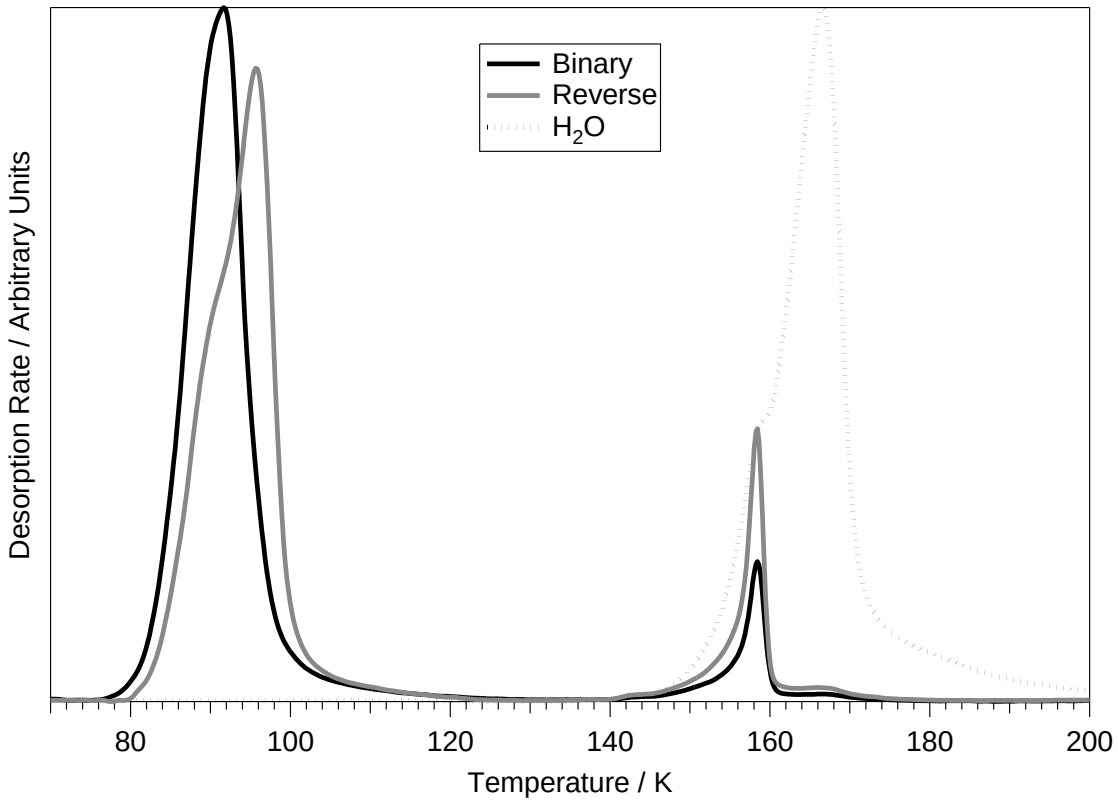

Fig 4.15. TPD spectra of a 20 L exposure of CO_2 adsorbed on a 100 L exposure of H_2O and a 100 L exposure of H_2O adsorbed on a 20 L exposure of CO_2, both adsorbed on HOPG at 33 K. Shown in black is the H_2O TPD spectrum following a 20 L exposure of CO_2 adsorbed on 100 L of H_2O on a HOPG surface at 33 K, for comparison.

at 96 K appears to have a bump on the low temperature side of the TPD peak. However, only a small range of exposures of CO_2 in the reverse layered ices were investigated, and as such this second contribution cannot be assigned. This broad feature at 96 K can only be accounted for in the TPD spectra of reversed binary ices of H_2O on CO_2 if diffusion of CO_2 through the ASW film occurs.

Comparing to TPD spectra of binary layered ices of CO_2 on H_2O as well as with the H_2O TPD spectrum, the features at 158 and 167 K can be assigned to volcano and co-desorption of CO_2 respectively. Comparing the integrated area of pure CO_2 desorbing from a HOPG surface at 33 K with the integrated area of the two high temperature peaks for the reverse layers, shows that the trapped features equate to a 12 L exposure of CO_2, as compared to an 8 L exposure for CO_2 adsorbed on ASW. This is also evident from the TPD spectra in figure 4.15, as the two high temperature peaks in the reverse binary layered ices are larger than their counterparts in the standard binary layered ice TPD spectrum. This is as expected, as desorption of CO_2 prior to the onset of the ASW - CI transition in reverse binary layered ices can only occur due to diffusion of CO_2 through the ASW film, since the ASW film is on top of the CO_2 ice. Therefore it is reasonable to expect that trapping of CO_2 in the ASW film is more likely to occur for the binary layers of CO_2 on ASW. This also explains the increase in peak temperature observed in figure 4.15, as desorption of the bulk of the CO_2 is hindered by the diffusion of CO_2 through the ASW film.

4.3.3. $CO_2/CH_3OH:H_2O$ Binary Ice Layers

To study the effect of the nature of the polar ice, whether pure ASW or CH_3OH-bearing H_2O ice, on the desorption of CO_2, RAIR and TPD spectra were obtained for CO_2 adsorbed on a 100 L exposure of a 15% $CH_3OH:H_2O$ mixture adsorbed on a HOPG surface at 33 K. Adsorption of any exposure of CO_2 onto the $CH_3OH:H_2O$ mixed ice does not show any alteration to the observed CH_3OH or H_2O features, which are shown in figure 4.16. Previous studies on $CH_3OH:H_2O$ mixtures[80] have shown that mixing CH_3OH and H_2O produces a characteristically altered ice film, caused by strong hydrogen bonding interactions between CH_3OH and H_2O. TPD spectra of $CH_3OH:H_2O$ mixtures show that the bump on the leading edge of the H_2O TPD trace, characteristic of the ASW - CI transition, is not visible for the $CH_3OH:H_2O$ mixed ice. The CH_3OH TPD trace shows a broad multi-component desorption feature at 144 K, and a desorption peak at 172 K assigned to co-desorption of CH_3OH with CI[80].

TPD. Figure 4.16 shows TPD spectra for a range of exposures of CO_2 adsorbed on 100 L of a 15% $CH_3OH:H_2O$ mixture adsorbed on HOPG at 33 K. Following a 20 L exposure of CO_2 on the

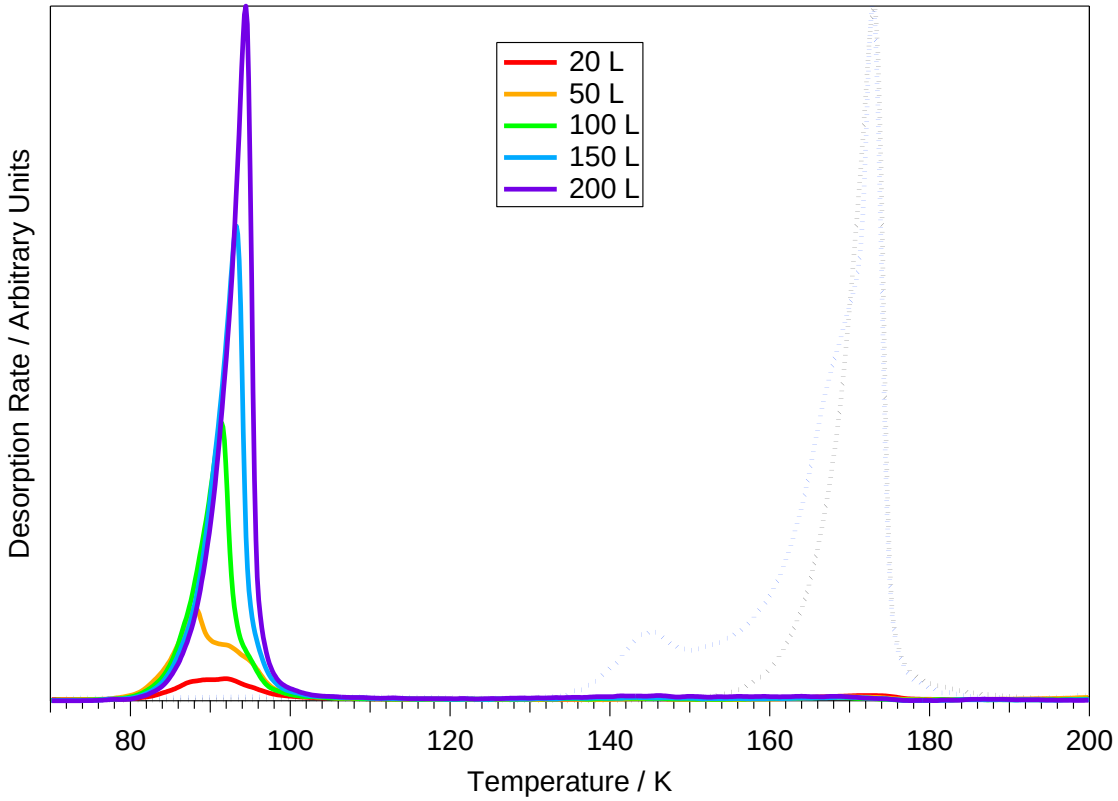

Figure 4.16. TPD spectra of a range of exposures of CO_2 adsorbed on 100 L of a 15% CH_3OH:H_2O mixture adsorbed on HOPG at 33 K. Shown in dotted black and blue are the H_2O and CH_3OH TPD spectra following a 200 L exposure of CO_2 adsorbed on a 100 L exposure of a 15% CH_3OH:H_2O mixture adsorbed on a HOPG surface at 33 K.

CH_3OH:H_2O mixture, three desorption features are observed; a broad, low temperature peak centred at 90 K and two high temperature peaks at 144 and 172 K, shown in figure 4.17. Upon increasing CO_2 exposure to 50 L, a sharp desorption feature appears on the low temperature peak at 88 K. This feature shifts to 94 K with increasing CO_2 exposure to 200 L, showing common leading edges on the set of TPD spectra. No change in the two high temperature peaks is observed with increasing CO_2 exposure. The H_2O desorption spectrum shows a single feature, with a peak temperature of 172 K. The CH_3OH TPD trace shows two desorption features, at 144 and 172 K, neither of which change with increasing CO_2 exposure.

TPD studies of CH_3OH:H_2O mixtures have previously been reported[80]. Comparing the H_2O desorption feature with TPD spectra for a pure H_2O film, as well as with binary layers of CO_2 and H_2O, shows the absence of the bump on the leading edge of the TPD spectrum, usually associated with the ASW - CI transition. This has also been observed in previous studies of layered ices of CH_3OH and ASW[81]. By inducing nucleation of H_2O, CH_3OH lowers the ASW - CI transition temperature of the H_2O film by 13 K[81]. Therefore the ASW - CI phase transition occurs prior to the onset of H_2O desorption and is not visible in the TPD spectrum. The H_2O desorption feature observed at 172 K, in figures 4.16 and 4.17, can therefore be assigned to desorption of CI.

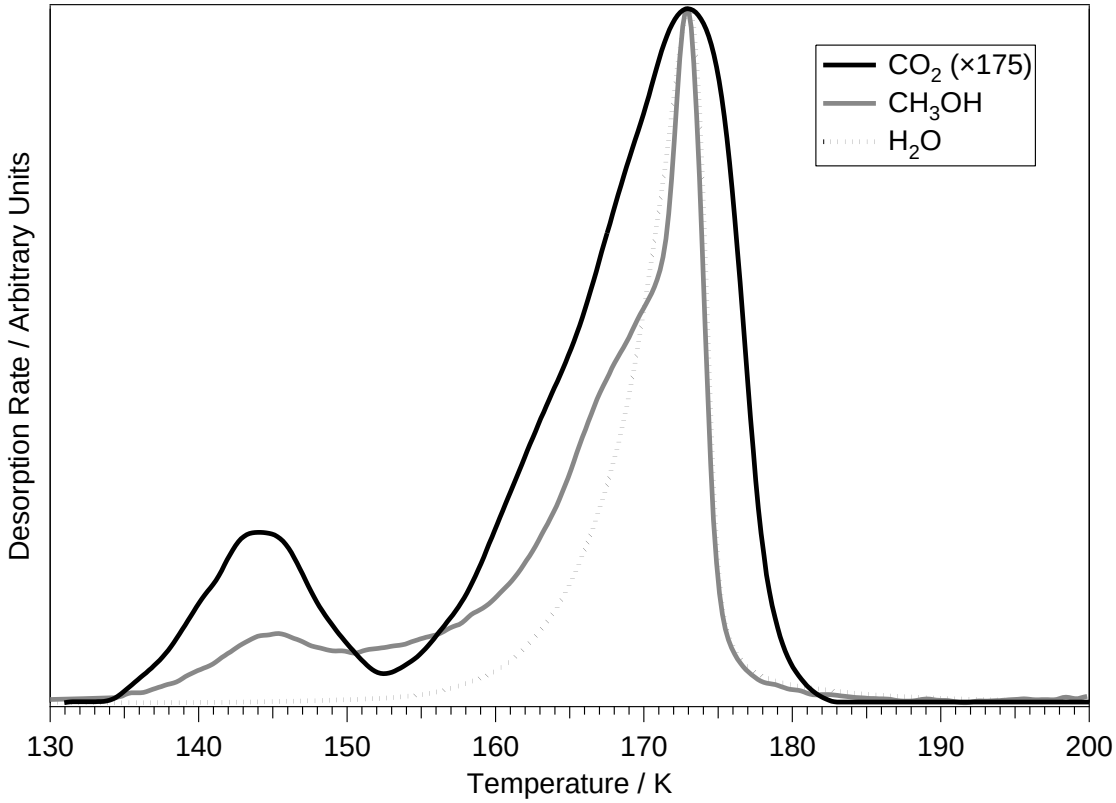

Figure 4.17. TPD spectra of a 20 L exposure of CO_2 adsorbed on a 100 L exposure of a 15% CH_3OH:H_2O mixture adsorbed on a HOPG surface at 33 K. Shown in dotted black and solid grey lines are the H_2O and CH_3OH TPD spectra following a 200 L exposure of CO_2 adsorbed on a 100 L exposure of a 15% CH_3OH:H_2O mixture adsorbed on a HOPG surface at 33 K respectively.

Comparing the CH_3OH TPD trace to previous studies of pure CH_3OH[56,58,82] ices, binary layered ices of CH_3OH and ASW[79,83] and to CH_3OH:H_2O mixtures[80], also shows striking differences upon mixing CH_3OH with ASW. TPD spectra of pure CH_3OH ices and binary layered ices of CH_3OH and ASW both show a sharp desorption feature around 144 K, assigned to the desorption of multilayer CH_3OH. A small CH_3OH desorption feature is also observed coincident with the H_2O desorption feature and is assigned to the co-desorption of CH_3OH with CI. However, mixed CH_3OH:H_2O ices show a broad complex multilayer desorption feature around 144 K, as well as a large desorption feature coincident with the CI desorption feature. The latter is assigned to co-desorption of CH_3OH with CI. The large co-desorption feature indicates a strong interaction between CH_3OH and H_2O molecules, where the formation of a hydrogen bonded complex is implied[80]. The broad, low temperature feature is observed near the natural sublimation temperature of CH_3OH on a bare HOPG surface, implying that CH_3OH can diffuse through the ASW film. However this is counter intuitive if strong interactions form between CH_3OH and H_2O. Instead this feature could be caused by release during a phase or morphology change of the ASW, either the ASW - CI transition lowered in temperature by the induced nucleation caused by CH_3OH, or a liquid phase of H_2O as discussed in previous studies[84-87], at

136 K. Therefore this broad peak will be simply assigned to desorption of weakly bound CH_3OH during the phase transition of H_2O.

The observed CO_2 desorption features can be assigned by comparison with TPD spectra of pure CO_2 (figure 4.2 and 4.3) and binary layered ices (figure 4.8 and 4.9) as well as with the CH_3OH and H_2O features observed in figures 4.16 and 4.17. The broad, low temperature, feature in the TPD spectra of a 20 L exposure of CO_2 on the CH_3OH:H_2O mixture, observed at 90 K, is similar to that observed for monolayer CO_2 adsorbed on a heterogeneous ASW surface. Increasing CO_2 coverage shows behaviour consistent with multilayer desorption of CO_2, showing 0^{th} order characteristics with common leading edges and increasing peak temperatures with increasing CO_2 exposure. This is in agreement with multilayer desorption of CO_2 from a bare HOPG surface as well as from a layer of pre-adsorbed ASW.

The two high temperature desorption features at 144 and 172 K are both well above the natural sublimation temperature of CO_2, and must be trapped within the CH_3OH:H_2O ice. However, comparing the two high temperature desorption features with those observed from TPD spectra of binary layered ices of CO_2 and ASW, striking differences are observed. Desorption of CO_2 from a layer of ASW showed two high temperature desorption features at 158 and 167 K, coincident with the ASW - CI transition and desorption of CI. However, CO_2 desorption from a CH_3OH:H_2O mixture at 144 and 172 K is coincident with the CH_3OH desorption features at 144 and 172 K, and the H_2O desorption feature at 172 K. The CH_3OH desorption features at 144 and 172 K have been assigned to desorption of weakly bound CH_3OH during the ASW - CI transition and co-desorption of CH_3OH with CI. Therefore the observed CO_2 desorption features at 144 and 172 K are assigned to co-desorption of CO_2 with weakly bound CH_3OH during the ASW - CI transition and co-desorption of CO_2 with CI respectively. The difference between the CO_2 desorption features seen at 158 and 144 K for binary layered ices of CO_2 on ASW, and the peaks observed for CO_2 desorption from CH_3OH:H_2O surfaces, is a direct consequence of the alteration of the ASW - CI transition, caused by the inclusion of CH_3OH in the ice.

Comparing the integrated area of CO_2 desorbing from a bare HOPG surface at 33 K with the integrated area of the two trapped CO_2 features from a CH_3OH:H_2O mixture, shows that the trapped features from a CH_3OH:H_2O mixture equates to a 2 L exposure of CO_2. In comparison, the trapped CO_2 feature desorbing from an ASW film equated to an 8 L exposure of CO_2. This suggests that the CH_3OH:H_2O mixture is not as capable as pure ASW at trapping small volatiles such as CO_2.

Quantitative analysis, as discussed in sections 2 and 4.3, was also conducted on the TPD spectra of multilayers of CO_2 adsorbed on a 100 L exposure of pre-adsorbed 15% CH_3OH:H_2O mixture on a HOPG surface at 33 K. CO_2 multilayers were shown to desorb from a 100 L film of

a 15% CH_3OH:H_2O mixture with a desorption order of 0, desorption energy of 24.3 ± 2.4 kJ mol^{-1} and pre-exponential factor of $2.30 \times 10^{29 \pm 0.8}$ molec m^{-2} s^{-1}. Comparing to the kinetic parameters found for multilayer desorption of CO_2 from a bare HOPG surface and ASW surface at 33 K, it can be seen that multilayer desorption occurs with the same order, energy and pre-exponential factor irrespective of the underlying surface. Again, this is expected as desorption of multilayer populations of CO_2 is actually describing CO_2 bound desorption of CO_2.

RAIRS. The characteristics of CO_2 trapping within a CH_3OH:H_2O mixture can also be probed by RAIRS, which when compared with TPD spectra, can provide wider evidence for the assignments made. Four infrared bands are observed in the RAIR spectrum following a 100 L exposure of a 15% CH_3OH:H_2O mixture, shown in figure 4.18. A very broad feature is observed around 3400 cm^{-1} and a smaller, but still broad, peak is seen at 1670 cm^{-1}, assigned previously to the $\nu_{(OH)}$ stretching mode and HOH scissors mode of ASW respectively[55]. A sharp feature at 1460 cm^{-1} and a small broad feature around 1020 cm^{-1} are also observed, assigned to the $\nu_{(CO)}$ stretching mode and the $\delta_{a(CH3)}$ mode of CH_3OH respectively[56,82]. Some infrared bands observed for pure CH_3OH are not seen however. For example the $\nu_{(OH)}$ mode of CH_3OH at 3260 cm^{-1} is obscured by the $\nu_{(OH)}$ of H_2O, and other bands may be too weak to observe. No changes to

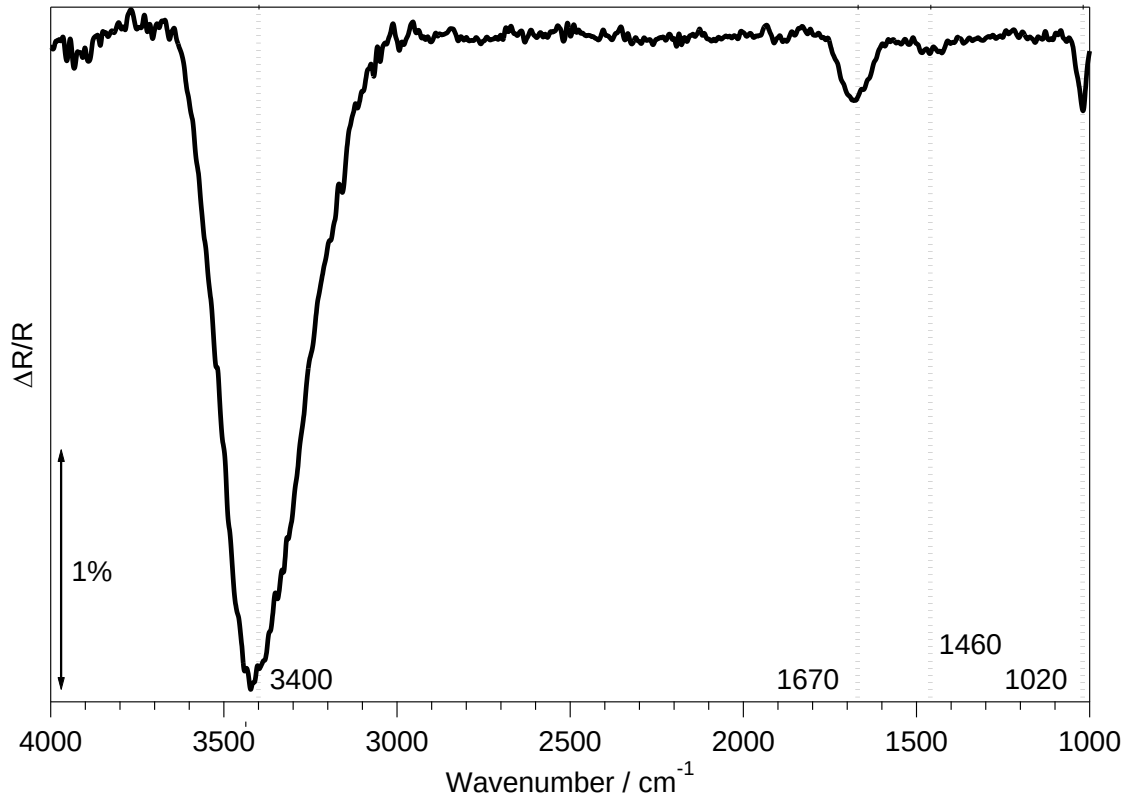

Figure 4.18. RAIR spectra of a 100 L exposure of a 15% CH_3OH:H_2O mixture adsorbed on a HOPG surface at 28 K.

either the CH_3OH or H_2O vibrational bands are observed in the RAIR spectrum upon exposing the CH_3OH:H_2O surface to any exposure of CO_2.

RAIR spectra of a range of exposures of CO_2 adsorbed on 100 L of a 15% CH_3OH:H_2O mixture on a HOPG surface at 28 K, in the wavenumber range of the $^{12}CO_2$ ν_3 vibration, 2400 to 2330 cm^{-1}, are shown in figure 4.19. Following a CO_2 exposure of 5 L, two bands are observed in the RAIR spectra, a sharp peak at 2372 cm^{-1} and a shallow, broad, peak centred around 2355 cm^{-1}. Increasing the CO_2 exposure shows a gradual increase in size and a shift in the frequency of the band at 2372 cm^{-1} to 2380 cm^{-1} following a 200 L exposure of CO_2. Following a CO_2 exposure of 100 L, another band can be observed in the RAIR spectrum at 2340 cm^{-1}, which increases in size but does not shift upon further exposure to CO_2.

Comparing the RAIR spectrum of a 100 L exposure of CO_2 adsorbed on a CH_3OH:H_2O surface with the RAIR spectrum of 100 L of CO_2 adsorbed on a bare HOPG or ASW surface (figures 4.5 and 4.12), the bands observed at 2380 and 2340 cm^{-1} can be assigned to the LO and TO phonon modes of the ν_3 vibration of multilayer CO_2 respectively. As also observed in RAIR spectra of CO_2 adsorbed on a bare HOPG or ASW surface, the LO phonon mode increases in frequency upon increasing CO_2 coverage. The band observed at 2355 cm^{-1} is one of the first bands observed in the RAIR spectra, along with the LO phonon mode at 2372 cm^{-1}. Therefore it

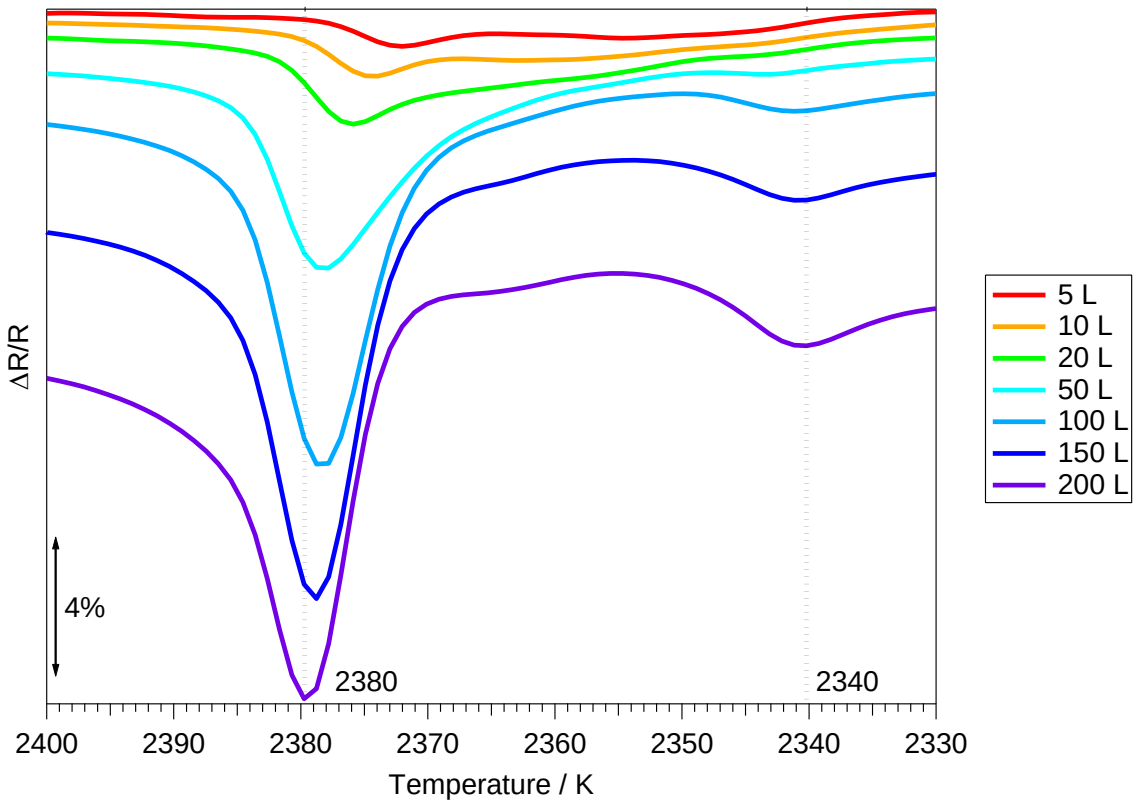

Figure 4.19. RAIR spectra of a range of exposures of CO_2 adsorbed on a 100 L exposure of a 15% CH_3OH:H_2O mixture on a HOPG surface at 28 K.

can be assigned to CO_2, bound to the CH_3OH:H_2O surface, in agreement with the H_2O-bound CO_2 feature observed in figure 4.12 between 2346 and 2355 cm^{-1}.

RAIR spectra of the $^{12}CO_2$ ν_3 and ν_{OH} vibrational regions, following warming of a 200 L exposure of CO_2 adsorbed on 100 L of a 15% CH_3OH:H_2O mixture, are shown in figures 4.20 and 4.21 respectively. No spectral shift of any observed infrared band is seen upon heating the HOPG surface up to 44 K. On warming to 61 - 73 K, the band at 2380 cm^{-1} shifts up in wavenumber to 2381 cm^{-1} (figure 4.20). Warming further to 85 K shows a shift in both bands at 2381 and 2340 cm^{-1}, to 2377 and 2342 cm^{-1} respectively, as well as a significant decrease in the size of all CO_2 bands. Warming further to 97 K shows desorption of most of the CO_2, whereby only a single CO_2 band is still observed at 2342 cm^{-1}. No changes are observed in the band at 2342 cm^{-1} between 97 and 134 K, whereas a slight broadening in the $\nu_{(OH)}$ band at 3400 cm^{-1} is observed from 97 K (figure 4.21). Unlike the RAIR spectra of binary layers of CO_2 and ASW, there is no significant shift of the $\nu_{(OH)}$ band at 3400 cm^{-1} prior to the desorption of H_2O. This is in agreement with the TPD spectra of CO_2 adsorbed on a CH_3OH:H_2O surface (figures 4.16 and 4.17), where the ASW - CI transition is not observed due to the insertion of CH_3OH in the H_2O ice.

Comparing the spectra in figures 4.19 and 4.20 to RAIR and TPD spectra of CO_2 adsorbing

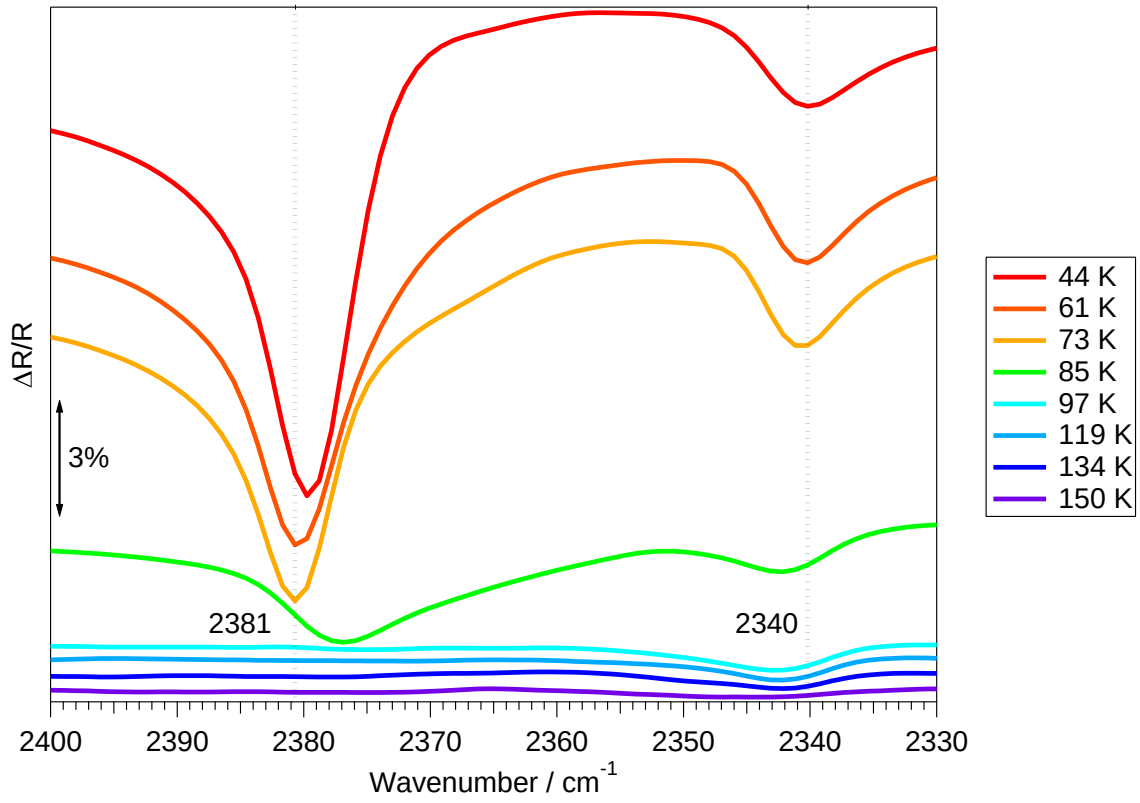

Figure 4.20. RAIR spectra of a 200 L exposure of CO_2 adsorbed on a 100 L exposure of a 15% CH_3OH:H_2O mixture adsorbed on HOPG at 28 K, prior to warming to a range of temperatures.

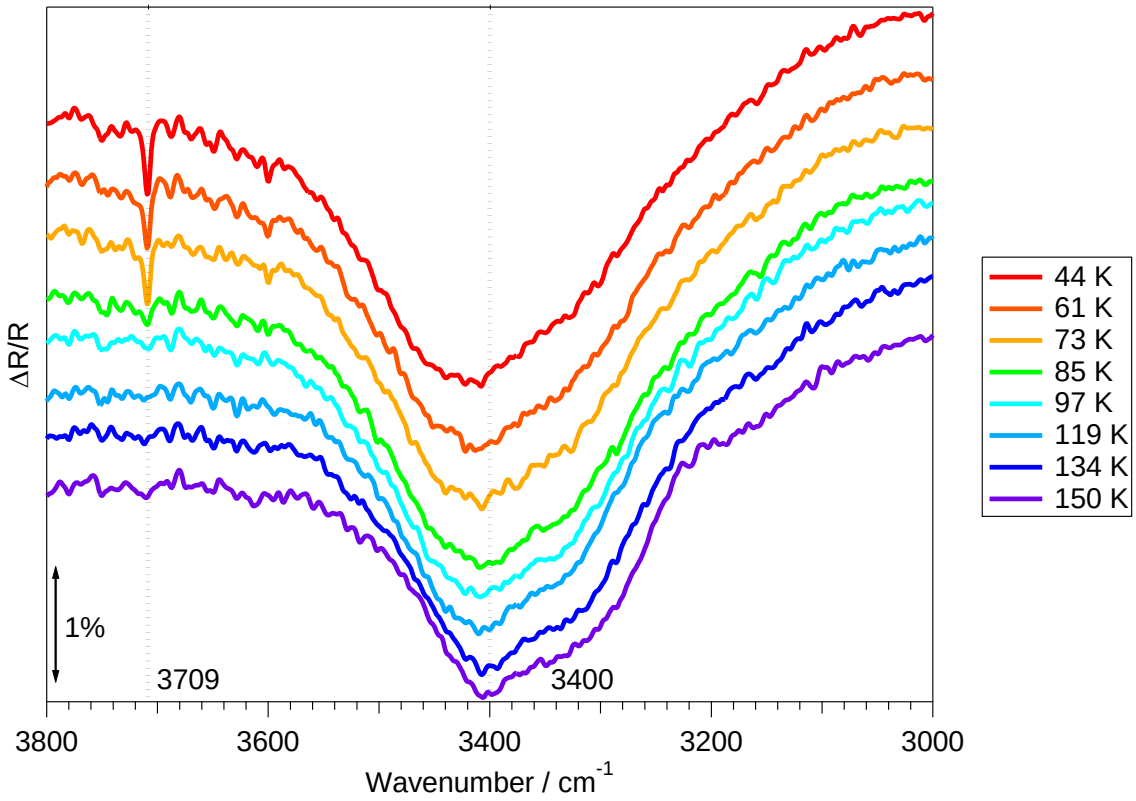

Figure 4.21. RAIR spectra of the $\nu_{(OH)}$ region of a 200 L exposure of CO_2 adsorbed on a 100 L exposure of a 15% CH_3OH:H_2O mixture adsorbed on HOPG at 28 K, prior to warming to a range of temperatures.

and desorbing from an ASW surface below 33 K can provide insight into the effect of the nature of the polar ice surface, whether pure ASW or CH_3OH-bearing H_2O ices, on the behaviour of CO_2. The temperature of the ASW - CI transition in CH_3OH-bearing H_2O ices is decreased when compared to pure ASW ice. This not only affects the desorption of H_2O and CH_3OH, but also affects the volatiles trapped within the polar ice. As has been observed, desorption of H_2O dictates the desorption of CO_2 trapped within the ice. Therefore a change in the behaviour of the H_2O, driven by the inclusion of CH_3OH in the ice, will inevitably change the behaviour of CO_2 desorption. In addition, the CH_3OH-bearing H_2O ice is characterised by the formation of a hydrogen bonded network, implying a more densely packed and ordered ice as compared to ASW. Therefore the physical differences between the ice films affect the diffusion and trapping of CO_2 through and within the respective ices.

4.3.4. CO_2:H_2O Ice Mixtures

RAIR and TPD spectra were obtained for a range of exposures of a 15% mixture of CO_2 and H_2O, co-deposited on a HOPG surface at 33 K. Mixtures of CO_2 and H_2O are the most

astrophysically relevant system studied here, providing the most realistic analogy to interstellar ices.

TPD. Figure 4.22 shows the TPD spectra of a range of exposures of a 15% CO_2:H_2O mixture co-deposited on a HOPG surface at 33 K. Three desorption features are observed following the lowest CO_2:H_2O mixture exposure of 20 L; a low temperature peak centred around 90 K and two high temperature peaks at 159 and 163 K. Increasing the CO_2:H_2O exposure, up to 200 L, shows an increase in the size of all observed desorption features, and no noticeable shift is observed in the desorption features around 90 K and 159 K. The CO_2 desorption feature at 163 K gradually increases in peak temperature upon increasing CO_2:H_2O exposure to reach 174 K following a 200 L exposure.

H_2O TPD spectra following a 20 L exposure of the CO_2:H_2O mixture show a single desorption feature with a peak temperature of 163 K and a bump on the leading edge at 159 K. Increasing the CO_2:H_2O exposure shows a gradual increase of the peak temperature to 174 K following a 200 L exposure, whereas the bump at 159 K does not shift. Comparing to TPD spectra of pure H_2O[55], the two observed H_2O desorption features can be assigned to the ASW - CI transition at 159 K and the desorption of CI between 163 and 174 K. As the exposure of H_2O increases with

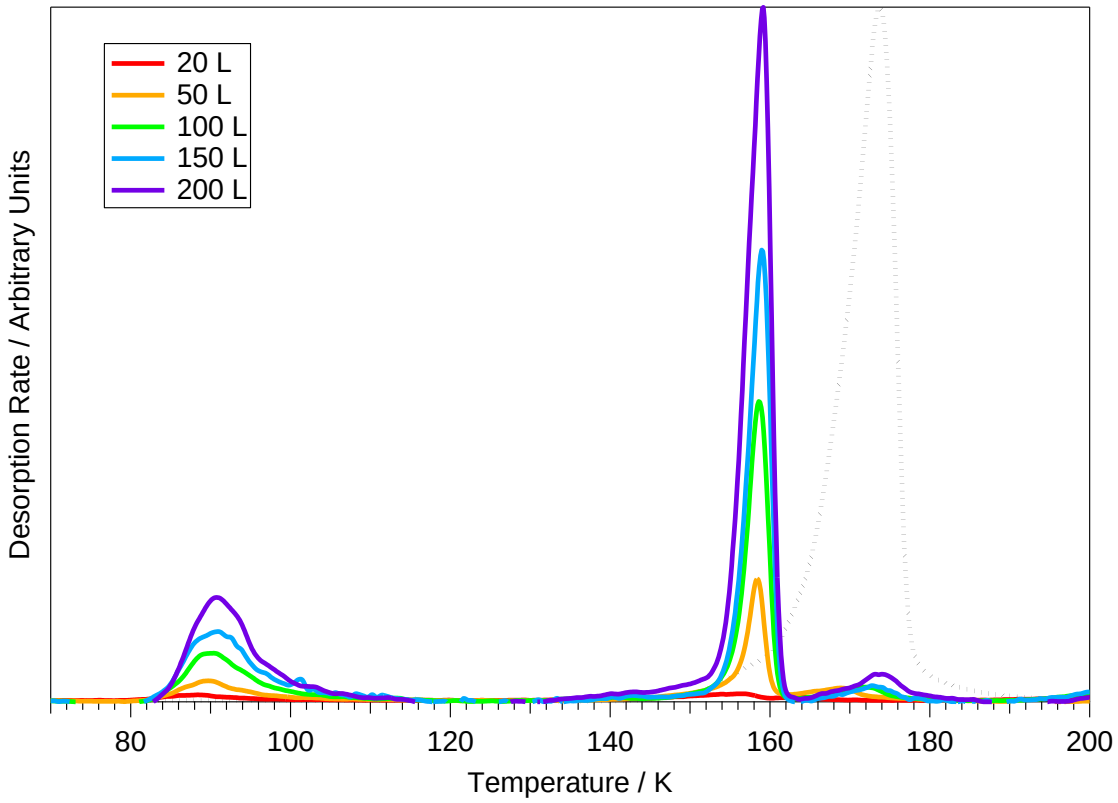

Figure 4.22. TPD spectra of a range of exposures of a 15% CO_2:H_2O mixture adsorbed on a HOPG surface at 33 K. Shown in black is the H_2O TPD spectrum following a 200 L exposure of a 15% CO_2:H_2O mixture adsorbed on HOPG at 33 K.

increasing CO_2:H_2O exposure, the temperature of the main H_2O desorption feature is observed to increase. This is consistent with previous TPD studies of pure H_2O[55].

By comparing the CO_2 and H_2O TPD spectra from the 15% CO_2:H_2O mixtures with those observed for binary layers of CO_2 and H_2O, the observed CO_2 desorption features can be assigned. It has previously been shown that H_2O dictates the desorption of CO_2 above its natural sublimation temperature. Therefore the CO_2 features observed at 159 K, coincident with the ASW - CI transition of H_2O, and between 163 and 174 K, coincident with the desorption of CI, can be assigned to volcano and co-desorption of CO_2 trapped with the H_2O matrix. As the CO_2:H_2O mixture is co-deposited on the surface, it is intimately mixed. Therefore, the low temperature CO_2 desorption feature at 90 K must be caused by diffusion of CO_2 through the mixed ice, comparable to that observed in the reverse binary layers of H_2O adsorbed on CO_2. Comparison between the trapped CO_2 desorption features from binary and reverse CO_2 and H_2O ice layers (figures 4.8, 4.9 and 4.15) with those of CO_2:H_2O mixtures (figure 4.22), shows that the trapped CO_2 features are larger for the mixtures.

Integration of the observed desorption features, as well as the total integrated area of all CO_2 peaks, shows a linear correlation between area and CO_2:H_2O exposure. Comparing the total CO_2 integrated area with that of the high temperature desorption features of CO_2 indicates that, for all CO_2:H_2O exposures, approximately 71% of the CO_2 is trapped within the ice mixture until the onset of H_2O desorption, and 29% of the CO_2 is able to diffuse through the mixture to desorb near the natural CO_2 sublimation temperature. The amount of CO_2 which traps in a 100 L exposure of the mixed CO_2:H_2O ice is equivalent to the amount of trapped CO_2 in the reverse binary layered ices of a 100 L exposure of H_2O on top of CO_2. This shows that thermal processing in the reversed binary ices of H_2O on CO_2, prior to complete desorption of the layered ice, may be a plausible method for producing binary mixed ices. This also indicates the upper limit of CO_2 inclusion, or saturation, in an ASW matrix.

RAIRS. Figures 4.23 and 4.24 show RAIR spectra for a 100 L exposure of a 15% CO_2:H_2O mixture adsorbed on HOPG at 33 K prior to being warmed to a range of temperatures. Following a 100 L exposure of a 15% CO_2:H_2O mixture, three infrared features are observed: a very broad feature at 3400 cm^{-1} and a small peak at 1670 cm^{-1}, analogous to the H_2O RAIR spectrum shown in figure 4.11. These are assigned to the $\nu_{(OH)}$ stretching mode and HOH scissors mode of ASW respectively[55]. Also observed in the wavenumber range of the $^{12}CO_2$ ν_3 vibration, 2400 to 2330 cm^{-1}, is a single infrared band at 2345 cm^{-1}. This band can be assigned to the $^{12}CO_2$ ν_3 vibration of H_2O associated CO_2 via comparison with RAIR spectra of binary layered ices of CO_2 on H_2O (figure 4.12) and CO_2 on CH_3OH:H_2O (figure 4.19). It is also immediately obvious that the band observed at 2382 cm^{-1}, assigned to the LO phonon mode of

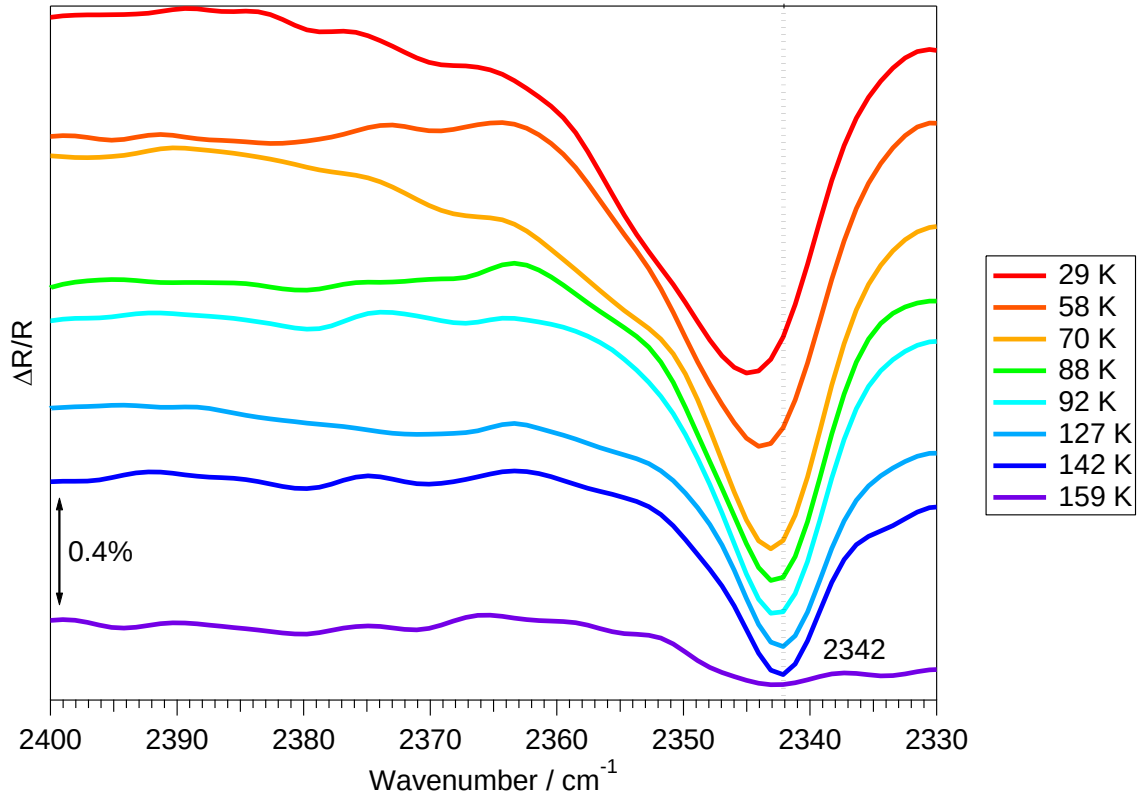

Figure 4.23 RAIR spectra of a 100 L exposure of a 15% CO_2:H_2O mixture adsorbed on HOPG at 28 K, prior to warming to a range of temperatures.

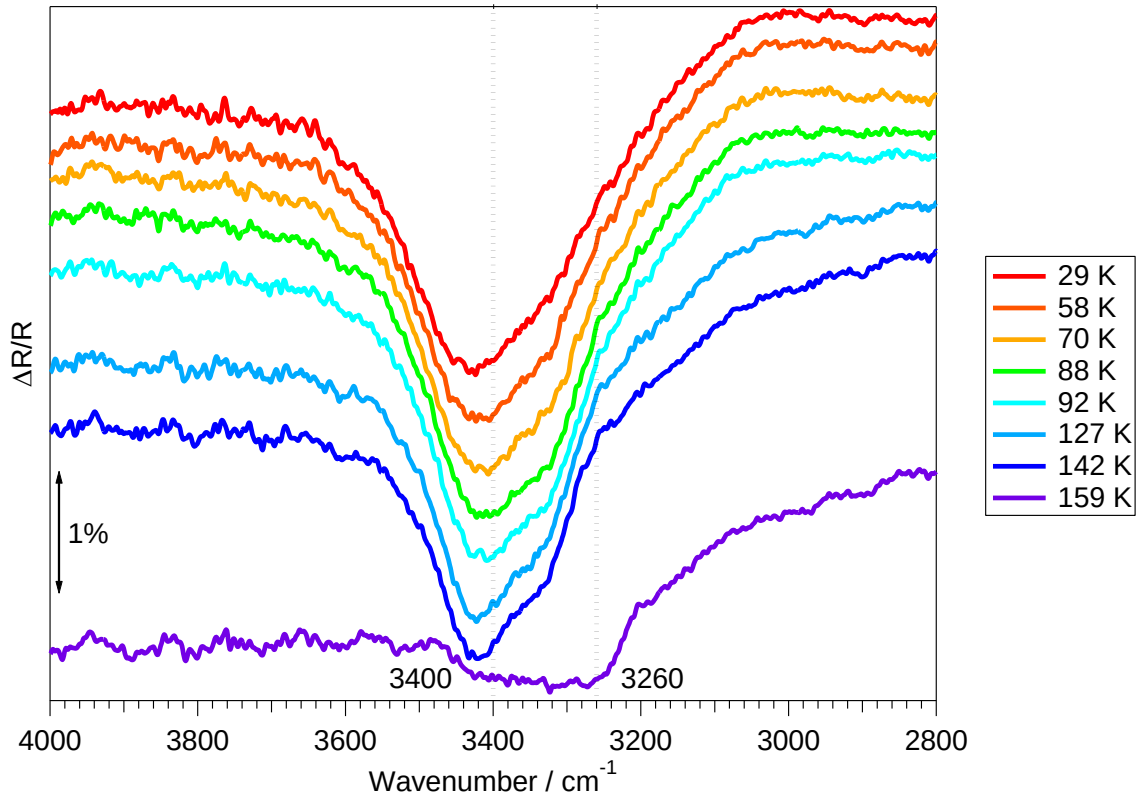

Figure 4.24. RAIR spectra of the $\nu_{(OH)}$ region of a 100 L exposure of a 15% CO_2:H_2O mixture adsorbed on HOPG at 28 K, prior to warming to a range of temperatures.

the $^{12}CO_2$ ν_3 vibration of multilayer CO_2 is not observed in the RAIR spectrum of a CO_2:H_2O mixture, and this is discussed shortly.

Warming to 70 K shows a gradual and slight spectral shift and sharpening in the band at 2345 to 2343 cm^{-1} (figure 4.23). Little change is observed in the RAIR spectrum upon warming the surface to 92 K. Warming to 127 K shows a decrease in size and slight shift in the observed infrared band to 2342 cm^{-1}. Complete desorption of CO_2 is indicated by the RAIR spectrum following warming to 159 K, where a corresponding shift in the H_2O $\nu_{(OH)}$ stretch (figure 4.24) from 3400 cm^{-1} to 3260 cm^{-1}, characteristic of the ASW - CI transition, is observed. No infrared features are observed in the RAIR spectrum following warming of the surface to 176 K where complete desorption of the CO_2:H_2O mixture has occurred.

The first and most noticeable difference between RAIR spectra of pure, binary and mixed CO_2: H_2O ice is the lack of an infrared band around 2382 cm^{-1}. The CO_2 and H_2O are intimately mixed in a CO_2:H_2O mixture. As discussed in chapter 3, H_2O ice does not show LO - TO phonon splitting of any infrared active vibrational band as the minimum and maximum of $|\varepsilon|$ for H_2O ice does not approach 0 and ∞ respectively. Therefore phonon vibrations within the CO_2:H_2O mixed ice will not become polarised with respect to the surface normal. As a result, only the TO mode of the $^{12}CO_2$ ν_3 vibration is observed as expected for infrared spectra at normal incidence to the surface. Changes to the position of the CO_2 vibration, attributed to H_2O bound CO_2, are also observed upon warming the mixed ice, where the band initially at 2345 cm^{-1} shifts to 2342 cm^{-1}. This is in line with observations in the layered ice of CO_2 on H_2O, where, upon adsorption, this band is initially observed at 2346 cm^{-1}. Upon warming the layered ice above the natural sublimation temperature of CO_2, an infrared band of trapped CO_2 at 2342 cm^{-1} is still observed in the spectrum. This is not to be confused with the TO phonon mode of the $^{12}CO_2$ ν_3 vibration of multilayer CO_2 which is observed between 2341 and 2340 cm^{-1} (figures 4.5, 4.12 and 4.19).

On warming the surface to above the natural sublimation temperature of CO_2, prior to the onset of desorption of H_2O, the single CO_2 infrared band shifts to 2342 cm^{-1}. Desorption of CO_2 from the mixture is observed to occur coincident with the ASW - CI transition, also in agreement with binary layered ices of CO_2 on H_2O, and TPD spectra of CO_2:H_2O mixed ices. However no CO_2 is observed in the RAIR spectra at surface temperatures between the ASW - CI transition and desorption of CI, as opposed to that observed in TPD spectra of CO_2:H_2O mixtures. As discussed for the desorption of binary layers of CO_2 on H_2O, this is likely due to experimental constraints on the sensitivity of the infrared spectrometer.

4.4. Summary and Conclusions

RAIR and TPD spectra have been collected for a range of CO_2 bearing ices adsorbed on a graphitic dust grain analogue below 33 K. It has been shown that multilayers of CO_2 grow on a HOPG surface, as well as on polar ice surfaces below 33 K. CO_2 is physisorbed on the surface, and desorbs with a sublimation temperature of around 90 K. The nature of the surface, whether bare HOPG or polar ice, has little effect on the adsorption and desorption of multilayer CO_2. This is expected as bulk, or multilayer, CO_2 is essentially bound to other CO_2 molecules. This is also evident from quantitative analysis of TPD spectra of multilayers of CO_2, as summarised in table 4.7, whereby desorption energies for multilayer desorption of CO_2 are all found to be the same within experimental error, irrespective of the nature of the underlying surface.

Table 4.7. Calculated kinetic parameters for multilayer CO_2 desorbing from a bare HOPG surface and a range of polar ice surfaces at 33 K.

	n	E_{des} / kJ mol^{-1}	ν_n / molec m^{-2} s^{-1}
Pure CO_2	0	24.8 ± 1.6	$1.07 \times 10^{30 \pm 1.5}$
CO_2/H_2O	0	25.4 ± 1.4	$2.06 \times 10^{30 \pm 0.5}$
$CO_2/CH_3OH:H_2O$	0	24.3 ± 2.4	$2.30 \times 10^{29 \pm 0.8}$

When adsorbed on a porous ice, CO_2 may trap within the ice matrix above its natural sublimation temperature, depending on the nature of the ice surface. ASW, a heterogeneous and disordered surface, traps CO_2 whereby it is released into the gas phase during a volcano desorption, coincident with the ASW - CI transition, and co-desorption, coincident with the desorption of CI. This is also observed for CO_2 desorption from a $CH_3OH:H_2O$ polar ice, however, the amount of CO_2 trapping within equivalent coverage of the polar ice surface is reduced to approximately 25% of that trapped in an ASW surface. This is likely caused by strong hydrogen bonds forming in the $CH_3OH:H_2O$ ice surface, creating a less heterogeneous and more ordered ice surface. Therefore the $CH_3OH:H_2O$ ice surface is less porous. The nature of the polar ice surface is obviously important for the behaviour of volatiles adsorbed on or within the ice.

Comparing binary layered ices of CO_2 on ASW and reverse binary layered ices of ASW on CO_2 shows the ability of CO_2 to diffuse through the polar ice to allow desorption close to its natural sublimation temperature. This is also seen to affect the amount of trapping of CO_2 within an equivalent coverage of ASW, whereby approximately 50% more CO_2 is seen to trap within the ASW ice when it first has to diffuse through the entire ice prior to desorption as opposed to surface bound CO_2 trapping within pores of the amorphous surface.

Finally CO_2:H_2O mixtures were studied. Growth of multilayer CO_2 was inhibited due to the inherent nature of the mixture. This greatly affected the RAIR spectra, whereby only one $^{12}CO_2$ ν_3 band was observed as opposed to the complex infrared spectra of bulk CO_2. Diffusion and trapping of CO_2 within the mixed ice was also observed, where approximately 71% of the CO_2 remained in the ice upon warming above the natural sublimation temperature of CO_2.

The trends observed here can be used to help identify the nature and composition of interstellar ices, where the kinetic data derived from TPD spectra can also be used to create models of interstellar ices in star forming regions, as shall be discussed in more detail in chapter 7.

4.5. References

1. Kessler M.F. et al, *Astron. Astrophys.*, **315**, (1996), L27-L31
2. de Graauw Th. et al, *Astron. Astrophys.*, **315**, (1996), L49-L54
3. van Dishoeck E.F. et al, *Astron. Astrophys.*, **315**, (1996), L349-L352
4. Allamandola L.J., Bernstein M.P., Sandford S.A. and Walker R.L., *Space Sci. Rev.*, **90**, (1999), 219-232
5. Boogert A.C.A. et al, *Astrophys. J. Supp. Ser.*, **154**, (2004), 359-362
6. Dartois E., Pontoppidan K., Thi W.F. and Muñoz Caro G.M., *Astron. Astrophys.*, **444**, (2005), L57-L60
7. Pontoppidan K.M. et al, *Astrophys. J.*, **622**, (2005), 463-481
8. Watson D.M. et al, *Astrophys. J. Supp. Ser.*, **154**, (2004), 391-395
9. d'Hendecourt L. et al, *Astron. Astrophys.*, **315**, (1996), L365-L368
10. de Graauw Th. et al, *Astron. Astrophys.*, **315**, (1996), L345-L348
11. Gerakines P.A. et al, *Astrophys. J.*, **522**, (1999), 357-377
12. Gibb E.L., Whittet D.C.B., Boogert A.C.A. and Tielens A.G.G.M., *Astrophys. J. Supp. Ser.*, **151**, (2004), 35-73
13. Nummelin A., Whittet D.C.B., Gibb E.L., Gerakines P.A. and Chiar J.E., *Astrophys. J.*, **558**, (2001), 185-193
14. van Broekhuizen F.A., Groot I.M.N., Fraser H.J., van Dishoeck E.F. and Schlemmer S., *Astron. Astrophys.*, **451**, (2006), 723-731
15. Whittet D.C.B. et al, *Astrophys. J.*, **655**, (2007), 332-341
16. Roser J.E., Vidali G., Manicò G. and Pirronello V., *Astrophys. J.*, **555**, (2001), L61-L64
17. Watanabe N. and Kouchi A., *Astrophys. J.*, **567**, (2002), 651-655
18. Lee C.W., Kim J.K., Moon E.S., Minh Y.C. and Kang H., *Astrophys. J.*, **697**, (2009), 428-435
19. Sandford S.A. and Allamandola L.J., *Astrophys. J.*, **355**, (1990), 357-372
20. Ehrenfreund P. et al, *Astron. Astrophys.*, **315**, (1996), L341-L344
21. Whittet D.C.B. et al, *Astron. Astrophys.*, **315**, (1996), L357-L360
22. Herzberg G.Infrared and Raman Spectra of Polyatomic Molecules. D. Van Nostrand Company: N.Y., 1945.
23. Dartois E., Demyk K., d'Hendecourt L. and Ehrenfreund P., *Astron. Astrophys.*, **351**, (1999), 1066-1074
24. Ehrenfreund P., Boogert A.C.A., Gerakines P.A., Tielens A.G.G.M. and van Dishoeck E.F., *Astron. Astrophys.*, **328**, (1997), 649-669
25. Ehrenfreund P. et al, *Astron. Astrophys.*, **350**, (1999), 240-253
26. Hodyss R., Johnson P.V., Orzechowska G.E., Goguen J.D. and Kanik I., *Icarus*, **194**, (2008), 836-842

27. Öberg K.I. et al, *Astron. Astrophys.*, **462**, (2007), 1187-1198
28. Ovchinnikov M.A. and Wight C.A., *J. Chem. Phys.*, **99(5)**, (1993), 3374-3379
29. Bernstein M.P., Cruikshank D.P. and Sandford S.A., *Icarus*, **179**, (2005), 527-534
30. Gerakines P.A., Schutte W.A., Greenberg J.M. and van Dishoeck E.F., *Astron. Astrophys.*, **296**, (1995), 810-818
31. Baratta G.A. and Palumbo M.E., *J. Opt. Soc. Am. A*, **15(12)**, (1998), 3076-3085
32. Baratta G.A., Palumbo M.E. and Strazzulla G., *Astron. Astrophys.*, **357**, (2000), 1045-1050
33. Gálvez O. et al, *Astron. Astrophys.*, **472**, (2007), 691-698
34. Gálvez O., Maté B., Herrero V.J. and Escribano R., *Icarus*, **197**, (2008), 599-605
35. Matè B., Gálvez O., Herrero V.J. and Escribano R., *Astrophys. J.*, **690**, (2009), 486-495
36. Palumbo M.E. et al, *Astron. Astrophys.*, **334**, (1998), 247-252
37. Palumbo M.E. and Baratta G.A., *Astron. Astrophys.*, **361**, (2000), 298-302
38. Kumi G., Malyk S., Hawkins S., Reisler H. and Wittig C., *J. Phys. Chem. A*, **110**, (2006), 2097-2105
39. Malyk S., Kumi G., Reisler H. and Wittig C., *J. Phys. Chem. A*, **111**, (2007), 13365-13370
40. Heidberg J. and Redlich B., *Surf. Sci.*, **368**, (1996), 140-146
41. Falk M., *J. Chem. Phys.*, **86(2)**, (1986), 560-564
42. Falk M. and Seto P.F., *Can. J. Spectrosc.*, **31(5)**, (1986), 134-137
43. Osberg W.E. and Hornig D.F., *J. Chem. Phys.*, **20(9)**, (1952), 1345-1347
44. Heidberg J. et al, *Vacuum*, **38(4/5)**, (1988), 275-277
45. Berg O. and Ewing G.E., *Surf. Sci.*, **220**, (1989), 207-229
46. Wood B.E. and Roux J.A., *J. Opt. Soc. Am.*, **72(6)**, (1982), 720-728
47. Pokrovski K., Jung K.T. and Bell A.T., *Langmuir*, **17**, (2001), 4297-4303
48. Stevens R.W.Jr., Siriwardane R.V. and Logan J., *Energy & Fuels*, **22**, (2008), 3070-3079
49. Mennella V., Baratta G.A., Palumbo M.E. and Bergin E.A., *Astrophys. J.*, **643**, (2006), 923-931
50. Andersson P.U., Någård M.B., Witt G. and Pettersson J.B.C., *J. Phys. Chem. A*, **108**, (2004), 4627-4631
51. Matè B. et al, *J. Phys. Chem. A*, **112**, (2008), 457-465
52. Öberg K.I., van Dishoeck E.F. and Linnartz H., *Astron. Astrophys.*, **496**, (2009), 281-293
53. Collings M.P. et al, *Mon. Not. R. Astron. Soc.*, **354**, (2004), 1133-1140
54. Ulbricht H., Zacharia R., Cindir N. and Hertel T., *Carbon*, **44**, (2006), 2931-2942
55. Bolina A.S., Wolff A.J. and Brown W.A., *J. Phys. Chem. B*, **109**, (2005), 16836-16845
56. Bolina A.S., Wolff A.J. and Brown W.A., *J. Chem. Phys.*, **122**, (2005), 044713
57. Dempster A.B. and Zerbi G., *J. Chem. Phys.*, **54(8)**, (1971), 3600-3609
58. Green S.D. et al, *Mon. Not. R. Astron. Soc.*, **398**, (2009), 357-367
59. Bolina A.S. and Brown W.A., *Surf. Sci.*, **598**, (2005), 45-56
60. Burke D.J., Wolff A.J., Edridge J.L. and Brown W.A., *J. Chem. Phys.*, **128**, (2008), 104702
61. Bryson C.E. and Levenson L.L., *Surf. Sci.*, **43(1)**, (1974), 29-43
62. Brown W.A., Viti S., Wolff A.J. and Bolina A.S., *Faraday Discussions*, **133**, (2006), 113-124
63. Brown W.A. and Bolina A.S., *Mon. Not. R. Astron. Soc.*, **374**, (2007), 1006-1014
64. Viti S., Collings M.P., Dever J.W., McCoustra M.R.S. and Williams D.A., *Mon. Not. R. Astron. Soc.*, **354(4)**, (2004), 1141-1145
65. Yamada H. and Person W.B., *J. Chem. Phys.*, **41(8)**, (1964), 2478-2487
66. Barnes J.A. and Gough T.E., *J. Chem. Phys.*, **86(11)**, (1987), 6012-6017
67. Disselkamp R. and Ewing G.E., *J. Chem. Soc. Faraday Trans.*, **86(13)**, (1990), 2369-2373
68. Ewing G.E. and Sheng D.T., *J. Phys. Chem.*, **92**, (1988), 4063-4066
69. Fleyfel F. and Devlin J.P., *J. Phys. Chem.*, **93(7292)**, (1989), 7294
70. Berreman D.W., *Phys. Rev.*, **130(6)**, (1963), 2193-2198
71. Collings M.P., Dever J.W., Fraser H.J., McCoustra M.R.S. and Williams D.A., *Astrophys. J.*, **583**, (2003), 1058-1062
72. Collings M.P., Dever J.W., Fraser H.J. and McCoustra M.R.S., *Astrophys. Space Sci.*, **285**, (2003), 633-659

73. Fraser H.J., Collings M.P., McCoustra M.R.S. and Williams D.A., *Mon. Not. R. Astron. Soc.*, **327**, (2001), 1165-1172
74. de Jong A.M. and Niemantsverdriet J.W., *Surf. Sci.*, **233**, (1990), 355-365
75. King D.A., *Surf. Sci.*, **47**, (1975), 384-402
76. Ehrenfreund P., Dartois E., Demyk K. and d'Hendecourt L., *Astron. Astrophys.*, **339**, (1998), L17-L20
77. Smith R.S., Huang C., Wong E.K.L. and Kay B.D., *Phys. Rev. Lett.*, **79(5)**, (1997), 909-912
78. Burke D.J., Wolff A.J., Edridge J.L. and Brown W.A., *Phys. Chem. Chem. Phys.*, **10(32)**, (2008), 4956-4967
79. Wolff A.J., Carlstedt C. and Brown W.A., *J. Phys. Chem. C*, **111**, (2007), 5990-5999
80. Burke D.J. and Brown W.A., *Phys. Chem. Chem. Phys.*, **12**, (2010), 5947-5969
81. Souda R., *Phys. Rev. B.*, **75**, (2007), 184116
82. Bolina A.S., PhD Thesis. University College London, (2005)
83. Wolff A.J., PhD Thesis. University College London, (2007)
84. Smith R.S. and Kay B.D., *Nature*, **398**, (1999), 788-791
85. Smith R.S., Dohnálek Z., Kimmel G.A., Stevenson K.P. and Kay B.D., *Chem. Phys.*, **258**, (2000), 291-305
86. Souda R., *Phys. Rev. Lett.*, **93**, (2004), 235502
87. Souda R., *J. Chem. Phys.*, **121**, (2004), 8676-8679

Chapter 5: Temperature Programmed Desorption and Reflection Absorption Infrared Spectroscopy of Carbon Disulphide bearing ices on Highly Oriented Pyrolytic Graphite

5.1. Introduction

The study of sulphur chemistry in the gas phase and on the surface of interstellar dust grains has been shown to be particularly useful as a tracer for chemical evolution in star forming regions[1-8]. The depletion of elemental sulphur is also a problem in astrophysics[9-11], where the total abundance of observed sulphur-bearing molecules in the gas phase accounts for approximately 0.1% of the solar sulphur abundance[11]. Steady state models of cold molecular clouds have shown that gas phase S, CS and SO accounts for the majority of the observed sulphur-bearing species[4,11]. The remaining sulphur is thought to be composed of sulphur-bearing ices on the surface of dust grains[3,10,12] or undetectable molecules or ions such as S_2 or S^+.[3,10]

Until recently it was hypothesised that CS_2 existed in the ices of a number of comets[13-15] to account for the relatively high abundances of the CS radical observed[15-19]. However it was not conclusively detected until a study by Jackson, Scodinu and Xu[20] of the comet de Vico. Detection of CS_2 was impaired due to low abundances, as it is readily photodissociated by ultraviolet radiation into CS and S fragments[21-23]. From the observed abundance of the daughter molecule CS, the abundance of CS_2 within a typical cometary ice has been found to be ≈0.2% with respect to H_2O[24]. It has also been shown, from comparison between the typical composition of cometary and interstellar ices, that the composition of these ices is closely related[24]. Although CS_2 has yet to be discovered within dense molecular clouds in the interstellar medium (ISM), CS has been detected in a number of regions, including near hot cores[1,3,4,24-26], in abundances up to 2×10^{-7} with respect to H_2. It has also been shown, via application of chemical modelling, that the source of sulphur bearing molecules in cometary ice cannot be accounted for by chemical processing alone[27]. Therefore it is believed that the chemical composition, within the core of cometary ices, is a record of the chemical composition of the primitive solar nebular in which they were formed[24,27].

The study of CS_2-bearing ices in comparison with the study of CO_2-bearing ices is also of interest to help to understand how the physical properties of the molecule affect its ability to trap and desorb from ices. CO_2 and CS_2 have bond lengths of 116.3 and 155.3 pm respectively. The relative sizes of O and S atoms can be described by their covalent radii at 66 and 105 pm

respectively. Therefore, due to the respective bond lengths and atom size, the CO_2 molecule is much smaller than CS_2. It is therefore expected that this may affect the ability of the larger CS_2 molecule to diffuse and trap within a H_2O matrix.

A range of experimental studies of CS_2 have been conducted. Of relevance to this study are those involving temperature programmed desorption[28] (TPD) and infrared techniques[29,30]. TPD studies of a range of astrophysically relevant molecules, including CS_2, adsorbed on a Au substrate and a pre-adsorbed film of amorphous solid water (ASW) at 8 – 10 K, were conducted[28]. It was discovered that multilayers of CS_2 desorb from the Au surface at approximately 100 K. A feature on the low temperature side of the TPD peak was also observed at approximately 90 K, caused by a phase transition of amorphous to crystalline CS_2. TPD spectra of CS_2 desorption from a pre-adsorbed ASW film showed two additional features, coincident with the desorption of the H_2O film. These were assigned to the volcano and co-desorption of trapped CS_2 within the ASW film. TPD spectra of CS_2:H_2O mixtures were also collected[28]. Only two TPD features were observed, coincident with the desorption of H_2O. As the CS_2 multilayer desorption peak was not observed, it was concluded that the diffusion of CS_2 through the H_2O film was limited, especially when compared to the ease of diffusion of smaller volatiles such as CO and CO_2[28].

Infrared and Raman spectra of gas phase[29,31] and solid CS_2 have also been recorded[30,32,33]. Gas phase infrared studies of CS_2 show two fundamental stretches at 396.8 and 1532.5 cm^{-1}, assigned to the bend, ν_2, and the asymmetric stretch, ν_3, respectively[29]. A number of combination bands above 2000 cm^{-1} were also detected. Gas phase Raman studies[31] of CS_2 also showed a fundamental stretch at 657.98 cm^{-1}, assigned to the infrared inactive symmetric stretch, ν_1, as well as a number of combination bands between 630 and 820 cm^{-1}. Infrared spectra of crystalline CS_2 condensed on a KBr surface at 85 K show orthogonal optical (LO) and transverse optical (TO) splitting of the ν_2 bending mode, at 401 and 394 cm^{-1} respectively, and of the ν_3 stretching mode of CS_2, at 1528 and 1495 cm^{-1} respectively[30].

Clearly the study of the adsorption and desorption properties of pure CS_2 and CS_2-bearing ices is of importance in order to better understand the properties of interstellar ices in cometary nuclei. Using TPD, the structure and desorption behaviour of CS_2 ices can be studied and kinetic information can be derived by rigorous quantitative analysis. RAIR spectra can also be used to probe the structure of CS_2 ices as well as the interaction of CS_2 with H_2O. Understanding the adsorption and desorption of pure ices is of great importance in understanding and characterising the adsorption and desorption of CS_2 from more complex systems, such as CS_2 on a H_2O surface. Investigating the interactions of CS_2 in layered ices is also relevant to understanding the characteristics of CS_2:H_2O mixed ices. Binary layered ices of CS_2 on H_2O and reverse layers of H_2O on CS_2 have been studied, in order to investigate the

diffusion and trapping characteristics of CS_2 in a H_2O matrix. Mixtures of CS_2 and H_2O have also been investigated, as these provide the most realistic analogy to cometary ices. This is the first detailed study of the adsorption and desorption of CS_2-bearing ices adsorbed on a model dust grain surface.

5.2. Experimental

The experimental apparatus has been described in detail in chapter 2. CS_2 (Sigma Aldrich, puriss. p.a., ≥99.9%) and H_2O (distilled, deionised) were used in these experiments, purified via repeated freeze-pump-thaw cycles. Ices were grown *in situ* by backfilling the chamber through a high precision leak valve. All exposures are measured in Langmuir, where 1 L = 10^{-6} mbar s, and were not corrected for ion gauge sensitivity. RAIR spectra were taken at a resolution of 4 cm^{-1} and are the result of the co-addition of 256 scans. For the warm RAIRS experiments, the sample temperature was raised and held at a predetermined temperature for 3 minutes, prior to recording RAIR spectra at base temperature. TPD spectra of masses 18 and 76, the major mass fragments of H_2O and CS_2 respectively, were recorded simultaneously. All TPD spectra were recorded at a heating rate of 0.48 ± 0.01 K s^{-1}.

5.3. Results and Discussion

RAIR and TPD spectra were recorded for CS_2 bearing ices adsorbed on a HOPG sample at 20 K. CS_2 and H_2O were dosed on to the HOPG sample under four dosing regimes: pure CS_2 adsorbed on bare HOPG; binary layered ices of CS_2 adsorbed on pre-adsorbed H_2O layers; reverse binary layered ices of H_2O adsorbed on pre-adsorbed CS_2 layers; and well defined mixtures of CS_2 and H_2O co-deposited on bare HOPG.

5.3.1. Pure CS_2 Ice

RAIR and TPD spectra were recorded for a range of exposures of CS_2 adsorbed on a bare HOPG sample at 20 K. The study of pure CS_2 ices is of importance to determine whether any adsorbate-substrate interactions are involved in the growth and desorption of the ices. Kinetic data concerning the desorption of pure ices from a bare surface can be derived from TPD spectra of pure ices[34-37].

5.3.1.1. TPD Data

Figures 5.1 and 5.2 show TPD spectra recorded for a range of exposures of pure CS_2 adsorbed on a HOPG surface at 20 K. At the lowest exposure of CS_2, 1 L, a single peak is observed in the TPD spectrum with a peak temperature of 135 K (figure 5.1). Increasing the CS_2 exposure to between 1 and 10 L shows a gradual decrease in peak temperature to 122 K following a 10 L exposure. Further increasing the exposure, to between 10 and 20 L, leads to a constant peak temperature of 122 K. At higher exposures of CS_2, between 20 and 200 L, the peak temperature increases gradually to reach 131 K following a 200 L exposure (figure 5.2). Above an exposure of 20 L, all TPD spectra show a single, asymmetric peak with a common leading edge.

Assignment of the observed peaks in the TPD spectra can be made by comparison with investigations of other adsorbates, physisorbed on a HOPG surface[34-36,38,39]. The TPD spectra can be split into three ranges of low, medium and high CS_2 exposures. At low CS_2 exposures, 1 to 10 L, the observed TPD peak shows a decreasing peak temperature with increasing exposure (figure 5.1). This is characteristic of an increasing number of next neighbour repulsions between CS_2 molecules[40]. As this peak is the first to be seen in the TPD spectra, it can be

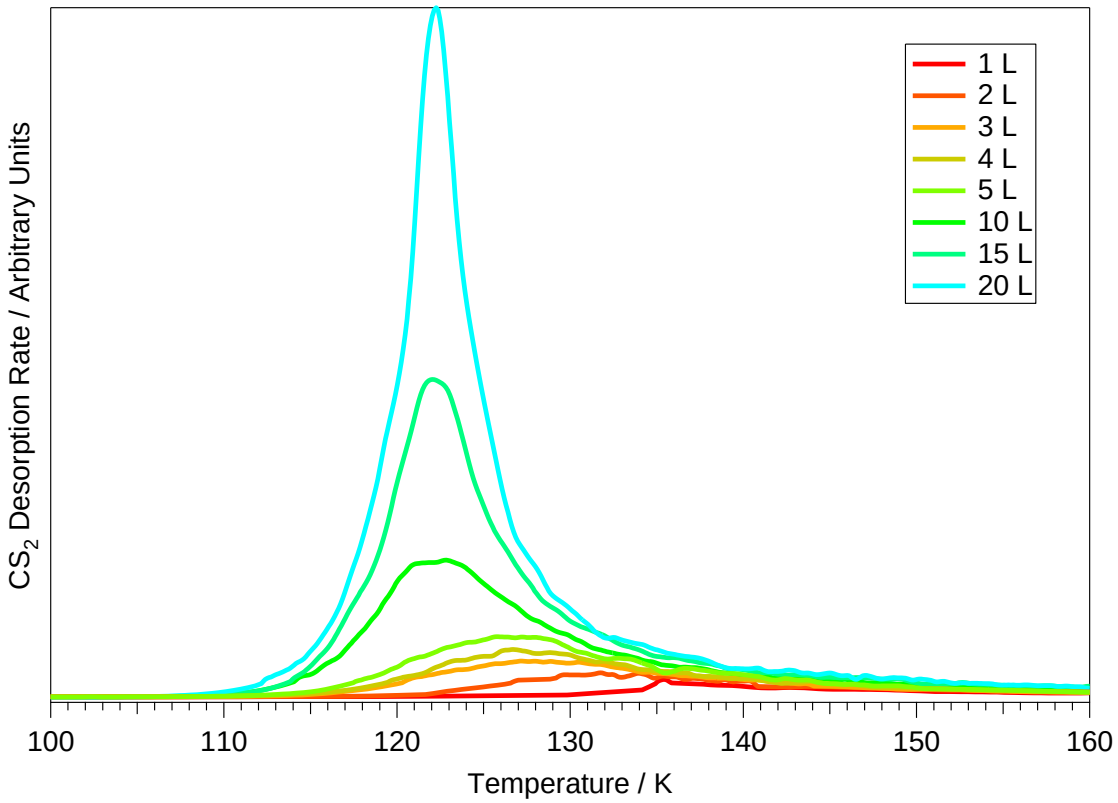

Figure 5.1. TPD spectra of low and medium exposures of CS_2, up to 20 L, desorbing from a bare HOPG surface at 20 K.

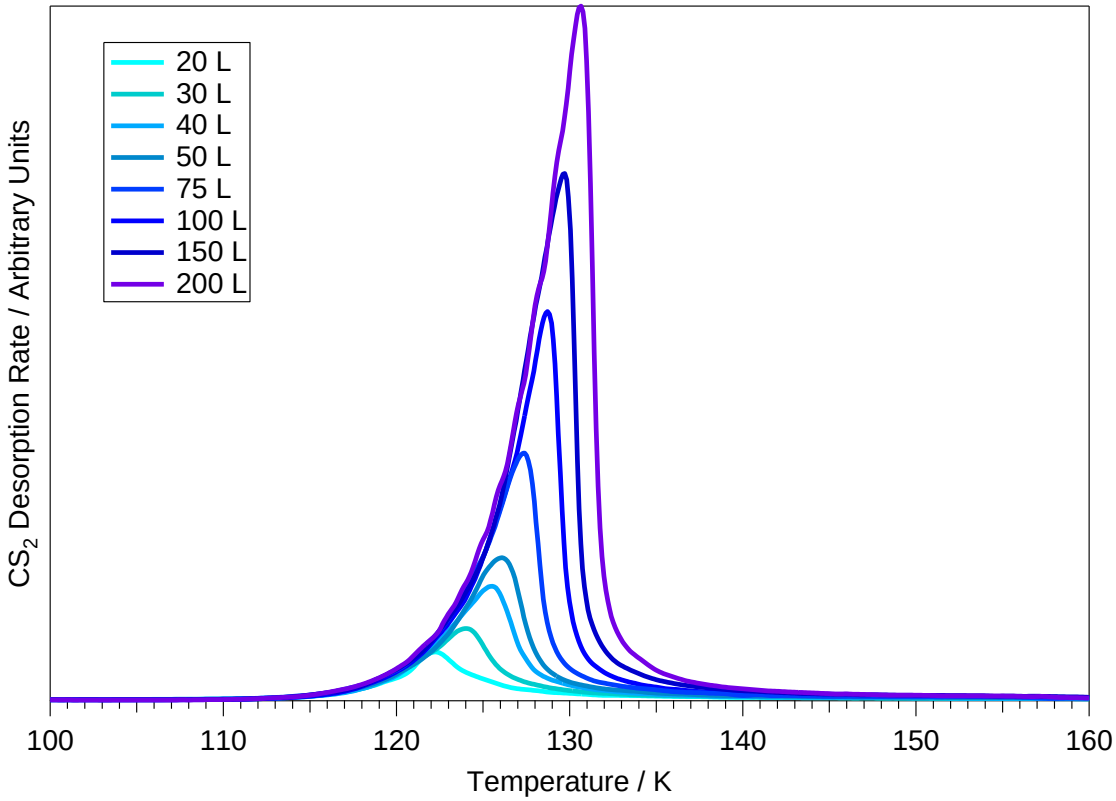

Figure 5.2. TPD spectra of high exposures of CS_2, above 20 L, desorbing from a bare HOPG surface at 20 K.

assigned to the desorption of sub-monolayer CS_2, adsorbed directly on the HOPG surface. A decreasing peak temperature was not seen for CO_2, chapter 4, hence clearly the large size of the CS_2 molecule causes repulsions between the adsorbed species. At medium CS_2 exposures, 10 to 20 L, the observed TPD peak shows a constant peak temperature with increasing exposure (figure 5.1). This behaviour is characteristic of 1st order desorption, and is common for monolayer species[41]. At high CS_2 exposures, 20 to 200 L, the observed peak shows an increasing peak temperature with increasing exposure and a common leading edge on the desorption peak (figure 5.2). This behaviour is characteristic of 0th order desorption, and is common for multilayers[41].

Integration of the area under the TPD spectra shows a linear relationship between CS_2 exposure and peak area, shown in figure 5.3, indicating a constant sticking probability for CS_2 adsorption on the HOPG surface. In addition, the TPD peak area does not saturate, indicating that multilayers of CS_2 are being formed, physisorbed on the HOPG surface at 20 K. The desorption temperature observed (≈120 - 140 K) also suggests that CS_2 is physisorbed on the surface.

Comparing with TPD spectra of pure CO_2 adsorbed on HOPG at 33 K (chapter 4), both monolayer and multilayer growth of physisorbed CO_2 and CS_2 are observed on HOPG below 33 K. However, low exposures of CO_2 do not show a decreasing peak temperature with

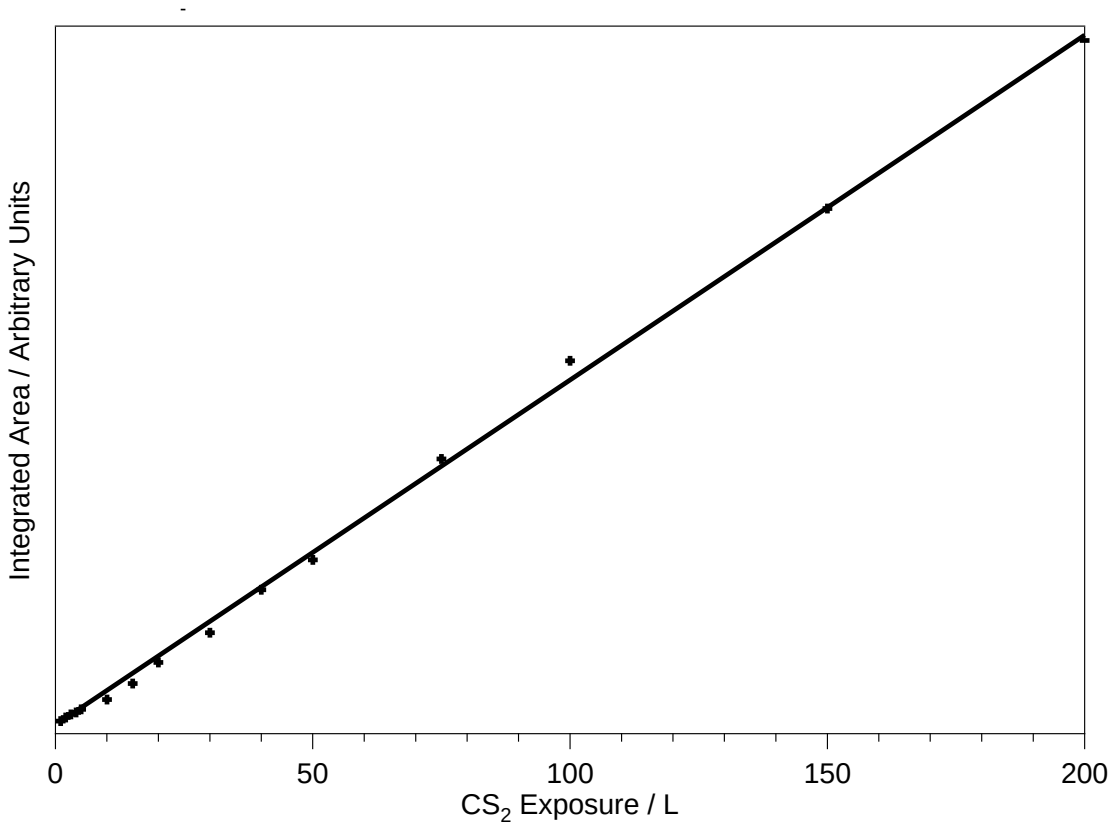

Figure 5.3. Integrated area of the TPD spectra shown in figures 5.1 and 5.2 as a function of CS_2 exposure. The line is supplied as a guide to the eye, and was produced using a linear fit to the data.

increasing exposure, suggesting no lateral interactions between sub-monolayer CO_2. Also of note is the increase in sublimation temperature between CO_2 and CS_2 multilayers, where the onset of desorption of CO_2 occurs around 75 K, as opposed to the onset of desorption of CS_2 occurring around 110 K. This increase in desorption temperature indicates an increase in stability of CS_2 adsorbed on the HOPG surface. As CS_2 is larger than CO_2, it is more readily polarised and, as a result, stronger van der Waals forces will form between the molecules within the ice and between the ice and the surface. This has been previously found for noble gases physisorbed on surfaces[42,43]. Therefore the energy for adsorption, and the related desorption energy, will be greater for CS_2 than for CO_2.

5.3.1.2. RAIRS Data

To confirm the assignments of the TPD spectra, RAIR spectra were collected for a range of exposures of CS_2 adsorbed on a bare HOPG surface at 20 K. These are shown in figure 5.4. Infrared bands are only observed in the wavenumber range between 1470 and 1580 cm^{-1}. At the lowest exposure of CS_2, 1 L, a single infrared band is observed at 1520 cm^{-1}. Increasing the CS_2 exposure to between 1 and 5 L shows a gradual increase in the wavenumber of this band

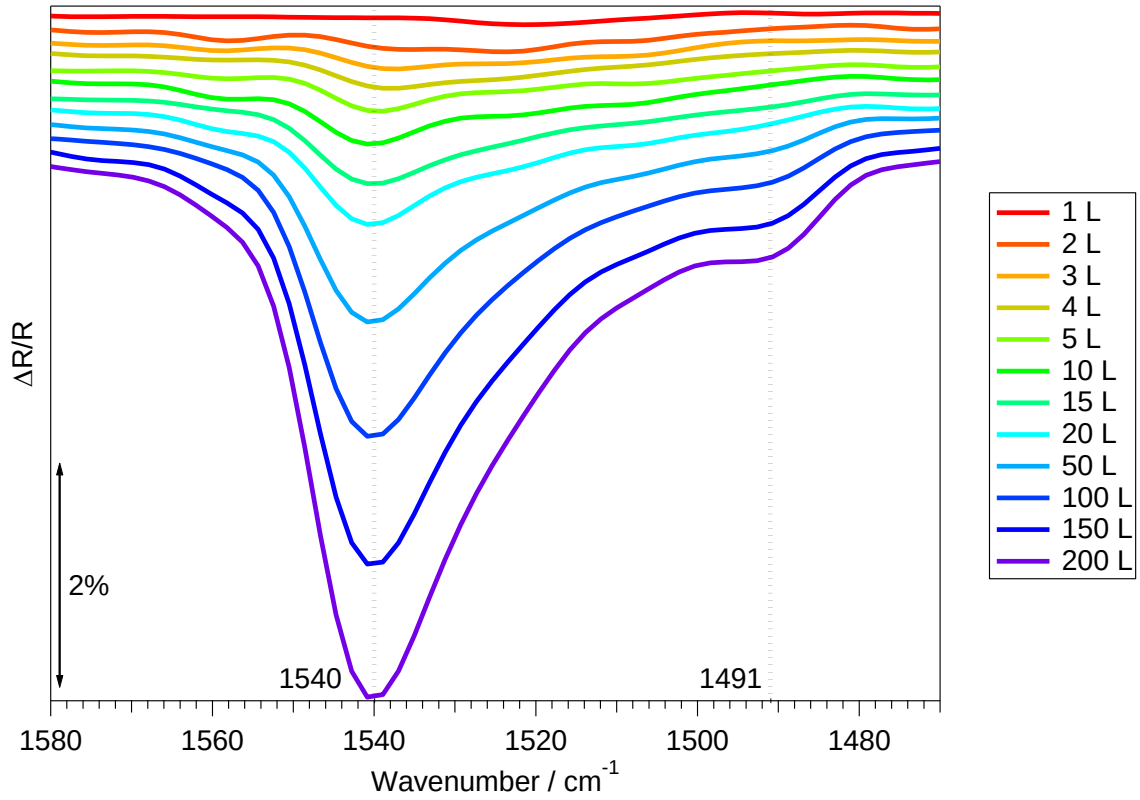

Figure 5.4. RAIR spectra of a range of exposures of CS_2 adsorbed on a bare HOPG surface at 20 K.

to 1539 cm^{-1} after a 5 L exposure. Increasing the exposure of CS_2 to 10 L shows a further increase in the position of the most prominent infrared band to 1540 cm^{-1}. A shoulder on the main infrared band becomes visible, following a CS_2 exposure of 50 L, at 1491 cm^{-1}. Further increase in CS_2 exposure, to 200 L, shows no shift in the infrared bands at 1540 and 1491 cm^{-1}.

The infrared bands at 1540 and 1491 cm^{-1} do not saturate with increasing CS_2 exposure, indicating that physisorbed multilayers of CS_2 are formed on the HOPG surface at 20 K. This is also suggested when comparing the observed infrared frequencies with those observed for the same vibrations in gas phase spectra. The CS_2 ν_3 vibration is observed at 1533 cm^{-1} in gas phase spectra[29], close to the observed band at 1540 cm^{-1} in this work, suggesting only a weak interaction upon adsorption.

Warming the HOPG surface incrementally can provide information about the temperature dependent behaviour of the CS_2 ice adsorbed on HOPG at 20 K. Figure 5.5 shows a 200 L exposure of CS_2 adsorbed on HOPG, warmed to a range of temperatures. Warming the ice to between 20 and 69 K shows no significant change in the observed infrared features. Upon warming the HOPG surface to 78 K, the main infrared band shifts slightly from 1540 to 1543 cm^{-1}, whereas the shoulder at 1491 cm^{-1} greatly increases in intensity and sharpens, to become an independent infrared band. Further warming, to between 78 and 112 K, shows no change in the band at 1543 cm^{-1}, whereas a very subtle shift in the band at 1491 to 1493 cm^{-1}

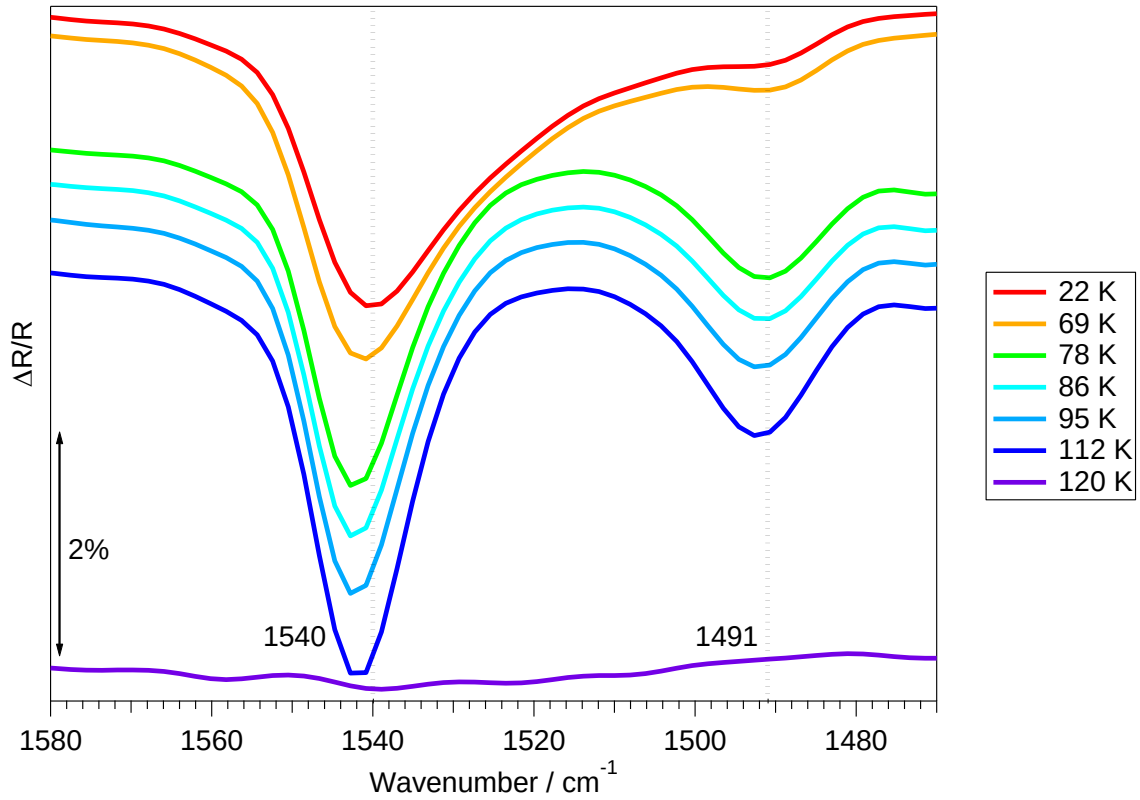

Figure 5.5. RAIR spectra of a 200 L exposure of CS_2 adsorbed on a bare HOPG surface at 20 K warmed to a range of temperatures.

is observed. Warming to 120 K leads to desorption of the CS_2 ice, in agreement with the TPD desorption temperature of ≈120 - 140 K.

Assignment of the observed infrared bands can be made by comparison with previous infrared studies of CS_2 in the gas phase[29] and on a KBr surface at 85 K[30]. Gas phase infrared studies show fundamental CS_2 stretches at 396.8 and 1532.5 cm^{-1}, assigned to the bend, ν_2, and the asymmetric stretch, ν_3, of CS_2 respectively[29]. Surface infrared spectra of crystalline CS_2 on a KBr surface at 85 K show splitting of the observed gas phase bands, with peaks at 1528 and 1495 cm^{-1}, assigned to the LO and TO modes of the ν_3 stretch respectively[30].

Due to the wavenumber range of this RAIRS experiment, the ν_2 bend of CS_2 is not visible in this study. However, comparing the ν_3 stretch of gas phase and surface infrared studies to the infrared bands observed here shows that the bands at 1540 and 1491 cm^{-1} can be assigned to the LO and TO modes of the ν_3 stretch of CS_2 ice respectively. The change in the RAIR spectra between 69 and 78 K is likely caused by a structure change of the CS_2 ice from a disordered or amorphous ice to an ordered or crystalline ice, in agreement with Collings et al[28]. This accounts for the increase in size of the TO mode at 1491 cm^{-1}, whereby the LO - TO splitting becomes more distinct as a direct result of the formation of crystalline ice.

The ν_3 stretch of CS_2 is first observed at 1520 cm^{-1} at low CS_2 coverage, gradually shifting to 1540 cm^{-1} following a 10 L CS_2 exposure. This shift may be caused by the same intermolecular

repulsions as observed in TPD spectra up to CS_2 exposures of 10 L (figure 5.1), or by a structure or orientation change of the CS_2 ice upon formation of a monolayer of CS_2. Hence the observed vibrational band between 1520 and 1540 cm^{-1}, up to CS_2 exposures of 10 L, is assigned to sub-monolayer CS_2. With further comparison to the TPD spectra for CS_2 desorption from HOPG, it can be seen that physisorbed multilayers of CS_2 are formed on the surface. Upon warming, a phase change in the CS_2 ice is observed in the RAIR spectra between 69 and 78 K. This is prior to the onset of desorption and is therefore not observed in the TPD spectra. Both TPD and RAIR spectra show CS_2 desorption occurring between ≈120 – 140 K.

5.3.1.3. Quantitative Analysis of TPD Data

To gain a better understanding of the desorption of CS_2 from a HOPG surface and to provide qualitative information for astrochemical models, analysis of the TPD data has been performed. The methodology used here has been described in detail in chapter 2. Sub-monolayer CS_2 TPD spectra show characteristics indicating intermolecular repulsions, characterised by a decreasing peak temperature with increasing CS_2 exposure. Performing quantitative analysis of these TPD spectra can only provide kinetic data for the combination of repulsion and desorption, where the desorption properties cannot be resolved. Therefore, quantitative analysis to determine the kinetic properties for CS_2 desorption was conducted on TPD spectra of monolayer and multilayer CS_2, following CS_2 exposures of 10 L and above.

Desorption orders. From equation 2.2, the desorption orders for monolayer and multilayer desorption can be determined from the gradient of a plot of $\ln[I(T)]$ against $\ln[\theta_{rel}]$ at a fixed temperature, for a set of TPD spectra with varying initial CS_2 coverages. This method assumes that the desorption energy and pre-exponential factor do not vary with coverage or temperature. This has previously been shown to be a valid assumption for H_2O[34], NH_3[36], CH_3OH[35] and C_2H_5OH[37] ices, as well as for CO_2 ices in chapter 4. Since CS_2 is physisorbed on the HOPG surface, it should also be a valid assumption in this case. Monolayer desorption rates were taken from the TPD spectra for CS_2 exposures of 10 to 20 L, whereas multilayer desorption rates were taken from the TPD spectra for CS_2 exposures of 20 to 200 L. Figure 5.6 (bottom left) shows an order plot for monolayer and multilayer desorption at a fixed temperature of 118 K, constructed from the TPD spectra in figures 5.1 and 5.2 (shown in figure 5.6 top left and right). Using a fixed temperature of 118 K, desorption orders of 0.92 and 0.15 were obtained for monolayer and multilayer CS_2 respectively. Using a range of relevant fixed temperatures, between 113 and 122 K, shown in table 5.1, average desorption orders for monolayer and multilayer CS_2 were found to be 0.88 ± 0.07 and 0.14 ± 0.05 respectively.

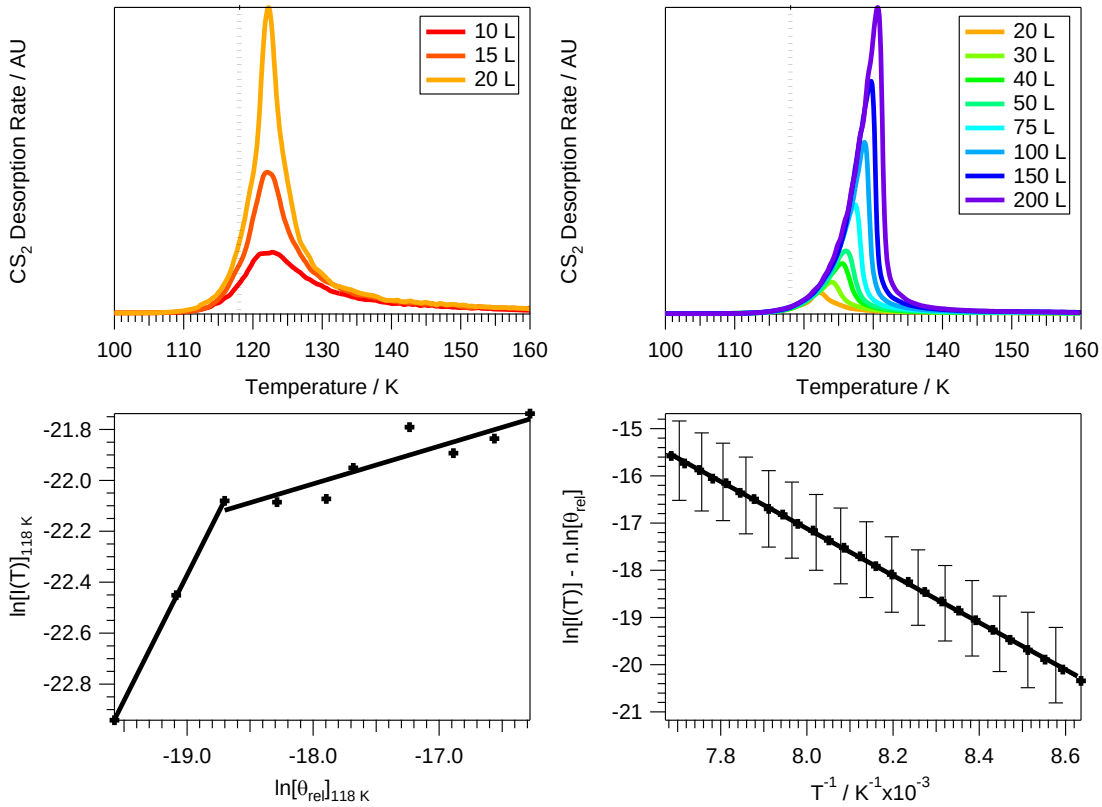

Figure 5.6. (Top left) TPD spectra of monolayer CS_2, taken from figure 5.1, showing CS_2 exposures of 10 to 20 L. (Top right) TPD spectra of multilayer CS_2, taken from figure 5.2, showing CS_2 exposures of 20 to 200 L. Also shown as a dotted line in both figures is the fixed temperature of 118 K. (Bottom left) Plot of ln[I(T)] against $\ln[\theta_{rel}]$ at a fixed temperature of 118 K producing gradients for monolayer and multilayer desorption orders. (Bottom right) Plot of $\ln[I(T)] - n.\ln[\theta_{rel}]$ against 1/T from the TPD spectrum following a 200 L exposure of CS_2, using n as 0.14 ± 0.05. This line has a gradient of $-E_{des}/R$.

Table 5.1. Calculated desorption orders for monolayer and multilayer CS_2 adsorbed on HOPG at 20 K.

Fixed Temperature / K	Monolayer Desorption Order, n	Multilayer Desorption Order, n
113	0.91	
114	0.86	
115	0.83	0.14
116	0.84	0.18
117	0.89	0.16
118	0.92	0.15
119		0.15
120		0.13
121		0.10
122		0.10

Monolayer and multilayer desorption are close to 1st and 0th order respectively. These values are in agreement with the qualitative analysis of the TPD spectra discussed above, and confirm the assignments given. Comparing to monolayer and multilayer desorption orders found for CO_2, 0.73 ± 0.02 and 0 respectively (chapter 4), shows that CS_2 monolayer desorption is closer to the expected 1st order desorption than the CO_2 monolayer is. However, this is

expected as CO_2 TPD spectra show overlap between monolayer and multilayer desorbing species (figure 4.2, chapter 4) reducing the value of, and making analysis difficult for, the CO_2 monolayer. In addition, due to the CO_2 multilayer TPD spectra showing unshared leading edges, the CO_2 multilayer desorption order was assumed to be 0. This is still close to that found for CS_2 multilayer desorption, and is as expected for multilayer desorption. As shown for sub-monolayer CS_2, lateral interactions within an ice also affect its desorption[40]. Therefore the increase in monolayer desorption order between CO_2 and CS_2 monolayers is also caused by increased repulsive intermolecular interactions within the monolayer. This is in agreement with the lack of observation of repulsive interactions in CO_2 sub-monolayers, where the sub-monolayer could not be resolved from monolayer CO_2.

Desorption Energies. It is also possible to determine the desorption energy of CS_2 monolayer and multilayers adsorbed on HOPG, to obtain an indication of the binding strength within the monolayer and multilayers and between the adsorbate and the surface. Using the desorption orders calculated above, the desorption energy of the monolayer and multilayer can be determined via a plot of $\ln[I(T)] - n\ln[\theta_{rel}]$ against 1/T, taking the gradient as $-E_{des}/R$. The error in $\ln[I(T)] - n\ln[\theta_{rel}]$ was taken to be $\Delta n.\ln[\theta_{rel}]$, thus the error in the desorption order contributes to the error in the desorption energy. Again, it is assumed that the pre-exponential factor and desorption energy do not change with coverage and temperature. Figure 5.6 (bottom right) shows a plot to determine the desorption energy for a 200 L exposure of CS_2, using a value of n of 0.14 ± 0.05. The gradient of the plot gives a desorption energy of 41.4 ± 2.1 kJ mol^{-1}. Average desorption energies for monolayer CS_2 were determined from TPD spectra of CS_2 for exposures of 10 to 20 L, whereas average desorption energies for multilayer CS_2 were calculated from TPD spectra for CS_2 exposures of 20 to 200 L, shown in table 5.2. Average desorption energies were found to be 45.3 ± 6.2 and 44.1 ± 6.0 kJ mol^{-1} for monolayer and multilayer CS_2 respectively.

Table 5.2. Calculated desorption energies for monolayer and multilayer CS_2 adsorbed on HOPG at 20 K.

CS_2 Exposure / L	Monolayer Desorption Energy, E_{des} / kJ mol^{-1}	Multilayer Desorption Energy, E_{des} / kJ mol^{-1}
10	43.8 ± 3.5	
15	45.5 ± 3.6	
20	46.5 ± 3.7	44.6 ± 5.8
30		44.7 ± 7.5
40		49.0 ± 3.1
50		44.7 ± 2.4
75		42.5 ± 2.6
100		44.6 ± 2.2
150		42.3 ± 2.2
200		41.4 ± 2.1

The monolayer and multilayer desorption energies calculated here are comparable to the desorption energies of other physisorbed species[34-37,41]. They are also similar to each other, which is reasonable as the monolayer and multilayer desorb at very similar temperatures. Comparing to the multilayer desorption energy found for CO_2, 24.8 ± 1.6 kJ.mol^{-1} (chapter 4), a substantial increase is observed for CS_2 desorption. This reflects the observed behaviour in the TPD spectra, whereby the onset of desorption and peak temperatures observed in CS_2 TPD spectra were higher than those for the CO_2 ices. As discussed previously, this effect is caused by stronger van der Waals forces caused by the higher polarisability of the CS_2[42,43].

Pre-exponential factors. The pre-exponential factor for desorption can also be determined from the TPD spectra. To determine the pre-exponential factor for the desorption process, the absolute coverage of CS_2 adsorbed on HOPG must be determined. This can be determined by calculating the rate of impingement of CS_2 molecules on the HOPG surface. Using the methodology described in chapter 2, the rate of impinging CS_2 molecules on the HOPG surface, as a function of CS_2 exposure, is 3.49×10^{14} molec L^{-1}. However, due to the 10 mm diameter aperture on the quadrupole mass spectrometer (QMS), only 39% of the molecules on the HOPG surface will be detected in the TPD experiment. Therefore the number of molecules which will pass through the QMS aperture as a function of CS_2 exposure will be 1.37×10^{14} molec L^{-1}. This number can then be used to convert the relative coverage, previously determined as the area under each TPD spectrum, to actual coverage by scaling using the relationship between the integrated TPD peak area and actual CS_2 exposure. From figure 5.3 the area under each TPD spectrum, in arbitrary units, and as a function of CS_2 exposure, produced a linear fit with a gradient of 4.33×10^{-10} L^{-1}. This gives a scaling factor for the surface coverage conversion of 3.16×10^{23} molec.

To determine the pre-exponential factor, the Polanyi-Wigner equation can be rearranged as shown in chapter 2, to give an expression for ν_n. The error in ν_n was taken as $\nu_n\sqrt{(\Delta n^2 + \Delta E_{des}{}^2)}$. Average pre-exponential factors for monolayer CS_2 were determined from TPD spectra for CS_2 exposures of 10 to 20 L, whereas average pre-exponential factors for multilayer CS_2 were calculated from TPD spectra for CS_2 exposures of 20 to 200 L. The results are shown in table 5.3. Average pre-exponential factors were thus calculated to be $3.39 \times 10^{21 \pm 1.4}$ (molec m^{-2})$^{0.12}$ s^{-1} and $1.60 \times 10^{31 \pm 1.5}$ (molec m^{-2})$^{0.86}$ s^{-1} for monolayer and multilayer CS_2 respectively, where the units are given as (molec m^{-2})$^{1-n}$ s^{-1}.

Table 5.3. Calculated pre-exponential factors for monolayer and multilayer CS_2 adsorbed on HOPG at 20 K.

CS_2 Exposure / L	Monolayer Pre-Exponential Factor, ν_n / (molec m^{-2})$^{0.12}$ s^{-1}	Multilayer Pre-Exponential Factor, ν_n / (molec m^{-2})$^{0.86}$ s^{-1}
10	$3.01 \times 10^{21 \pm 1.2}$	
15	$3.26 \times 10^{21 \pm 1.1}$	
20	$3.91 \times 10^{21 \pm 1.1}$	$1.80 \times 10^{31 \pm 1.0}$
30		$1.75 \times 10^{31 \pm 1.0}$
40		$1.59 \times 10^{31 \pm 1.0}$
50		$1.67 \times 10^{31 \pm 1.0}$
75		$1.78 \times 10^{31 \pm 1.1}$
100		$1.51 \times 10^{31 \pm 1.0}$
150		$1.60 \times 10^{31 \pm 1.1}$
200		$1.13 \times 10^{31 \pm 1.2}$

Pre-exponential factors for multilayer desorption of a range of physisorbed adsorbates[34-38,41] have been found to range from 8×10^{25} molec m^{-2} s^{-1} for NH_3[36] to 2×10^{37} molec m^{-2} s^{-1} for C_2H_5OH[37]. This is in agreement with the value determined for CS_2 multilayers and with that found for multilayer CO_2 desorption (chapter 4). Variations in the pre-exponential factor of multilayers are thought to be caused by variations in the size of the adsorbed molecule[44], which is also in agreement with the trend observed between CO_2 and CS_2. The vales for the multilayer pre-exponential factor as a function of CS_2 exposure (table 5.3) show very little variation with increasing CS_2 coverage. This backs up the assumption made previously for analysis of the desorption order and energy, where the pre-exponential factor was assumed to remain constant with increasing CS_2 coverage. Pre-exponential factors for a 1st order desorption process are often taken to be $1 \times 10^{12 - 13}$ s^{-1},[45-47] the vibrational frequency of a molecule on a surface. However the CS_2 monolayer pre-exponential factor found here is not within the range of the expected values. This is likely caused by the small number of TPD spectra available which show monolayer desorption, hindering accurate analysis of the monolayer, and may also be affected by the sub-monolayer repulsions observed for low CS_2 coverage.

Comparing the kinetic parameters for CS_2 desorption determined here, summarised in table 5.4, with those found for CO_2 desorption (chapter 4), shows agreement between the monolayer and multilayer desorption orders as well as multilayer pre-exponential factors for CO_2 and CS_2 ices. This is expected, as desorption orders and pre-exponential factors are dominated heavily by the population of molecules within an ice, and therefore reflect the characteristics of monolayer and multilayer desorption of CO_2 and CS_2. The desorption energies found for CO_2 and CS_2 ices show significant variation, as discussed previously, a reflection of the increased desorption temperature of the CS_2 ices from HOPG.

Table 5.4. Average kinetic parameters for monolayer and multilayer CS_2 desorbing from a bare HOPG surface at 20 K.

CS_2 ice	n	E_{des} / kJ mol^{-1}	ν_n / (molec m^{-2})$^{1-n}$ s^{-1}
Monolayer	0.88 ± 0.07	45.3 ± 6.2	$3.39 \times 10^{21 \pm 1.4}$
Multilayer	0.14 ± 0.05	44.1 ± 6.0	$1.60 \times 10^{31 \pm 1.5}$

5.3.1.4. TPD Simulation

TPD simulations have also been conducted using the data obtained from quantitative analysis of experimental TPD spectra to test the quantitative analysis method and check the kinetic parameters found for CS_2 desorption. This was achieved using the Chemical Kinetics Simulator (Version 1.0, IBM Almaden Research Centre, 1995), a stochastic integration package. By assuming an initial state where an ideal ice is already deposited on the surface, simple TPD simulations of the ice can be achieved by describing the desorption process by two reactions. First the adsorbed molecules desorb from the surface to become gas phase molecules, as described by the temperature dependent reaction 5.1.

$$CS_{2a} \rightarrow CS_{2g} \qquad (5.1)$$

For the simulation to work, this step could include, but does not require, a second reaction product describing the free surface adsorption site created by desorption of a molecule of CS_2.

Secondly, to reproduce the experimental TPD spectra, the constant pumping of the gas phase CS_2 also needs to be simulated, as described by the temperature independent reaction 5.2.

$$CS_{2g} \rightarrow CS_{2p} \qquad (5.2)$$

Using the kinetic parameters found from quantitative analysis of experimental TPD spectra of CS_2 as the starting conditions for reaction 5.1, and using an experimental heating rate of 0.5 K s^{-1}, experimental TPD spectra can be reproduced by plotting the gas phase concentration of CS_2 as a function of temperature. Multilayer TPD spectra were simulated using an initial surface concentration of 3.49×10^{16} molec cm^{-2}, the expected surface concentration for a 200 L exposure of CS_2 calculated from the rate of impingement, assuming a sticking probability of 1. Figure 5.7 shows simulated TPD spectra using n = 0.14 ± 0.05, E_{des} = 44.1 ± 6.0 kJ mol^{-1} and $\nu_n = 1.57 \times 10^{31 \pm 1.5}$ (molec m^{-2})$^{0.86}$ s^{-1}. Varying the value of desorption order within error range, holding the desorption energy and pre-exponential factor constant at the average values (figure 5.7 top) shows the least variation in the peak temperature of the simulated TPD

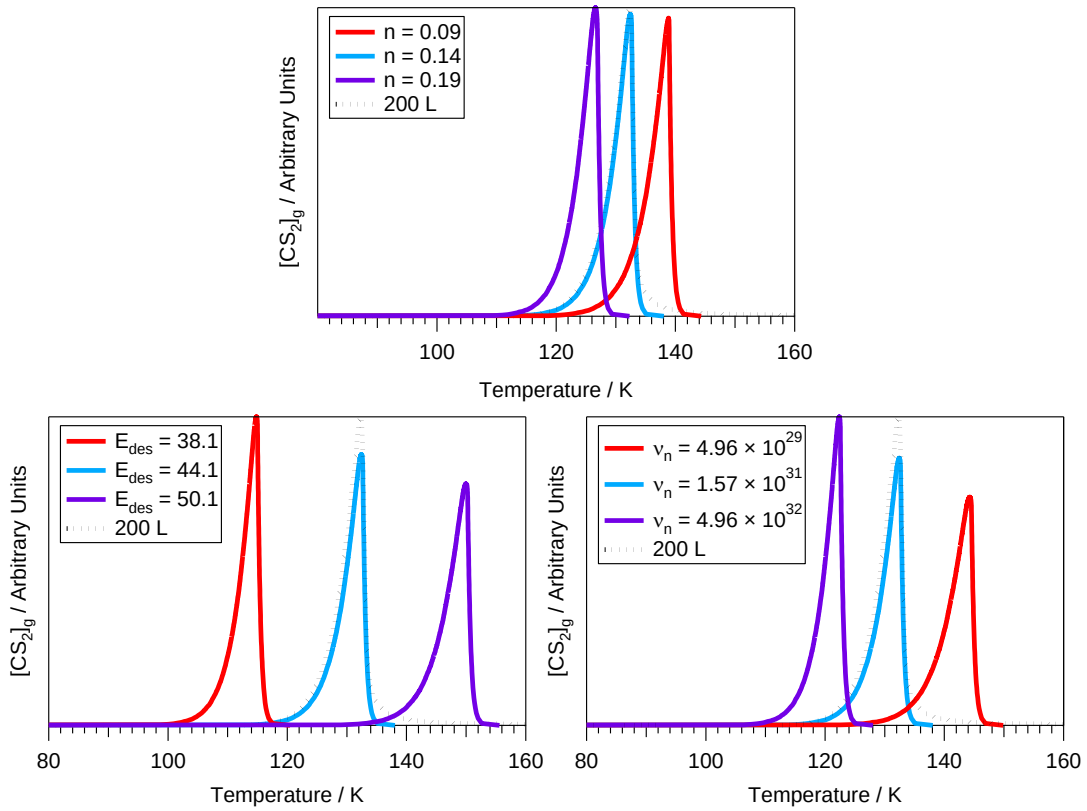

Figure 5.7. Simulated TPD spectra of multilayer CS_2 ice using kinetic parameters derived from qualitative analysis of experimental TPD spectra, n = 0.14 ± 0.05, E_{des} = 44.1 ± 6.0 kJ mol^{-1} and ν_n = 1.57 × $10^{31 \pm 1.5}$ (molec m^{-2})$^{0.86}$ s^{-1}. (Top) Systematic variation of n by Δn with constant E_{des} and ν_n. (Bottom left) Systematic variation of E_{des} by ΔE_{des} with constant n and ν_n. (Bottom right) Systematic variation of ν_n by $\Delta\nu_n$ with constant n and E_{des}. Also shown as a dotted line in all figures is the experimental TPD spectrum following a 200 L exposure of CS_2 from figure 5.2.

spectra. Conversely, varying the value of desorption energy within the error range, holding the desorption order and pre-exponential factor constant at the average values (figure 5.7 bottom left) shows the most variation in the peak temperature of the simulated TPD spectra. Also shown in all plots in figure 5.7 is the experimental TPD spectrum for a 200 L exposure of CS_2, taken from figure 5.2. This shows very close agreement with the simulated TPD spectra using the average values for n, E_{des} and ν_n. Clearly the experimental TPD spectrum is well within the range of the errors found in quantitative analysis. This indicates that the method for quantitative analysis is accurate and reliable.

5.3.2. CS_2/H_2O Ice Layers

The study of binary layered ices of CS_2 adsorbed on H_2O and reverse layered ices of H_2O adsorbed on CS_2 is important to understand the effect of H_2O on the adsorption and desorption of CS_2. There is evidence that H_2O rich ices undergo segregation upon warming[48] and so the study of binary and reverse layered ices, not just mixed ices, is of direct relevance

to astrochemistry. It is also necessary to characterise CS_2/H_2O binary and reverse ices in order to better understand more complex systems, such as CS_2:H_2O mixtures. RAIR and TPD spectra were obtained for CS_2 adsorbed on a 100 L exposure of pre-adsorbed ASW and a 100 L exposure of ASW adsorbed on a range of pre-adsorbed exposures of CS_2 on a HOPG surface at 20 K.

5.3.2.1. TPD Data

Binary Layers. Figures 5.8 and 5.9 show TPD spectra for a range of exposures of CS_2 adsorbed on 100 L of pre-adsorbed H_2O, adsorbed on HOPG at 20 K. At the lowest exposure of CS_2, 2 L, a single peak is observed in the TPD spectrum with a peak temperature of 164 K (figure 5.8). Increasing the exposure of CS_2 to 5 L, a second peak is observed in the TPD spectrum with a peak temperature of 177 K. Neither of these TPD peaks were observed for pure CS_2 ices. Both peaks appear to saturate following a CS_2 exposure between 150 and 200 L (figure 5.9), as shown by the overlap of the high temperature features in the 150 and 200 L TPD spectra. Following a CS_2 exposure of 20 L, a third peak grows in with a peak temperature of 123 K. This peak is very broad, indicating a complex desorption processes. Increasing the CS_2

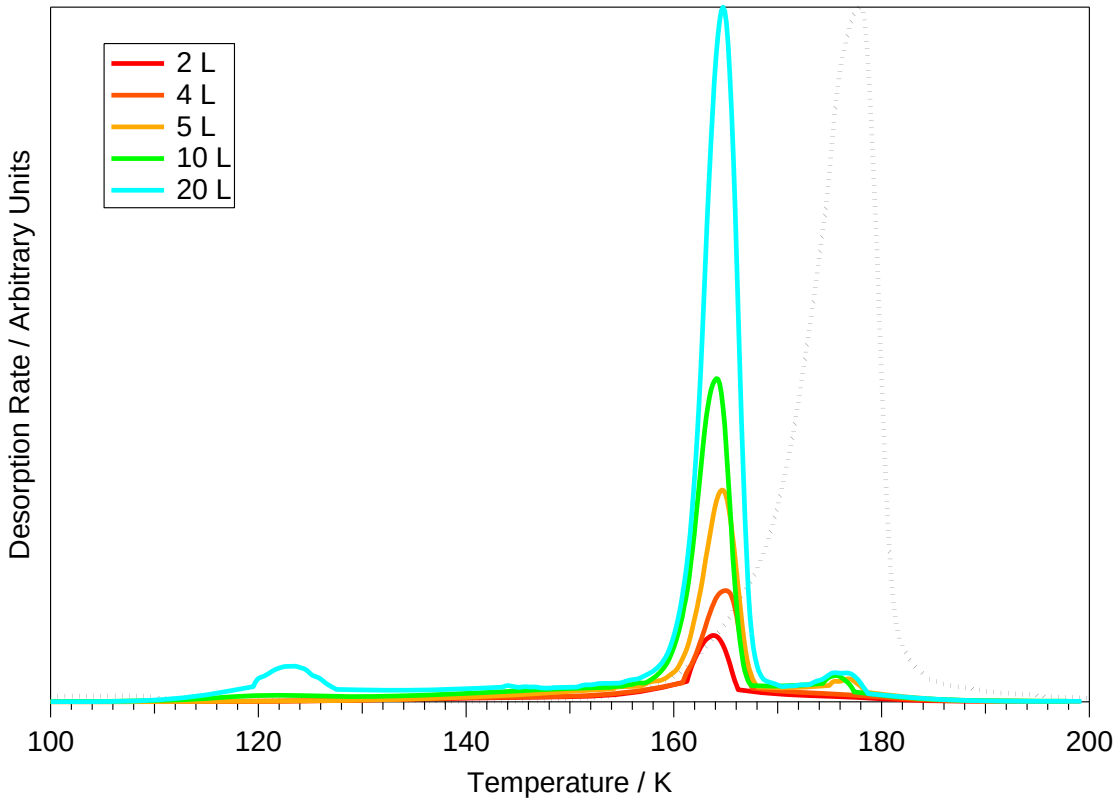

Figure 5.8. TPD spectra of low exposures of CS_2, up to 20 L, adsorbed on 100 L of H_2O on a HOPG surface at 20 K. The H_2O TPD spectrum following a 20 L exposure of CS_2 adsorbed on 100 L of H_2O is shown in black.

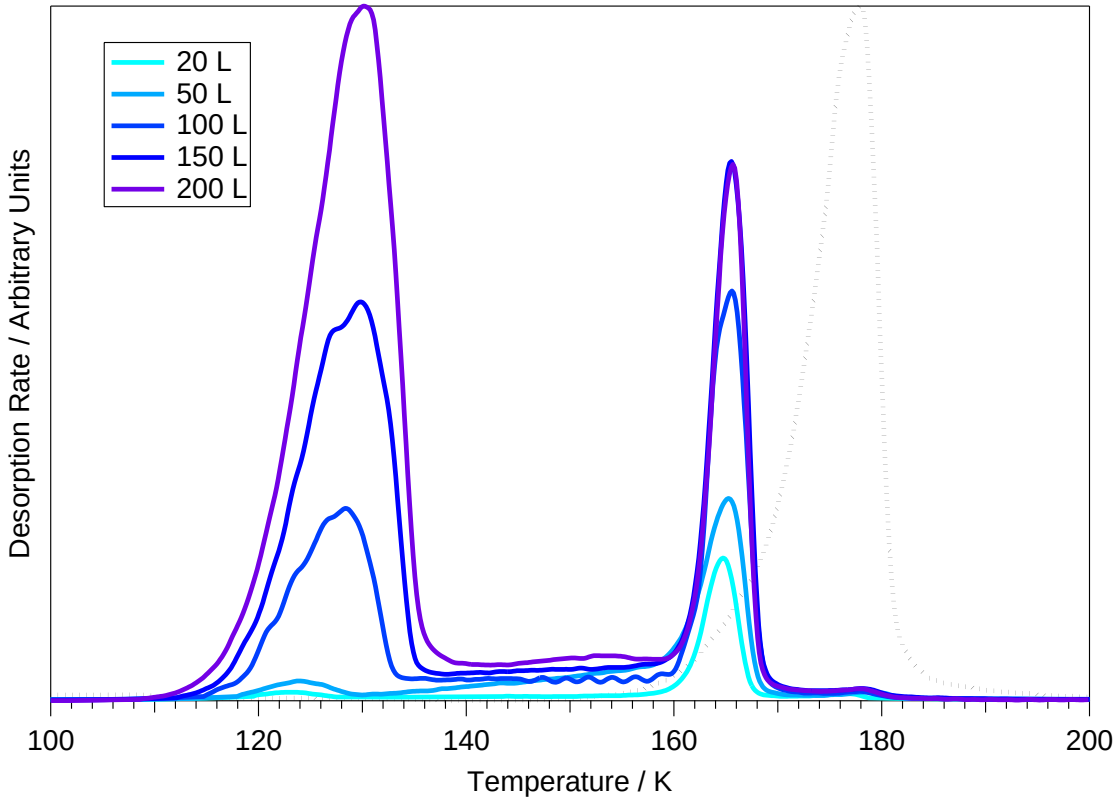

Figure 5.9. TPD spectra of high exposures of CS_2, above 20 L, adsorbed on 100 L of H_2O on a HOPG surface at 20 K. The H_2O TPD spectrum following a 200 L exposure of CS_2 adsorbed on 100 L of H_2O is shown in black.

exposure up to 200 L, shows a gradual increase in the temperature of this peak to 130 K.

Figures 5.8 and 5.9 also show a H_2O TPD spectrum. No changes in the H_2O spectrum are observed with increasing CS_2 exposure. The observed H_2O TPD spectrum shows a large peak, with a temperature of 177 K and a bump on the leading edge of the spectrum at 164 K. The bump at 164 K is assigned to the irreversible phase change of ASW to crystalline ice (CI), caused by a change in the vapour pressure of ASW and CI, and the peak at 177 K is assigned to the desorption of multilayers of physisorbed CI[34].

Integration of the CS_2 TPD spectra from figures 5.8 and 5.9 shows a linear relationship between the total area of the CS_2 signal and the exposure of CS_2, shown in figure 5.10. This indicates a constant sticking probability for CS_2 on ASW at 20 K. The total integrated area of the CS_2 TPD spectra does not saturate, indicating that multilayers of physisorbed CS_2 form on the ASW surface at 20 K. Figure 5.10 also shows the contributions to the total CS_2 area from the low temperature TPD peak, at 123 - 130 K, and the two high temperature peaks at 164 and 177 K. Clearly the high temperature peaks saturate following a CS_2 exposure of approximately 150 L, whereas the low temperature peak does not appear until a CS_2 exposure of between 20 and 50 L. As the H_2O surface dictates the desorption of the high temperature CS_2 TPD features, and the H_2O surface has a finite surface area, the high temperature features saturate. This is

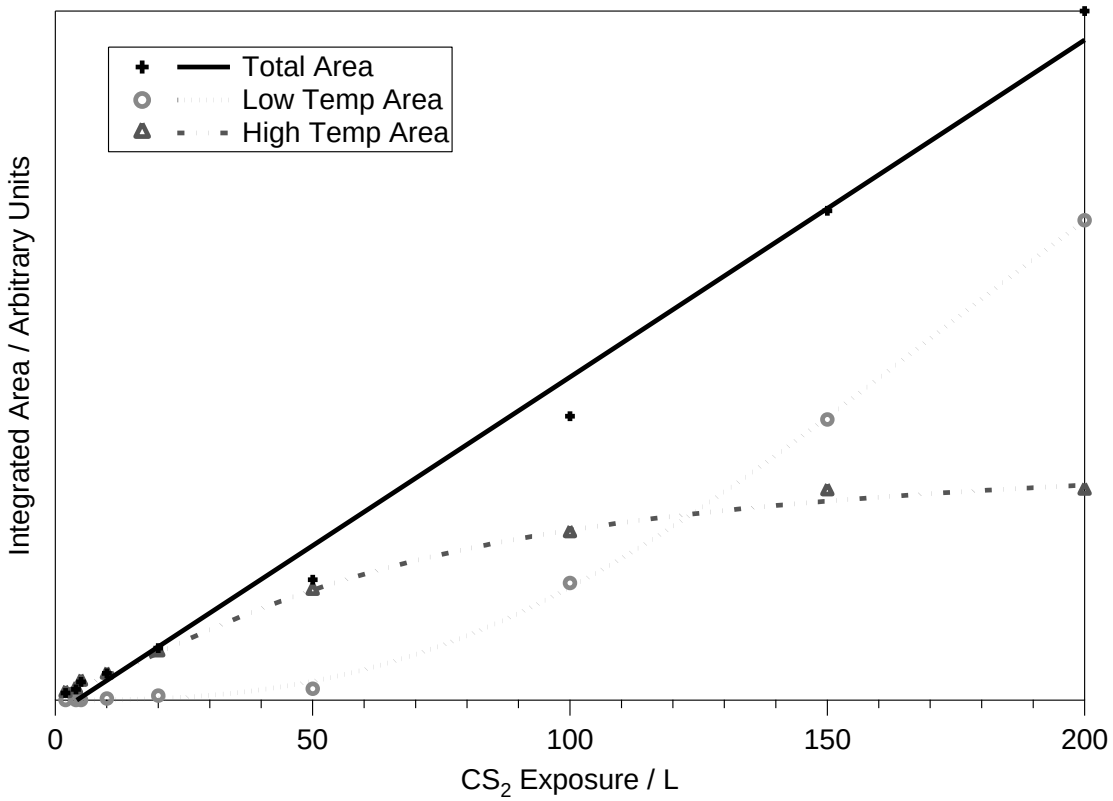

Figure 5.10. Integrated area of the TPD spectra shown in figures 5.8 and 5.9 as a function of exposure of CS_2. Shown are the areas from the low temperature, 123 to 130 K, peaks, the combined areas from the two high temperature peaks at 164 and 177 K, and the total area from all three peaks. Lines are supplied as a guide to the eye.

observed in the TPD spectra following CS_2 exposures of 150 L, as well as in the plot of the integration of the high temperature CS_2 peaks as a function of CS_2 exposure. Once the H_2O surface has become saturated with CS_2, growth of multilayers can begin. The total area of the two high temperature peaks, after saturation, equates to a 44 L exposure of CS_2. This is in contrast to the 8 L exposure of CO_2 shown to be trapped on a saturated ASW surface at 33 K. This is an indication of the diffusion ability of CS_2, whereby CS_2 trapped within pores of the ASW surface cannot diffuse to desorb at its natural sublimation temperature. However CO_2 can diffuse to desorb at its natural sublimation temperature, and hence less CO_2 remains trapped to desorb with the H_2O features. This is a result of the increased size of the CS_2 molecule.

Assignment of the CS_2 desorption features from an ASW surface can be made by comparison with the TPD spectra of pure CS_2 on a HOPG surface (figures 5.1 and 5.2), as well as with previous studies of binary ices of other volatile molecules on H_2O[28,49-51], including CO_2 (chapter 4). The two high temperature CS_2 TPD peaks occur coincidentally with the ASW - CI transition and the desorption of CI respectively. They can therefore be assigned to CS_2 trapped within the porous ASW surface. In particular the feature at 164 K can be assigned to volcano desorption of CS_2, whereas the feature at 177 K can be assigned to co-desorption of CS_2 with the H_2O film. The low temperature peak, 123 – 130 K, can be assigned to multilayer CS_2 on top

of the ASW. The low temperature peak in the TPD spectra of binary layers of CS_2 on ASW is broader than that in the pure CS_2 TPD spectra, reflecting the heterogeneity of the ASW surface, where a range of binding sites for CS_2 adsorption exist.

Quantitative analysis was also conducted for the TPD spectra of CS_2 adsorbed on 100 L of H_2O from figure 5.9. The data obtained are summarised in table 5.5. Multilayer CS_2 was found to desorb from a 100 L film of ASW with an order of 0.67 ± 0.07, desorption energy of 30.4 ± 7.5 kJ mol^{-1} and pre-exponential factor of $9.50 \times 10^{16 \pm 1.7}$ (molec m^{-2})$^{0.33}$ s^{-1}. Compared with the kinetic parameters found for multilayer desorption of CS_2 from a bare HOPG surface at 20 K, desorption occurs with a fractional order rather than 0^{th} order. This is a consequence of the amorphous nature of the ASW surface, with a larger surface area and variety of adsorption sites from which CS_2 will desorb. This inevitably affects the pre-exponential factor, which is sensitive to the value of the desorption order. Therefore as the desorption order is fractional, the pre-exponential factor is found to be in between values expected for 0^{th} and 1^{st} order desorption. As the ASW surface is rough and heterogeneous, desorption of CS_2 occurs from a range of sites, characterised by the broad TPD spectrum. This is also reflected in the desorption energy found for multilayer CS_2 bound to an ASW surface, which is lower than that found for pure CS_2 multilayers.

Table 5.5. Average kinetic parameters for monolayer and multilayer CS_2 desorbing from 100 L of H_2O on HOPG at 20 K.

CS_2-bearing ice	n	E_{des} / kJ mol^{-1}	ν_n / (molec m^{-2})$^{1-n}$ s^{-1}
Pure CS_2	0.14 ± 0.05	44.1 ± 6.0	$1.60 \times 10^{31 \pm 1.5}$
CS_2 on ASW	0.67 ± 0.07	30.4 ± 7.5	$9.50 \times 10^{16 \pm 1.7}$

Reverse Layers. To gain better insight into the trapping and diffusion of CS_2 in and through an ASW film, TPD spectra of reverse layered ices of H_2O adsorbed on CS_2 on a bare HOPG surface at 20 K were collected. Figure 5.11 shows a comparison between TPD spectra for a 100 L exposure of CS_2 adsorbed on 100 L of H_2O and a 100 L exposure of H_2O adsorbed on top of 100 L of CS_2, both adsorbed on HOPG at 20 K. Two desorption features are observed in the TPD spectra of reverse binary ice layers at 166 and 177 K. Assignments can be made by comparison with TPD spectra of binary layered ices of CS_2 on ASW (figures 5.8 and 5.9) as well as with H_2O TPD spectra, and the reverse binary layer studies of H_2O on CO_2 (chapter 4). The features at 166 and 177 K can be assigned to volcano desorption of CS_2 and co-desorption of CS_2 with CI respectively.

Comparing with the TPD spectra of a 100 L exposure of CS_2 on 100 L ASW shows no low temperature peak around 130 K in the reverse layered ice. As diffusion of CS_2 through the H_2O matrix is necessary in order to observe a peak at 130 K in the TPD spectrum of H_2O on CS_2, this

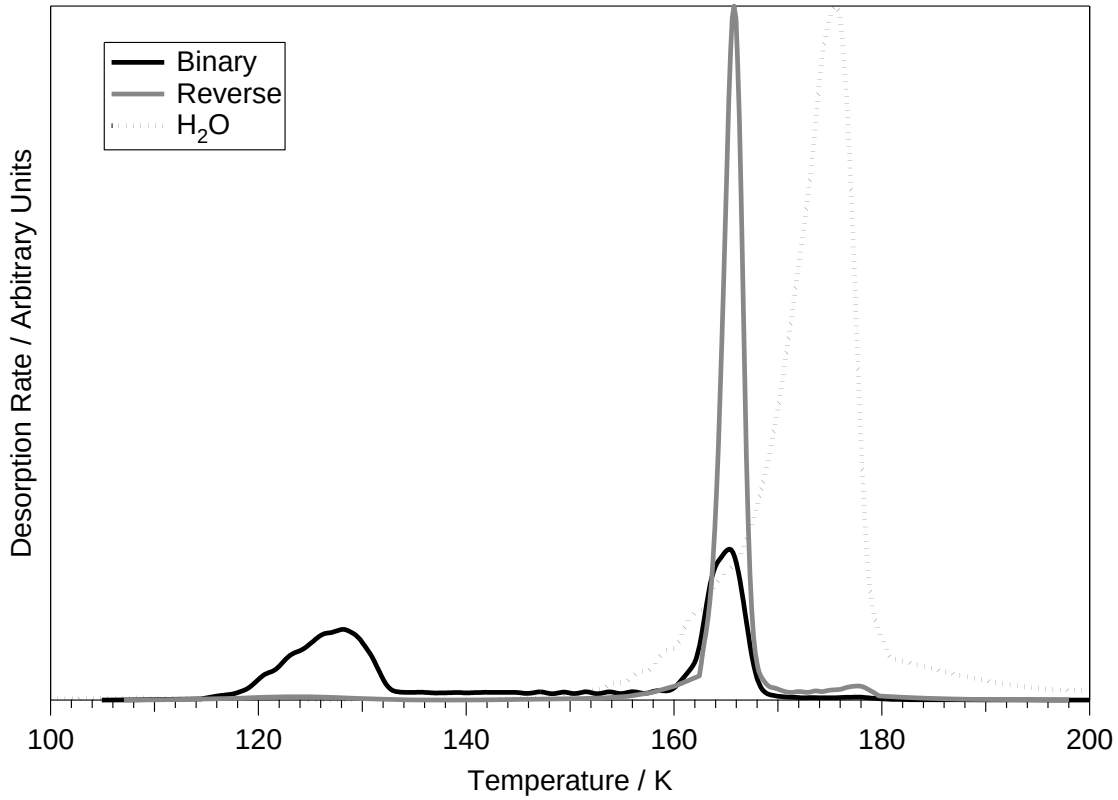

Figure 5.11. TPD spectra of a 100 L exposure of CS_2 adsorbed on a 100 L exposure of H_2O and 100 L exposure of H_2O adsorbed on a 100 L exposure of CS_2, adsorbed on a HOPG surface at 20 K. Shown in black is the H_2O TPD spectra following a 100 L exposure of CS_2 adsorbed on 100 L of H_2O on a HOPG surface at 20 K.

indicates that diffusion of CS_2 through ASW does not occur. Comparing with the diffusion of CO_2 through an ASW ice (chapter 4), whereby ≈40% of the total CO_2 was able to diffuse through the ASW ice, indicates that it is the increase in the size of CS_2 molecule that hinders its ability to diffuse through the ASW ice.

5.3.2.2. RAIRS Data

The characteristics of CS_2 trapping within an ASW film can also be probed by RAIRS, which when compared with TPD spectra can provide further evidence for the assignments made. A range of exposures of CS_2 were adsorbed on 100 L of H_2O on HOPG at 20 K. The RAIR spectrum characteristic of pure ASW, is shown in figure 4.11 (chapter 4). Following a 100 L exposure of H_2O, two infrared bands are observed in the RAIR spectrum. A very broad feature is observed around 3420 cm^{-1} and a smaller, but still broad, peak is observed at 1670 cm^{-1}. These are assigned to the $\nu_{(OH)}$ stretching mode and HOH scissors mode of ASW respectively[34]. No changes are observed in the H_2O vibrational bands following exposure of the H_2O surface to CS_2.

RAIR spectra of a range of exposures of CS_2, adsorbed on 100 L of H_2O on HOPG at 20 K, in the wavenumber range of the CS_2 ν_3 vibration, 1470 to 1580 cm^{-1}, are shown in figure 5.12. At the lowest exposure, 1 L, a single infrared band is observed at 1528 cm^{-1}. Upon further exposure, the band broadens and shifts to 1540 cm^{-1}, following a 100 L exposure of CS_2. The asymmetric shape of the infrared feature suggests that it is composed of more than one peak, however no distinct contributions to the band are easily distinguished. In contrast to the adsorption of CS_2 on the bare HOPG surface (figure 5.4), the TO mode of the ν_3 vibration at 1491 cm^{-1} is not easy distinguishable, however the position of the LO mode at 1540 cm^{-1} is in agreement with that observed for pure CS_2.

Warming the HOPG surface can provide information about the temperature dependent behaviour of the CS_2 ice adsorbed on H_2O, as well as investigating the characteristics of trapped CS_2 in ASW. RAIR spectra following warming of a 100 L exposure of CS_2 adsorbed on 100 L of H_2O are shown in figures 5.13 and 5.14. Warming the HOPG surface to between 20 and 82 K shows a broadening of the observed infrared band, with an associated shift in wavenumber from 1540 to 1528 cm^{-1} (figure 5.13). Between 91 and 109 K two features can be identified in the broad infrared band at 1506 and 1528 cm^{-1}. Warming the HOPG surface further shows a decrease in the size and width of the observed infrared band, with a shift in

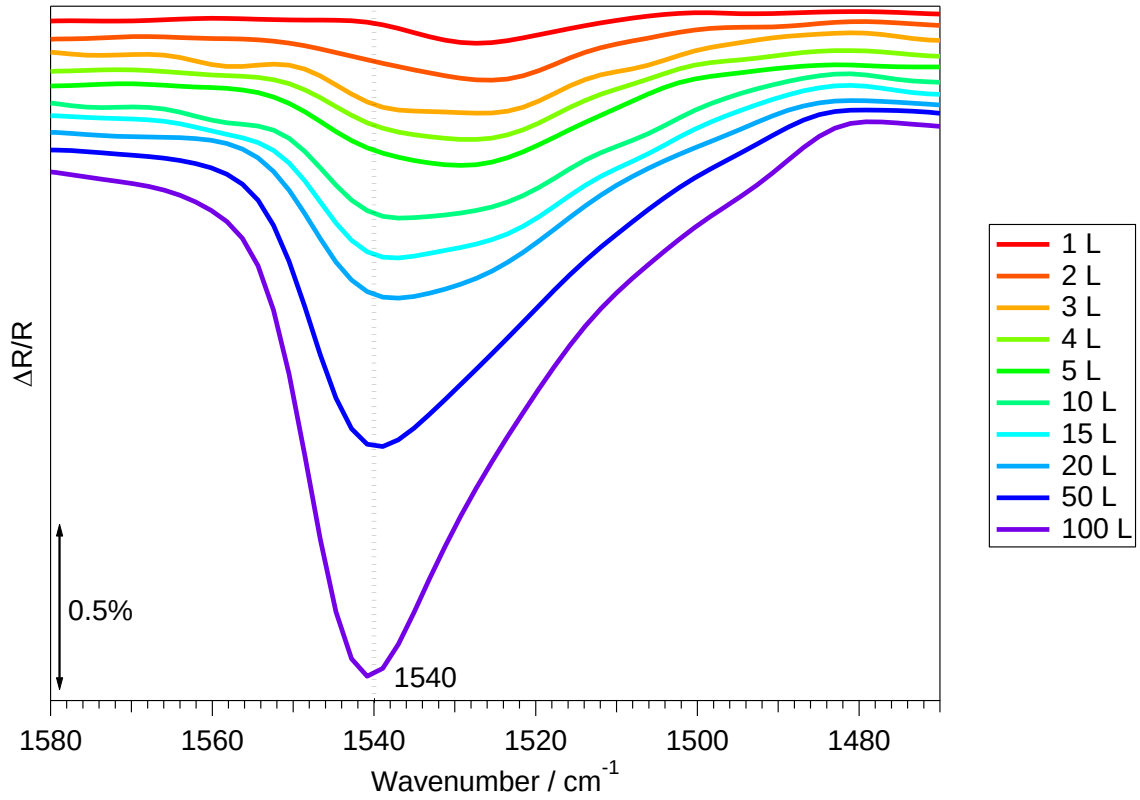

Figure 5.12. RAIR spectra of a range of exposures of CS_2 adsorbed on a 100 L exposure of H_2O adsorbed on a HOPG surface at 20 K.

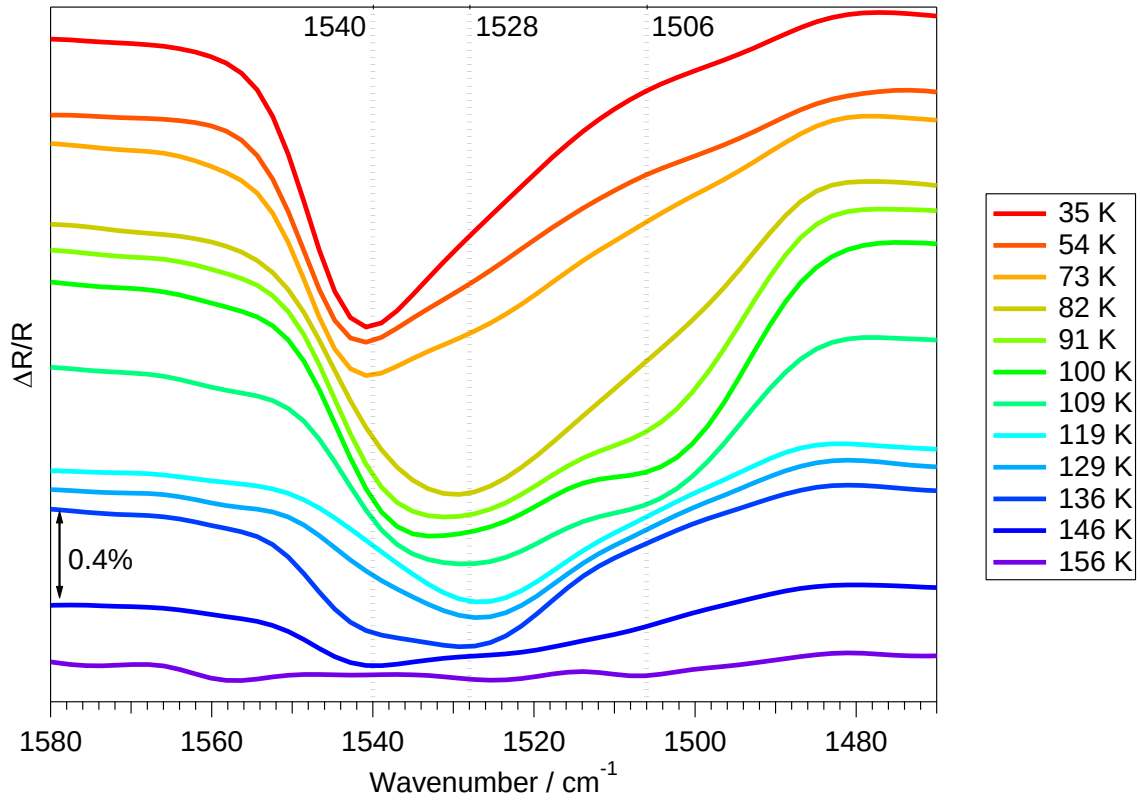

Figure 5.13. RAIR spectra of a 100 L exposure of CS_2 adsorbed on 100 L of H_2O adsorbed on a HOPG surface at 20 K, prior to warming to a range of temperatures.

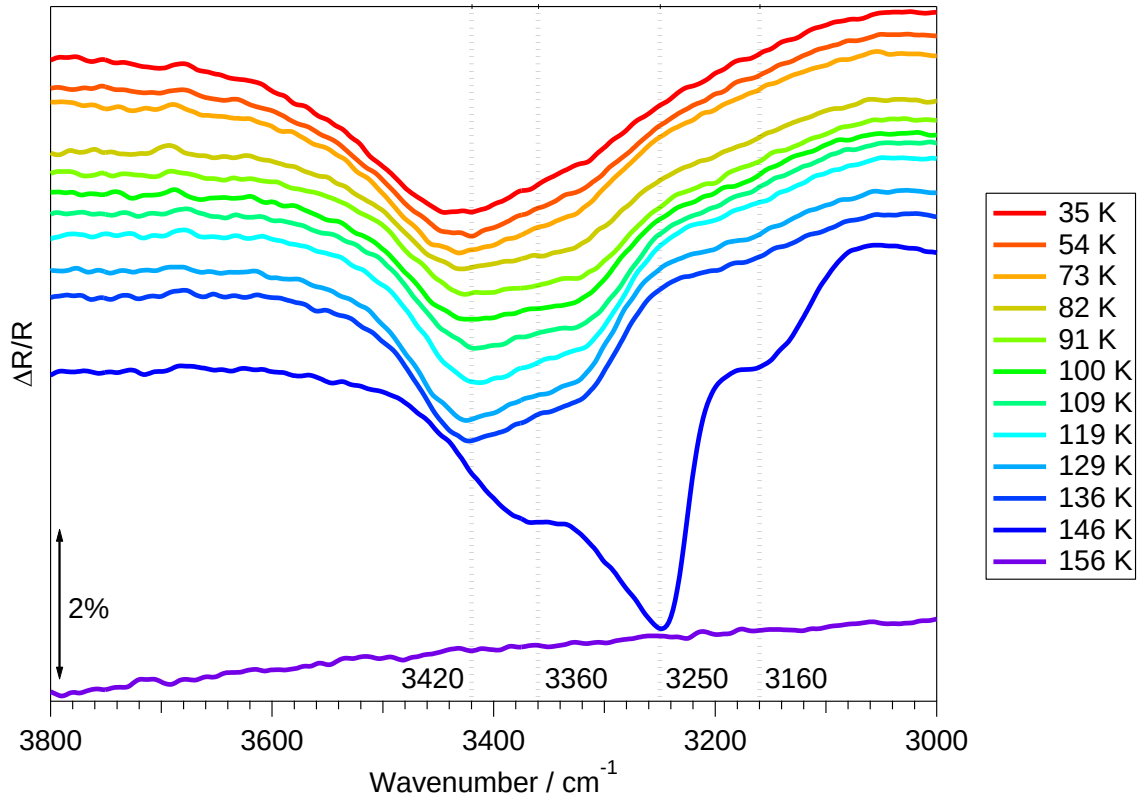

Figure 5.14. RAIR spectra of the $\nu_{(OH)}$ region of 100 L of CS_2 adsorbed on 100 L of H_2O adsorbed on a HOPG surface at 20 K, prior to warming to a range of temperatures.

wavenumber from 1528 cm^{-1} to 1539 cm^{-1} with increasing surface temperature from 119 to 146 K. An increase in size and a splitting of the $\nu_{(OH)}$ stretch of ASW into a three component infrared band with peaks at 3160, 3240 and 3360 cm^{-1} (figure 5.14) is also observed following warming to 146 K. This change in the infrared spectrum of ASW is assigned to the ASW - CI transition[34]. Following warming to 156 K no infrared features are observed, indicating desorption of the CS_2/H_2O ice from the surface. The observed features and trends are very different to those observed in the RAIR spectra of pure CS_2 ice (figures 5.4 and 5.5).

Assignments of the observed infrared bands can be made by comparing with the RAIR spectra of pure CS_2 adsorbed on HOPG at 20 K (figures 5.4 and 5.5). Upon adsorption of low exposures of CS_2 on the ASW surface, a band is first observed at 1528 cm^{-1}, shifting to 1540 cm^{-1} upon increasing CS_2 exposure. This is similar behaviour to that observed in the pure CS_2 spectra on a bare HOPG surface, whereby a band was first observed at 1520 cm^{-1}, shifting to 1540 cm^{-1} with increasing CS_2 exposure. The difference in the bands at 1528 and 1520 cm^{-1} is likely caused by the underlying substrate on which CS_2 is deposited, where the ASW surface has a greater surface area than HOPG, and hence the saturation of the surface by a monolayer requires a greater exposure of CS_2. The band at 1520 cm^{-1} was assigned to CS_2 bound directly to the HOPG surface. Therefore as the band at 1528 cm^{-1} is the first to be observed, it is assigned to CS_2 bound directly to the ASW surface. The shift in the ν_3 vibration at low exposure for pure CS_2 ice was assigned to sub-monolayer CS_2, prior to the formation of a monolayer and then multilayers, which saturates after an exposure of 10 L. This is not the case in binary layered ices, where the band, initially at 1528 cm^{-1}, shifts to 1540 cm^{-1} following a 50 L exposure of CS_2. Comparing the RAIR spectra of a 100 L exposure of CS_2 on a HOPG and ASW surface (figures 5.4 and 5.12) shows agreement in the position of the LO mode of the ν_3 stretch at 1540 cm^{-1}. However, the pure CS_2 spectrum shows a second band at 1491 cm^{-1}, assigned to the TO mode of the ν_3 stretch. Although this is not observed in the binary layered RAIR spectrum of CS_2 on ASW, the LO band at 1540 cm^{-1} does have a long tail towards low wavenumber, which may be composed of a contribution from the TO mode of the vibration. As the observation of the LO vibrational mode in amorphous ice is dependent on a local minimum where $|\varepsilon| \leq 1$ (chapter 3), and both ices are amorphous at 20 K, the differences noted in the observation of the TO mode must be a function of the strength of the dielectric constant in binary layered ice. In other words, and as observed in chapter 3, the LO - TO splitting is more easily observed in RAIR spectra as the minimum in $|\varepsilon|$ approaches 0, as the LO mode of the vibration is less mixed with the TO mode. Therefore, the ASW surface must affect the dielectric properties of the CS_2 adlayer, inhibiting the polarisation of the phonon modes within the ice.

Upon warming, pure CS_2 shows characteristics of an amorphous to crystalline phase transition between 69 and 78 K, prior to desorbing between 112 and 120 K (figure 5.5). However, the RAIR spectrum of binary layers of CS_2 on ASW is complex (figure 5.13). Between 73 and 91 K the CS_2 infrared feature undergoes a shift and splits from 1540 cm^{-1} to form two bands at 1528 and 1506 cm^{-1}. This is not the amorphous to crystalline phase transition of CS_2, as observed in pure CS_2 ices, as no significant shift was observed in the positions of the LO and TO modes of the ν_3 stretch. However, as adsorption of CS_2 on ASW has been shown to affect the LO - TO splitting of the ν_3 stretch, the bands at 1528 and 1506 cm^{-1} can tentatively be assigned to the LO and TO modes of crystalline CS_2 within pores, and on the surface, of ASW. Warming the binary layered ice to between 109 and 119 K shows a significant decrease in the intensity of the CS_2 infrared feature, leaving a small band in the RAIR spectrum at 1528 cm^{-1}. This decrease in intensity is caused by the sublimation of multilayer CS_2 from the ASW surface, in agreement with RAIR (figure 5.5) and TPD spectra (figure 5.2) of CS_2 ice from a HOPG surface, as well as with TPD spectra of CS_2 ice desorbing from an ASW surface (figure 5.9). The remaining infrared band, at 1528 cm^{-1}, must be trapped CS_2 within the pores of the ASW surface. This is in agreement with the position of the H_2O bound CS_2 infrared peak observed in the RAIR spectrum of the lowest exposure of CS_2 on the ASW surface (figure 5.12), and with the trends observed for CO_2 desorption from an ASW surface (chapter 4). Further warming to between 136 and 146 K shows a change in the ν_{OH} vibrational band from an infrared feature characteristic of ASW, to an infrared feature characteristic of CI (figure 5.14), suggesting that the ASW - CI transition has occurred[34]. This is coincident with a further decrease in intensity of the CS_2 ν_3 stretch and a corresponding shift to 1539 cm^{-1}, and is caused by volcano desorption of CS_2 (figure 5.13). This is in agreement with TPD spectra of binary and reverse layered ices of CS_2 and H_2O (figures 5.8, 5.9 and 5.11) and with trends observed for CO_2-bearing H_2O ices (chapter 4). Further warming to between 146 and 156 K shows complete desorption of the CS_2-bearing H_2O ice, indicating co-desorption of CS_2 with CI, also in agreement with TPD spectra of binary and reverse layered ices of CS_2 and H_2O (figures 5.8, 5.9 and 5.11), and with trends observed for CO_2-bearing H_2O ices (chapter 4).

In summary, both RAIR and TPD spectra of layered ices of CS_2 and ASW show features characteristic of the trapping of CS_2 in ASW ice, where the H_2O film dictates the desorption of CS_2 above its natural sublimation temperature. This is in agreement with observations for layered ices of CO_2 and ASW (chapter 4), where volcano and co-desorption of CO_2 with H_2O are observed. Comparison between TPD spectra of binary and reverse layered ices indicates that diffusion of CS_2 through an ASW matrix is not allowed. This is not in agreement with CO_2 layered ices, where diffusion is allowed. Therefore the increased size of CS_2 limits its diffusion through the porous ASW film. The RAIR spectra of CS_2 layered ice also suggest a modification in

the dielectric properties of amorphous and crystalline CS_2 ice, as compared to pure CS_2 ices, which is likely to be seen for CS_2:H_2O mixtures.

5.3.3. CS_2:H_2O Mixtures

RAIR and TPD spectra were obtained for a range of exposures of a 10% mixture of CS_2 and H_2O, co-deposited on a HOPG surface at 20 K. Mixtures of CS_2 and H_2O are the most astrophysically relevant system studied here, providing the most realistic analogy to cometary ices.

5.3.3.1. TPD Data

Figure 5.15 shows the TPD spectrum of a 100 L exposure of a 10% CS_2:H_2O mixture adsorbed on HOPG at 20 K. Three peaks are observed in the CS_2 spectrum, a very low intensity feature at 118 K and two higher temperature peaks at 160 and 171 K. The H_2O TPD spectrum shows a desorption feature at 171 K, with a bump on the leading edge at 164 K, characteristic of the desorption of CI and the ASW - CI transition of H_2O respectively[34].

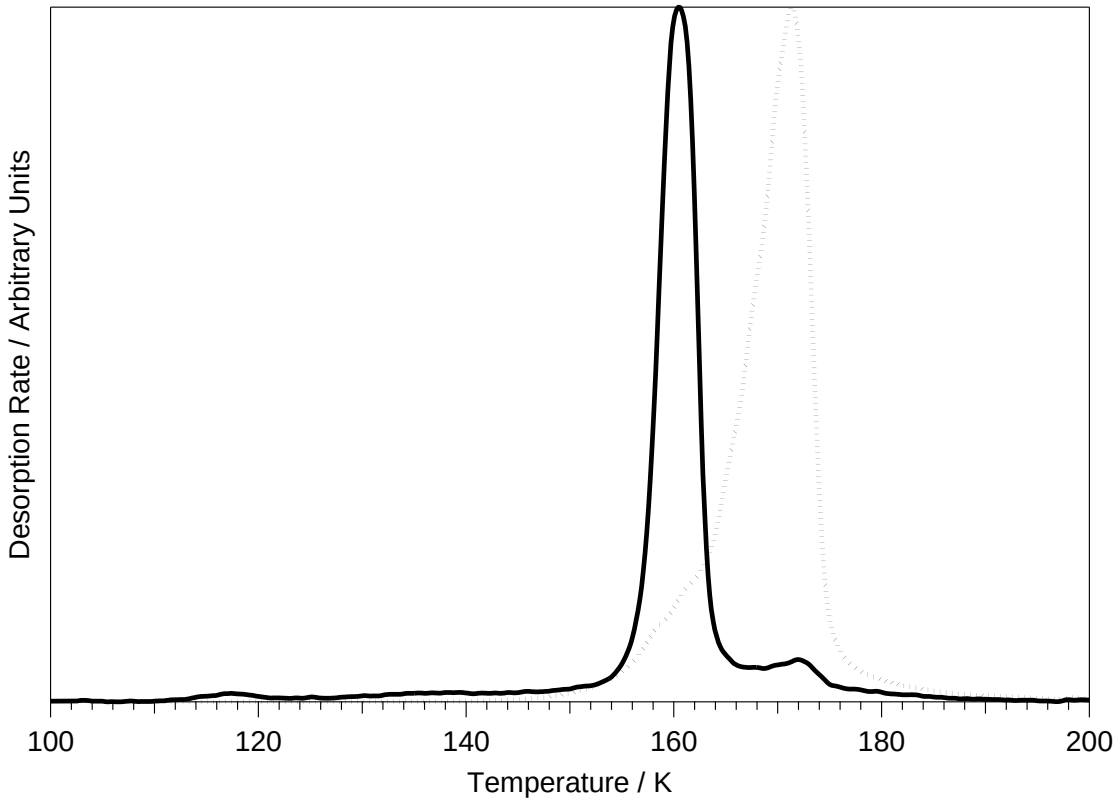

Figure 5.15. TPD spectrum of a 100 L exposure of a 10% CS_2:H_2O mixture adsorbed on a HOPG surface at 20 K. CS_2 and H_2O contributions are shown by solid and dashed lines respectively.

Assignments for the features and behaviour observed can be made by comparing the CS_2:H_2O mixture TPD spectrum with TPD spectra for binary and reversed layers of CS_2 and ASW (figures 5.8, 5.9 and 5.11). The two high temperature CS_2 features at 160 and 171 K are coincident with the ASW - CI transition and desorption of CI respectively, as also observed in binary and reverse TPD spectra of CS_2 and ASW, and CO_2-bearing H_2O ices (chapter 4). Therefore they are assigned to volcano and co-desorption of CS_2 from H_2O ice respectively. The feature observed at 118 K, around the natural sublimation temperature of CS_2, must be desorption of CS_2 from the surface of the CS_2:H_2O mixture. As diffusion of CS_2 through a H_2O matrix is not allowed, as already shown in TPD spectra of reverse layered ices (figure 5.11), this peak cannot be attributed to the diffusion of CS_2. In addition, as the ice is intimately mixed, formation of multilayer CS_2 on the surface of the ice is not possible. Hence the low temperature peak must be caused by loosely bound CS_2 within the ice surface, a reasonable assignment given the small size of the peak. Integration of the CS_2 feature at 118 K shows that < 1% of the total CS_2 desorbs from the ice surface at 118 K.

CO_2:H_2O mixtures (chapter 4) show that 29% of the CO_2 is able to diffuse through the mixed ice, with 71% remaining trapped to desorb with the H_2O features. This is in contrast to CS_2:H_2O mixtures where no diffusion is allowed and < 1% of the CS_2 desorbs near its natural sublimation temperature. This is in agreement with the trends already observed for CO_2 (chapter 4) and CS_2 in binary and reverse layered ices (section 5.3.2).

5.3.3.2. RAIRS Data

Figures 5.16 and 5.17 show RAIR spectra, in the wavenumber range of the CS_2 ν_3 stretch, 1470 to 1580 cm^{-1}, and $\nu_{(OH)}$ stretch region, 3000 - 3800 cm^{-1}, respectively, for a 100 L exposure of a 10% CS_2:H_2O mixture on HOPG at 20 K prior to being warmed to a range of temperatures. Upon adsorption of a 100 L exposure of the 10% CS_2:H_2O mixture, three infrared features are observed in the RAIR spectrum. A very broad feature is observed around 3420 cm^{-1} and a smaller, but still broad, peak is observed at 1670 cm^{-1}, in agreement with the RAIR spectra of a 100 L exposure of pure H_2O (figure 4.11, chapter 4). These are assigned to the $\nu_{(OH)}$ stretching mode and HOH scissors mode of ASW respectively[34]. A CS_2 infrared feature is also observed in the spectrum, at 1525 cm^{-1}, assigned to the ν_3 stretch of H_2O bound CS_2. This is in contrast to the CS_2 infrared features observed in RAIR spectra, at 1540 and 1491 cm^{-1}, for multilayer CS_2 on HOPG (figure 5.4) and at 1540 cm^{-1} for multilayer CS_2 on ASW (figure 5.12). However, the CS_2 infrared feature first observed in binary layered ices of CS_2 on ASW at 1528 cm^{-1}, assigned to H_2O bound CS_2, does resemble the CS_2 infrared features observed in the mixed ices.

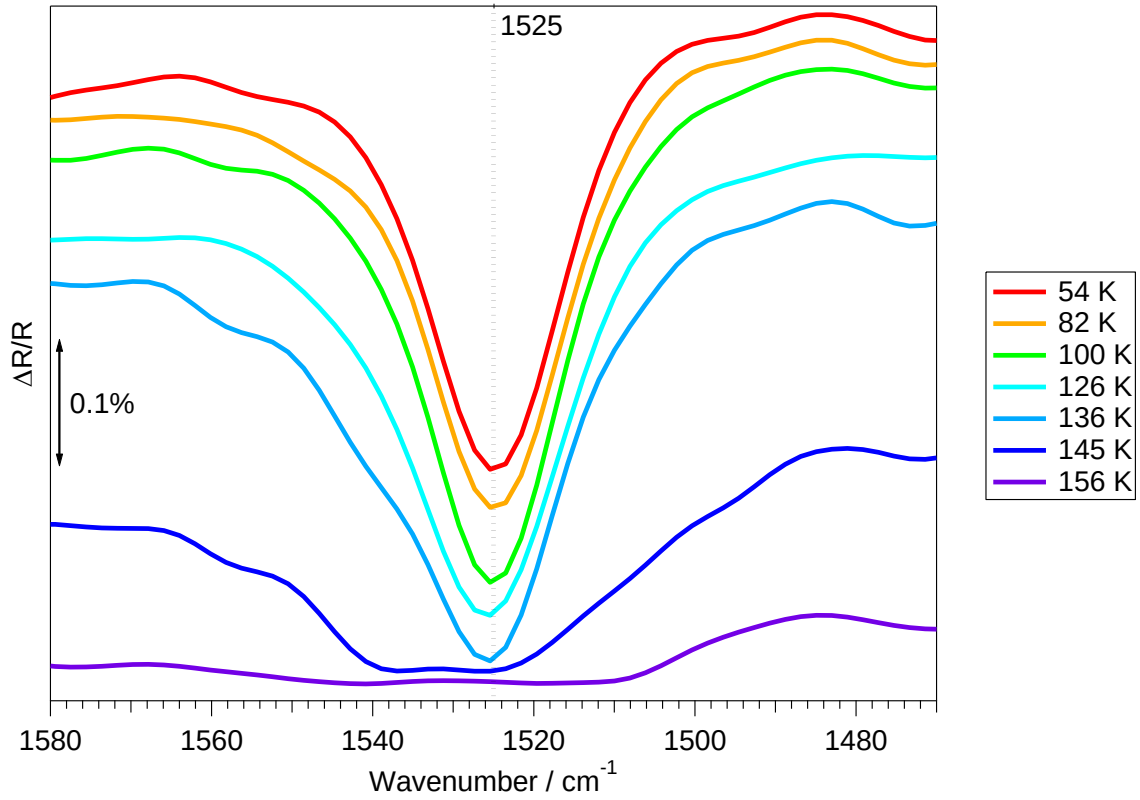

Figure 5.16. RAIR spectra of 100 L of a 10% CS_2:H_2O mixture adsorbed on a HOPG surface at 20 K, prior to warming to a range to temperatures.

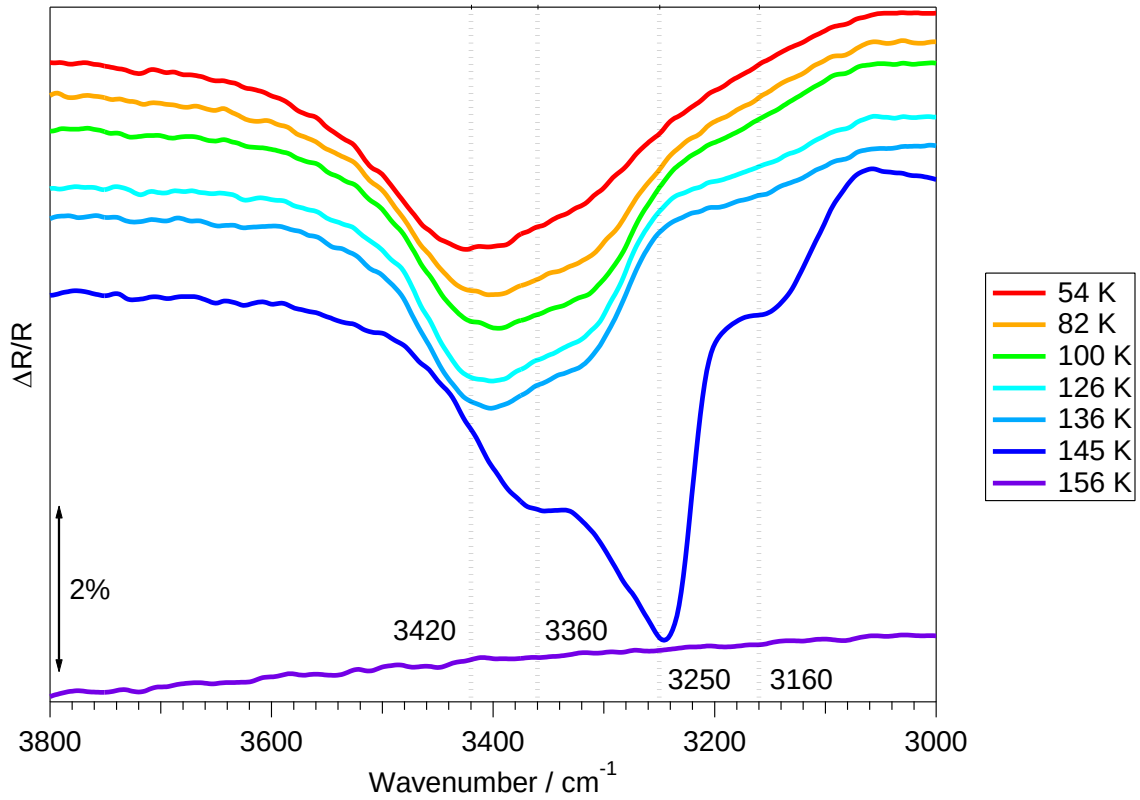

Figure 5.17. RAIR spectra of the $\nu_{(OH)}$ region of 100 L of a 10% CS_2:H_2O mixture adsorbed on a HOPG surface at 20 K, prior to warming to a range of temperatures.

No significant changes to the CS_2 and H_2O infrared features are observed in the RAIR spectra when warming the HOPG surface to between 20 and 126 K. Warming the HOPG surface to 136 K shows a slight broadening of the CS_2 feature at 1525 cm^{-1}, with no associated shift in position (figure 5.16). Further warming of the HOPG surface to 145 K shows a decrease in the intensity and broadening of the observed CS_2 feature, which shows a complex infrared band with components at 1539 and 1525 cm^{-1}. Following warming to 145 K, changes are also observed in the H_2O infrared feature at 3420 cm^{-1} (figure 5.17), indicative of the ASW - CI transition of H_2O. No infrared features are observed in the RAIR spectra when warming the HOPG surface to 156 K, indicating that desorption of the CS_2:H_2O mixture is complete, in agreement with TPD spectra (figure 5.15).

Assignment of the observed infrared features can be made, as well as discussion of the trapping behaviour of CS_2 in a H_2O ice, via comparison with the observed features in the RAIR spectra of binary layered ices of CS_2 and H_2O (figures 5.12 and 5.13). Upon adsorbing low exposures of CS_2 onto a pre-adsorbed H_2O surface, an infrared band was observed in the wavelength range of the CS_2 ν_3 stretch at 1528 cm^{-1}, assigned to H_2O bound CS_2. Upon warming the mixed ice, this CS_2 infrared feature remains in the RAIR spectra well above the natural sublimation temperature of CS_2, in agreement with the trapped CS_2 feature in RAIR spectra of warmed binary layers of CS_2 on ASW (figure 5.13). There is little change in the area or position of the CS_2 feature upon warming the mixed ice. This indicates that there is minimal or no desorption of CS_2 around the natural sublimation temperature of CS_2, indicating that diffusion within the H_2O ice is limited. This is in agreement with the TPD spectra of CS_2:H_2O mixtures, as < 1% of the CS_2 desorbs at its natural sublimation temperature (figure 5.15). Comparing to RAIR spectra of pure CS_2 and CS_2-bearing H_2O ices warmed to a range of temperatures (figures 5.5 and 5.13), where behaviour characteristic of an amorphous to crystalline phase transition of CS_2 is observed at around 80 K, shows that this behaviour is not observed in CS_2:H_2O mixed ices. This indicates that the mixed CS_2:H_2O ice does not segregate upon warming, and the CS_2 remains intimately mixed and distributed within the ice. This inhibits the formation of clumps of CS_2, and hence amorphous or crystalline CS_2 does not form.

5.4. Summary and Conclusions

RAIR and TPD spectra of pure CS_2 ices, binary and reverse layered ices of CS_2 and H_2O and CS_2:H_2O mixtures adsorbed on HOPG at 20 K have been collected. RAIR and TPD spectra of pure CS_2 ices indicate that physisorbed multilayers of amorphous CS_2 form on the HOPG surface at 20 K following the growth of sub-monolayer and monolayer species. Upon warming,

the ice undergoes a phase change between 69 and 78 K. Sublimation of multilayers occurs between 110 and 130 K, depending on the thickness of the CS_2 ice.

RAIR and TPD spectra of binary layered ices of CS_2 on pre-adsorbed H_2O suggest the formation of a H_2O associated CS_2 layer on the ASW surface, observed prior to the formation of multilayer CS_2. Upon warming, TPD data show that a 20 L exposure of CS_2 on 100 L of H_2O is required to fully saturate the ASW surface before the growth of multilayers of CS_2 is observed. RAIR spectra have been used to identify the differences between H_2O associated CS_2 and multilayer CS_2, which can then be used to identify any trapping of CS_2 within the H_2O matrix. The H_2O associated CS_2 film becomes trapped in the ASW surface upon warming, above its natural sublimation temperature, and desorbs with H_2O. Reverse layers of H_2O adsorbed on CS_2 show no CS_2 desorption features associated with multilayers. This indicates that CS_2 cannot diffuse through the H_2O matrix, probably due to its large size, as compared to the size of the pores of ASW.

RAIR and TPD spectra of CS_2:H_2O mixtures show that multilayers of CS_2 do not form. From comparison of the RAIR spectra of binary layers and mixtures of CS_2 and H_2O, only H_2O associated CS_2 is observed in the mixed ice. Upon warming the mixtures, no evidence for segregation of the ice or for diffusion of the CS_2 is seen, and all desorption occurs coincident with the desorption of H_2O.

Quantitative analysis of the TPD spectra of CS_2 ice adsorbed on HOPG and on ASW has also been conducted. Kinetic data for CS_2 desorption from these surfaces has been determined, and is summarised in table 5.6. Due to repulsive lateral interactions observed in sub-monolayer coverages of CS_2, perfect monolayer CS_2 desorption was only observed in TPD spectra of CS_2 exposures between 10 and 20 L. Monolayer CS_2 desorbs with an order approaching 1. Multilayer desorption of pure CS_2 occurs with a desorption order approaching 0, and pre-exponential factor of around 1×10^{31} molec m^{-2} s^{-1}, both common for multilayer desorption. The desorption energy of pure monolayer and multilayer CS_2 were both found to be around 44 ± 6 kJ mol^{-1}. Comparing to the kinetic data for CS_2 desorption from an ASW surface, shows that the desorption of CS_2 is affected by the underlying substrate. The desorption order and pre-exponential factor for CS_2 desorption from an ASW surface are characteristic of fractional order desorption, a consequence of the increased surface area and heterogeneity of the ASW surface. The desorption energy for CS_2 from ASW was also found to be lower than that for pure CS_2 desorption. This is likely caused by the ASW surface, where a variety of binding sites for adsorption exist, leading to a range of desorption energies.

Table 5.6. Calculated kinetic parameters for monolayer and multilayer CS_2 desorbing from a bare HOPG surface and an ASW surface at 20 K.

	Monolayer		
	n	E_{des} / kJ mol^{-1}	ν_n / (molec $m^{-2})^{1-n}$ s^{-1}
Pure CS_2	0.88 ± 0.07	45.3 ± 6.2	$3.39 \times 10^{21 \pm 1.4}$
	Multilayer		
	n	E_{des} / kJ mol^{-1}	ν_n / (molec $m^{-2})^{1-n}$ s^{-1}
Pure CS_2	0.14 ± 0.05	44.1 ± 6.0	$1.60 \times 10^{31 \pm 1.5}$
CS_2/H_2O	0.67 ± 0.07	30.4 ± 7.5	$9.50 \times 10^{16 \pm 1.7}$

The technique employed for quantitative analysis of TPD spectra, and the values determined with this method for multilayer CS_2 desorption were tested via the use of a stochastic integration package. TPD spectra were simulated, via the use of a standard temperature dependent rate equation using the kinetic parameters found for multilayer CS_2, which accurately reproduced the experimental TPD spectra of multilayer CS_2 desorbing from a HOPG surface at 20 K, validating the qualitative analysis method.

Comparing the adsorption and desorption of CS_2 with CO_2, from chapter 4, can provide information on the role of the size of the volatile, especially when considering the ability of the species to diffuse and trap within a H_2O matrix. Table 5.7 shows the kinetic data calculated from the TPD spectra of multilayers of pure CO_2 and CS_2 ices adsorbed on a HOPG surface at 33 and 20 K respectively. As can be seen from table 5.7, the desorption order and pre-exponential factors are comparable, and are also common for other physisorbed multilayer desorbing species[34-37]. However, an increase in desorption energy of approximately 19 kJ mol^{-1} is observed when comparing CO_2 and CS_2. This shows that pure CS_2 ices are more stable on the HOPG surface. This is also shown by the TPD spectra of pure CO_2 and CS_2 multilayers, whereby desorption occurs approximately 30 K higher for CS_2 ices than for CO_2 ices.

Table 5.7. Kinetic data derived from TPD spectra of multilayers of pure CO_2 and CS_2 ices adsorbed on a HOPG surface at 33 and 20 K respectively.

Ice	n	E_{des} / kJ mol^{-1}	ν_n / (molec $m^{-2})^{1-n}$ s^{-1}
CO_2 Multilayer	0	24.8 ± 1.6	$1.07 \times 10^{30 \pm 1.5}$
CS_2 Multilayer	0.14 ± 0.05	44.1 ± 6.0	$1.60 \times 10^{31 \pm 1.5}$

Trapping of both CO_2 and CS_2 ices in binary layered or mixed polar ices is observed in RAIR and TPD spectra. Both volcano and co-desorption features of CO_2 and CS_2 with H_2O were observed in the TPD spectra. However, reverse layered ices and mixed polar ices of CO_2 show desorption of CO_2 around its natural sublimation temperature. This is not observed in CS_2 ices, as the diffusion of CS_2 through the H_2O matrix is hindered. Therefore, due to the smaller size of the CO_2 molecule, both diffusion and trapping are observed, and the replacement of the O atom with the S atom hinders diffusion through an ASW film.

5.5. References

1. Charnley S.B., *Astrophys. J.*, **481**, (1997), 396-405
2. Doty S.D., van Dishoeck E.F., van der Tak F.F.S. and Boonman A.M.S., *Astron. Astrophys.*, **389**, (2002), 446-463
3. Duley W.W., Millar T.J. and Williams D.A., *Mon. Not. R. Astron. Soc.*, **192**, (1980), 945-957
4. Millar T.J. and Herbst E., *Astron. Astrophys.*, **231**, (1990), 466-472
5. Benz A.O. et al, *Astron. Astrophys.*, **475**, (2007), 549-558
6. Buckle J.V. and Fuller G.A., *Astron. Astrophys.*, **399**, (2003), 567-581
7. van der Tak F.F.S., Boonman A.M.S., Braakman R. and van Dishoeck E.F., *Astron. Astrophys.*, **412**, (2003), 133-145
8. Yamada M., Osamura Y. and Kaiser R.I., *Astron. Astrophys.*, **395**, (2002), 1031-1044
9. Caselli P., Hasegawa T.I. and Herbst E., *Astrophys. J.*, **421(1)**, (1994), 206-210
10. Ruffle D.P., Hartquist T.W., Caselli P. and Williams D.A., *Mon. Not. R. Astron. Soc.*, **306**, (1999), 691-695
11. Tieftrunk A., Pineau des Forêts G., Schilke P. and Walmsley C.M., *Astron. Astrophys.*, **289**, (1994), 579-596
12. Trasferetti B.C., Davanzo C.U., Zoppi R.A., da Cruz N.C. and de Moraes M.A.B., *Phys. Rev. B.*, **64**, (2001), 125404
13. Jackson W.M., Halpern J.B., Feldman P.D. and Rahe J., *Astron. Astrophys.*, **107**, (1982), 385-389
14. Jackson W.M., Butterworth P.S. and Ballard D., *Astrophys. J.*, **304**, (1986), 515-518
15. Despois D., Crovisier J., Bockelée-Morvan D. and Colom P., Formation of comets: Constraints from the abundance of Hydrogen Sulfide and other sulfur species. *at Astrochemistry of Cosmic Phenomena* (IAU), Singh P.D. (Ed.), (1992), 459-460
16. Bergeman T. and Cossart D., *J. Molec. Spectr.*, **87**, (1981), 119-195
17. Feldman P.D. et al, *Nature*, **286**, (1980), 132-135
18. Smith A.M., Stecher T.P. and Casswell L., *Astrophys. J.*, **242**, (1980), 402-410
19. Weaver H.A., Feldman P.D., Festou M.C., A'Hearn M.F. and Keller H.U., *Icarus*, **47**, (1981), 449-463
20. Jackson W.M., Scodinu A. and Xu D., *Astrophys. J.*, **607**, (2004), L139-L141
21. Butler J.E., Drozdoski W.S. and McDonald J.R., *Chem. Phys.*, **50**, (1980), 413-421
22. Greening F.R. and King G.W., *J. Molec. Spectrosc.*, **59**, (1976), 312-325
23. Yang S.C., Freedman A., Kawasaki M. and Bersohn R., *J. Chem. Phys.*, **72(7)**, (1980), 4058-4062
24. Bockelée-Morvan D. et al, *Astron. Astrophys.*, **353**, (2000), 1101-1114
25. Sutton E.C. et al, *Astrophys. J. Supp. Ser.*, **97**, (1995), 455-496
26. Blake G.A., Sutton E.C., Masson C.R. and Phillips T.G., *Astrophys. J.*, **315**, (1987), 621-645
27. Rodgers S.D. and Charnley S.B., *Advances in Space Research*, **38**, (2006), 1928-1931
28. Collings M.P. et al, *Mon. Not. R. Astron. Soc.*, **354**, (2004), 1133-1140
29. Bailey C.R. and Cassie A.B.D., *Proc. Roy. Soc.*, **140**, (1933), 605
30. Ito M., *J. Chem. Phys.*, **42(3)**, (1965), 815-818
31. Stoicheff B.P., *Can. J. Phys.*, **36**, (1958), 218
32. Allen H.C., Plyler E.K. and Blaine L.R., *J. Amer. Chem. Soc.*, **78(19)**, (1956), 4843-4844
33. Blanquet G. et al, *J. Molec. Struc.*, **780-781**, (2006), 171-177
34. Bolina A.S., Wolff A.J. and Brown W.A., *J. Phys. Chem. B*, **109**, (2005), 16836-16845
35. Bolina A.S., Wolff A.J. and Brown W.A., *J. Chem. Phys.*, **122**, (2005), 044713
36. Bolina A.S. and Brown W.A., *Surf. Sci.*, **598**, (2005), 45-56
37. Burke D.J., Wolff A.J., Edridge J.L. and Brown W.A., *J. Chem. Phys.*, **128**, (2008), 104702
38. Brown W.A. and Bolina A.S., *Mon. Not. R. Astron. Soc.*, **374**, (2007), 1006-1014
39. Burke D.J. and Brown W.A., *Phys. Chem. Chem. Phys.*, **12**, (2010), 5947-5969
40. Lehner B., Hohage M. and Zeppenfeld P., *Chem. Phys. Lett.*, **369**, (2003), 275-280

41. Green S.D. et al, *Mon. Not. R. Astron. Soc.*, **398**, (2009), 357-367
42. Kramer H.M. and Suzanne J., *Surf. Sci.*, **1976**, (2010), 659-669
43. Meixner D.L. and George S.M., *Surf. Sci.*, **297**, (1993), 27-39
44. Ulbricht H., Zacharia R., Cindir N. and Hertel T., *Carbon*, **44**, (2006), 2931-2942
45. de Jong A.M. and Niemantsverdriet J.W., *Surf. Sci.*, **233**, (1990), 355-365
46. King D.A., *Surf. Sci.*, **47**, (1975), 384-402
47. Sandford S.A. and Allamandola L.J., *Astrophys. J.*, **355**, (1990), 357-372
48. Ehrenfreund P., Dartois E., Demyk K. and d'Hendecourt L., *Astron. Astrophys.*, **339**, (1998), L17-L20
49. Burke D.J., Wolff A.J., Edridge J.L. and Brown W.A., *Phys. Chem. Chem. Phys.*, **10(32)**, (2008), 4956-4967
50. Malyk S., Kumi G., Reisler H. and Wittig C., *J. Phys. Chem. A*, **111**, (2007), 13365-13370
51. Wolff A.J., Carlstedt C. and Brown W.A., *J. Phys. Chem. C*, **111**, (2007), 5990-5999

Chapter 6: Temperature Programmed Desorption and Reflection Absorption Infrared Spectroscopy of Sulphur Dioxide bearing ices on Highly Oriented Pyrolytic Graphite

6.1. Introduction

Sulphur dioxide (SO_2) has been found in the interstellar medium (ISM), within dense molecular clouds towards star forming regions and massive protostars[1-7], in the comae of comets[8,9] and in planetary ices and atmospheres[10-15]. Discovery of interstellar SO_2 was made by infrared detection of the vibration at 7.58 μm (1319 cm^{-1})[16] and radio detection of a range of rotations, including a strong transition at 83.7 GHz[4]. In dense molecular clouds, SO_2 has been found in the gas phase as well as frozen out on the surface of interstellar dust grains[17]. The abundance of SO_2 in dense clouds has been found to be up to 1×10^{-8} with respect to H_2, accounting for up to 5% of the elemental sulphur in these regions[18,19]. Detection of solid SO_2 on the surface of the Jovian moons, Io and Europa, has also been made from the identification of the $\nu_1 + \nu_3$ infrared combination mode of solid SO_2 at 4.07 μm[10,12,14,20]. SO_2 ices containing trace amounts of H_2O have been detected on the surface of Io[13] and mixed SO_2:H_2O ices have been detected on Europa[20].

SO_2 has been shown to be predominantly formed in the gas phase in the ISM. In hot core regions, it is formed by the reaction between OH and SO, a product of the destruction and oxygenation of H_2S[18]. As this reaction is in competition with the formation of H_2O, the magnitude of SO_2 formation is reduced at temperatures above ≈200 K. Once formed in the ISM gas phase SO_2 has a very long lifetime, $\approx 10^6$ years, as it is predominantly destroyed by C^+, which has a low abundance in the ISM, and by H_3^+ which cycles back to SO_2 via HSO_2^+.[18] Due to the temperature dependence of the formation of SO_2, it is considered to be a good tracer for understanding the age and temperature of star forming, hot core regions. SO_2 is also particularly interesting for understanding shocks within dense clouds[2,21]. Due to the energy from the shockwave, formed as a consequence of the death of a star, enhanced molecular abundances are often observed in regions where no core warming is apparent. For example, the Orion KL plateau has an enhanced abundance of OH due to the destruction of H_2O[1,5,22]. This enhances the abundance of SO_2, up to around 10^{-7} with respect to H_2, in regions where trace SO_2 is expected[2].

Previous experiments studying the ionisation of SO_2 and SO_2-bearing ices have been conducted with the principal aim of investigating the formation of more complex sulphur-

containing species[23-26]. Irradiation of pure SO_2 ices shows that the formation of SO_3 dominates[24]. However, irradiating SO_2-bearing H_2O ices produces ices containing pre-cursors to the formation of sulphuric acid, H_2SO_4, including HSO_4^- and SO_4^{2-}, as well as hydrogen peroxide, H_2O_2.[25,26] These studies have also shown the formation of SO_2 , as well as other sulphur-bearing species including OCS, via the irradiation of H_2S-containing H_2O ices[23,26]. This has implications for star forming regions as well as for planetary ices.

The study of sulphur chemistry in the gas phase, and on the surface of interstellar dust grains is important in order to understand the depletion of elemental sulphur, via the formation of molecular ices such as SO_2, in the ISM[17-19,27,28]. It is also of interest to understand the evaporation of SO_2-bearing H_2O ices, since the injection of SO_2 into the gas phase in star forming regions and its influence on the gas phase chemistry of sulphur bearing species is not completely understood. SO_2 has been found to make up to 1% with respect to H_2O of a typical interstellar ice[29]. Therefore the study of SO_2 and SO_2-bearing H_2O ices on the surface of an interstellar dust grain analogue is of importance to further understand ices in star forming regions.

Table 6.1. Frequencies of the fundamental vibrational modes observed in previous studies of pure SO_2 ice, including orthogonal optical (LO) and transverse optical (TO) modes. Combination modes and vibrational bands from isotopic SO_2 are omitted.

Assignment		Infrared						Raman	
		30 K	90 K	20 K	77 K	77 K	117 K	20 K	77 K
		Au[30]		AgBr[31-34]		KBr[35]	Crystalline SO_2[36]	Cu[32,37]	
ν_2	A_1 (TO)	520	521	525	528	522	521	522	525
	A_1 (LO)				535				543
	A_2							520	521
ν_1	A_1 (TO)	1146	1143	1147		1145	1147	1148	1148
	A_1 (LO)								1153
	A_2							1144	1144
ν_3	B_1 (TO)	1316	1311	1313	1310	1315	1308	1310	1311
	B_2 (TO)		1322	1327	1322	1323	1330	1324	1323
	B_1 (LO)				1334				1339
	B_2 (LO)								1349

Gas phase SO_2 infrared spectra show 3 bands at 518, 1151 and 1361 cm^{-1} assigned to the ν_2 bend and the ν_1 and ν_3 symmetric and asymmetric stretches of SO_2 respectively[38,39]. A range of infrared and Raman studies of amorphous and crystalline SO_2 have also been conducted[30-37,40-44], and the positions of the observed fundamental vibrational bands are summarised in table 6.1. The amorphous to crystalline phase transition of SO_2 occurs around 70 K[30]. Four infrared active fundamental bands of solid SO_2 are expected, corresponding to the A_1 mode of the ν_2 bend and ν_1 stretch and the B_1 and B_2 modes of the ν_3 stretch. The A_2 mode of the ν_2 bend and ν_1 stretch are infrared inactive and therefore only visible in Raman spectra. A range of combination modes are also observed in the infrared and Raman spectra of solid SO_2, including

the $2\nu_1$ and $\nu_1 + \nu_3$ combination modes around 1608 and 2288 cm^{-1} respectively[30], as well as from isotopic forms of SO_2. These are omitted from table 6.1.

The infrared and Raman spectrum of crystalline SO_2 is further complicated by the presence of orthogonal optical (LO) and transverse optical (TO) splitting of the fundamental vibrational modes[30,41,44]. LO - TO splitting of vibrational bands is described in detail in chapter 3. The LO and TO modes of an infrared active vibration are observed in crystalline ices as a result of the interaction of polarised phonon modes within the ice with the incident radiation. This effect is forbidden in infrared inactive vibrational modes, and as such the A_2 mode of the ν_2 bend and ν_1 stretch do not show LO - TO splitting. Therefore the vibrational spectrum of amorphous SO_2 should show 4 infrared active and 2 infrared inactive vibrational modes, whereas the vibrational spectrum of solid crystalline SO_2 should show 8 infrared active and 2 infrared inactive vibrational modes, as shown in previous studies[30-37,40,44].

Infrared spectra have also been collected for pure SO_2 ices, and for SO_2-bearing H_2O ice layers and mixtures, on a Au substrate at 10 K[30] and on a CsI window at 20 K[16]. The amorphous to crystalline phase transition, around 70 K, and sublimation, between 108 and 120 K, of pure SO_2 ice were observed[16,30]. SO_2 was found to physisorb on an amorphous solid water (ASW) surface, with a similar infrared spectrum to that observed for pure SO_2 ices[30]. Annealing of SO_2-bearing H_2O mixed ices showed trapping of SO_2 within the H_2O matrix[30].

A number of temperature programmed desorption (TPD) experiments have also been conducted on pure SO_2 and SO_2-bearing H_2O ices adsorbed on a range of metal surfaces[45-50]. Physisorption of SO_2 is observed on a Au surface[45,46] and reversible chemisorption is also observed on Ag and Cu(111) surfaces[46-48], whereas decomposition of SO_2 is found on most other metal surfaces[46]. TPD studies of pure SO_2 on a Au and Cu(111) surface at 8 and 90 K respectively show the formation of multilayer SO_2, which desorbs around 100 - 110 K[45,46]. TPD spectra of SO_2-bearing H_2O ices show characteristics indicating trapping of SO_2 within the H_2O film. Previous studies of the TPD spectra of H_2O on a HOPG surface at 92 K have shown that H_2O multilayers desorb around 164 K, showing a bump on the low temperature side of the main peak at 152 K[51]. These two TPD peaks correspond to the desorption of crystalline ice (CI) and the amorphous to crystalline phase transition of ASW respectively. Desorption of SO_2 from SO_2-bearing layered and mixed H_2O ices is observed well above the natural sublimation temperature of SO_2, coincident with the ASW - CI transition and with the desorption of CI[45].

As well as providing insight into the qualitative desorption and trapping of SO_2-bearing ices, TPD can also provide quantitative information on the kinetics of desorption. Derivation of desorption energies has been conducted for infrared spectra of pure SO_2 ice, and has been found to be 28.8 ± 0.3 kJ mol^{-1}.[43] However, deriving desorption energies from infrared studies of multilayer SO_2 requires the assumption that the desorption order is 0, and the pre-

exponential factor is 2.4×10^{12} s^{-1}, the average lattice vibration frequency of solid SO_2. This is not a valid assumption as a desorption order of 0 is common for the desorption of multilayers of an ideal adsorbate[52], whereas a pre-exponential factor of 2.4×10^{12} s^{-1} is common for desorption of monolayers[52]. It has also been shown previously that multilayers can desorb with a fractional desorption order, and a consequently altered pre-exponential factor[51,53-55]. Therefore assumptions based on an ideal adsorbate are not always valid. Hence high quality TPD spectra of a wide range of SO_2-bearing ices are needed, not only to gain a better understanding of the trapping and diffusion behaviour of SO_2 within SO_2-bearing ices, but also to derive realistic kinetic parameters for the desorption of SO_2, described in more detail in chapter 2, which can be used in astronomical models of star forming regions[56-58].

The study of SO_2-bearing ices, in comparison with the study of CO_2- and CS_2-bearing ices, is of interest to help to understand how the physical properties of the molecule affect its ability to trap and desorb from ices. CO_2, SO_2 and CS_2 have bond lengths of 116.3, 143.1 and 155.3 pm respectively. The relative sizes of O, C and S atoms can be described by their covalent radii at 66, 73 and 105 pm respectively. CO_2 and CS_2 are the smallest and largest molecules respectively. It is therefore expected that this may affect the ability of SO_2 to diffuse and trap within a H_2O matrix when compared to CO_2 and CS_2.

Given the importance of SO_2 containing ices in the ISM as a tool for measuring the age and thermal history of star forming regions, a complete investigation into the adsorption and desorption properties of a range of SO_2-bearing ices adsorbed on a model carbonaceous grain surface has been undertaken. Previous work[52] shows the importance of investigating adsorption and desorption on a wide range of astrophysically relevant surfaces. Reflection absorption infrared spectroscopy (RAIRS) and TPD have been used to study pure SO_2 ices, binary layered SO_2 and H_2O ices and SO_2:H_2O mixed ices. TPD spectra have also been used to derive kinetic information about the desorption of SO_2 by rigorous quantitative analysis.

6.2. Experimental

The experimental apparatus and techniques used for all experiments have been described in detail in chapter 2. SO_2 (CK Gas, 99.9%) and H_2O (distilled, deionised) were used in these experiments, purified via repeated freeze-pump-thaw cycles. Ices were grown *in situ* by backfilling the chamber through a high precision leak valve. All exposures are measured in Langmuir, where 1 L = 10^{-6} mbar s, and were not corrected for ion gauge sensitivity. RAIR spectra were taken at a resolution of 4 cm^{-1} and are the result of the co-addition of 256 scans. For the warm RAIRS experiments, the sample temperature was raised and held at a predetermined temperature for 3 minutes, prior to recording RAIR spectra at the base

temperature. TPD spectra of masses 18 and 64, the major mass fragments of H_2O and SO_2 respectively, were recorded simultaneously. All TPD spectra were recorded at a heating rate of 0.53 ± 0.01 K s^{-1}.

6.3. Results and Discussion

RAIR and TPD spectra were recorded for SO_2-bearing ices adsorbed on a HOPG surface at 20 K. SO_2 and H_2O were dosed on the HOPG sample under four dosing regimes: pure SO_2 adsorbed on bare HOPG; binary layered ices of SO_2 adsorbed on pre-adsorbed H_2O layers; reverse binary layered ices of H_2O adsorbed on pre-adsorbed SO_2 layers; and well defined mixtures of SO_2 and H_2O co-deposited on bare HOPG.

6.3.1. Pure SO_2 Ice

RAIR and TPD spectra were recorded for a range of exposures of SO_2 adsorbed on a bare HOPG sample at 20 K.

6.3.1.1. TPD Data

Figures 6.1 and 6.2 show TPD spectra recorded for a range of exposures of pure SO_2 adsorbed on a HOPG surface at 20 K. At the lowest exposure of SO_2, 1 L, a single broad peak is observed in the TPD spectrum with a peak temperature of 114 K (figure 6.1). Increasing the SO_2 exposure to 3 L shows no change in the peak temperature at 114 K. Further increasing the SO_2 exposure, to between 3 and 10 L, leads to a gradual increase in peak temperature to 117 K following a 10 L exposure of SO_2. All TPD spectra following SO_2 exposures up to 10 L show a single, asymmetric peak with no common leading edge. At higher SO_2 exposures, between 10 and 200 L, the peak temperature gradually increases until it reaches 125 K following a SO_2 exposure of 200 L (figure 6.2). Above SO_2 exposures of 10 L, all TPD spectra show a single, asymmetric peak with a common leading edge. The size of the TPD peak increases gradually with increasing SO_2 exposure.

Assignment of the peaks in the TPD spectra can be made by comparison with investigations of other adsorbates physisorbed on a HOPG surface[51,53,54,57,59]. At low SO_2 exposures, 1 to 10 L, the observed TPD spectrum shows a single, asymmetric peak with no shared leading edge and a small increase in peak temperature with increasing exposure (figure 6.1). This behaviour indicates 1st order desorption, characterised by a constant peak temperature and no shared

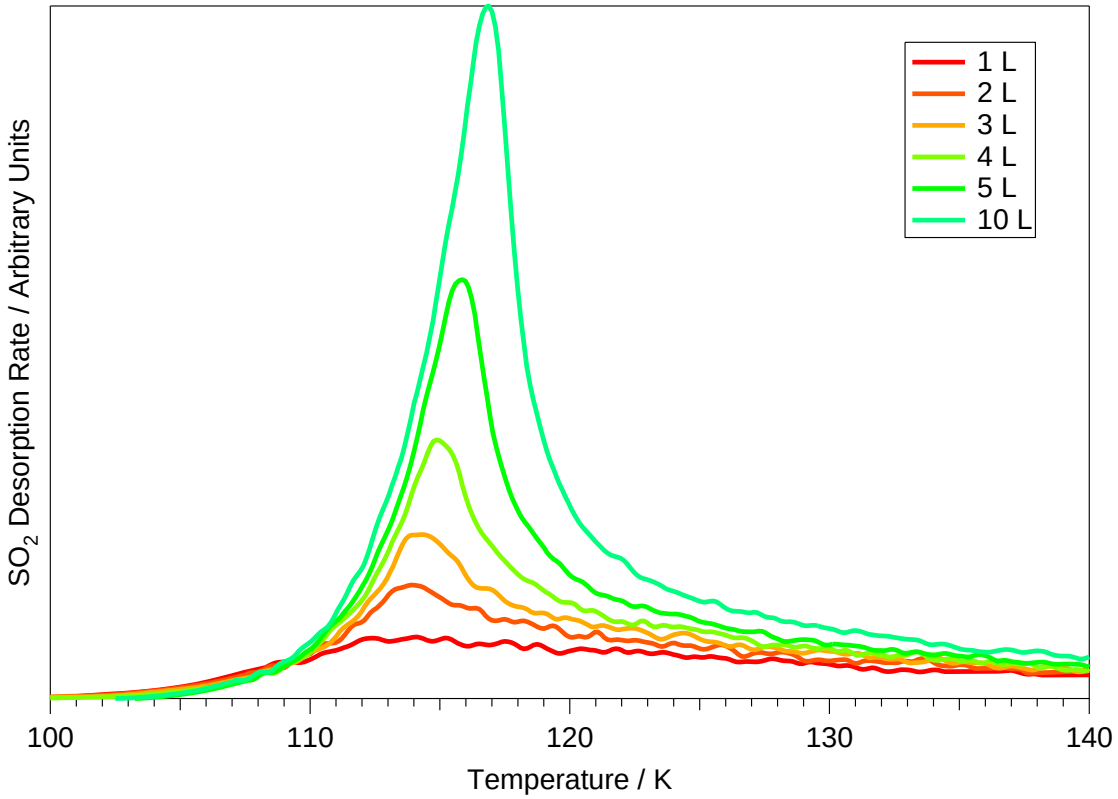

Figure 6.1. TPD spectra of low exposures of SO_2, up to 10 L, desorbing from a bare HOPG surface at 20 K.

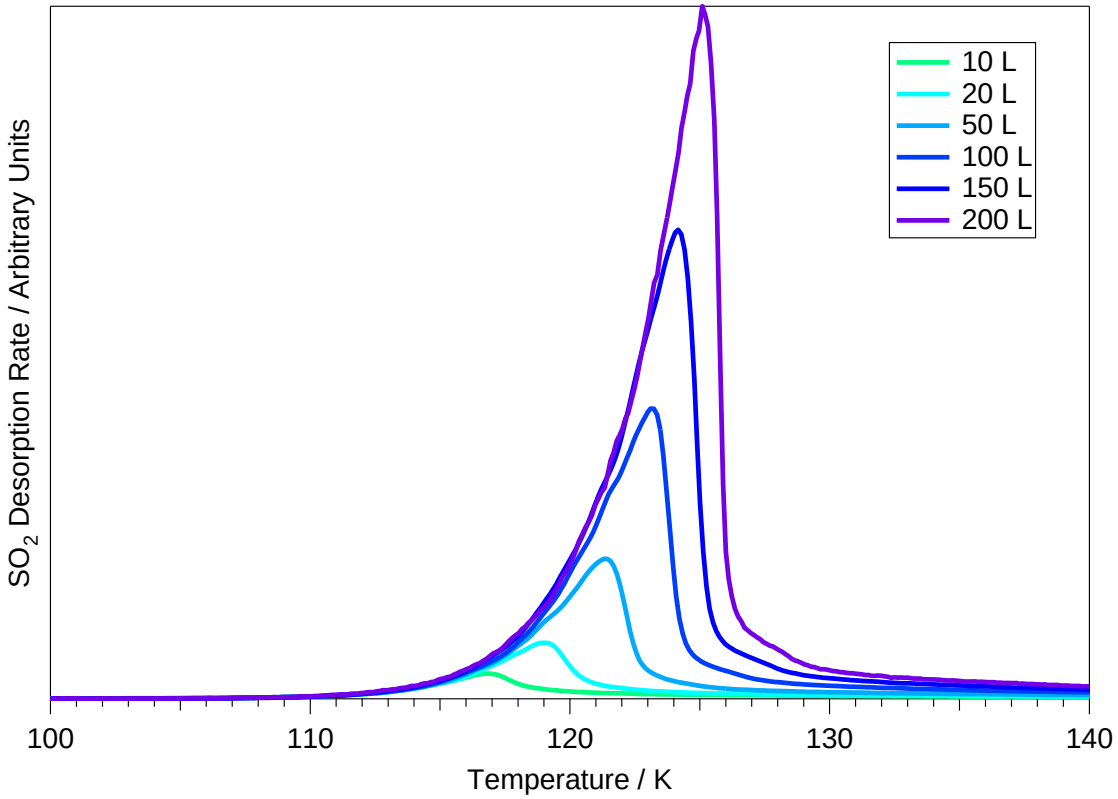

Figure 6.2. TPD spectra of high exposures of SO_2, above 10 L, desorbing from a bare HOPG surface at 20 K.

leading edge. First order desorption is common for monolayer species[52], which are expected to be formed at low SO_2 exposures. At high SO_2 exposures, 10 to 200 L, the observed TPD spectrum shows a single, asymmetric peak, with common leading edges and an increase in peak temperature with increasing exposure (figure 6.2). This behaviour is characteristic of 0^{th} order desorption and is common for multilayer species[52].

Integration of the area under the TPD spectra shows a linear relationship between SO_2 exposure and peak area, shown in figure 6.3, indicating a constant sticking probability for SO_2 adsorption on the HOPG surface. In addition, the peak area does not saturate, indicating that multilayers of SO_2 are being formed on the HOPG surface at 20 K. The desorption temperature observed (≈115 - 125 K) also suggests that SO_2 is physisorbed on the surface. This is in agreement with the observation of physisorbed multilayers of SO_2 on a Au surface at 8 K[45], and on a Cu(111) surface at 90 K[46].

Comparing with TPD spectra of pure CO_2 and CS_2 ice adsorbed on HOPG at 33 and 20 K (chapters 4 and 5 respectively), both monolayer and multilayer growth are observed. An increase in the sublimation temperature of the pure ice is observed as we go from CO_2 to SO_2 to CS_2 multilayers. This increase in desorption temperature indicates an increase in the stability of SO_2 adsorbed on HOPG. Likewise, the similarity in desorption temperature between CS_2 and

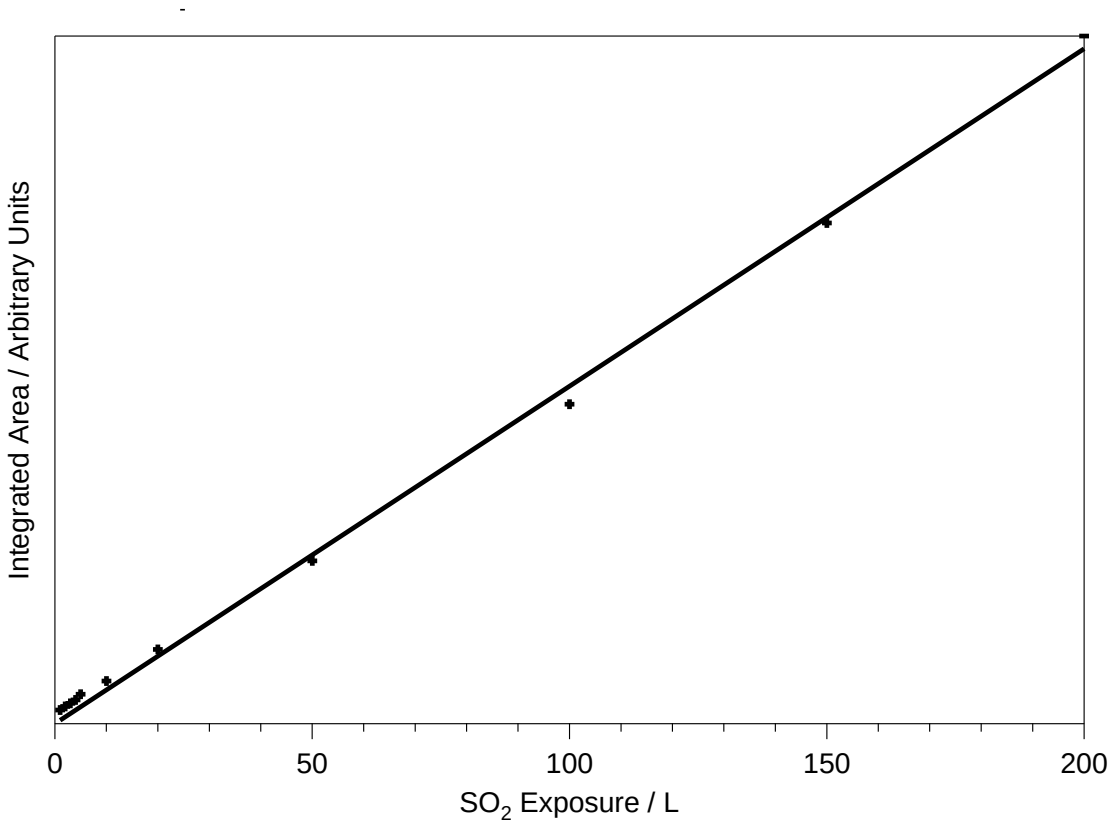

Figure 6.3. Integrated area of the TPD spectra shown in figures 6.1 and 6.2 as a function of SO_2 exposure. The line is supplied as a guide to the eye, and was produced using a linear fit to the data.

SO_2 ice indicates a similar stability of SO_2 adsorbed on the HOPG surface. Larger molecules often show higher desorption energy when physisorbed on a surface[60,61]. This is due to the increased polarisability of larger molecules, and as a result stronger van der Waals forces are formed between the molecules within the ice and the surface. This trend is in agreement with the relative sizes of CO_2, SO_2 and CS_2, where CO_2 is smaller than SO_2 which, in turn, is smaller than CS_2.

6.3.1.2. RAIRS Data

RAIR spectra were collected for a range of exposures of SO_2, adsorbed on a bare HOPG surface at 20 K, shown in figure 6.4. Infrared bands are only observed in the wavenumber range between 1100 and 1400 cm^{-1}. At the lowest exposure of SO_2, 1 L, two infrared bands are observed at 1151 and 1346 cm^{-1}. Increasing SO_2 exposure, up to 200 L, shows an increase in the size of the observed infrared bands, with no shift in wavenumber. The infrared band at 1151 cm^{-1} is symmetric, whereas that at 1346 cm^{-1} is asymmetric, with a skew towards low wavenumber, suggesting that the band at 1346 cm^{-1} is composed of a number of vibrational modes.

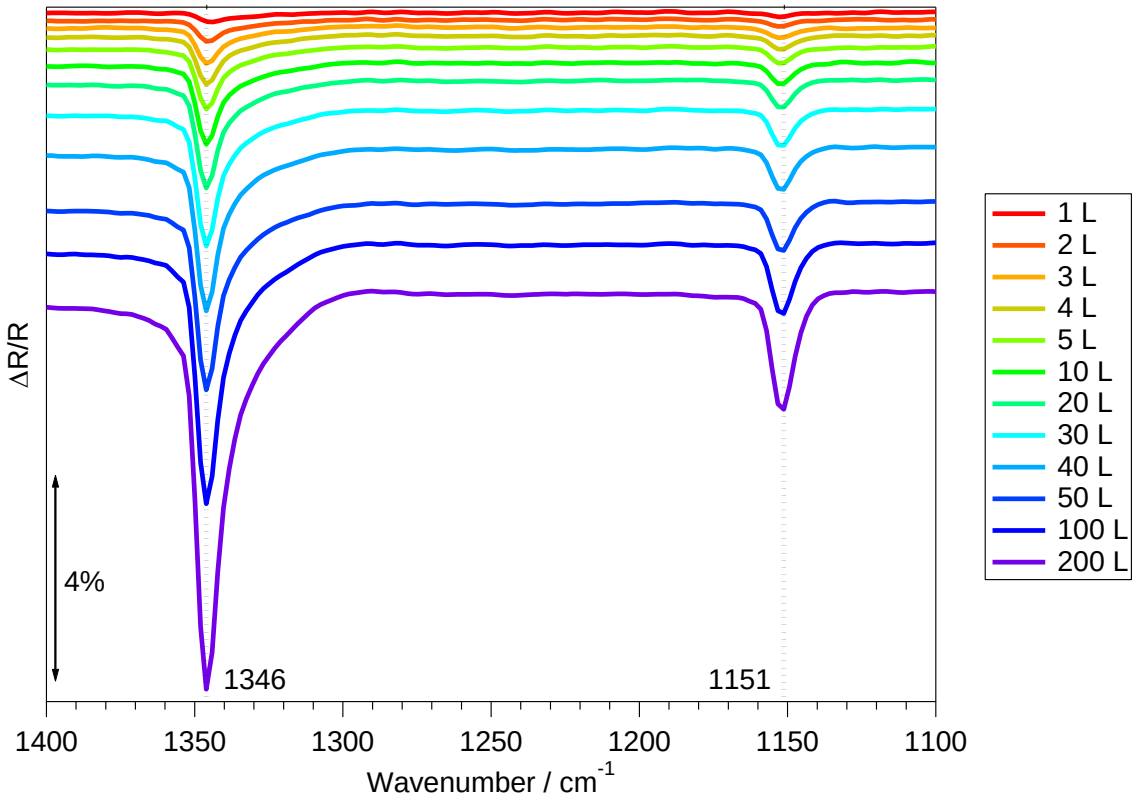

Figure 6.4. RAIR spectra of a range of exposures of SO_2 adsorbed on a bare HOPG surface at 20 K.

The infrared band at 1151 cm^{-1} is assigned to the ν_1 stretch of amorphous SO_2 ice, seen at 1148 cm^{-1} in previous studies[32,37]. The infrared band at 1346 cm^{-1} is assigned to the LO phonon mode of the B_2 ν_3 stretch of SO_2. LO - TO splitting is usually only observed in crystalline ices, as discussed in chapter 3, however, the observation of LO and TO modes has been observed in amorphous ices with particular optical properties. The refractive index and extinction coefficient of SO_2 ice are less than unity in the wavelength range of the ν_3 vibration[44]. This suggests that the dielectric constant of the SO_2 ice, $|\varepsilon|$, will approach 0 and as a consequence, the LO - TO splitting of this vibration will be observed, even in amorphous ice. Hence the band at 1346 cm^{-1} is assigned to the LO phonon mode of the B_2 ν_3 stretch of amorphous SO_2. The 1346 cm^{-1} band has a long tail towards low wavenumber, suggesting that it may be composed of a number of infrared modes. This is in agreement with the position of the TO mode of the B_1 and B_2 ν_3 stretch and the LO mode of the B_1 ν_3 stretch seen in previous work[30-37,40,44].

The bands at 1346 and 1151 cm^{-1} do not saturate with increasing SO_2 exposure, indicating that physisorbed multilayers of SO_2 are formed on the HOPG surface at 20 K. This is also suggested when comparing with the gas phase frequencies of the ν_1 and ν_3 stretches at 1151 and 1361 cm^{-1} respectively[38,39], and is in agreement with TPD spectra. Integration of the area of the ν_1 and ν_3 bands shows two regions where a linear fit can be applied as a function of SO_2 exposure, shown in figure 6.5. A linear fit can be applied for exposures between 1 and 5 L, and between 5 and 200 L. As observed in figure 6.3, a constant sticking probability is suggested from TPD spectra of SO_2 ice for all exposures of SO_2. Therefore this change in infrared band strength must be caused by a change in the structure of the SO_2 film.

The band at 1346 cm^{-1} is much larger than the band at 1151 cm^{-1}, as evident in figure 6.4, implying that there is a greater contribution from the asymmetric stretch to the total integrated area. By considering the metal surface selection rule, this suggests that the SO_2 is oriented on the surface with the ν_3 stretch predominantly normal to the surface. However, as the ice is amorphous, the SO_2 molecules are not exclusively oriented in this manner. As the change in the rate of growth of the ν_1 and ν_3 stretches at 5 L is the same, as indicated in figure 6.5, the change in structure of the SO_2 ice is not due to a change in the molecular orientation. Therefore this structure change following a 5 L exposure of SO_2 may be caused by a density change, or some other structural change of the SO_2 film.

The structure change of the ice at 5 L may be a consequence of a change in the underlying substrate on which the SO_2 molecules adsorb. At the lowest exposures of SO_2, the molecules adsorb on the bare HOPG surface. However, once the HOPG surface is saturated, the remaining SO_2 will adsorb on pre-adsorbed SO_2. This suggests that the formation of monolayer and multilayer SO_2 is observed in the RAIR spectra, and that the monolayer saturation coverage occurs following a SO_2 exposure of 5 L. The observation of monolayer and multilayer

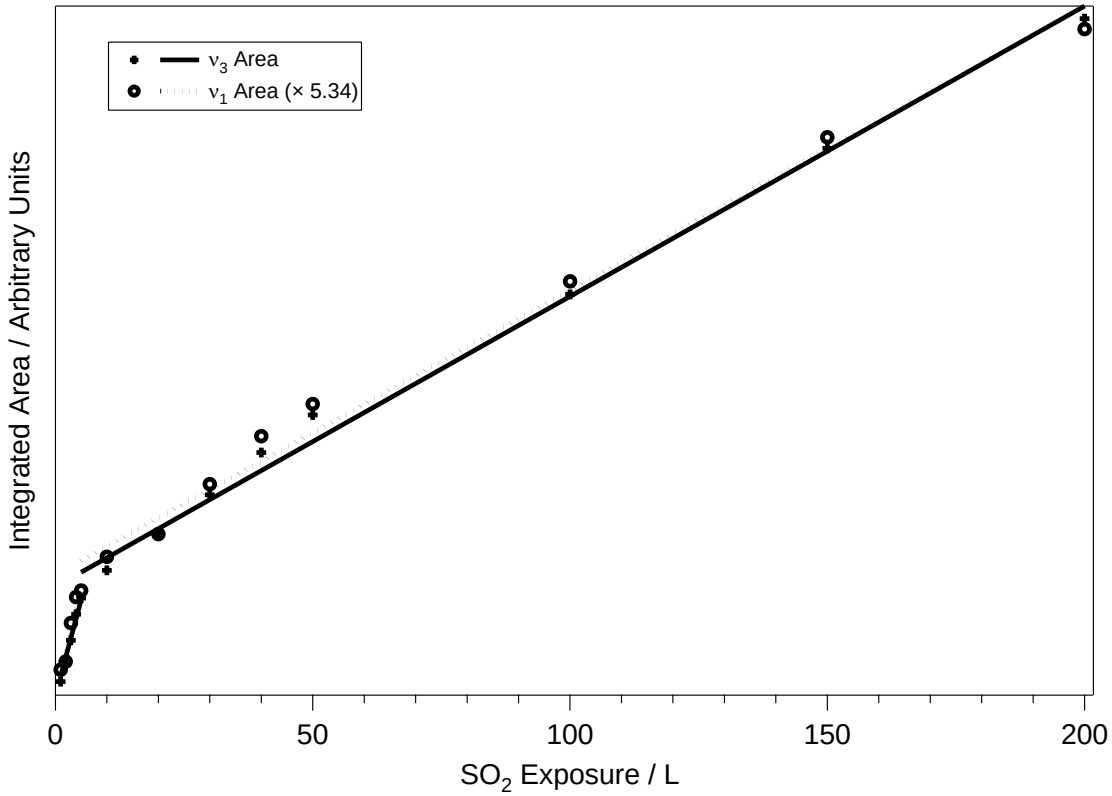

Figure 6.5. Integrated area of the symmetric and asymmetric stretches of SO_2 from the RAIR spectra shown in figure 6.4 as a function of SO_2 exposure. The solid and dotted lines are supplied as a guide to the eye of integrated areas of the ν_3 and ν_1 stretches respectively, and were produced using a linear fit to the data.

SO_2, physisorbed on the HOPG surface at 20 K, is also in agreement with the TPD spectra, where monolayer and multilayer SO_2 were observed below and above exposures of 10 L respectively.

Warming the HOPG surface can provide information about the temperature dependent behaviour of the SO_2 ice adsorbed on HOPG at 20 K. Figure 6.6 shows a 200 L exposure of SO_2 adsorbed on HOPG, warmed to a range of temperatures. Warming the ice to between 20 and 58 K shows no significant change in the observed infrared features. Upon warming the HOPG surface to 68 K, a slight shift in the infrared band at 1151 cm^{-1} to 1149 cm^{-1} is observed, along with the appearance of two very small bands on the low wavenumber side of the 1346 cm^{-1} band at 1317 and 1306 cm^{-1}. Further warming to 96 K shows no change in the spectrum. Warming to 103 K shows a slight decrease in the size of all bands. Complete desorption of the SO_2 ice is observed following warming to 114 K, in agreement with the TPD desorption temperature of ≈115 - 125 K.

Comparing with previous studies of solid SO_2, the observed changes in the RAIR spectra of SO_2 between 58 and 68 K are a result of the amorphous to crystalline phase transition of SO_2, observed previously at 70 K[30]. As discussed previously, the LO mode of the B_1 ν_3 stretch is observed in amorphous ice as $|\varepsilon|$ approaches 0. It was also suggested that the low

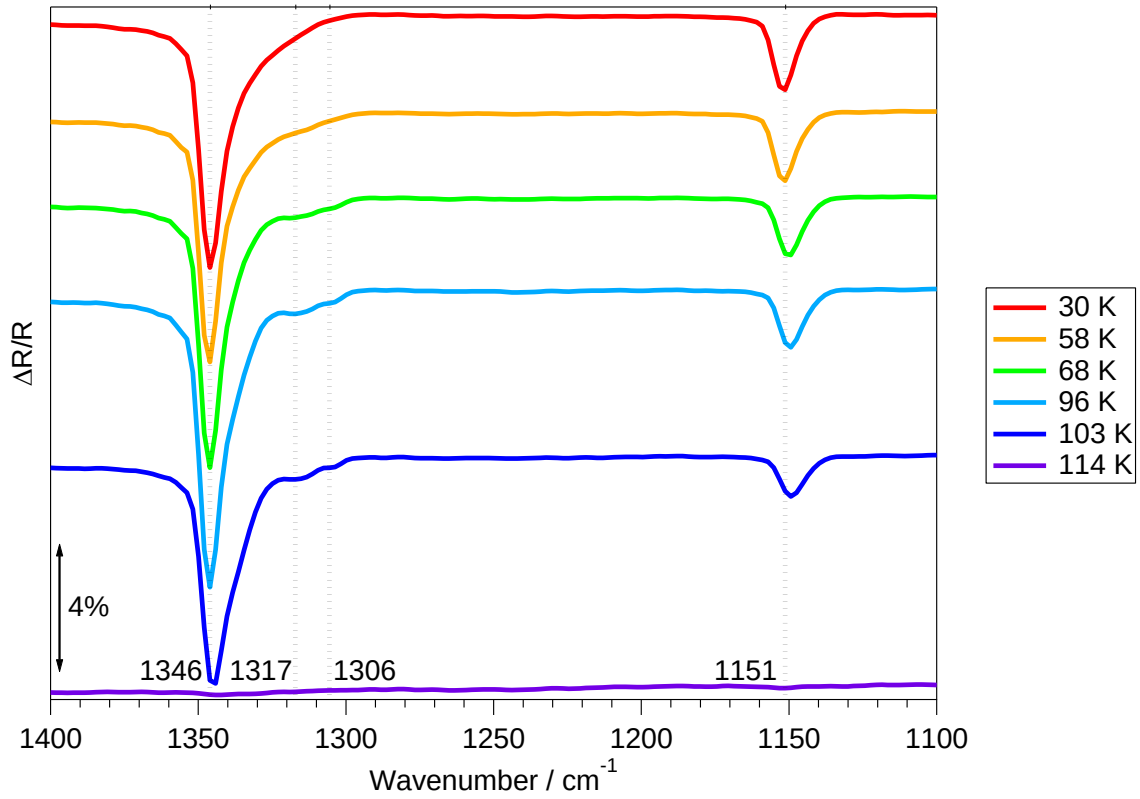

Figure 6.6. RAIR spectra of a 100 L exposure of SO_2 adsorbed on a bare HOPG surface at 20 K, warmed to a range of temperatures.

wavenumber tail of the band at 1346 cm^{-1} was composed of the remaining infrared active bands of the ν_3 stretch. This is confirmed by comparison of the infrared spectra of crystalline SO_2 with previous studies of solid SO_2.[30-37,40,44] In particular, the two new bands at 1306 and 1317 cm^{-1} can be assigned to the TO phonon modes of the B_1 and B_2 modes of the ν_3 stretch respectively, previously observed at 1311 and 1322 cm^{-1} respectively[30]. The bands at 1306 and 1317 cm^{-1} become observable due to the increase in order of the crystalline SO_2 ice. A slight reduction in the position of the ν_1 stretch, from 1151 to 1149 cm^{-1} from amorphous to crystalline ice, is also in agreement with previous studies of solid SO_2.

6.3.1.3. Quantitative Analysis of TPD Data

Desorption orders. From equation 2.2, the desorption orders for monolayer and multilayer SO_2 can be determined from the gradient of a plot of $\ln[I(T)]$ against $\ln[\theta_{rel}]$ at a fixed temperature for a set of TPD spectra with varying initial SO_2 coverages. This method assumes that the desorption energy and pre-exponential factor do not vary with coverage or temperature. This is valid for H_2O[51], NH_3[54], CH_3OH[53] and C_2H_5OH[55] ices, as well as for CO_2 and CS_2 ices in chapters 4 and 5 respectively. Since SO_2 is physisorbed on the HOPG surface, it should also be a valid assumption in this case. Monolayer desorption rates were taken from

the TPD spectra for SO_2 exposures of 1 to 5 L, whereas multilayer desorption rates were taken from the TPD spectra for SO_2 exposures of 10 to 200 L. Figure 6.7 (bottom left) shows an order plot for monolayer and multilayer desorption at a fixed temperature of 112 K, constructed from the TPD spectra in figures 6.1 and 6.2 (shown in figure 6.7 top left and top right). Using a fixed temperature of 112 K, desorption orders of 0.72 and 0.05 were obtained for monolayer and multilayer SO_2 respectively. Using a range of fixed temperatures between 110 and 114 K, shown in table 6.2, average desorption orders for monolayer and multilayer SO_2 were found to be 0.72 ± 0.04 and 0.05 ± 0.04 respectively.

Monolayer desorption is found to be fractional, rather than 1st order as expected from qualitative analysis of the low SO_2 exposure TPD spectra (figure 6.1). This suggests that the desorption of monolayer SO_2 is not as coverage dependent as would otherwise be expected for monolayer desorption of an ideal adsorbate. Multilayer desorption however is 0th order, in agreement with qualitative analysis of the high SO_2 exposure TPD spectra (figure 6.2), confirming the assignments given. Comparing with the monolayer and multilayer desorption

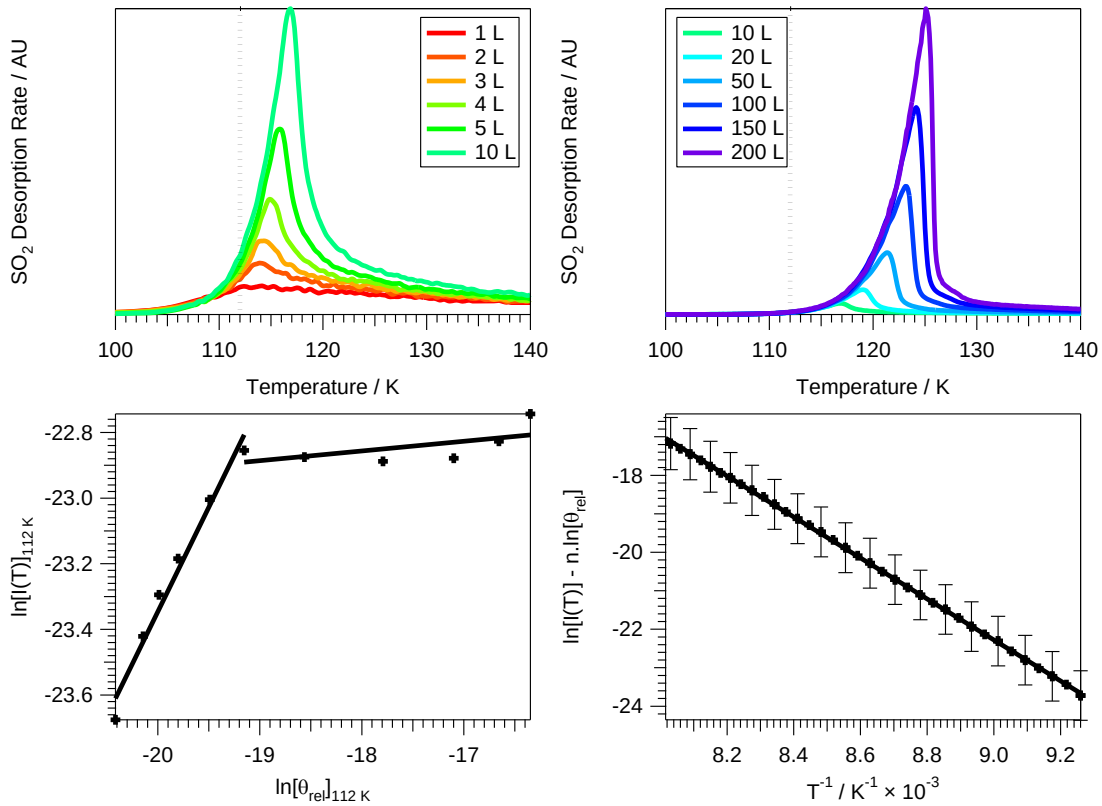

Figure 6.7. (Top left) TPD spectra of monolayer SO_2, taken from figure 6.1, showing SO_2 exposures of 1 to 10 L. (Top right) TPD spectra of multilayer SO_2, taken from figure 6.2, showing SO_2 exposures of 10 to 200 L. Also shown as a dotted line in both figures is the fixed temperature of 112 K. (Bottom left) Plot of ln[I(T)] against ln[θ_{rel}] at a fixed temperature of 112 K, producing desorption orders for monolayer and multilayer desorption. (Bottom right) Plot of ln[I(T)] – n.ln[θ_{rel}] against 1/T from the TPD spectrum produced following a 200 L exposure of SO_2, using n as 0.05 ± 0.04. This line has a gradient of -E_{des}/R.

Table 6.2. Calculated desorption orders for monolayer and multilayer SO_2 adsorbed on HOPG at 20 K.

Set Temperature / K	Monolayer Desorption Order, n	Multilayer Desorption Order, n
110.0		0.03
110.5		0.03
111.0		0.04
111.5		0.03
112.0	0.72	0.05
112.5	0.71	0.06
113.0	0.75	0.07
113.5		0.07
114.0		0.07

orders found for CO_2 and CS_2 ices (chapters 4 and 5 respectively), summarised in table 6.3, shows no specific trends for the monolayer desorption order found for each ice. However, analysis of the monolayer desorbing species is often difficult as the rate of desorption is inherently smaller for monolayers, and there is a finite adsorbate exposure range over which monolayers are observed in the TPD spectra. The CO_2, SO_2 and CS_2 monolayer ices are all close to 1st order, as expected for monolayer desorption. A trend in the multilayer desorption order is observed for the sulphur substituted analogues of CO_2, where a slight increase in the desorption order coincides with increasing molecule size. However, the multilayer desorption order for CO_2 ice was assumed to be 0 from inspection of CO_2 TPD spectra (chapter 4).

Table 6.3. Average desorption orders for monolayer and multilayer CO_2, SO_2 and CS_2 adsorbed on HOPG at 33, 20 and 20 K respectively.

Ice	Monolayer Desorption Order, n	Multilayer Desorption Order, n
CO_2	0.73 ± 0.02	0
SO_2	0.65 ± 0.02	0.05 ± 0.04
CS_2	0.88 ± 0.07	0.14 ± 0.05

Desorption Energies. It is also possible to determine the desorption energy of SO_2 monolayers and multilayers adsorbed on HOPG, to obtain an indication of the binding strength within the monolayer and multilayers, and between the adsorbate and the surface. Using the desorption orders calculated above, the desorption energy of the monolayer and multilayer can be determined via a plot of $\ln[I(T)] - n\ln[\theta_{rel}]$ against 1/T, taking the gradient as $-E_{des}/R$. The error in $\ln[I(T)] - n.\ln[\theta_{rel}]$ was taken to be $\Delta n.\ln[\theta_{rel}]$, thus the error in the desorption order contributes to the error in the desorption energy. Figure 6.7 (bottom right) shows a plot to determine the desorption energy for a 200 L exposure of SO_2, using a value of n of 0.05 ± 0.04. The gradient of the plot gives a desorption energy of 44.3 ± 1.3 kJ mol^{-1}. The average desorption energy for monolayer SO_2 was determined for exposures between 1 and 5 L, and the average desorption energy for multilayer SO_2 was determined for exposures between 10 and 200 L, shown in table 6.4. Average desorption energies were found to be 38.0 ± 3.4 and 44.2 ± 4.5 kJ mol^{-1} for monolayer and multilayer species respectively.

The monolayer and multilayer desorption energies calculated here are comparable to those of other physisorbed species[51-55]. However, the desorption energy of pure SO_2 ices determined from infrared spectra of multilayer SO_2, 28.8 ± 0.3 kJ mol^{-1},[43] is in disagreement with the energy of multilayer SO_2 found here. This is likely to be due to the assumptions used in the method for determining the desorption energy from infrared spectra. As discussed previously, deriving desorption energies from infrared studies of multilayer SO_2 requires the assumption that the desorption order is 0, and that the pre-exponential factor is 2.4×10^{12} s^{-1}. This is not a valid assumption, as a desorption order of 0 is common for multilayers and a pre-exponential factor of 2.4×10^{13} s^{-1} is common for monolayers of an ideal adsorbate[52].

Table 6.4. Calculated desorption energies for monolayer and multilayer SO_2 adsorbed on HOPG at 20 K.

Monolayer		Multilayer	
SO_2 exposure / L	Desorption Energy, E_{des} kJ mol^{-1}	SO_2 exposure / L	Desorption Energy, E_{des} / kJ mol^{-1}
3	33.0 ± 2.4	10	41.2 ± 2.4
4	39.0 ± 1.7	20	44.3 ± 2.4
5	42.1 ± 1.8	50	43.8 ± 1.8
		100	45.5 ± 1.5
		150	46.0 ± 1.3
		200	44.3 ± 1.3

Comparing with the monolayer and multilayer desorption energies found for CO_2 and CS_2 ices (chapters 4 and 5 respectively), summarised in table 6.5, shows that the multilayer energies of SO_2 and CS_2 ices are comparable. Comparing the desorption energies for monolayer and multilayer CO_2 ice (chapter 4) with those for SO_2 ice, shows an increase in the desorption energy with increasing molecule size. This was also observed when comparing CO_2 and CS_2 ices, and again is in agreement with the trend observed in the sublimation temperature from CO_2 and SO_2 TPD spectra.

Table 6.5. Average desorption energies for monolayer and multilayer CO_2, SO_2 and CS_2 ice adsorbed on HOPG at 33, 20 and 20 K respectively.

Ice	Monolayer Desorption Energy, E_{des} / kJ mol^{-1}	Multilayer Desorption Energy, E_{des} / kJ mol^{-1}
CO_2	20.2 ± 2.2	24.8 ± 1.6
SO_2	38.0 ± 3.4	44.2 ± 4.5
CS_2	45.3 ± 6.2	44.1 ± 6.0

Pre-exponential factors. The pre-exponential factor for desorption can also be determined from the TPD spectra. To determine the pre-exponential factor for the desorption process, the absolute coverage of SO_2 adsorbed on HOPG must be determined. This can be determined by calculating the rate of impingement of SO_2 molecules on the HOPG surface. Using the method described in chapter 2, the rate of impinging SO_2 molecules on the HOPG surface, as a function

of SO_2 exposure, is 3.80×10^{14} molec L^{-1}. However, due to the 10 mm diameter aperture on the quadrupole mass spectrometer (QMS), only 39% of the molecules on the HOPG surface will be detected in the TPD experiment. Therefore the number of molecules which will pass through the QMS aperture as a function of SO_2 exposure will be 1.49×10^{14} molec L^{-1}. This number can be used to convert the relative coverage, previously determined as the area under each TPD spectrum, to actual coverage by scaling using the relationship between the integrated TPD peak area and actual SO_2 exposure. From figure 6.3, the area under each TPD spectrum as a function of SO_2 exposure, in arbitrary units, produced a linear fit with a gradient 3.94×10^{-10} L^{-1}. This gives a scaling factor for the surface coverage conversion of 3.79×10^{23} molec.

Table 6.6. Calculated pre-exponential factors for monolayer and multilayer SO_2 adsorbed on HOPG at 20 K.

Monolayer		Multilayer	
SO_2 exposure / L	Pre-Exponential Factor, ν_n / (molec m^{-2})$^{0.28}$ s^{-1}	SO_2 exposure / L	Pre-Exponential Factor, ν_n / (molec m^{-2})$^{0.95}$ s^{-1}
1	$1.86 \times 10^{22 \pm 0.6}$	10	$3.21 \times 10^{33 \pm 0.9}$
2	$1.78 \times 10^{22 \pm 0.6}$	20	$2.56 \times 10^{33 \pm 0.9}$
3	$1.39 \times 10^{22 \pm 0.6}$	50	$2.86 \times 10^{33 \pm 1.0}$
4	$1.25 \times 10^{22 \pm 0.5}$	100	$2.48 \times 10^{33 \pm 1.0}$
5	$1.15 \times 10^{22 \pm 0.6}$	150	$2.90 \times 10^{33 \pm 1.0}$
		200	$2.81 \times 10^{33 \pm 1.0}$

To determine the pre-exponential factor, the Polanyi-Wigner equation can be rearranged as shown in chapter 2. The error in ν_n was taken as $\nu_n\sqrt{(\Delta n^2 + \Delta E_{des}{}^2)}$. Average pre-exponential factors for monolayer SO_2 were determined from TPD spectra for SO_2 exposures of 1 to 5 L, whereas average pre-exponential factors for multilayer SO_2 were determined from TPD spectra for SO_2 exposures of 10 to 200 L. The results are shown in table 6.6. Average pre-exponential factors were thus calculated to be $1.49 \times 10^{22 \pm 1.0}$ (molec m^{-2})$^{0.28}$ s^{-1} and $2.80 \times 10^{33 \pm 1.4}$ (molec m^{-2})$^{0.95}$ s^{-1} for monolayer and multilayer SO_2 respectively, where the units are given as (molec m^{-2})$^{1-n}$ s^{-1}.

The multilayer pre-exponential factor determined here is in agreement with the multilayer pre-exponential factors found for a range of physisorbed adsorbates[51,53-55,57], and with that found for multilayer CO_2 and CS_2 desorption (chapters 4 and 5 respectively), summarised in table 6.7. Monolayer pre-exponential factors are often taken as $1 \times 10^{12 - 13}$ s^{-1},[62-64] the vibrational frequency of a molecule on a surface. However, this is not observed for monolayer SO_2 and CS_2 ice (chapter 5). This may be caused by the fractional desorption orders found for SO_2 and CS_2 monolayer ice, where the monolayer desorption is not perfect 1st order as expected.

Table 6.7. Average desorption pre-exponential factors for monolayer and multilayer CO_2, SO_2 and CS_2 ices adsorbed on HOPG at 33, 20 and 20 K respectively.

Ice	Monolayer Pre-Exponential Factor, ν_n / (molec $m^{-2})^{n-1}$ s^{-1}	Multilayer Pre-Exponential Factor, ν_n / (molec $m^{-2})^{n-1}$ s^{-1}
CO_2	$9.32 \times 10^{14 \pm 0.9}$	$1.07 \times 10^{30 \pm 1.5}$
SO_2	$1.49 \times 10^{22 \pm 1.0}$	$2.80 \times 10^{33 \pm 1.4}$
CS_2	$3.39 \times 10^{21 \pm 1.4}$	$1.60 \times 10^{31 \pm 1.5}$

6.3.2. SO_2/H_2O Ice Layers

The study of binary layered ices of SO_2 adsorbed on H_2O, and reverse layered ices of H_2O adsorbed on SO_2 is important to understand the effect of H_2O on the adsorption and desorption of SO_2. There is evidence that H_2O rich ices undergo segregation upon warming[65] and so the study of layered ices is of direct relevance to astrochemistry. It is also necessary to characterise SO_2/H_2O binary and reverse ices in order to better understand more complex systems, such as SO_2:H_2O mixtures. RAIR and TPD spectra were obtained for SO_2 adsorbed on a 100 L exposure of pre-adsorbed ASW, and a 100 L exposure of H_2O adsorbed on a range of pre-adsorbed exposures of SO_2 on a HOPG surface at 20 K.

6.3.2.1. TPD Data

Binary Layers. Figures 6.8 and 6.9 show TPD spectra for a range of exposures of SO_2 adsorbed on 100 L of H_2O, adsorbed on HOPG at 20 K. At the lowest exposure of SO_2, 1 L, three peaks are observed in the TPD spectrum; a broad peak centred at 120 K, and two high temperature peaks at 163 and 172 K (figure 6.8). The two high temperature peaks were not observed in TPD spectra of pure SO_2 ice (figures 6.1 and 6.2). Increasing the SO_2 exposure, up to 200 L, shows no change in the peak temperature of either high temperature peak. Increasing the SO_2 exposure to 20 L shows little change in the temperature of the low temperature peak, which remains at 120 K. Further increase of the SO_2 exposure, between 20 and 200 L, shows a gradual increase in the temperature of the lower peak to 125 K following a 200 L exposure of SO_2 (figure 6.9). TPD spectra of SO_2 exposures between 20 and 200 L also show shared leading edges on the low temperature peak.

Figures 6.8 and 6.9 also show a H_2O TPD spectrum for a 100 L exposure of H_2O covered by SO_2. The spectrum shows a large peak, with a temperature of 172 K, and a bump on the leading edge at 163 K. The bump at 163 K arises due to the irreversible phase change of ASW to CI, and the peak at 173 K is assigned to the desorption of multilayers of physisorbed CI[51]. No changes in the H_2O spectrum are observed with increasing SO_2 exposure.

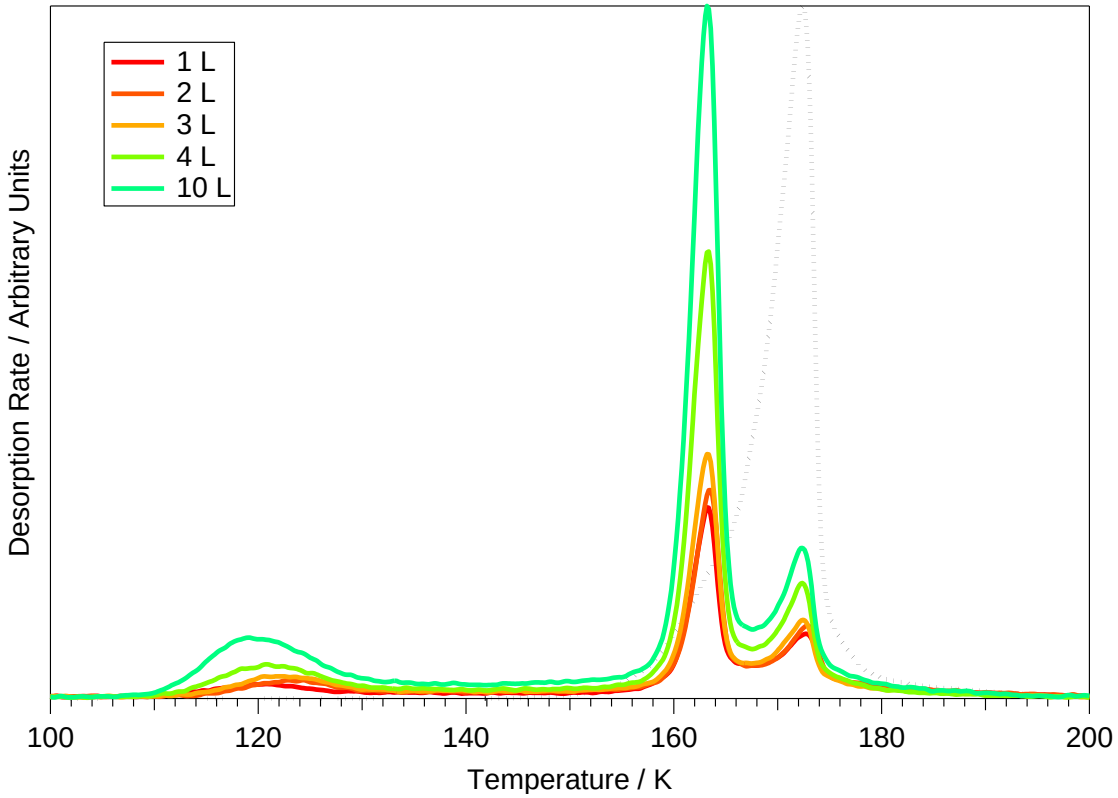

Figure 6.8. TPD spectra of low exposures of SO_2, up to 10 L, adsorbed on 100 L of H_2O on a HOPG surface at 20 K. The H_2O TPD spectrum following a 10 L exposure of SO_2 adsorbed on 100 L of H_2O is shown in black.

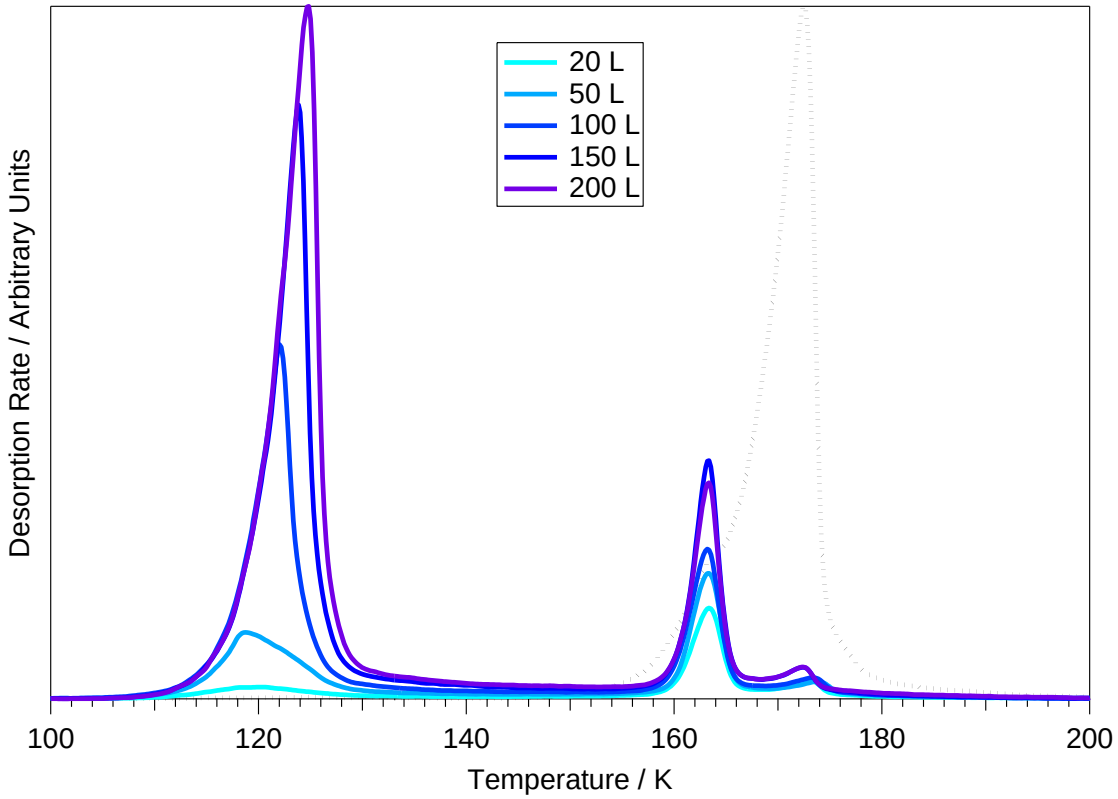

Figure 6.9. TPD spectra of high exposures of SO_2, above 20 L, adsorbed on 100 L of H_2O on a HOPG surface at 20 K. The H_2O TPD spectrum following a 200 L exposure of SO_2 adsorbed on 100 L of H_2O is shown in black.

Integration of the SO_2 TPD spectra from figures 6.8 and 6.9 shows a linear relationship between the total area and exposure of SO_2, shown in figure 6.10. This indicates a constant sticking probability for SO_2 adsorption on the ASW surface at 20 K. The total integrated area does not saturate up to exposures of 200 L, indicating that multilayers of physisorbed SO_2 form on the ASW surface at 20 K.

Assignment of the desorption features can be made by comparison with the TPD spectra of pure SO_2 on a HOPG surface (figures 6.1 and 6.2) as well as with previous studies of binary ices of other volatile molecules on H_2O[45,66-68], including CO_2 and CS_2 (chapters 4 and 5). The two high temperature SO_2 TPD features are coincident with the ASW - CI transition and the desorption of CI respectively. They can therefore be assigned to SO_2 trapped within the porous ASW surface, as also observed for binary ices of CO_2 and CS_2 on ASW (chapters 4 and 5). In particular the feature at 163 K can be assigned to the volcano desorption of SO_2, whereas the feature at 172 K can be assigned to the co-desorption of SO_2 with the H_2O film. The low temperature peak, between 120 - 125 K, can be assigned to monolayer and multilayer SO_2 formation on the ASW surface, in agreement with pure SO_2 TPD spectra (figures 6.1 and 6.2). The low temperature peaks in the TPD spectra of monolayer coverages of SO_2 adsorbed on an

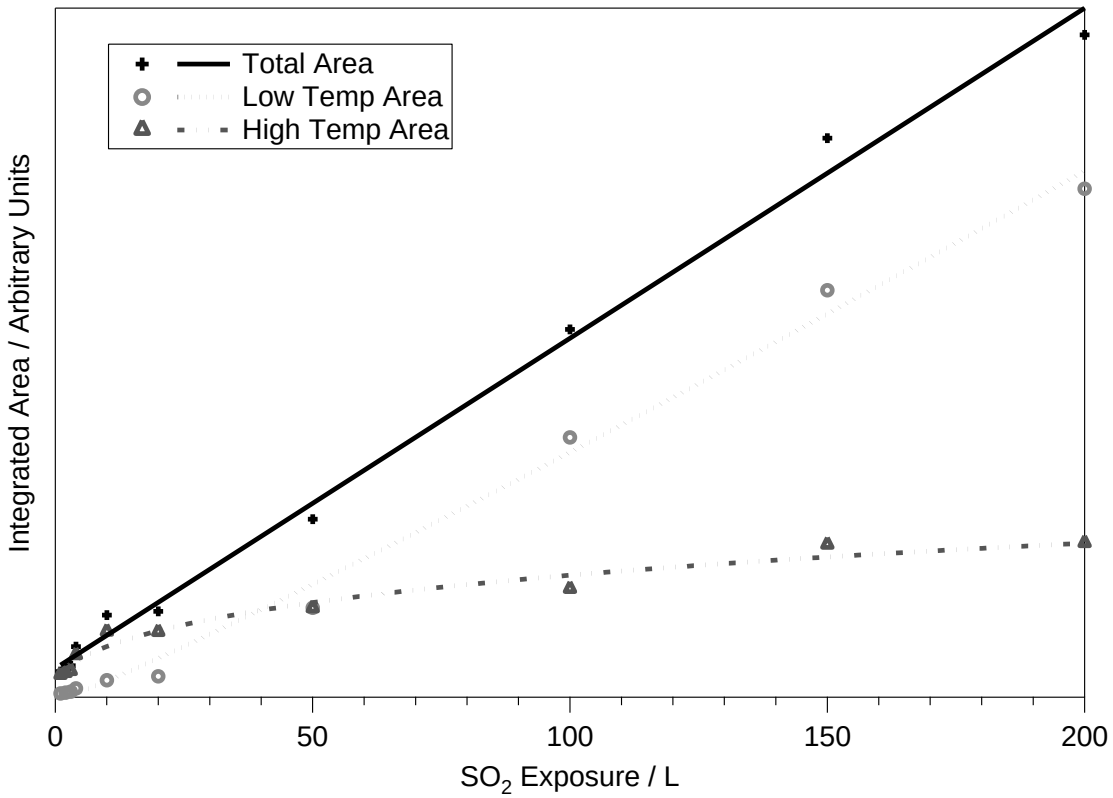

Figure 6.10. Integrated area of the TPD spectra shown in figures 6.8 and 6.9 as a function of exposure of SO_2. The areas of the low temperature peaks, the combined areas of the two high temperature peaks at 163 and 172 K, and the total SO_2 area from all three peaks, are shown. Lines are supplied as a guide to the eye.

ASW film are broader than those for pure SO_2. This reflects the heterogeneity of the ASW surface, where a larger range of binding sites exist on a rough ASW surface than on a flat HOPG surface.

Figure 6.10 also shows the contributions to the total SO_2 area from the low temperature peak at 120 - 125 K, and the two high temperature peaks at 163 and 172 K. Clearly, the high temperature peaks, relating to SO_2 trapped within the ASW surface, begin to saturate following an exposure of approximately 100 L. The total area of the two trapped features, following saturation of the ASW surface above exposures of 100 L, equates to a 42 L exposure of SO_2. The trapped features in the CO_2 and CS_2 TPD spectra were found to be due to 8 and 44 L equivalent exposures respectively (chapters 4 and 5). This shows that CO_2 readily diffuses through the ASW surface, whereas SO_2 and CS_2 show more limited diffusion, and remain trapped to desorb with the H_2O. Upon adsorption of CO_2, SO_2 or CS_2 on ASW, the pores of the ASW surface fill with the adsorbate until the surface is covered. Upon warming, as the pores of the ASW surface close, the adsorbed molecules within these pores become trapped. Smaller adsorbates, such as CO_2, can diffuse through the H_2O film to desorb close to their natural sublimation temperature. However, larger molecules such as SO_2 and CS_2, will not as readily diffuse through the H_2O matrix, and hence a greater volume of SO_2 and CS_2 traps within the ASW surface.

Quantitative analysis was also conducted on the TPD spectra for SO_2 adsorbed on 100 L of H_2O, summarised in table 6.8. Monolayer SO_2 was found to desorb with an order of 0.80 ± 0.04 and pre-exponential factor of $1.85 \times 10^{14 \pm 1.3}$ (molec m^{-2})$^{0.2}$ s^{-1}, both of which are common for monolayer desorption. The monolayer desorption energy for SO_2 on an ASW surface was found to be 28.3 ± 10.6 kJ mol^{-1}, considerably smaller than the energy for monolayer desorption of pure SO_2 ice, 38.0 ± 3.4 kJ mol^{-1}. However, the desorption of monolayer SO_2 will be greatly affected by the nature of the underlying surface. As the ASW surface is rough and heterogeneous, there are a large number of binding sites from which surface bound SO_2 can desorb. This results in a broad TPD feature, creating difficulty in analysis of an accurate monolayer desorption energy, resulting in an energy with a large error and a fractional desorption order. This is in agreement with previous studies, where monolayer desorption from amorphous surfaces give rise to a fractional desorption order[52]. The monolayer energies for SO_2 desorption from a HOPG and ASW surface are both within the range of expected values for a physisorbed adsorbate, as well as within each others error range.

Multilayer SO_2 was found to desorb with an order of 0.02 ± 0.02 and pre-exponential factor of $2.19 \times 10^{33 \pm 0.9}$ (molec m^{-2})$^{0.98}$ s^{-1}, both of which are common for multilayer desorption and in agreement with pure SO_2 desorption. The energy for multilayer SO_2 desorption from an ASW

surface is 42.5 ± 3.2 kJ mol^{-1}, also in agreement with the desorption of pure SO_2 ice, 44.2 ± 4.5 kJ mol^{-1}.

Table 6.8. Average kinetic parameters for monolayer and multilayer SO_2 desorbing from 100 L of H_2O on HOPG at 20 K.

SO_2 population	N	E_{des} / kJ mol^{-1}	ν_n / (molec m^{-2})$^{1-n}$ s^{-1}
Monolayer	0.80 ± 0.04	28.3 ± 10.6	$1.85 \times 10^{14 \pm 1.3}$
Multilayer	0.02 ± 0.02	42.5 ± 3.2	$2.19 \times 10^{33 \pm 0.9}$

Reverse Layers. To gain better insight into the trapping and diffusion of SO_2 in and through an ASW film, TPD spectra of reverse binary layered ices of H_2O adsorbed on SO_2 on a bare HOPG surface at 20 K were collected. Figure 6.11 shows a comparison between TPD spectra for a 20 L exposure of SO_2 adsorbed on 100 L of H_2O, and a 100 L exposure of H_2O adsorbed on top of a 20 L exposure of SO_2, both adsorbed on HOPG at 20 K. Two desorption features are observed in the SO_2 TPD spectra of reverse binary ice layers, at 163 and 172 K. The H_2O TPD spectrum from reverse binary ice layers is the same as that from binary ice layers of SO_2 on H_2O, showing a large peak, with peak temperature of 172 K, and a bump on the leading edge at 163 K.

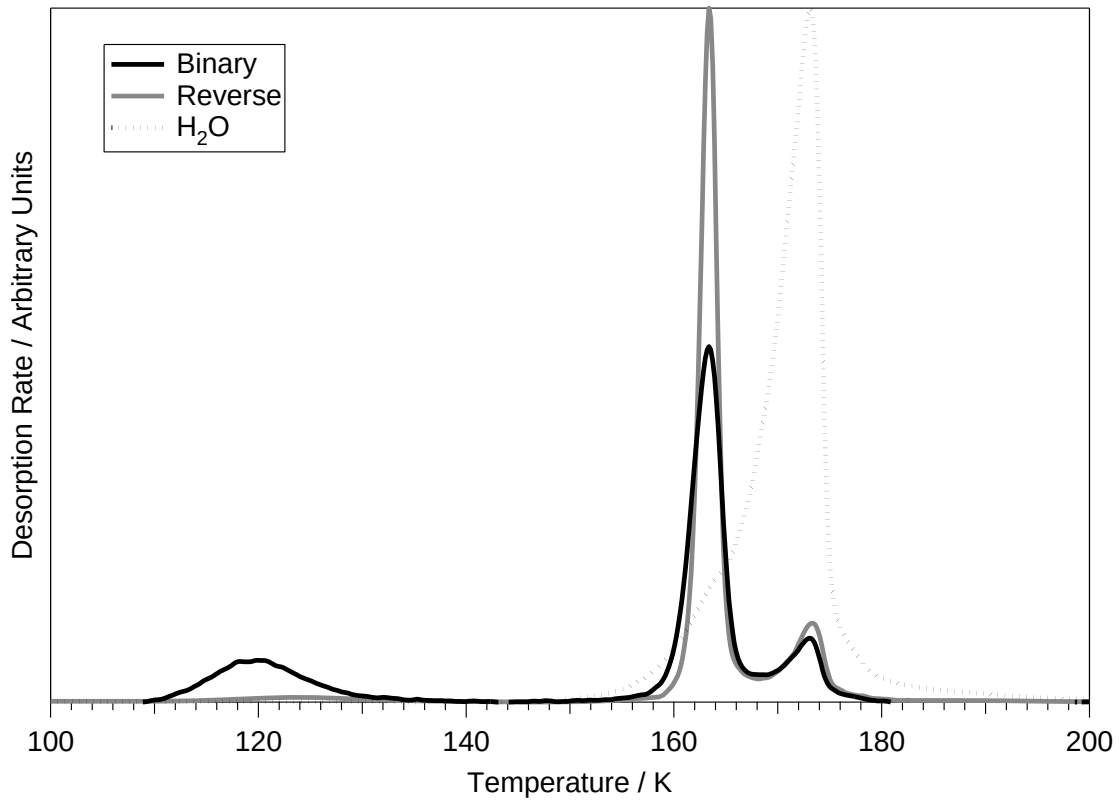

Fig 6.11. TPD spectra of a 20 L exposure of SO_2 adsorbed on a 100 L exposure of H_2O and a 100 L exposure of H_2O adsorbed on a 20 L exposure of SO_2, adsorbed on a HOPG surface at 20 K. Shown in black is the H_2O TPD spectrum following a 20 L exposure of SO_2 adsorbed on 100 L of H_2O on a HOPG surface at 20 K.

Assignments of the SO_2 TPD peaks are the same as those for layered ices of SO_2 on H_2O. Desorption of SO_2 at its natural sublimation temperature does not occur in reverse binary layered ices of H_2O on SO_2. As SO_2 would have to diffuse through the ASW film in order for this to happen, the lack of this peak indicates that the ability of SO_2 to diffuse through ASW is limited. This is in agreement with reverse binary ices of H_2O on CS_2 (chapter 5). However, diffusion is observed in reverse layered ices of H_2O on CO_2 (chapter 4), and so the lack of diffusion for SO_2 and CS_2 through an ASW film is caused by the increased size of the SO_2 and CS_2 molecules.

6.3.2.2. RAIRS Data

A range of exposures of SO_2 were adsorbed on 100 L of H_2O on HOPG at 20 K. Following a 100 L exposure of H_2O, two infrared bands are observed in the RAIR spectrum as shown in figure 4.11 (chapter 4). A very broad feature is observed around 3420 cm^{-1} and a small peak is observed at 1670 cm^{-1}. These are assigned to the $\nu_{(OH)}$ stretching mode and HOH scissors mode of ASW respectively[51]. No changes are observed in the H_2O vibrational bands following exposure of the H_2O surface to SO_2.

RAIR spectra of a range of exposures of SO_2 adsorbed on 100 L of H_2O on HOPG at 20 K, in the wavenumber range of the SO_2 ν_1 and ν_3 stretches (1100 to 1400 cm^{-1}), are shown in figure 6.12. At the lowest exposure of SO_2, 1 L, two broad infrared bands are observed at 1342 and 1153 cm^{-1}. Further exposure of SO_2 shows no significant change in the infrared spectra, and the two bands gradually shift to reach 1346 and 1151 cm^{-1} respectively following an exposure of 100 L.

Integration of the infrared bands as a function of exposure shows the same trends as observed for the pure SO_2 RAIR spectra (figure 6.5). In agreement with the trend previously observed, a linear fit can be applied for exposures between 1 and 5 L, and between 5 and 200 L. As discussed previously, this effect is not due to a change in the sticking probability of SO_2 adsorption, nor is it likely to be due to a change in the molecular orientation of SO_2 on the surface. Instead, this trend suggests the formation of monolayer and multilayer SO_2 as also observed in TPD spectra of binary layers of SO_2 on ASW (figures 6.8 and 6.9). At first glance, this appears to be counter-intuitive, as ASW has a larger surface area than the HOPG surface, and therefore it would be expected that a greater exposure of SO_2 would be required to saturate the ASW surface with a monolayer. However, this is not too dissimilar to the trend observed in the TPD spectra of pure SO_2 and layered ice of SO_2 on H_2O (figures 6.1, 6.2, 6.8 and 6.9), where monolayer saturation appears to occur for an exposure of SO_2 between 10 and 20 L. The unexpected similarities in the onset of multilayer formation and monolayer

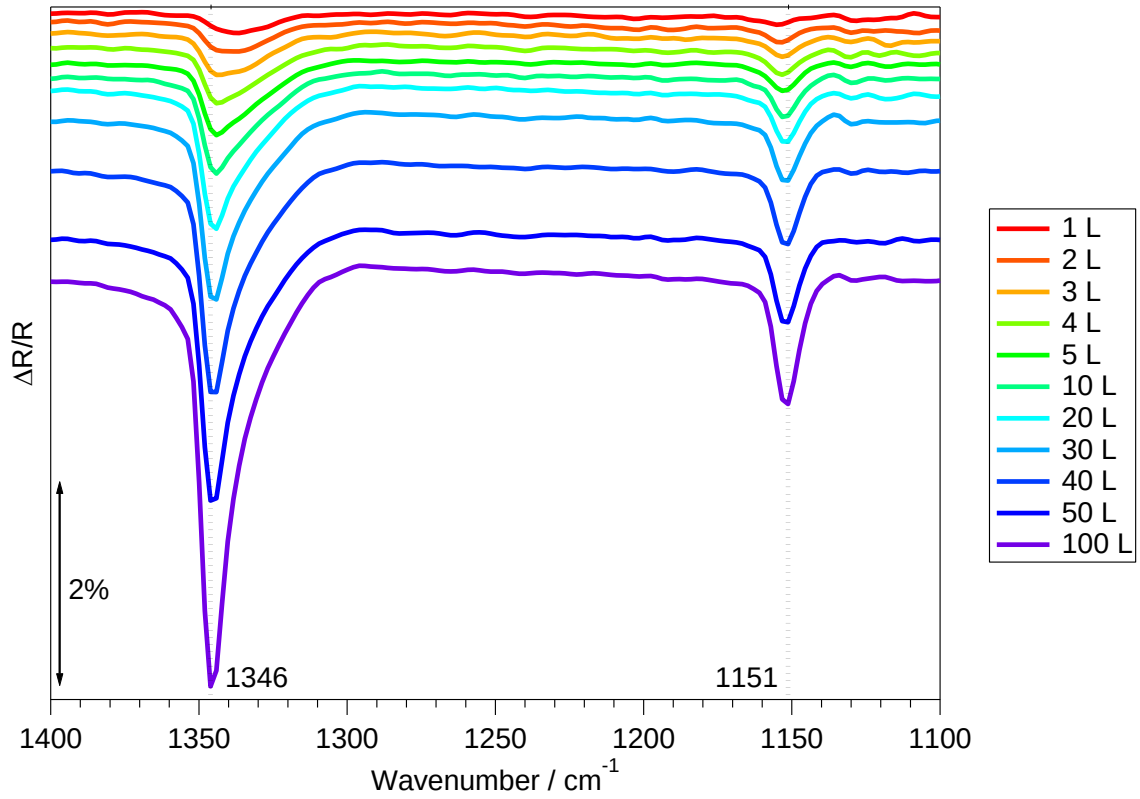

Figure 6.12. RAIR spectra of a range of exposures of SO_2 adsorbed on a 100 L exposure of H_2O adsorbed on a HOPG surface at 20 K.

saturation of SO_2 on a bare HOPG surface and ASW surface in the RAIR and TPD spectra may be due to the size of SO_2, with respect to the size of the pores in the ASW surface. For example, if SO_2 is too large to fill the pores within the ASW surface, its relative surface area will not be very different to the ordered HOPG surface. In this case the onset of multilayer formation and saturation of the monolayer would be expected to occur following the same SO_2 exposure, as observed.

Warming the HOPG surface provides information about the temperature dependent behaviour of the SO_2 ice adsorbed on ASW, as well as investigating the characteristics of trapped SO_2 in ASW. RAIR spectra following warming of a 100 L exposure of SO_2 adsorbed on 100 L of H_2O are shown in figure 6.13. The trends observed for the H_2O $\nu_{(OH)}$ stretch are the same as those observed in the RAIR spectra of CO_2 on H_2O (figure 4.14, chapter 4). Warming the HOPG surface to between 20 and 40 K shows no significant changes to the observed infrared features (figure 6.13). Upon warming the HOPG surface to 50 K, a slight shift in the infrared band at 1151 cm^{-1} to 1149 cm^{-1} is observed, as well as the appearance of two very small bands on the low wavenumber side of the 1346 cm^{-1} band, at 1317 and 1306 cm^{-1}. Further warming to 90 K shows a broadening of the band at 1346 cm^{-1} with an associated shift to 1342 cm^{-1}. Warming to 100 K shows further broadening of the band at 1342 cm^{-1} and a further shift to 1338 cm^{-1}. The band at 1149 cm^{-1} also sharpens slightly following warming to

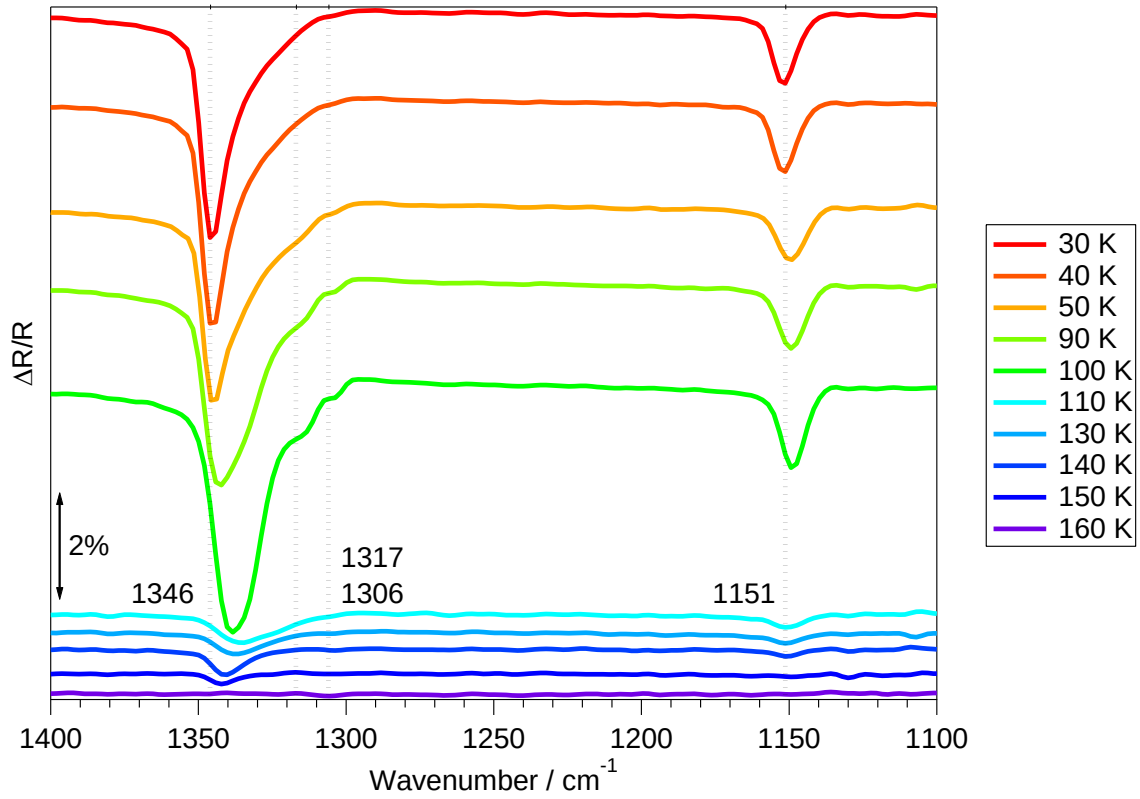

Figure 6.13. RAIR spectra of a 100 L exposure of SO_2 adsorbed on a 100 L exposure of H_2O adsorbed on a HOPG surface at 20 K, prior to warming to a range of temperatures.

100 K. Further warming to 110 K shows a large decrease in the intensity of the SO_2 infrared bands so that only two shallow bands are observable at 1335 and 1151 cm^{-1}. Warming to 140 K shows a gradual increase in the wavenumber of the 1335 cm^{-1} band to 1340 cm^{-1}. The band at 1151 cm^{-1} is no longer visible in the RAIR spectra upon warming to 150 K, and the size of the band at 1340 cm^{-1} has decreased further. An increase in size and a split of the $\nu_{(OH)}$ stretch of ASW into a three component infrared band, with peaks at 3360, 3245 and 3160 cm^{-1} (similar to that observed in figure 4.14, chapter 4), characteristic of CI[51], is also observed upon warming to 150 K. Following warming to 160 K, no infrared features are observed, indicating desorption of the SO_2 and H_2O ice from the HOPG surface.

Integration of the SO_2 infrared bands as a function of temperature shows the thermal behaviour of the ice, and provides further evidence for trapping of SO_2 within the H_2O ice. Figure 6.14 shows the integrated area of the infrared band initially observed at 1346 cm^{-1}, as a 100 L exposure of SO_2 on 100 L of H_2O and a 100 L exposure of SO_2 on HOPG is incrementally warmed, from figures 6.13 and 6.6 respectively. As evident from figure 6.14, the onset of desorption of SO_2 begins around 100 K. By 120 K complete desorption has occurred for the pure SO_2 ice, whereas a certain amount of SO_2 remains on the surface in the H_2O-dominant layer. The integrated area of the SO_2 infrared band does not change between 120 and 140 K, indicating no evaporation of SO_2 from the H_2O film in this temperature range. As observed in

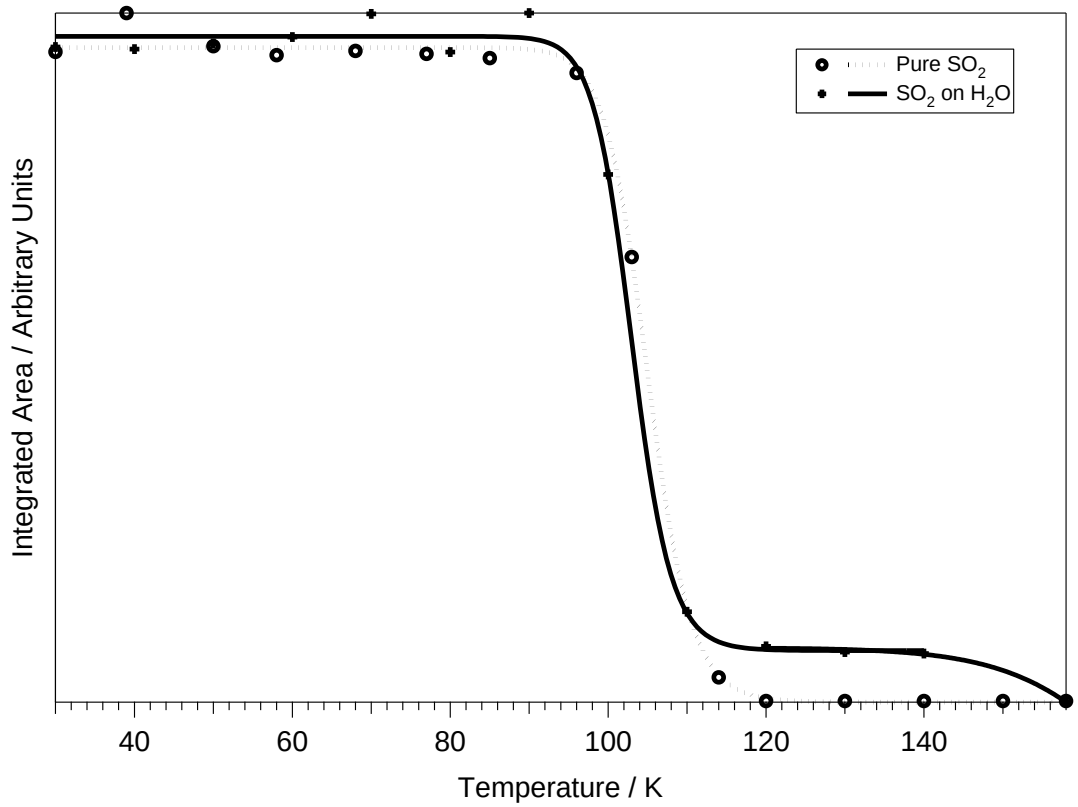

Figure 6.14. Integrated area of the asymmetric stretch of a 100 L exposure of SO_2 on HOPG (dotted line) and on 100 L of H_2O (solid line), from figures 6.6 and 6.13 respectively, as a function of ice temperature. The lines are supplied as a guide to the eye.

the RAIR spectra of layered SO_2/H_2O ice, the complete desorption of SO_2 occurs between 140 and 160 K.

Assignment of the observed infrared bands can be made by comparing with the RAIR spectra of pure SO_2 adsorbed on HOPG at 20 K (figures 6.4 and 6.5). The SO_2 infrared bands observed upon adsorption on an ASW surface are in agreement with those observed on a HOPG surface, and therefore the bands at 1151 and 1346 cm^{-1} can be assigned to the ν_1 stretch and LO mode of the ν_3 stretch respectively. No significant differences are observed in the RAIR spectra of SO_2 ices adsorbed on a HOPG or ASW surface, prior to warming each ice.

Upon warming, similar trends are observed in the RAIR spectra of SO_2 ice on a HOPG and ASW surface up to a surface temperature of ≈90 - 100 K. Above 90 K however, the RAIR spectra of SO_2 ice adsorbed on HOPG and ASW are no longer comparable. In the layered ices of SO_2 on H_2O the infrared band, initially observed at 1346 cm^{-1}, shifts to 1338 cm^{-1} at 100 K (figure 6.13). Following warming to 110 K, desorption of the bulk of the SO_2 is observed in the RAIR spectra. This is in agreement with the RAIR spectra of pure SO_2 ice (figure 6.5), as well as with the onset of desorption from TPD spectra of SO_2 on HOPG and ASW (figures 6.1, 6.2, 6.8 and 6.9). However, two SO_2 infrared bands are still observed in the RAIR spectra of SO_2 on ASW, at 1335 and 1151 cm^{-1}, which are not observed in the pure SO_2 RAIR spectra. Warming

further shows a gradual increase in the wavenumber of the band at 1335 cm^{-1} to 1340 cm^{-1} at 140 K. At 150 K the band at 1151 cm^{-1} is no longer visible in the RAIR spectrum. This is coincident with the decrease in intensity of the SO_2 infrared band at 1340 cm^{-1} and with the changes observed in the $\nu_{(OH)}$ stretch, characteristic of the formation of CI. Therefore, from the changes in the $\nu_{(OH)}$ stretch, the ASW - CI transition has occurred between 140 and 150 K, and partial desorption of trapped SO_2 is observed. As the band at 1340 cm^{-1} and $\nu_{(OH)}$ stretch are not visible in the RAIR spectra upon warming to 160 K, complete desorption of the ice has occurred, and the remaining SO_2 has co-desorbed with CI. These high temperature features are in agreement with those observed in TPD spectra of binary layers of SO_2 on H_2O. This is also in agreement with previous studies of SO_2-bearing H_2O ices[30].

6.3.3. SO_2:H_2O Mixtures

RAIR and TPD spectra were obtained for a range of exposures of a 10% mixture of SO_2 and H_2O, co-deposited on a HOPG surface at 20 K. Mixtures of SO_2 and H_2O are the most astrophysically relevant system studied here, providing the most realistic analogy to interstellar ices.

6.3.3.1. TPD Data

Figure 6.15 shows TPD spectra of a range of exposures of a 10% SO_2:H_2O mixture adsorbed on HOPG at 20 K. Three desorption features are observed following the lowest SO_2:H_2O mixture exposure of 20 L; a broad peak centred at 121 K, and two high temperature peaks at 161 and 167 K. Increasing the SO_2:H_2O mixture exposure, up to 200 L, shows an increase in the size of all observed desorption features. No noticeable shift is observed in the peak at 161 K upon increasing the SO_2:H_2O mixture exposure to 200 L. The low temperature SO_2 peak at 121 K remains broad but becomes progressively more complex, and gradually increases in peak temperature to approximately 124 K upon increasing SO_2:H_2O exposure. An increase in the peak temperature of the high temperature SO_2 peak is also observed from 167 to 173 K following a 200 L exposure of the SO_2:H_2O mixture.

H_2O TPD spectra following a 20 L exposure of the SO_2:H_2O mixture show a single desorption feature with a peak temperature of 167 K. Although the bump on the H_2O TPD spectrum, characteristic of the ASW - CI transition, is not evident, the observation of SO_2 desorption at 161 K indicates that volcano desorption does occur, and therefore the phase transition also occurs at 161 K. The ASW - CI bump should be observed in the TPD spectra, in agreement with RAIR spectra, where its apparent lack may be caused by a low signal sensitivity during the

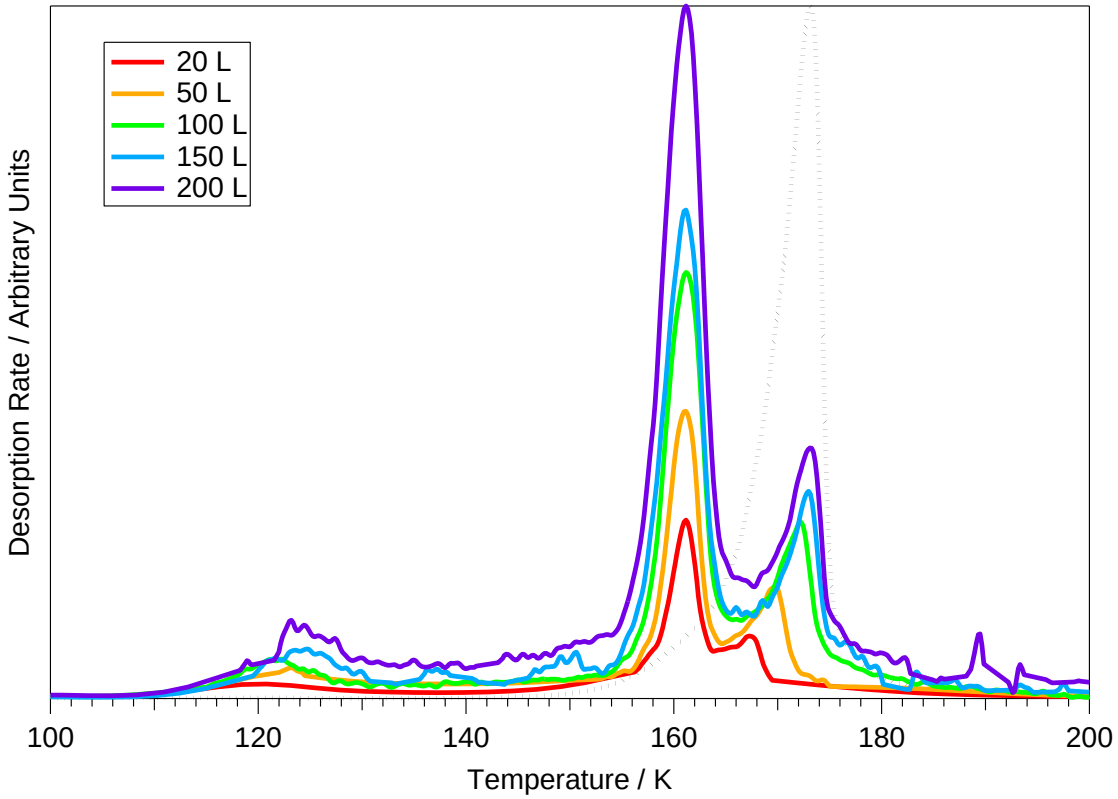

Figure 6.15. TPD spectra of a range of exposures of a 10% SO_2:H_2O mixture adsorbed on a HOPG surface at 20 K. Shown in black is the H_2O TPD spectra following a 200 L exposure of a 10% SO_2:H_2O mixture adsorbed on a HOPG surface at 20 K. Spectra were smoothed using a 7 point binomial function.

experiment, also causing the noisy SO_2 TPD spectra. Increasing the SO_2:H_2O mixture exposure to 200 L shows a gradual increase in the peak temperature of the H_2O peak to 173 K, whereas the bump at 161 K does not shift. Comparing with TPD spectra of pure H_2O ice[51], the two H_2O desorption features observed can be assigned to the ASW - CI transition at 161 K and to the desorption of CI between 167 and 173 K. As the exposure of H_2O increases with increasing SO_2:H_2O exposure, the peak temperature of the CI desorption feature increases, consistent with previous TPD studies of H_2O ice[51].

Assignments of the observed SO_2 desorption features are the same as those for layered ices. Diffusion of SO_2 through a H_2O matrix has been shown to be limited from TPD spectra of reverse layered ices of H_2O on SO_2 (figure 6.11). However, as the SO_2:H_2O mixture is intimately mixed, a proportion of the SO_2 will be found on, or close to, the surface of the ice and hence observation of SO_2 desorption at its natural sublimation temperature is observed from mixed ices. As the exact surface area and thickness of the mixed ice is unknown, the relative amount of surface bound SO_2 is also unknown. Desorption of SO_2 at its natural sublimation temperature from a mixed SO_2:H_2O ice is also in agreement with desorption of surface bound SO_2 from an ASW surface (figures 6.8 and 6.9).

Integration of the observed desorption features, as well as the total integrated area of all SO_2 peaks, shows a linear correlation between area and SO_2:H_2O mixture exposure. Comparing the total SO_2 integrated area with that of the high temperature desorption features indicates that, for all SO_2:H_2O exposures, approximately 86% of the SO_2 is trapped within the ice until the onset of H_2O desorption, and 14% of the SO_2 desorbs near its natural sublimation temperature.

6.3.3.2. RAIRS Data

The characteristics of SO_2:H_2O mixtures can also be probed by RAIRS, which when compared with TPD spectra, provides further evidence for the assignments made. Figure 6.16 shows RAIR spectra for a 100 L exposure of a 10% SO_2:H_2O mixture on HOPG at 20 K prior to being warmed to a range of temperatures. Upon adsorption of a 100 L exposure of the 10% SO_2:H_2O mixture, four infrared features are observed. A very broad feature is observed around 3420 cm^{-1} and a smaller, but still broad, peak is observed at 1670 cm^{-1}, in agreement with the RAIR spectra of a 100 L exposure of pure H_2O (figure 4.11, chapter 4). These are assigned to the $\nu_{(OH)}$ stretching mode and HOH scissors mode of ASW respectively[51]. Two SO_2 infrared

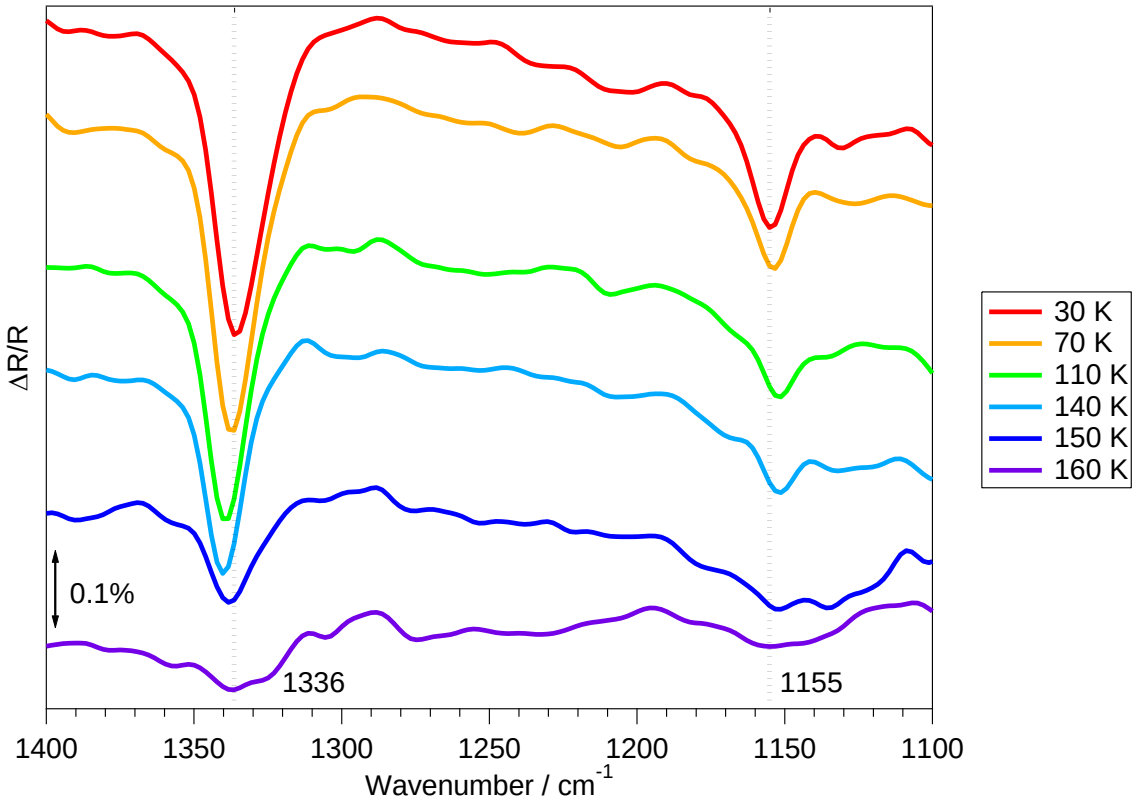

Figure 6.16 RAIR spectra of a 100 L exposure of a 10% SO_2:H_2O mixture adsorbed on a HOPG surface at 20 K prior to warming to a range of temperatures.

features are observed in the spectrum, at 1336 and 1155 cm^{-1}, assigned to the ν_3 and ν_1 stretches of SO_2 respectively. Obviously evident, from comparison with RAIR spectra of SO_2 adsorbed on a HOPG or ASW surface (figures 6.4 and 6.12 respectively), is the lack of the LO mode of the ν_3 stretch at 1346 cm^{-1}. This is a direct consequence of the nature of the mixed SO_2:H_2O ice, as the optical and physical properties of the SO_2 ice which are responsible for the observed LO - TO splitting are disrupted in intimately mixed ices with H_2O, which does not show LO - TO splitting (chapter 3). This is also observed for CO_2:H_2O and CS_2:H_2O mixtures (chapters 4 and 5 respectively). Instead, the band observed at 1336 cm^{-1} may be caused by H_2O bound SO_2, analogous to the RAIR spectra of mixed CO_2:H_2O and CS_2:H_2O ices (chapters 4 and 5 respectively).

Warming the HOPG surface to 70 K shows little change in the RAIR spectra of the SO_2:H_2O mixture. Further warming to between 70 and 110 K shows a gradual shift in the bands at 1336 and 1155 cm^{-1} to 1340 and 1151 cm^{-1} respectively (figure 6.16), and a marginal decrease in the size of the infrared bands at 110 K. Further warming to 140 K shows no change in the RAIR spectra. The band at 1151 cm^{-1} is no longer distinguishable in the RAIR spectra following warming to 150 K. A shift in the band at 1336 to 1338 cm^{-1} and a splitting of the $\nu_{(OH)}$ stretch of ASW into a three component infrared band with peaks at 3383, 3302 and 3164 cm^{-1}, characteristic of CI[51], is also observed in the RAIR spectrum at 150 K. The observed features in the H_2O $\nu_{(OH)}$ stretch are similar to those observed for layered and mixed CO_2-bearing H_2O ices (figures 4.14 and 4.24, chapter 4). Following warming to 160 K no infrared features are observed, indicating complete desorption of the SO_2:H_2O mixed ice from the HOPG surface.

The marginal decrease in the size of the infrared bands following warming to 110 K is in agreement with the desorption of SO_2 at its natural sublimation temperature from binary layers of SO_2 on ASW (figure 6.13). However, this decrease is only marginal which is in agreement with TPD spectra of SO_2:H_2O mixtures (figure 6.15), where only 14% of the SO_2 desorbs at its natural sublimation temperature. Between 140 and 150 K the ASW - CI transition has occurred, which coincides with partial desorption of the trapped SO_2. This is in agreement with the volcano desorption peak in the TPD spectra of SO_2:H_2O mixtures (figure 6.15). At 160 K complete desorption of the SO_2:H_2O mixture has occurred, relating to the co-desorption of SO_2 with CI peak in TPD spectra of SO_2:H_2O mixtures (figure 6.15).

6.4. Summary and Conclusions

RAIR and TPD spectra of pure SO_2 ices, binary and reverse layered ices of SO_2 and H_2O and SO_2:H_2O mixtures adsorbed on a bare HOPG surface at 20 K have been collected. RAIR and TPD spectra of pure SO_2 ice indicate that monolayer SO_2 forms, physisorbed on the HOPG surface,

followed by multilayer SO_2, also physisorbed on the SO_2 monolayer. Upon warming, RAIR spectra indicate that the SO_2 ice undergoes a phase change between 58 and 68 K, in agreement with previous studies[30]. Monolayer formation of SO_2, physisorbed on an ASW surface, followed by physisorbed multilayer SO_2 formation, has also been observed in RAIR and TPD spectra of binary layered ices of SO_2 on ASW.

Comparison of the TPD spectra of pure SO_2 with binary layered and mixed SO_2-bearing H_2O ices shows the characteristics of the trapping and diffusion of SO_2 through a H_2O matrix, as shown in figure 6.17. Three desorption processes have been observed for SO_2-bearing ices, occurring with varying degrees in each ice system. Pure SO_2 ices only show one desorption feature, at its natural sublimation temperature between 115 and 125 K, depending on ice thickness. Little modification to the natural sublimation peak of SO_2 is observed in the layered ices, as multilayer SO_2 forms on monolayer SO_2 in both pure and layered ices. However, this feature is greatly modified in mixed ices, as only surface bound species may desorb at the natural sublimation temperature of SO_2, and diffusion is limited. This is in agreement with reverse layered ices of H_2O on SO_2 where no SO_2 desorption at its natural sublimation temperature is observed, and hence diffusion of SO_2 does not occur.

Layered ices show a small degree of trapped SO_2, evidenced by the coincidence of SO_2

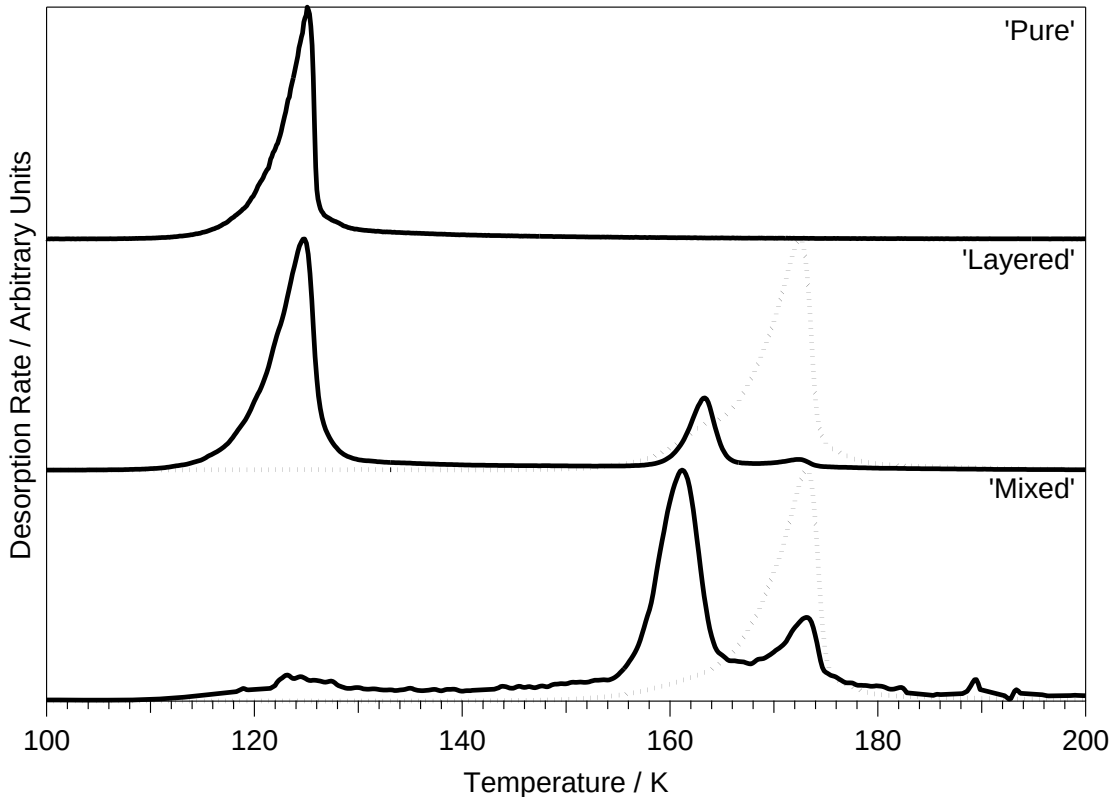

Figure 6.17. TPD spectra of; top - a 200 L exposure of SO_2, middle - a 200 L exposure of SO_2 on 100 L H_2O, bottom - a 200 L exposure of a 10% SO_2:H_2O mixture adsorbed on HOPG at 20 K.

desorption with the desorption of H_2O. The trapped SO_2 feature in layered ices is relatively small, as only surface bound SO_2 may trap within the pores of ASW as diffusion is limited. This is contrary to the observation of trapped features in mixed ices, where the majority of SO_2 desorption occurs with the H_2O features. This behaviour has direct implications for astrochemical models, where the injection of SO_2 into the gas phase will occur predominantly with H_2O, rather than at the natural sublimation temperature of SO_2.

Quantitative analysis of TPD spectra of SO_2 ice adsorbed on a HOPG and ASW surface at 20 K has been conducted. Kinetic data for desorption from these surfaces has been determined, and is summarised in table 6.9. Desorption orders, energies and pre-exponential factors for multilayer SO_2 desorption from a HOPG and ASW surface are the same, irrespective of the underlying surface. This is expected as multilayer SO_2 desorption is describing desorption of SO_2 bound to monolayer SO_2, irrespective of whether the monolayer is bound to a HOPG or ASW surface. Desorption orders and pre-exponential factors for multilayer desorption are approximately 0 and 1×10^{33} molec m^{-2} s^{-1} respectively, as expected for the desorption of physisorbed multilayers.

Table 6.9. Calculated kinetic parameters for monolayer and multilayer SO_2 desorbing from a bare HOPG surface and a ASW surface at 20 K.

	Monolayer		
	n	E_{des} / kJ mol^{-1}	ν_n / (molec m^{-2})$^{1-n}$ s^{-1}
Pure SO_2	0.72 ± 0.04	38.0 ± 3.4	$1.49 \times 10^{22 \pm 1.0}$
SO_2/H_2O	0.80 ± 0.04	28.3 ± 10.6	$1.85 \times 10^{14 \pm 1.3}$
	Multilayer		
	n	E_{des} / kJ mol^{-1}	ν_n / (molec m^{-2})$^{1-n}$ s^{-1}
Pure SO_2	0.05 ± 0.04	44.2 ± 4.5	$2.80 \times 10^{33 \pm 1.4}$
SO_2/H_2O	0.02 ± 0.02	42.5 ± 3.2	$2.19 \times 10^{33 \pm 0.9}$

Quantitative analysis of monolayer SO_2 desorption from a HOPG and ASW surface was challenging. The TPD spectra of monolayer SO_2 on an ASW surface showed characteristics of the amorphous and heterogeneous ASW surface, where a range of adsorption sites for SO_2 adsorption produce a broad, multi-component TPD peak. This affects the analysis by producing fractional desorption orders and a less accurate desorption energy. Pure SO_2 monolayer desorption has an energy similar to that of SO_2 multilayers, as expected from the similarity in peak temperatures of monolayer and multilayer SO_2 in pure TPD spectra.

6.5. References

1. Blake G.A., Sutton E.C., Masson C.R. and Phillips T.G., *Astrophys. J.*, **315**, (1987), 621-645
2. Keane J.V., Boonman A.M.S., Tielens A.G.G.M. and van Dishoeck E.F., *Astron. Astrophys.*, **376**, (2001), L5-L8
3. Pickett H.M. and Davis J.H., *Astrophys. J.*, **227**, (1979), 446-449
4. Snyder L.E. et al, *Astrophys. J.*, **198**, (1975), L81-L84
5. Sutton E.C. et al, *Astrophys. J. Supp. Ser.*, **97**, (1995), 455-496
6. van der Tak F.F.S., Boonman A.M.S., Braakman R. and van Dishoeck E.F., *Astron. Astrophys.*, **412**, (2003), 133-145
7. Wakelam V. et al, *Astron. Astrophys.*, **413**, (2004), 609-622
8. Bockelée-Morvan D. et al, *Astron. Astrophys.*, **353**, (2000), 1101-1114
9. Despois D., Crovisier J., Bockelée-Morvan D. and Colom P., Formation of comets: Constraints from the abundance of Hydrogen Sulfide and other sulfur species. *at Astrochemistry of Cosmic Phenomena* (IAU), Singh P.D. (Ed.), (1992), 459-460
10. Fanale F.P., Brown R.H., Cruikshank D.P. and Clark F.O., *Nature*, **280**, (1979), 761-763
11. Howell R.R., Nash D.B., Geballe T.R. and Cruikshank D.P., *Icarus*, **78**, (1989), 27-37
12. Nash D.B. and Nelson R.M., *Nature*, **280**, (1979), 763-766
13. Salama F. et al, *Icarus*, **83**, (1990), 66-82
14. Smythe W.D., Nelson R.M. and Nash D.B., *Nature*, **280**, (1979), 766
15. Trafton L.M. et al, *Icarus*, **89**, (1991), 264-276
16. Boogert A.C.A., Schutte W.A., Helmich F.P., Tielens A.G.G.M. and Wooden D.H., *Astron. Astrophys.*, **317**, (1997), 929-941
17. Duley W.W., Millar T.J. and Williams D.A., *Mon. Not. R. Astron. Soc.*, **192**, (1980), 945-957
18. Charnley S.B., *Astrophys. J.*, **481**, (1997), 396-405
19. Millar T.J. and Herbst E., *Astron. Astrophys.*, **231**, (1990), 466-472
20. Lane A.L., Nelson R.M. and Matson D.L., *Nature*, **292**, (1981), 38-39
21. Hartquist T.W., Oppenheimer M. and Dalgarno A., *Astrophys. J.*, **236**, (1980), 182-188
22. Melnick G.J., Genzel R. and Lugten J.B., *Astrophys. J.*, **321**, (1987), 530-542
23. Ferrante R.F., Moore M.H., Spiliotis M.M. and Hudson R.L., *Astrophys. J.*, **684**, (2008), 1210-1220
24. Moore M.H., *Icarus*, **59**, (1984), 114-128
25. Moore M.H. and Hudson R.L., *Icarus*, **145**, (2000), 282-288
26. Moore M.H., Hudson R.L. and Carlson R.W., *Icarus*, **189**, (2007), 409-423
27. Doty S.D., van Dishoeck E.F., van der Tak F.F.S. and Boonman A.M.S., *Astron. Astrophys.*, **389**, (2002), 446-463
28. Ruffle D.P., Hartquist T.W., Caselli P. and Williams D.A., *Mon. Not. R. Astron. Soc.*, **306**, (1999), 691-695
29. Ehrenfreund P. and Charnley S.B., *Annu. Rev. Astron. Astrophys.*, **38**, (2000), 427-483
30. Schriver-Mazzuoli L., Chaabouni H. and Schriver A., *J. Molec. Struc.*, **644**, (2003), 151-164
31. Anderson A. and Walmsley S.H., *Mol. Phys.*, **10(4)**, (1966), 391-396
32. Anderson A. and Campbell M.C.W., *J. Chem. Phys.*, **67(9)**, (1977), 4300-4302
33. Giguere P.A. and Falk M., *Can. J. Chem.*, **34(12)**, (1956), 1833-1835
34. Giguere P.A. and Savoie R., *Can. J. Chem.*, **43(8)**, (1965), 2357
35. Barbe A., Delahaigue A. and Jouve P., *Spectrochimica Acta.*, **27A**, (1971), 1439-1446
36. Wiener R.N. and Nixon E.R., *J. Chem. Phys.*, **25(1)**, (1956), 175
37. Anderson A. and Savoie R., *Can. J. Chem.*, **43(8)**, (1965), 2271
38. Barker E.F., *Rev. Modern Phys.*, **14**, (1942), 198-203
39. Polo S.R. and Wilson M.K., *J. Chem. Phys.*, **22(5)**, (1954), 900-903
40. Brooker M.H., *J. Molec. Struc.*, **112**, (1984), 221-232
41. Brooker M.H. and Chen J., *Spectrochimica Acta.*, **47A(3/4)**, (1991), 315-322
42. Nash D.B. and Betts B.H., *Icarus*, **117**, (1995), 402-419

43. Sandford S.A. and Allamandola L.J., *Icarus*, **106**, (1993), 478-488
44. Khanna R.K., Zhao G., Ospina M.J. and Pearl J.C., *Spectrochimica Acta.*, **44A(6)**, (1988), 581-586
45. Collings M.P. et al, *Mon. Not. R. Astron. Soc.*, **354**, (2004), 1133-1140
46. Wassmuth H.W., Ahner J., Höfer M. and Stolz H., *Prog. Surf. Sci.*, **42**, (1993), 257-268
47. Ahner J., Effendy A. and Wassmuth H.W., *Surf. Sci.*, **269-270**, (1992), 372-376
48. Höfer M., Stolz H. and Wassmuth H.W., *Surf. Sci.*, **272(1-3)**, (1992), 342-346
49. Köhler U. and Wassmuth H.W., *Surf. Sci.*, **126(1-3)**, (1983), 448-454
50. Köhler U., Alavi M. and Wassmuth H.W., *Surf. Sci.*, **136(1)**, (1984), 243-256
51. Bolina A.S., Wolff A.J. and Brown W.A., *J. Phys. Chem. B*, **109**, (2005), 16836-16845
52. Green S.D. et al, *Mon. Not. R. Astron. Soc.*, **398**, (2009), 357-367
53. Bolina A.S., Wolff A.J. and Brown W.A., *J. Chem. Phys.*, **122**, (2005), 044713
54. Bolina A.S. and Brown W.A., *Surf. Sci.*, **598**, (2005), 45-56
55. Burke D.J., Wolff A.J., Edridge J.L. and Brown W.A., *J. Chem. Phys.*, **128**, (2008), 104702
56. Brown W.A., Viti S., Wolff A.J. and Bolina A.S., *Faraday Discussions*, **133**, (2006), 113-124
57. Brown W.A. and Bolina A.S., *Mon. Not. R. Astron. Soc.*, **374**, (2007), 1006-1014
58. Viti S., Collings M.P., Dever J.W., McCoustra M.R.S. and Williams D.A., *Mon. Not. R. Astron. Soc.*, **354(4)**, (2004), 1141-1145
59. Burke D.J. and Brown W.A., *Phys. Chem. Chem. Phys.*, **12**, (2010), 5947-5969
60. Kramer H.M. and Suzanne J., *Surf. Sci.*, **1976**, (2010), 659-669
61. Meixner D.L. and George S.M., *Surf. Sci.*, **297**, (1993), 27-39
62. de Jong A.M. and Niemantsverdriet J.W., *Surf. Sci.*, **233**, (1990), 355-365
63. King D.A., *Surf. Sci.*, **47**, (1975), 384-402
64. Ulbricht H., Zacharia R., Cindir N. and Hertel T., *Carbon*, **44**, (2006), 2931-2942
65. Ehrenfreund P., Dartois E., Demyk K. and d'Hendecourt L., *Astron. Astrophys.*, **339**, (1998), L17-L20
66. Burke D.J., Wolff A.J., Edridge J.L. and Brown W.A., *Phys. Chem. Chem. Phys.*, **10(32)**, (2008), 4956-4967
67. Malyk S., Kumi G., Reisler H. and Wittig C., *J. Phys. Chem. A*, **111**, (2007), 13365-13370
68. Wolff A.J., Carlstedt C. and Brown W.A., *J. Phys. Chem. C*, **111**, (2007), 5990-5999

Chapter 7: Summary & Astrophysical Implications

This thesis reports investigations of the adsorption and desorption of a range of astrophysically relevant ices on an interstellar dust grain analogue. Understanding of the infrared spectra of these ices, the principal method for their detection in the interstellar medium (ISM), has been achieved via the creation of a model. This model has been used to provide a discussion of the optical and physical properties of an adsorbate, responsible for the vibrational modes observed in their infrared spectra. H_2O-rich ices containing CO_2 and its sulphur substituted analogues, namely CS_2 and SO_2, were also studied to investigate the effect of trapping and diffusion of volatile molecules through a H_2O matrix. Previous astrophysical models, describing the evaporation of ices and subsequent gas phase formation of molecular species in star forming regions, have assumed that the sublimation of molecular ices occurs spontaneously[1,2]. This assumption implies that all of the ice molecules are injected into the gas phase to take part in these formation reactions at the same time. However, this study has shown that the structural properties and sublimation of a H_2O rich ice dictates the desorption of other trace species within the ice. Therefore the evaporation of each ice species occurs over a temperature range, and hence time scale, as the star forming region warms. This will affect the subsequent gas phase reactions by dictating the abundance of the required chemical reactants.

7.1. Summary

A model, simulating the reflection absorption infrared (RAIR) spectra of simple ices on a highly oriented pyrolytic graphite (HOPG) surface, has been created to investigate the optical and physical properties of an ice responsible for the observed infrared features. This model has shown, via comparison with experimental RAIR spectra of analogous ices, that the observed infrared features are affected by the changes to the wavenumber dependent complex refractive indices, n and k, and complex dielectric constant, $\tilde{\varepsilon}$, of the solid ice film. In particular, RAIR spectra of pure CO, CO_2 and H_2O ices on a HOPG surface have been simulated for the first time. Of significance to the ices studied here, is the observation of orthogonal optical (LO) and transverse optical (TO) phonon modes in the RAIR spectra of amorphous CO and CO_2 ices. LO - TO splitting is typically only observed in crystalline ices, where a simplistic model describes the optical modes as coupled vibrations within the ice, hence a regular periodicity is implied. However, the LO and TO phonon modes of a vibration are in fact described by the interaction of infrared light with polarised phonon modes within the ice, dependent on the dielectric

properties of the ice which are usually associated with periodic vibrations. This is known as the Berreman effect[3]. Understanding the exact physical and optical properties of the ice responsible for the observed LO - TO splitting has been achieved via discussion of the changes in $\tilde{\varepsilon}$, n and k in the wavenumber region corresponding to these infrared features. In particular, this effect has now been observed for vibrations of amorphous CO and CO_2 ice corresponding to a decrease in $\tilde{\varepsilon}$, in particular when $|\varepsilon| < 1$. This is in agreement with previous studies of amorphous CO and CO_2 ices, where LO - TO splitting was observed due to an increased reflectivity as a function of $k^2 - n^2$ in the wavenumber region where $n < 1$.[4-7] The study in this thesis has been used to show that LO - TO splitting is expected in amorphous ices of NH_3 and OCS, as well as in CS_2 and SO_2 ice (chapters 5 and 6 respectively), and is confirmed via comparison to experimental investigations[8,9].

Chapters 4 - 6 describe experimental results obtained from RAIR and temperature programmed desorption (TPD) studies of CO_2, SO_2 and CS_2-bearing H_2O dominated ices adsorbed on HOPG at ≥ 20 K. TPD spectra of pure CO_2, SO_2 and CS_2 ices show the formation of monolayer and multilayer ices, physisorbed on the HOPG surface. Quantitative analysis of the TPD spectra of multilayer CO_2, SO_2 and CS_2 was conducted, the results of which are summarised in table 7.1.

Table 7.1. Kinetic data derived from TPD spectra of multilayers of pure CO_2, CS_2 and SO_2 ices adsorbed on a HOPG surface at 33 K for CO_2 ices and 20 K for CS_2 and SO_2 ices.

Ice	n	E_{des} / kJ mol^{-1}	ν_n / $(molec\ m^{-2})^{1-n}\ s^{-1}$
CO_2	0	24.8 ± 1.6	$1.07 \times 10^{30 \pm 1.5}$
SO_2	0.05 ± 0.04	44.2 ± 4.5	$2.80 \times 10^{33 \pm 1.4}$
CS_2	0.14 ± 0.05	44.1 ± 6.0	$1.60 \times 10^{31 \pm 1.5}$

The desorption orders, n, and pre-exponential factors, ν_n, for the ices show characteristics of 0^{th} order desorption, common for multilayer desorption. The desorption energies, E_{des}, for CO_2, SO_2 and CS_2 are characteristic of physisorbed species. Several trends are observed when comparing the TPD spectra, and subsequently derived kinetic data, for multilayer CO_2, SO_2 and CS_2 desorption. Most significant is the increase in the desorption energy of SO_2 and CS_2 when compared to CO_2. As discussed briefly in chapters 5 and 6, the higher desorption energy is caused by increased van der Waals interactions between the ice molecules and the surface. This is a direct consequence of the increased size of the SO_2 and CS_2 molecules, as compared with CO_2. As SO_2 and CS_2 are larger than CO_2, they are more readily polarised and therefore form stronger van der Waals interactions with the HOPG surface. This is directly related to the desorption energy for physisorbed molecules as van der Waals forces are the main interactions binding the ice together and to the surface. A similar general trend is also observed in the pre-exponential factors for CO_2, SO_2 and CS_2, where the value of the pre-exponential is partially

related to the size of the adsorbed molecule. Therefore the size of the adsorbed molecule has an effect on the natural sublimation of the adsorbate ice.

Layered ices of CO_2, SO_2 and CS_2 adsorbed on a thick multilayer film of H_2O were also investigated (chapters 4 - 6). The TPD spectra of a 200 L exposure of CO_2, SO_2 and CS_2, adsorbed on a 100 L H_2O surface are shown in figure 7.1. Three desorption features for CO_2, SO_2 and CS_2 are observed in the TPD spectra of H_2O-bearing layered ices, one at the natural sublimation temperature of the ice, the other two are coincident with the H_2O TPD features. Two features are observed in the TPD spectra of H_2O multilayers, assigned to the phase transition of amorphous solid water (ASW) to crystalline ice (CI) and the desorption of CI[10]. CO_2, SO_2 and CS_2 all exhibit volcano desorption with the ASW - CI transition as well as co-desorption with CI, both of which indicate trapping of the molecules within the pores of the ASW surface. However, as evident in figure 7.1, the relative size of the trapped TPD features, with respect to the natural sublimation TPD peak, increases from CO_2 to SO_2 to CS_2. This is an indication of the ability of the molecules to trap within the pores of the ASW surface, as well as giving information about their ability to diffuse through the H_2O matrix to desorb. Upon warming the binary layered ices, pores on the surface of the ASW film begin to close, trapping any surface bound adsorbate molecules. Smaller molecules, such as CO_2, are able to diffuse

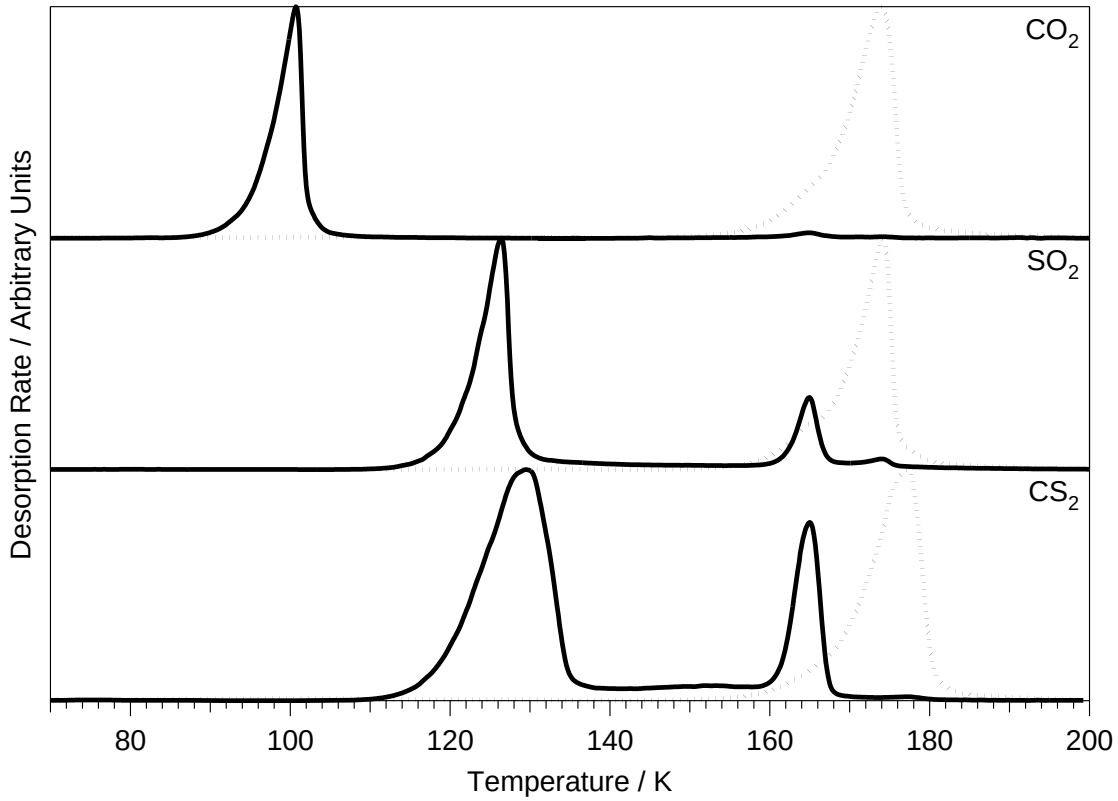

Figure 7.1. TPD spectra of a 200 L exposure of CO_2, SO_2 and CS_2 (top to bottom) each adsorbed on 100 L H_2O adsorbed on a HOPG surface at ≥ 20 K.

through the H_2O matrix to desorb at their natural sublimation temperature. Therefore the size of the trapped CO_2 TPD features is small. Conversely a larger molecule, such as CS_2, cannot readily diffuse through the H_2O matrix, and hence larger trapped features are evident in the TPD spectra. The surface bound CS_2, now trapped, desorbs with the H_2O TPD features. Therefore the size of the adsorbed molecule has a great effect on the diffusion, and degree of trapping, within and through a H_2O film.

Finally, mixed ices of CO_2, SO_2 and CS_2 with H_2O were also investigated. Figure 7.2 shows the TPD spectra of a 200 L exposure of a 15% CO_2:H_2O, 10% SO_2:H_2O and 10% CS_2:H_2O mixture, each adsorbed on HOPG at ≥ 20 K. In agreement with the TPD spectra of H_2O-bearing ice layers (figure 7.1), three desorption features are observed for CO_2, SO_2 and CS_2, two of which are coincident with the H_2O TPD features. As the ices are intimately mixed, the observation of desorption at the natural sublimation temperature of the molecules is an indication of the diffusion ability of the molecules through the H_2O matrix. As CO_2 is the smallest molecule, it can more readily diffuse through the mixed CO_2:H_2O ice and therefore more CO_2 will desorb at its natural sublimation temperature, as observed in figure 7.2. For SO_2 and CS_2 mixed ices, the size of the natural sublimation TPD feature decreases and the trapped TPD features increase. By integrating the area of each TPD feature, it was found that 71% of the total CO_2 remains

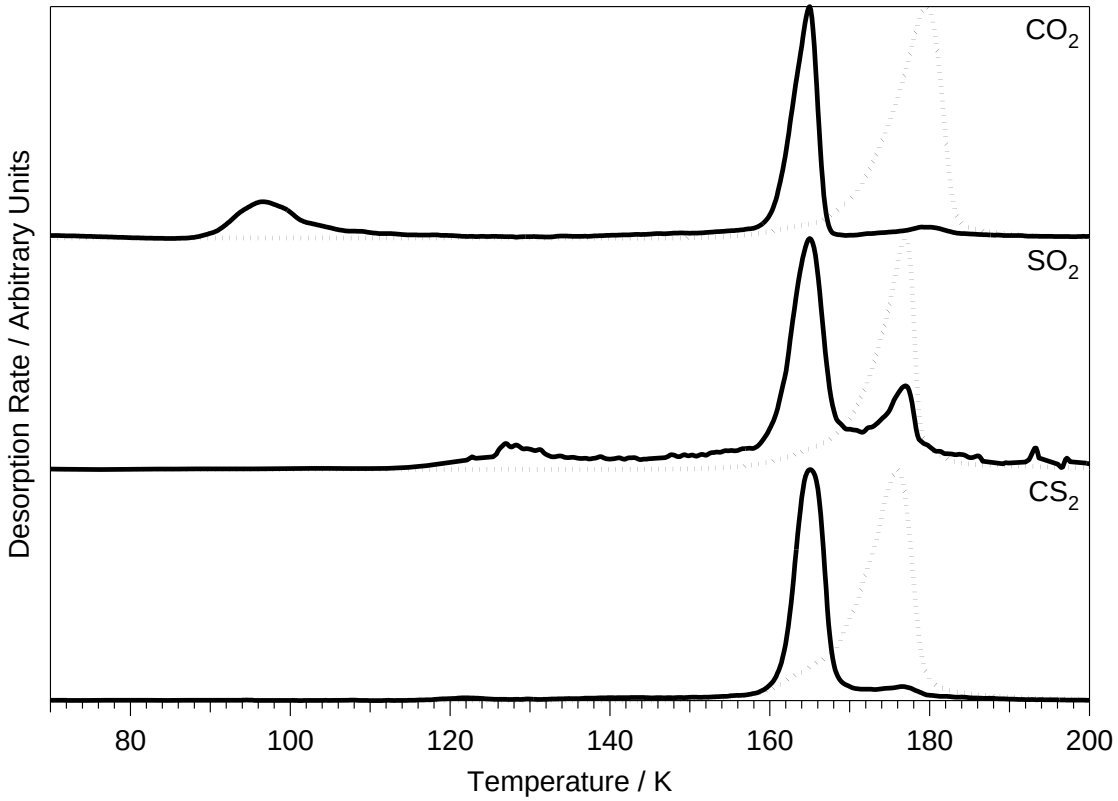

Figure 7.2. TPD spectra of a 200 L exposure of a 15% CO_2:H_2O, 10% SO_2:H_2O and a 10% CS_2:H_2O mixture (top to bottom) adsorbed on a HOPG surface at ≥ 20 K.

trapped within the ice mixture to desorb with the H_2O.For SO_2 and CS_2 86% and 99% of the molecules remain trapped in the ice mixture respectively.

Several factors clearly play a key role in the trapping and diffusion of volatile molecules in and through an ASW matrix, including the size of the molecules with respect to the size of the pores in the ASW. This plays a significant role in the trapping of species within the ASW ice, as varying degrees of trapping are observed with respect to the size of the molecule. From this study, the ability for a small molecule, for example CO_2, to diffuse through a porous H_2O ice is much greater than a larger molecule, for example CS_2. Therefore less CO_2 remains trapped within a mixed ice with H_2O than the respective ice with CS_2. Translating this to the evaporation of an interstellar ice mantle indicates that upon warming in a hot core, smaller molecules such as CO and CO_2 will mostly desorb at their natural sublimation temperatures, at a lower temperature and earlier time scale. Conversely, larger molecules, such as SO_2 and CS_2, are expected to evaporate with H_2O. Due to the higher surface binding energy of H_2O on a surface, this will occur at higher temperatures, and therefore at a later time scale.

7.2. Astrochemical Model

As discussed in chapter 1, astrochemical models simulating the evaporation of interstellar ices, and the subsequent gas phase chemistry in hot core regions, can be created, incorporating the kinetic data obtained from experimental TPD spectra. To show how this kinetic data can be incorporated into these simulations, as well as to show how the slow heating rate in the ISM affects the desorption of molecular ices, a simple model can be created to recreate the TPD spectra on astronomical timescales. This model, based upon the TPD simulation used in chapter 5 to confirm the validity of the quantitative analysis method, was created using the Chemical Kinetics Simulator (Version 1.0, IBM Almaden Research Centre, 1995). The heating rate was taken to be the heating rate characteristic of the warming in a hot core surrounding a medium sized, 25 $M_\odot$ star, as used previously by Brown et al[11]. This heating rate is non-linear, unlike the linear heating rate used in the laboratory of 0.5 K s^{-1}, and obeys the relationship:

$$T_{dust} = A \times time^{B} \qquad (7.1)$$

where T_{dust} is the temperature of the dust grain as a function of the age of the core, time is taken as the amount of time, in years, since the hot core began warming. A and B are taken as $A = 1.706 \times 10^{-4}$ K yr^{-B}, B = 1.289 for a star of 25 $M_\odot$.[11]

Contrary to the model used in chapter 5, the model used here simulates the desorption of an astronomically relevant, H_2O dominated mixed ice, containing CO, CO_2, OCS, SO_2 and CS_2. To help illustrate the fact that interstellar ices do not evaporate all together, as a function of the size of the molecule, CO and OCS ices were included in the simulation. This provides an example of a very small molecule, CO, and completes the series of sulphur substituted analogues to CO_2, namely OCS. CH_3OH was omitted from the model, despite being a major constituent of interstellar ices as it has been shown to be a 'H_2O-like' desorbing species[12], and as such will only show one desorption feature in this model, coincident with the desorption of H_2O.

The composition of the ice was taken from the fractional abundances of the mixed interstellar ices observed in the star forming region W33A[13-22], as shown in table 1.2 (chapter 1), summarised again in table 7.2. As definitive detection of CS_2 has not been made in the molecular ices within star forming regions, the CS_2 abundance was assumed to be equal to the least abundant species which has been observed in these regions, namely OCS with an abundance of 0.2% with respect to H_2O.

Table 7.2. Relative abundances, with respect to H_2O, of a typical H_2O dominated molecular ice observed within the star forming region W33A[13-22]. †CS_2 abundance was assumed to be equal to the least abundant species, OCS, with an abundance of 0.2% with respect to H_2O.

Molecular ice	% abundance with respect to H_2O
H_2O	100
CO	8
CO_2	13
OCS	0.2
SO_2	0.31
CS_2 †	0.2

The three desorption features, as observed in TPD spectra of CO_2, SO_2 and CS_2-bearing H_2O ices, were simulated by combining the method used in chapter 5 with a simplified version of the model used by Collings et al[12]. The desorption of the molecular ices at their natural sublimation temperature was simulated via reaction 7.2:

$$X_{NS} \rightarrow X_g \qquad (7.2)$$

where X is the molecule and can be H_2O, CO, CO_2, OCS, SO_2 or CS_2. X_{NS} describes the ice molecules on the surface of the dust grain, which are free to diffuse through the ice mixture to desorb at the natural sublimation temperature of the molecule. X_g describes the gas phase molecules, which are monitored and used to produce the simulated TPD spectra.

The trapped TPD features are recreated by adapting the model of Collings et al[12], via reactions 7.3 - 7.5:

$$X_{ASW} \rightarrow X_g \quad (7.3)$$

$$X_{ASW} \rightarrow X_{CI} \quad (7.4)$$

$$X_{CI} \rightarrow X_g \quad (7.5)$$

where X_{ASW} describes the molecules in the ASW matrix, which are not free to diffuse through the ice mixture and hence are trapped. In particular X_{ASW}, and reaction 7.3, describe the molecules which desorb in a molecular volcano with the ASW - CI transition. X_{CI} describes the ice molecules which remain in the ice mixture after the ASW - CI transition, to co-desorb with CI in reaction 7.5. Reaction 7.4 is used to convert a portion of trapped molecules to sites within the ice which will lead to co-desorption in reaction 7.5. Using this method requires the initial concentrations of both X_{NS} and X_{ASW} species to be specified, as the number of trapped molecules are not explicitly calculated within the model. This has the advantage whereby the different relative amounts of trapping as a function of molecular size, as observed in experimental TPD spectra, can be applied to the simulation.

Table 7.3. List of kinetic parameters used in the simulation of the evaporation of an astrophysically relevant ice, including the abundances of each molecule in the molecular ice, as well as the fraction of each species remaining trapped in the ice mixture to desorb with the H_2O.

Reaction	E_{des} / kJ mol^{-1}	n	ν_n / (molec m^{-2})$^{1-n}$ s^{-1}	Number of molecules / molec	% Trapped
$H_2O_{NS} \rightarrow H_2O_g$ [†]	48.0	1	1.0×10^{11}	2.40×10^{18}	0
$CO_{NS} \rightarrow CO_g$ [†]	6.87[†]	0	7.0×10^{26}	1.54×10^{17}	65[#]
$CO_{2\,NS} \rightarrow CO_{2\,g}$	24.8	0	1.1×10^{30}	1.99×10^{17}	71
$OCS_{NS} \rightarrow OCS_g$ [‡]	28.6	0.11	4.2×10^{32}	2.63×10^{15}	79[*]
$SO_{2\,NS} \rightarrow SO_{2\,g}$	44.2	0.05	2.8×10^{33}	3.94×10^{15}	86
$CS_{2\,NS} \rightarrow CS_{2\,g}$	44.1	0.14	1.6×10^{31}	2.33×10^{15}	99
$X_{ASW} \rightarrow X_g$ [†]	39.9	1	1.9×10^{11}	-	-
$X_{ASW} \rightarrow X_{CI}$ [†]	39.9	1	0.1×10^{11}	-	-
$X_{CI} \rightarrow X_g$ [†]	48	1	1.0×10^{11}	-	-

[†]kinetic data taken from references [6, 8], [‡]kinetic data taken from reference [9], [#]fraction of trapped CO taken from reference [10] and [*]fraction of trapped OCS derived from trends in trapped CO_2, SO_2 and CS_2.

The kinetic parameters used in this model, shown in table 7.3, were taken from chapters 4 - 6 for CO_2, SO_2 and CS_2 and from Bolina et al[10], Burke et al[9] and Collings et al[12], for H_2O, OCS and CO respectively. The kinetic parameters used to simulate the desorption of trapped species, reactions 7.3 - 7.5, are shown in table 7.3. The initial surface coverage of H_2O was taken as 1.20×10^{18} molec cm^{-2}, as calculated by considering the atomic radii of O and H, and the O-H

bond length, of H_2O. This surface coverage corresponds to a H_2O ice thickness of 0.3 μm, comparable to the thicknesses of interstellar ices[23,24]. The number of CO, CO_2, OCS, SO_2 and CS_2 molecules were then calculated from the initial H_2O coverage, using the fractional abundances observed in interstellar ices with respect to H_2O, table 7.2. As the concentration of trapped and 'non-trapped' molecules can be varied, via alteration of the initial concentrations of X_{NS} and X_{ASW}, the total number of molecules of CO_2, SO_2 and CS_2 was used to calculate X_{NS} and X_{ASW} via the relative amounts of trapping observed in experimental TPD spectra, chapters 4 - 6, as a function of molecular size. The amount of trapped CO was calculated from the fractions used by Viti et al[2], whereas the amount of trapped OCS was assumed from the trends observed between CO_2, SO_2 and CS_2.

As shown in chapter 5, to recreate experimental TPD spectra an extra step is also required to remove the gas phase molecules via a pumping mechanism;

$$X_g \rightarrow X_p \tag{7.6}$$

where a temperature independent rate of 3.4×10^{-9} s^{-1} was used, in line with that used by Brown et al[23].

To test the validity of the model, as well as to show the effect of the astrophysical heating rate on the desorption of mixed ices, the TPD spectra of CO_2:H_2O, SO_2:H_2O and CS_2:H_2O mixed ices were simulated, analogous to those in figure 7.2. These are shown in figure 7.3. Several similarities are observed when comparing the TPD spectra in figures 7.2 and 7.3. Most prominently, the size of the natural sublimation peak of CO_2, SO_2 and CS_2 decreases with increasing molecular size. The main differences observed are in the peak temperatures of each desorption process, as well as the shape and separation between the trapped desorption features. As the model utilises a simplified version of that used by Collings et al[12], the simulated H_2O TPD spectrum does not recreate the characteristic 'bump' on the leading edge, observed in the experimental H_2O TPD spectrum. This is because the model does not properly simulate the ASW - CI transition, where only the volcano and co-desorption of the trapped species are simulated. This assumption is valid however, as the ASW - CI transition occurs at a lower temperature than the onset of desorption of H_2O upon application of the astronomical heating rate. Therefore the characteristic 'bump' would not be observed even if it was included in the model. However, the volcano and co-desorption features are simulated, which is the main focus of this simulation.

As evidenced via comparison of figures 7.2 and 7.3, is the fact that the peak temperature of each desorption process is much lower than that observed in the experimental TPD spectra. This is in agreement with previous simulations[2,12,23] where a slower heating rate, to the order

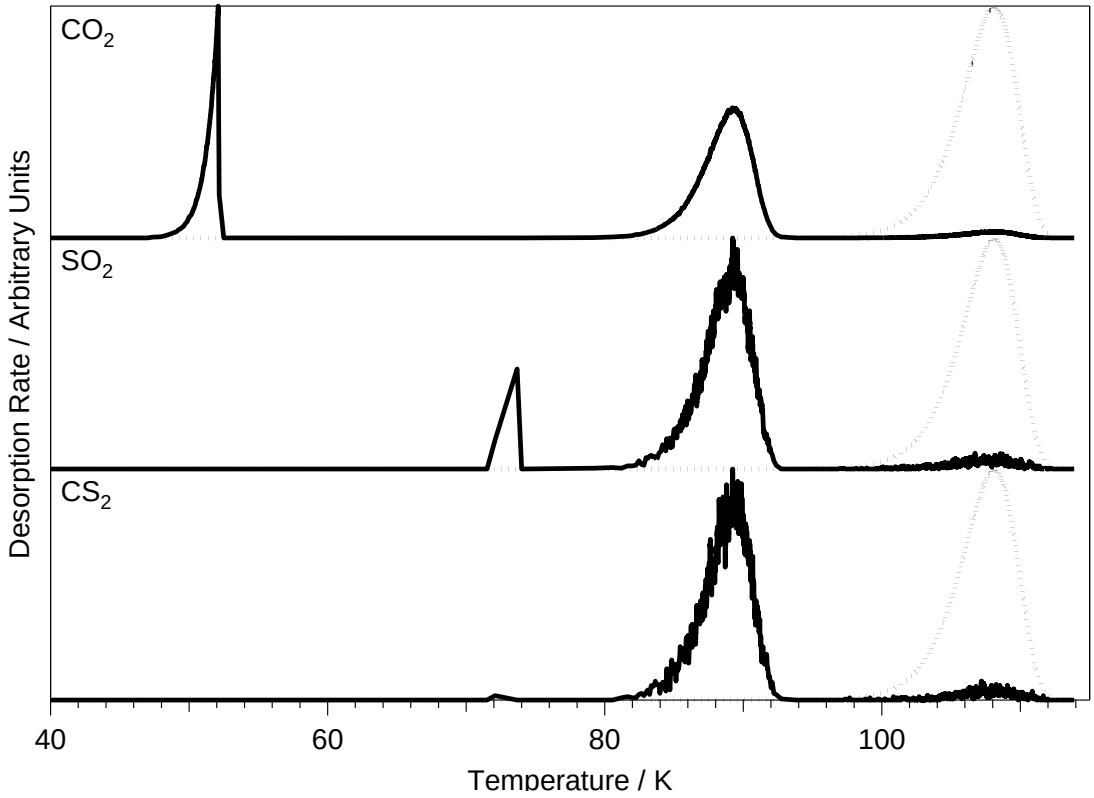

Figure 7.3. Simulated TPD spectra of a 0.3 μm thick, 13% CO_2:H_2O, 0.3% SO_2:H_2O and a 0.2% CS_2:H_2O (top to bottom) mixture using an astrophysically relevant heating rate of $T = 1.706 \times 10^{-4} \times t^{1.289}$, characteristic of the warming in a hot core near a 25 $M_\odot$ star. (See text).

of 0.4 K century^{-1} is used, as opposed to 0.5 K s^{-1} in the laboratory, greatly reduces the temperature at which evaporation is observed. Therefore the model used here shows the TPD spectra as if they were to be taken over several centuries. Simulating the TPD spectra of each desorption process, using an astrophysical heating rate, is of importance, as astrophysical models are created using the desorption temperature of each species and process, rather than their kinetic parameters, n, E_{des} and ν_n. For example, Viti et al[2] report the temperatures of the volcano and co-desorption processes as a function of the mass of the star.

To simulate the evaporation of interstellar ices, and hence show the ejection of molecular species into the gas phase, the model has to be slightly modified, and reaction 7.6 for each molecule removed. This is important as there is no removal of gas phase species via pumping in star forming regions, where the removal of gas phase species predominantly occurs in these regions via gas phase chemical reactions. This approach to simulating the evaporation of interstellar ices is different to the models employed by astrophysicists, as each desorption process in this model is simulated from their kinetic parameters, n, E_{des} and ν_n. Therefore these results could be compared to astrophysical models as a comparison between the two approaches.

Figure 7.4 shows the gas phase abundances of a range of astrophysically relevant ice species, following evaporation from an icy mantle analogue. As immediately observed, the evaporation of each species does not occur spontaneously, where the evaporation of the bulk of the CO, for example, occurs at two times, separated by ≈20,000 years. This may have a significant impact on the gas phase reactions which occur in star forming regions due to the availability of other gas phase species to form more complex molecules. For example, at low time scales the availability of reactive species such as H or OH may result in a higher abundance of saturated organic molecules. Conversely, the availability of these species may be depleted at later time scales, and hence may result in the formation of other molecules.

As discussed in chapter 1, SO_2 can be used as a *'chemical clock'* to determine the age of a hot core region as the gas phase formation of SO_2 from H_2S has been well studied[25,26]. This has been shown to be particularly important for 'young' hot cores, less than 10^5 years old. However as observed in figure 7.4, the evaporation of SO_2 from an icy mantle occurs at both 2.3 and 2.7 × 10^4 years, and would therefore affect the use of SO_2 as a chemical clock if evaporation from a dust grain surface were not considered. For example, from figure 7.4, excluding the injection of SO_2 into the gas phase via evaporation from an interstellar ice reduces the expected gas phase abundance of SO_2 by 1.64 × 10^{-3} with respect to H_2O. This

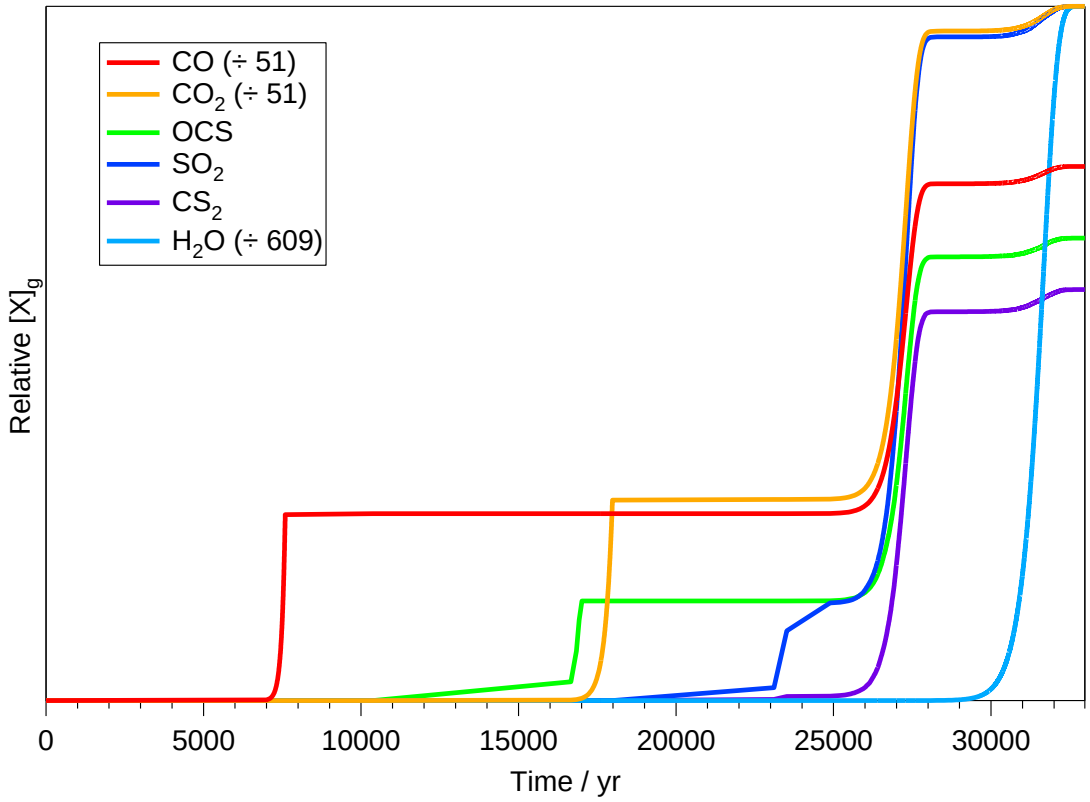

Figure 7.4. Simulated gas phase abundances of molecular species, following evaporation from an interstellar ice mantle in a hot core surrounding a 25 $M_\odot$ star.

means that a degree of inaccuracy is incorporated into the precision of the use of SO_2 as a chemical clock. This error is enhanced by the fact that the injection of SO_2 into the gas phase is partially complete at 2.3×10^4 years, the remaining occurring 4000 years later.

This thesis has shown the importance of the adsorption and desorption of H_2O dominated molecular ices. The desorption of H_2O dominates the desorption features of minor species contained within the ice, where the size of the volatile molecules also plays an important role in the diffusion and trapping ability in a H_2O matrix. This has immediate consequences for the gas phase chemistry in star forming regions, where the reaction routes change as a function of time as certain reactive species, such as OH, are depleted. The observation of these ices in the ices of comets can also provide a direct insight into the chemistry and nature of the stellar nursery in which our solar system was formed to provide clues on the composition of dense molecular clouds which may be capable of supporting life.

7.3. References

1. Viti S. and Williams D.A., *Mon. Not. R. Astron. Soc.*, **305**, (1999), 755-762
2. Viti S., Collings M.P., Dever J.W., McCoustra M.R.S. and Williams D.A., *Mon. Not. R. Astron. Soc.*, **354(4)**, (2004), 1141-1145
3. Berreman D.W., *Phys. Rev.*, **130(6)**, (1963), 2193-2198
4. Baratta G.A. and Palumbo M.E., *J. Opt. Soc. Am. A*, **15(12)**, (1998), 3076-3085
5. Ehrenfreund P., Boogert A.C.A., Gerakines P.A., Tielens A.G.G.M. and van Dishoeck E.F., *Astron. Astrophys.*, **328**, (1997), 649-669
6. Palumbo M.E. and Strazzulla G., *Astron. Astrophys.*, **269**, (1993), 568-580
7. Palumbo M.E., Baratta G.A., Collings M.P. and McCoustra M.R.S., *Phys. Chem. Chem. Phys.*, **8**, (2006), 279-284
8. Binbrek O.S. and Anderson A., *Chem. Phys. Lett.*, **15(3)**, (1972), 421-427
9. Burke D.J. and Brown W.A., *Phys. Chem. Chem. Phys.*, **12**, (2010), 5947-5969
10. Bolina A.S., Wolff A.J. and Brown W.A., *J. Phys. Chem. B*, **109**, (2005), 16836-16845
11. Brown W.A., Viti S., Wolff A.J. and Bolina A.S., *Faraday Discussions*, **133**, (2006), 113-124
12. Collings M.P., Dever J.W., Fraser H.J. and McCoustra M.R.S., *Astrophys. Space Sci.*, **285**, (2003), 633-659
13. Boogert A.C.A. et al, *Astron. Astrophys.*, **315**, (1996), L377-L380
14. Boogert A.C.A. et al, *Astron. Astrophys.*, **336**, (1998), 352-358
15. Chiar J.E., Adamson A.J. and Whittet D.C.B., *Astrophys. J.*, **472**, (1996), 665-672
16. Chiar J.E. et al, *Astrophys. J.*, **498**, (1998), 716-727
17. Dartois E. et al, *Astron. Astrophys.*, **342**, (1999), L32-L35
18. Gibb E.L. et al, *Astrophys. J.*, **536**, (2000), 347-356
19. Palumbo M.E., Tielens A.G.G.M. and Tokunaga A.T., *Astrophys. J.*, **449**, (1995), 674-680
20. Geballe T.R., *Mon. Not. R. Astron. Soc.*, **251**, (1991), 24-25
21. Smith R.G., *Mon. Not. R. Astron. Soc.*, **249**, (1991), 172-176
22. Boogert A.C.A., Schutte W.A., Helmich F.P., Tielens A.G.G.M. and Wooden D.H., *Astron. Astrophys.*, **317**, (1997), 929-941
23. Brown W.A. and Bolina A.S., *Mon. Not. R. Astron. Soc.*, **374**, (2007), 1006-1014
24. Collings M.P. et al, *Mon. Not. R. Astron. Soc.*, **354**, (2004), 1133-1140
25. Millar T.J. and Herbst E., *Astron. Astrophys.*, **231**, (1990), 466-472
26. Charnley S.B., *Astrophys. J.*, **481**, (1997), 396-405